A N N U A L R E P O R T

2019

and list of publications

Bayerisches Forschungsinstitut
für Experimentelle Geochemie und Geophysik
Universität Bayreuth

Bayerisches Geoinstitut
Universität Bayreuth
95440 Bayreuth
Germany

Telephone: +49-(0)921-55-3700
Telefax: +49-(0)921-55-3769
e-mail: bayerisches.geoinstitut@uni-bayreuth.de
www: http://www.bgi.uni-bayreuth.de

Editorial compilation by: Florian Heidelbach and Petra Buchert
Section editors: Andreas Audétat, Tiziana Boffa Ballaran, Audrey Bouvier,
Leonid Dubrovinsky, Dan Frost, Florian Heidelbach, Gregor Golabek,
Tomoo Katsura, Hans Keppler, Catherine McCammon,
Nobuyoshi Miyajima, Dave Rubie, Gerd Steinle-Neumann, Tony Withers

Staff and guests of the Bayerisches Geoinstitut in **July 2019**:

Die Mitarbeiter und Gäste des Bayerischen Geoinstituts im **Juli 2019:**

first row, from left (1. Reihe, v. links) Nobuyoshi Miyajima, Iuliia Koemets, Biao Wang, Anand Dwivedi, Saiana Khandarkhaeva, Marija Putak Juriček, Greta Rustioni, Tiziana Boffa Ballaran, Sumith Abeykoon, Rong Huang, Danielle Silva Souza

second row, from left (2. Reihe, v. links) Laura Cialdella, Florian Heidelbach, Petra Buchert, Hongzhan Fei, Filippe Ferreira, Tomo Katsura, Victoria Szlachta, Giacomo Criniti, Dorothea Wiesner, Ulrike Trenz, Ning Ma

third row, from left (3. Reihe, v. links) Jie Yao, Ingrid Blanchard, Dan Frost, Egor Zakharchenko, Anna Spivak, Anna Dinius, Keisuke Nishida, Alena Krupp, Sven Linhardt, Gerald Bauer, Stefan Übelhack

fourth row, from left (4. Reihe, v. links) Egor Koemets, Artem Chanyshev, Tomonori Ohashi, Thomas Meier, Florian Trybel, Marcel Thielmann, Andreas Audétat, Heinz Fischer, Svyatoslav Shcheka

fifth row, from left (5. Reihe, v. links) Timofey Fedotenko, Takayuki Ishii, Leonid Dubrovinsky, Holger Kriegl, Raphael Njul, Alexander Rother, Hans Keppler, Detlef Krauße, Gerd Steinle-Neumann, Dave Rubie, Oliver Rausch

Absent (Es fehlten) Dmitry Bondar, Audrey Bouvier, Serena Dominijanni, Dmitry Druzhbin, Lisa Eberhard, Philipp Eichheimer, Gregor Golabek, Alexander Kurnosov, Enrico Marzotto, Catherine McCammon, Caterina Melai, Sergey Ovsyannikov, Anke Potzel, Janina Potzel, Niccoló Satta, Romina Scharfenberg, Nicki Siersch, Kirill Vlasov, Tony Withers, Longjian Xie

Contents

Foreword

Research at the Bayerisches Geoinstitut is largely carried out by young scientists, particularly postdocs and Ph.D. students. I am therefore very pleased that this annual report contains several remarkable scientific advancements that were achieved by our students. The contribution by Lisa Eberhard and her colleagues on page 51 investigates the oxidation state of fluids in subduction zones. There is a general belief that these fluids are always rather oxidized and their high oxidation state may for example be essential for the enrichment of certain trace elements, such as copper and molybdenum, to economically usable ore deposits that provide most of the world supply of these metals. One important source of the aqueous fluids in subduction zones is the dehydration of serpentine. Eberhard and coworkers carefully studied the incorporation of Fe^{3+} in serpentine, which controls the redox state of the fluids released. The incorporation of Fe^{3+} appears to be coupled with Al^{3+} and can be accurately described by a thermodynamic model. The model suggests that at relatively low temperatures, in the forearc, the conditions in the subducted slab are actually quite reduced, such that sulfides and graphite become stable. Only at temperatures of 600-700 °C, as they are expected below the volcanic arc, oxygen fugacity increases sufficiently to oxidize sulfides to sulfate and graphite to carbonate. Interestingly, this effect could cause some concentration and focusing of copper and molybdenum in the volcanic arc, since these metals will remain locked up in insoluble sulfides in the forearc, while they become fluid mobile only once the slab reaches the depth below the volcanic front.

The combination of *in situ* X-ray diffraction and simultaneous Brillouin scattering in diamond cells is a technology that has been very much advanced at Bayerisches Geoinstitut. It allows very precise measurements of seismic wave velocities and full elastic tensors of minerals under high pressure; these data are essential for interpreting seismic data and converting them into mineralogical models of Earth's interior. One problem in such studies has always been that it was impossible to measure the elastic properties of $MgSiO_3$ bridgmanite, the main mineral of the lower mantle, to high pressures, since its Brillouin peaks overlap with the very strong peaks from the diamond anvils. But elastic properties are anisotropic. By carefully choosing the orientation of the bridgmanite crystal relative to the diamond, Giacomo Criniti and coworkers (page 85) managed to carry out experiments where *e.g.* the minimum of the p wave velocity of bridgmanite coincided with the direction of the maximum s wave velocity in diamond, such that the two peaks could be separately observed. This provided long-sought after constraints on the elastic properties of the lower mantle. In another study using similar methods, Nicki Siersch and her colleagues (page 86) investigated the elastic properties of $MgSiO_3$ akimotoite, a phase that may be stable in subducted slabs. The results obtained suggest that the seismic wave anisotropies observed in the deep transition zone of the mantle, just above the 660 km discontinuity, may be related to the accumulation of material from subducted oceanic slabs.

While the scientific activities at Bayerisches Geoinstitut keep expanding thanks to a constant influx of young scientists, we also received in 2019 the sad news that our long-time colleague Prof. Ahmed El Goresy had passed away peacefully at home. Ahmed was a famous meteorite researcher. After retirement from the MPI for Nuclear Physics in Heidelberg he had spent more than a decade at our institute. Many scientists from all over the world visited him to benefit from his unique abilities in studying meteorites and finding unusual phases with the polarizing microscope. We will miss him a lot.

On the behalf of my colleagues, I would like to thank the *Free State of Bavaria* as represented by the *Bavarian State Ministry of Science, Research and Art*, as well as the *Commission for High-Pressure Research in Geoscience* for their continuing support and strong commitment to the Bayerisches Geoinstitut. I would further like to thank the *President and Leadership of the University of Bayreuth* for their high regard of our institute. We also gratefully acknowledge generous support from external funding agencies, in particular the *Alexander von Humboldt Foundation*, the *European Union*, the *German Science Foundation,* and the *Federal Ministry of Education and Research*, which continue to contribute greatly to the further development and success of the Geoinstitut.

Bayreuth, March 2020 Hans Keppler

Vorwort

Die Forschung am Bayerischen Geoinstitut wird vor allem durch junge Wissenschaftler (Doktoranden und Postdoktoranden) vorangetrieben. Es ist daher sehr erfreulich, dass dieser Jahresbericht mehrere bemerkenswerte Leistungen unserer Doktoranden enthält. Der Beitrag von Lisa Eberhard auf Seite 51 untersucht den Oxidationszustand von Fluiden in Subduktionszonen. Es wird allgemein angenommen, dass diese Fluide generell ziemlich oxidiert sind. Ihr hoher Oxidationszustand ist möglicherweise eine wesentliche Voraussetzung für die Anreicherung bestimmter Spurenelemente wie Kupfer oder Molybdän zu den Erzlagerstätten, die den größten Teil der Weltproduktion dieser Metalle liefern. Eine wichtige Quelle wässriger Fluide in Subduktionszonen ist die Dehydratation von Serpentin. Eberhard und Mitarbeiter haben den Einbau von Fe^{3+} in Serpentin untersucht, der den Redoxzustand von Fluiden kontrolliert. Der Einbau von Fe^{3+} ist gekoppelt mit Al^{3+} und kann mit einem thermodynamischen Modell genau beschrieben werden. Das Modell zeigt, dass bei relativ niedrigen Temperaturen im Vorbereich der Subduktionszone die Bedingungen in der subduzierten Platte tatsächlich ziemlich reduzierend sind, so dass Sulfide und Graphit stabil sind. Erst bei Temperaturen von 600-700 °C, wie sie unterhalb der vulkanischen Zone erwartet werden, steigt die Sauerstofffugazität soweit an, dass Sulfide zu Sulfat und Graphit zu Karbonaten oxidiert werden. Dies könnte zu einer Konzentration von Kupfer und Molybdän in der vulkanischen Zone führen, da diese Metalle im flachen Teil der Subduktionszone in unlöslichen Sulfiden gespeichert und erst unterhalb der vulkanischen Front durch Oxidation freigesetzt werden.

Die Kombination von in-situ-Röntgenbeugung und Brillouin-Spektroskopie in Diamantstempelzellen ist eine Technik, die am Bayerischen Geoinstitut wesentlich weiterentwickelt wurde. Sie erlaubt sehr genaue Messungen der seismischen Geschwindigkeiten und der vollständigen elastischen Tensoren von Mineralen unter hohem Druck. Diese Daten sind wesentlich für die Interpretation seismischer Daten und für die Entwicklung mineralogischer Modelle des Erdinnern. Bisher war es jedoch unmöglich, die elastischen Eigenschaften von $MgSiO_3$-Bridgmanit, dem Hauptmineral des unteren Mantels bei hohem Druck zu messen, da die entsprechenden Brillouin-Banden mit dem Brillouin-Spektrum der Diamantstempel überlappten. Elastische Eigenschaften von Mineralen sind jedoch anisotrop. Durch sorgfältige Kontrolle der Orientierung des Bridgmanit-Kristalls relativ zum Diamant konnten Giacomo Criniti und Mitarbeiter (Seite 85) Experimente ausführen, in denen zum Beispiel das Minimum der P-Wellen-Geschwindigkeit des Bridgmanits zusammenfiel mit dem Maximum der S-Wellen-Geschwindigkeit im Diamant, sodass beide Banden separat beobachtet werden konnten. Dies lieferte lange gesuchte Daten über die elastischen Eigenschaften des unteren Mantels. In einer weiteren Studie haben Nicki Siersch und Mitarbeiter (Seite 86) mit ähnlichen Methoden die elastischen Eigenschaften von $MgSiO_3$-Akimotoit untersucht, eine Phase, die möglicherweise in subduzierten Platten stabil ist. Die Ergebnisse lassen vermuten, dass die beobachtete Anisotropie in den seismischen Geschwindigkeiten in der tiefen Übergangszone des Erdmantels, knapp über der 660 km-Diskontinuität, möglicherweise auf die Akkumulation von subduzierter ozeanischer Kruste zurückzuführen ist.

Während die wissenschaftlichen Aktivitäten des Bayerischen Geoinstituts dank zahlreicher junger Forscher weiter expandieren, erreichte uns 2019 auch die traurige Nachricht, dass unser langjähriger Kollege Prof. Ahmed El Goresy friedlich zuhause verstorben ist. Ahmed war ein weltberühmter Meteoritenforscher. Nach Emeritierung am MPI für Kernphysik in Heidelberg hat er mehr als ein Jahrzehnt an unserem Institut gearbeitet. Viele Wissenschaftler aus der ganzen Welt haben ihn besucht, um von seinen einmaligen Fähigkeiten bei der Untersuchung von Meteoriten und der Identifizierung ungewöhnlicher Minerale mit dem Polarisations-mikroskop zu profitieren. Wir werden ihn sehr vermissen.

Meine Kollegen und ich möchten dem *Freistaat Bayern*, vertreten durch das *Bayerische Staatsministerium für Wissenschaft, Forschung und Kunst*, und dem *Beirat für Geowissenschaftliche Hochdruckforschung der Bayerischen Akademie der Wissenschaften* unseren Dank für ihre fortwährende Unterstützung des Bayerischen Geoinstituts aussprechen. Darüber hinaus möchten wir dem Präsidenten und der Hochschulleitung der Universität Bayreuth ausdrücklich für ihre zuverlässige und kontinuierliche Unterstützung unseres Instituts danken. Wir sind auch für die großzügige Förderung durch externe Geldgeber dankbar, insbesondere der *Alexander-von- Humboldt-Stiftung*, der *Europäischen Union* und der *Deutschen Forschungsgemeinschaft*, die ebenfalls wesentlich zur Entwicklung und zum Erfolg des Bayerischen Geoinstituts beigetragen haben.

Bayreuth, im März 2020 Hans Keppler

1. Advisory Board and Directorship

1.1 Advisory Board

The *Beirat für Geowissenschaftliche Hochdruckforschung der Bayerischen Akademie der Wissenschaften* advises on the organisation and scientific activities of the institute. Members of this board are:

Prof. Dr. Gerhard BREY	Institut für Geowissenschaften der Johann Wolfgang Goethe-Universität, Frankfurt am Main
Prof. Dr. Ulrich CHRISTENSEN	Max-Planck-Institut für Sonnensystemforschung, Katlenburg-Lindau
Prof. Dr. Rudolf GROSS (Vice Chairman)	Walther-Meißner-Institut für Tieftemperatur-forschung (WMI), Garching
Prof. Dr. Rüdiger KNIEP	Emeritus, Max-Planck-Institut für Chemische Physik fester Stoffe, Dresden
Prof. Dr. Herbert PALME	Emeritus, Institut für Mineralogie und Geochemie der Universität zu Köln – Senckenberg Forschungsinstitut und Naturmuseum Frankfurt/M.
Prof. Dr. Markus RIEDERER (Chairman)	Julius-von-Sachs-Institut für Biowissenschaften, Würzburg
Prof. Dr. Ekhard SALJE, FRS, FRSA	Department of Earth Sciences, University of Cambridge
Prof. Dr. Christine THOMAS	Institut für Geophysik der Westfälischen Wilhelms-Universität Münster

The Advisory Board held a meeting in Bayreuth (17.05.2019).

1.2 Leadership

Prof. Dr. Hans KEPPLER (Director)
Prof. Dr. Dan FROST (Deputy Director)
Prof. Dr. Tomoo KATSURA

2. Staff, Funding and Facilities

2.1 Staff

At the end of 2019 the following staff positions existed in the Institute:

- Scientific staff: **15**
- Technical staff: **14**
- Administrative staff: **2**
- Administrative officer: **1**

During 2019, 41 scientific positions (355 months) were funded by grants raised externally by staff members of the institute. In addition, 4 long-term scientific positions (20 months) were funded by the resources of the BGI Visiting Scientists' Programme (see Sect. 8) which also supported short-term visits for discussing future projects or presenting research results (see Sect. 5). 8 student assistants (68.5 months) were funded by externally raised grants. 6 scientists (41 months) were supported by personal grants or stipends.

2.2 Funding

In 2018, the following financial resources were available from the Free State of Bavaria:

- Visiting Scientists' Programme: 167.000 €
- Consumables: 887.000 €
- Investment funding: 60.000 €

The total amount of national/international external funding *("Drittmittel"*) used for ongoing research projects in 2019 was 3.417.000 € (Positions: 1.842.000 €; equipment, consumables and travel grants: 1.575.000 €).

	positions	**equipment, consumables, travel grants**	**total**
• AvH	9.000 €	12.000 €	21.000 €
• BMBF	155.000 €	110.000 €	265.000 €
• DFG	1.578.000 €	854.000 €	2.432.000 €
• EU	84.000 €	592.000 €	676.000 €
• Others	16.000 €	7.000 €	23.000 €
	1.842.000 €	**1.575.000 €**	**3.417.000 €**

(AvH = Alexander von Humboldt Foundation; BMBF = Federal Ministry of Education and Research; DFG = German Science Foundation; EU = European Union; Others: DAAD, Chinese Science Council, Japanese Society for the Promotion of Science, Swiss National Science Foundation)

In the following list only the BGI components of the funding are listed in cases where joint projects involved other research institutions. Principal investigators and the duration of the grants are listed in brackets. Total project funding refers to the funding over the entire duration of this project.

Funding institution	Project, Funding	Total Project Funding
BAdW	Bavarian Academy of Sciences research project (2016-2019) (H. Marquardt)	36.000 €
BMBF	05K16WCA (H. Keppler – 7/16-6/19) "Aufbau einer Hochdruckpresse vom Multi-Anvil-Typ an der Forschungs-Neutronenquelle FRM II in Garching" Total funding:	410.278 €
BMBF	05K19WCA (H. Keppler – 7/19-6/22) "Aufbau einer Hochdruckpresse vom Multi-Anvil-Typ an der Forschungs-Neutronenquelle FRM II in Garching" Total funding:	579.116 €
BMBF	05K16WC2 (T. Katsura – 7/16-6/21, extended) "Erweiterung der Druckbereiche der In-Situ-Röntgen-beobachtung mit der Großvolumen-Hochdruckapparatur an der PETRA-III-Extension des Deutschen Elektronen-Synchrotrons DESY" Positions E 12-E 15: (increased) 349.727 € Consumables and travel funding: (increased) 421.540 € Equipment: (increased) 43.000 € Overhead: (increased) 162.857 €	(increased) 977.124 €
DFG	BO 2550/7-2 (T. Boffa Ballaran, A. Woodland – 10/17-9/19) "Stabilities and properties of Mg, Al and Cr-bearing solid solutions of newly discovered Fe^{3+}-Fe^{2+} oxides at transition zone conditions: approaching geologically relevant compositions" Position: student assistant 7.500 € Consumables and travel funding: 7.000 € Overhead: 3.200 €	17.700 €
DFG	DU 393/9-2 (L.S. Dubrovinsky – 1/18-12/20) TP 7 'Chemische Reaktionen zwischen Karbonaten und pyrolitischem Erdmantel und Entstehung ultratiefer Diamanten', "Structures, properties and reactions of carbonates at high temperatures and pressures" Positions: E 13 (67 %), 36 months 132.800 € Consumables: 32.250 € Overhead: 36.300 €	201.350 €

DFG	DU 393/13-1 (L.S. Dubrovinsky – 4/17-3/20) "Mantel formende Materialien von Super Erden bei Statischen Drücken von über 500 GPa und hohen Temperaturen" Positions: E 13, 36 months 209.400 € student assistant 8.000 € Consumables: 27.750 € Overhead: 53.900 €			299.050 €
DFG	FR 1555/11-1 (D.J. Frost – 3/16-2/23) Gottfried Wilhelm Leibniz-Preis 2016			2.500.000 €
DFG	GRK 2156/1 (D.J. Frost, et al. – 4/16-10/20) Internationales Graduiertenkolleg "Deep Earth Volatile Cycles"			3.257.358 €
DFG	IS 350/1-1 (T. Ishii – 4/19-9/20) "Hochdruck-Temperatur-Phasenbeziehungen der basaltischen Kruste unter Bedingungen des unteren Mantels: Auswirkungen auf die chemische Heterogenität im unteren Mantel" Position: E 13, 18 months: 107.800 € Consumables and travel funding: 24.000 € Overhead: 29.000 €			160.800 €
DFG	KA 3434/3-2 (T. Katsura – 7/18-6/21) "Dislocation recovery experiment of hydrous olivine as a function of water content and crystallographic orientation" Positions: E 13, 12 months 69.300 € E 13 (75 %), 12 months 48.100 € student assistant 5.000 € Consumables: 20.000 € Overhead: 31.300 €			173.700 €
DFG	KA 3434/8-1 (T. Katsura – 4/15-3/19) "Messung von Si-Selbstdiffusionskoeffizienten in Wadsleyit als Funktion des Wassergehaltes" Positions: E 13, 36 months 195.300 € student assistant 5.000 € Consumables and travel funding: 16.000 € Overhead: 43.300 €			259.600 €
DFG	KA 3434/9-1 (T. Katsura – 9/15-8/19) "Bestimmung des Drei-Phasen-Stabilitätsfelds des Postspinell-Übergangs in $(Mg,Fe)_2SiO_4$: Erörterung der extremen Schärfe der 660-km-Diskontinuität und deren Bedeutung für die chemische Struktur und die Dynamik des tiefen Erdmantels" Positions: E 13, 36 months 196.600 € student assistant 5.000 € Consumables and travel funding: 45.750 € Overhead: 49.500 €			296.850 €

DFG	KA 3434/11-1 (T. Katsura – 12/18-11/21) "Determining the water dissociation constant from the relationship between water solubility in ringwoodite and oxygen fugacity" Positions: E 13, 24 months 141.700 € Consumables: 23.500 € Overhead: 36.300 €	201.500 €
DFG	KA 3434/12-1 (T. Katsura – 10/18-12/21) "Determination of water partition coefficients between upper mantle minerals and melts as a function of pressure, temperature, and CO_2 content using a rapid quench cell in multi-anvil experiments" Positions: E 13, 24 months 142.700 € Consumables: 40.000 € Overhead: 40.200 €	222.900 €
DFG	KE 501/11-2 (H. Keppler – 2018-2020) "Electrical conductivity and dissociation of fluids in crust and mantle" Total funding:	209.600 €
DFG	KE 501/15-1 (H. Keppler – 2017-2019) "Hochdrucklabore des Bayerischen Geoinstituts" Total funding:	371.878 €
DFG	KU 3447/1-1 (A. Kurnosov – 10/17-9/20) "Einkristall-Elastizität von Mars-Mineralen und ein flexibles CO_2 Laserheizsystem" Position: E 13, 36 months 217.700 € Consumables and travel funding: 15.250 € Overhead: 51.200 €	284.150 €
DFG	MA 4534/5-1 (H. Marquardt – 6/17-5/20) "Experimentelle Untersuchung von planetaren Eis-Verbindungen bei hohen Drücken mittels dynamisch-betriebener Diamantstempelzellen" Position: E 13 (75 %), 36 months: 145.700 € Consumables: 27.750 € Overhead: 38.200 €	211.650 €
DFG	MA 6287/5-1 (S. Chakraborty, K. Marquardt, T. Fockenberg – 10/16-9/19) "Experimentelle Kalibrierung von Granat-Pyroxen Diffusionschronometrie für Anwendungen in terrestrische und planetare Proben" Position: student assistant 5.000 € Consumables: 5.000 € Overhead: 2.200 €	12.200 €

DFG	MA 6287/6-1 (K. Marquardt – 11/16-10/19) "Änderungen der Korngrenzcharakterverteilung in Olivin-dominierten Gesteinen als Funktion des Chemismus" Positions: E 13 (75 %), 36 months: 147.000 € student assistant 5.000 € Consumables, global funding: 45.030 € Overhead: 43.300 €	240.330 €
DFG	MC 3/20-2 (C.A. McCammon – 1/18-12/20) DFG FOR 2125 (CarboPaT) "Elastic properties of carbonates at high pressure and high temperature" Position: E 13 (67 %), 36 months: 132.800 € Equipment, consumables and travel funding: 27.750 € Overhead: 35.300 €	195.850 €
DFG	MC 3/21-1 (C.A. McCammon – 6/17-5/20) "Fe Spinübergang im Erdmantel: Einblicke durch Röntgen-Raman-Streuung und Röntgenabsorptionsspektroskopie" Position: student assistant (Bachelor) 9.482 € Equipment, consumables and travel funding: 6.000 € Overhead: 3.400 €	18.882 €
DFG	ME 5206/3-1 (T. Meier – 6/19-5/22) "Wasserstoffbrückenbindungen unter extremen Bedingungen: Kernquanteneffekte und Symmetrisierung der Wasserstoff-brückenbindung untersucht mit ^{1}H-NMR in Diamantstempel-zellen" Position: E 13, 36 months: 221.500 € Consumables and travel funding: 29.250 € Overhead: 55.200 €	305.950 €
DFG	MI 1721/3-1 (N. Miyajima – 9/19-8/22) "Al, Si-Interdiffusion in Bridgmanit und die Viskosität des unteren Mantels" Position: E 13 (75 %), 36 months: 157.000 € student assistant 7.500 € Consumables and travel funding: 29.500 € Overhead: 41.000 €	227.500 €
DFG	OV 110/3-1 (S.V. Ovsyannikov – 9/18-8/20) "High-pressure synthesis and properties of novel simple oxides with unusual stoichiometries" Position: E 13, 24 months 141.600 € Consumables and travel funding: 30.250 € Overhead: 37.800 €	209.650 €

DFG	RU 1323/10-1 (D.C. Rubie – 1/17-12/19) DFG SPP 1833 'Building a Habitable Earth' "Entstehung und Entwicklung des Magmaozeans und Differentiation von Kern und Mantel während der Akkretion der Erde" Position: E 13, 36 months 206.700 € Consumables: 7.250 € Overhead: 42.800 €	256.750 €
DFG	STE 1105/12-1 (G. Steinle-Neumann, D.J. Frost, N. Tosi – 11/16-10/19) DFG SPP 1833 'Building a Habitable Earth' "Kristallisation des irdischen Magmaozeans: Thermo- und Geodynamik" Positions: E 13 (75%), 36 months 143.600 € student assistant 5.000 € Consumables: 8.250 € Overhead: 31.400 €	188.250 €
DFG	STE 1105/13-1 (G. Steinle-Neumann – 8/17-7/20) DFG through FOR 2440 (Matter Under Planetary Interior Conditions) "Thermodynamic properties of silicate solids and liquids and iron to the TPa range from *ab initio* calculations" Positions: E 13 (75%), 36 months 145.700 € student assistant 15.000 € Consumables: 7.750 € Overhead: 37.100 €	205.550 €
DFG	Emmy Noether-Programm (H. Marquardt – 2014-2019) "Structure and Elasticity of GeoMaterials at Extreme Conditions (GeoMaX)" Positions: group leader, E 14/E 15, 60 months: 375.400 € post doc, E 13, 60 months: 317.200 € 2 PhD students, E 13 (67%), 36 months: 264.400 € student assistant: 11.904 € Consumables, travel funding: 222.550 € Investments: 127.714 € Overhead: 184.400 €	1.503.568 €
EU	European Research Council (ERC) Advanced Grant No. 787 527 (T. Katsura – 10/18-9/23) "Chemistry and transport properties of bridgmanite controlling lower-mantle dynamics" ("UltraLVP") Positions (post docs): 860.144 € Travel funding: 187.380 € Equipment: 49.250 € Consumables: 997.722 € In-kind contributions: 24.000 € Overhead: 523.624 €	2.642.120 €

2.3 Laboratory and office facilities

The institute occupies an area of

ca. 1350 m^2	laboratory space
ca. 480 m^2	infrastructural areas (machine shops, computer facilities, seminar room, library)
ca. 460 m^2	office space

in a building which was completed in 1994.

2.4 Experimental and analytical equipment

The following major equipment is available at the Bayerisches Geoinstitut:

I. High-pressure apparatus
- 15 MN/1500 tonne Kawai-type multianvil high-pressure apparatus (40 GPa, 2000 K)
- 6 x 8 MN/6x800 tonne independently acting-anvil press (25 GPa, 3000 K)
- 50 MN/5000 tonne multianvil press (25 GPa, 3000 K)
- 12 MN/1200 tonne multianvil press (25 GPa, 3000 K)
- 10 MN/1000 tonne multianvil press (25 GPa, 3000 K)
- 5 MN/500 tonne multianvil press (20 GPa, 3000 K)
- 5 MN/500 tonne press with a deformation DIA apparatus
- 5 piston-cylinder presses (4 GPa, 2100 K)
- Cold-seal vessels (700 MPa, 1100 K, H_2O), TZM vessels (300 MPa, 1400 K, gas), rapid-quench device
- Internally-heated autoclave (1 GPa, 1600 K)
- High-pressure gas loading apparatus for DAC

II. Structural and chemical analysis
- 1 X-ray powder micro-diffractometer
- 1 X-ray powder diffractometer with furnace and cryostat
- 2 automated single-crystal X-ray diffractometers
- High-brilliance X-ray system
- Single crystal X-ray diffraction with super-bright source
- 1 Mössbauer spectrometer (1.5 - 1300 K)
- 3 Mössbauer microspectrometers
- 2 FTIR spectrometers with IR microscope
- FEG transmission electron microscope (TEM), 200 kV analytical, with EDS
- FEG scanning TEM, 80-200 kV analytical, with 4-SDDs EDS and post-column energy filter (EFTEM/EELS)
- FEG scanning electron microscope (SEM) with BSE detector, EDS, EBSD and CL
- Dual beam device, focused ion beam (FIB) and FEG SEM. In situ easy-lift manipulator, STEM, EDS and EBSD detectors, and beam deceleration option
- 3 Micro-Raman spectrometers with ultraviolet and visible lasers

Tandem-multipass Fabry-Perot interferometer for Brillouin scattering spectroscopy
JEOL JXA-8200 electron microprobe; fully-automated with 14 crystals, 5 spectrometer configuration, EDX, capability for light elements
193 nm Excimer Laser-Ablation ICP-MS
Water content determination by Karl-Fischer titration
GC/MS-MS for organic analyses
Confocal 3D surface measurement system
1.4 Tesla sweepable ESR magnet
Solid state 300 MHz NMR spectrometer

III. *In situ* determination of properties

Diamond anvil cells for powder and single crystal X-ray diffraction, Mössbauer, IR, Raman, optical spectroscopy, NMR specroscopy, electrical resistivity measurements over 200 GPa
Facility for in situ hydrothermal studies in DAC
Externally heated DACs for in situ studies at pressures to 100 GPa and 1200 K
1-atm furnaces to 1950 K, gas mixing to 1600 K, zirconia fO_2 probes
1-atm high-temperature creep apparatus
Gigahertz ultrasonic interferometer with interface to resistance-heated diamond-anvil cells
Freezing-heating stage for fluid inclusion studies
Impedance/gain-phase analyser for electrical conductivity studies
Apparatus for in situ measurements of thermal diffusivity at high P and T
Laser-heating facility for DAC
Portable pulsed laser heating system for DAC

The Geoinstitut is well equipped with machine shops, an electronic workshop and sample preparation laboratories. It also has access to the university computer centre.

3. Forschungsprojekte

3.1 Struktur und Dynamik der Erde und Planeten

Planetesimale und Planeten entstanden in kurzer Zeit im frühen Sonnensystem. Die Kondensation begann vor ≈ 4,57 Milliarden Jahren mit der Entstehung der Calcium-Aluminium-reichen Einschlüsse (CAI). Diese CAI definieren den Startpunkt der Chronologie der Planetenentstehung. Meteoritenstudien zeigen, dass viele ihrer Mutterkörper in kurzer Zeit Kern, Mantel und Kruste ausgebildet haben, sogar vor dem Ende der Entstehungsphase von Chondrulen und Chondriten. Modelle, die auf Isotopenstudien der kurzlebigen Hf-W und Fe-Ni Systeme beruhen, zeigen dass Mars innerhalb von 5 Millionen Jahren nach der CAI-Entstehung 90 % seiner finalen Masse erreicht hat. Dagegen hatte die Erde eine längere Akkretionsgeschichte, die bis zu 100 Millionen Jahre dauerte, wobei 10 % der Masse durch einen großen Einschlag beigetragen wurde, der zur Mondentstehung führte. Nach dem Ende der Kernentstehung folgte für mehrere hundert Millionen Jahre die Phase der späten Akkretion. Während dieser letzten wichtigen Phase der Erdentstehung kamen siderophile Elemente und möglicherweise leichtflüchtige Elemente auf die Erde, die sich heutzutage in Erdmantel und Kruste befinden.

Astrophysikalische Theorien und thermische Modelle von Meteoriten-Ursprungskörpern zeigen, dass Planetesimale Größen zwischen einem Dutzend und Hunderten Kilometern aufwiesen. Der Zerfall des kurzlebigen radiogenen Isotops ^{26}Al (Halbwertszeit 0,708 Millionen Jahre) war die Hauptwärmequelle in diesen Planetesimalen. Diese radiogene Heizung durch den Zerfall von ^{26}Al und die Umwandlung von potentieller Energie in Wärme trugen zur Entstehung von Magmaozeanen sowohl in Planetesimalen als auch Protoplaneten bei. Weniger Informationen sind für planetare Körper im äußeren Sonnensystem verfügbar, da diese weniger zugänglich sind. Der erste Beitrag beschreibt numerische Modelle, welche die thermische Entwicklung von frühen kometaren Objekten, sogenannten Kometesimalen, behandeln. Die Studie berücksichtigt sowohl Größe als auch Entstehungszeit, beides wichtige Parameter, welche die frühe thermische Entwicklung beeinflussen und damit kontrollieren ob sehr flüchtige Verbindungen wie CO im Körper verbleiben oder ins Weltall entweichen. Die Ergebnisse weisen darauf hin, dass nur kleine oder spät entstandene Kometesimale diese sehr flüchtigen Verbindungen zurückbehalten konnten.

Die Differentiation der Planeteninneren und die Homogenität in stabilen Isotopen (z. B. Sauerstoff, Chrom, Titan) bei den meisten achondritischen Meteoritengruppen und terrestrischen Proben weisen darauf hin, dass ihre Mutterkörper eine Magmaozean-Phase durchlebt haben. Die Kristallisationsmechanismen und die Dynamik der Abkühlung eines Magmaozeans sind bis heute nicht gut verstanden. Zum Beispiel wird das Schicksal von Kohlenstoff, dessen Präsenz im Magmaozean der Erde erwartet wird, bis heute debatiert. Frühere Studien schlugen vor, dass der Großteil des Kohlenstoffs als Legierung in den Erdkern gelangte. In ihrem Beitrag diskutieren Keppler und Golabek, ob nicht ein Teil dieses

Kohlenstoffs stattdessen Graphit bilden konnte. Ihre Resultate zeigen, dass unter reduzierenden Bedingungen dies für etwa die Hälfte des Kohlenstoffs möglich war. Wegen seiner geringen Dichte konnte dieses Graphit entsprechend Richtung Oberfläche aufsteigen und dort eine Graphit-reiche Schicht bilden. Analytische Berechnungen zeigen, dass dieser Graphit-Aufstieg für kleine terrestrische Planeten wie Merkur am wahrscheinlichsten war. Dies wird durch Beobachtungen der NASA-Mission MESSENGER unterstützt, welche auf das Vorhandensein solch einer Graphit-reichen Oberflächenschicht hindeuten.

Sekundäre Prozesse, die mit der Wiederaufarbeitung von planetaren Krusten durch Einschläge verbunden sind, veränderten die Evolution und die Zusammensetzung von Planetesimalen. Frossard und Kollegen untersuchten die Elementzusammensetzung von Pyroxen und Plagioklas für einen einzigartigen, nicht klassifizierten Achondriten namens NWA 8486, der im inneren Sonnensystem entstanden war. Sie fanden, dass starke positive Anomalien bei den Elementen Strontium und Europium sowohl in beiden Mineralen als auch im Gesamtgestein nur durch die Teilaufschmelzung einer anorthositischen Kruste entstehen konnten. Dynamische Modelle deuten darauf hin, dass das Aufschwimmen von Plagioklas in kleinen Planetesimalen innerhalb von weniger als 1 Million Jahren stattfinden konnte. Bislang wurde anorthositische Kruste nur auf dem Mond und in großen Intrusionskörpern auf der Erde beobachtet, während Anorthosit in Meteoritensammlungen fehlt.

Am Ende der Planetenentstehung hatte die Erde eine differenzierte Struktur, die den Erdmantel und den Erdkern umfasste, die beide mit der Zeit abkühlten. Der Erdkern besteht größtenteils aus Eisen und Nickel mit kleinen Beimengungen mehrerer zusätzlicher Elemente. Basierend auf den seismischen Geschwindigkeiten und der Dichte des inneren Erdkerns wird erwartet, dass einige dieser leichten Elemente während der Kristallisation des inneren Erdkerns in diesem verbleiben. Eines der möglichen leichten Elemente ist Silizium. Indem sowohl die seismische Geschwindigkeit als auch die Dichte für ein Eisen-Nickel-Silizium-Gemisch unter Hochdruck-bedingungen gemessen wurde, konnten Dominijanni und Kollegen bestimmen, dass Silizium in der Tat ein mögliches leichtes Element im inneren Erdkern darstellt.

Sowohl der Ursprung der leichtflüchtigen Elemente auf den terrestrischen Planeten als auch der Zeitpunkt ihrer Ankunft sind noch unbeantwortete Schlüsselfragen. Entweder wurden leichtflüchtige Elemente mit den Bausteinen der Planeten während der Akkretionsphase geliefert oder die terrestrischen Planeten entstanden aus trockenem Material. In letzterem Fall müsste Material, das reich an leichtflüchtigen Elementen war, nach dem Ende der Kernbildung während der späten Akkretionsphase auf die Planeten gelangen, um die Präsenz von siderophilen Elementen im Erdmantel erklären zu können. Dieses Thema wurde von zwei Studien behandelt.

Die Studie von Blanchard, Shcheka und Kollegen aus Paris untersuchte das Verhalten von Zinn-Isotopen mittels einer Mehrstempel-Presse, um das Elementverhalten von Zinn und die Fraktionierung der Isotope während der Kern-Mantel Gleichgewichtseinstellung zu ermitteln.

Dabei untersuchten sie den Einfluss von Temperatur, Druck, Sauerstofffugazität und Metall- und Silikat-Zusammensetzung auf das Fraktionierungsverhalten von Zinn zwischen Metall und Silikaten. Basierend auf den Resultaten geochemischer Modellrechnungen wurde vorgeschlagen, dass das Zinn-Budget der Erde und ihre Isotopenzusammensetzung erklärt werden können, falls leichtflüchtige Elemente während der späten Akkretion durch kohlige Chondrite auf die Erde kamen und der Erdkern 2-4 Gewichtsprozent an Schwefel enthält.

Da die Venus höchstwahrscheinlich niemals stehende Gewässer aufwies, ist ihre Atmosphärenevolution weniger komplex verlaufen als die der Erde, da zwar Einschläge und vulkanische Ausgasung Wasser in die Atmosphäre bringen konnten, aber das Wasser nicht ins Innere des Planeten transportiert werden konnte. Indem dynamische Modelle der späten Akkretion mit Modellen der Mantel- und Atmosphärenevolution über einen Zeitraum von 4.5 Milliarden Jahren verbunden wurden, studierten Golabek und Kollegen verschiedene Szenarien und Zusammensetzungen der späten Akkretion. Auf diese Weise war es möglich zu bestimmen, ob eine trockene oder eine wasserreiche Zusammensetzung der späten Akkretion mit dem heutigen Gehalt an leichtflüchtigen Verbindungen in der Venusatmosphäre übereinstimmt. Die Resultate zeigen, dass auf der Venus eine größtenteils trockene späte Akkretionsphase stattfand.

Der letzte Beitrag von Zhang und Kollegen beschäftigt sich mit der Einschlagsgeschichte des Mondes basierend auf Einschlagsschmelz-Brekzien, die von der Apollo 17-Mission stammen. Wegen ihrer räumlichen Nähe wurden diese Brekzien lange Zeit als Resultat des Serenitatis-Einschlags behandelt. Zhang und Kollegen fanden, dass enthaltene Mikro-Zirkone ein Alter von 3921±14 Millionen Jahre aufweisen. Außerdem weisen sie Texturen und Konzentrationen an Spurenelementen auf, die vergleichbar sind mit denen von Zirkonen aus Imbrium-Brekzien. Diese Resultate weisen darauf hin, dass die Spitze an gemessenen Altern von Apollo-Mondproben bei 3,9 Milliarden Jahren auf das Auswurfmaterial des Imbrium Einschlagskraters zurückgehen könnte, welches über die erdzugewandte Seite des Mondes verteilt wurde.

3.2 Geochemie

Die Mehrheit der geologischen Prozesse kann nicht direkt beobachtet werden, da sie entweder extrem langsam oder tief in der Erde ablaufen. Die Prozesse hinterlassen jedoch Spuren in der Form chemischer Signaturen in Gesteinen und Mineralen, anhand derer die Prozesse rekonstruiert werden können. Die meisten der in diesem Abschnitt behandelten Studien haben zum Zweck, anhand experimenteller Daten eine Grundlage zur Interpretation von geochemischen Signaturen zu schaffen, um so Informationen über die Ursachen und Bedingungen zu erhalten, die zur Bildung der Erde und der anderen Planeten geführt haben.

Die ersten drei Beiträge in diesem Kapitel befassen sich mit Prozessen, die mit der Kernbildung einhergehen. Eine seltene Art von Meteoriten, welche Pallasite genannt werden, bestehen aus Silikatmineralen, die in einer Eisenlegierung eingebettet sind. Es wurde bisher angenommen,

dass diese Meteoriten aus dem Kern-Mantel-Grenzbereich kleiner Planeten stammen. In der ersten Studie wurden chemische Analysen an einem natürlichen Pallasit sowie Deformationsexperimente an einem synthetischen Analog-Material durchgeführt um zu überprüfen, ob die Metallschmelze mit den Silikatmineralen im Gleichgewicht war oder durch einen späteren Impakt in die Silikate hineingepresst wurde. Während die Resultate der Deformationsexperimente die Impakt-Hypothese unterstützen, zeigen die geochemischen Daten keinen Hinweis für ein spätes Eindringen metallischer Schmelze. Die nächste Studie befasst sich mit Experimenten in der Laser-geheizten Diamanstempelzelle, um das Fraktionierungsverhalten von Kohlenstoff während der Kern-Mantel-Separation zu erforschen. Es stellte sich heraus, dass Kohlenstoff unter diesen Bedingungen viel weniger stark in die Eisenschmelze fraktioniert als bei geringeren Drücken, was erklärt, weshalb der Erdmantel noch relativ viel Kohlenstoff enthält. Im nachfolgenden Beitrag wurde experimentell untersucht, wieviel Schwefel in Silikatschmelzen unter hohen Drücken und Temperaturen gelöst werden kann. Bisher waren noch keine Informationen darüber vorhanden, wieviel Schwefel maximal in Silikatschmelzen gelöst werden kann, deren Zusammensetzung dem gesamten aufgeschmolzenen Silikatanteil der Erde entspricht. Die Resultate zeigen, dass dieser maximale Schwefelgehalt sehr viel höher ist als bisher gedacht, was u. a. für die Modellierung der Segregation von Sulfiden aus dem Erdmantel in den Erdkern von großer Wichtigkeit ist.

Die nächsten drei Beiträge handeln von Mineraleinschlüssen in Diamanten, welche unsere einzigen natürlichen Zeugen aus dem tiefen Erdmantel darstellen. Der häufigste Typ von Einschlüssen sind Eisensulfidschmelzen. In der ersten Studie wird der Sauerstoffgehalt von Einschlüssen aus Eisensulfidschmelze benutzt, um deren Entstehungstemperatur abzuschätzen. Die Resultate zeigen, dass Diamanten über eine beträchtliche Temperaturspannweite entstanden sind, welche von der geschätzten Temperatur von heißem, asthenosphärischen Mantel bis hin zu kühlem, kratonischen lithosphärischen Mantel reicht. Diamanten aus dem tiefen, konvektierendem Mantel sind selten und enthalten meist Einschlüsse aus Ferroperiklas. Untersuchungen an solchen Ferroperiklas-Einschlüssen ergaben, dass sie oft Bereiche aus Fe^{3+}-reichen Oxiden enthalten, welche aus dem Ferroperiklas entmischt wurden. In einer der Studien wurden daher die Phasenbeziehungen von Oxidmineralien untersucht, um zu verstehen, unter welchen Bedingungen diese Entmischungen entstanden. Die wahrscheinlichste Erklärung ist, dass die Diamanten im heißen, konvektierenden Mantel entstanden und dann nachträglich im kühleren lithosphärischen Mantel verweilten, wo die Eisenoxide entmischten. In der letzten Diamant-bezogenen Studie wurden Experimente in komplexen Silikat+Karbonat-Systemen durchgeführt, um die Entstehungsbedingungen entsprechender Einschlüsse näher einzugrenzen. Eine der wichtigsten Erkenntnisse ist, dass in karbonathaltigen Systemen Magnesiowüstite bereits unter Bedingungen der Mantel-Übergangszone gebildet werden können, während in der Vergangenheit immer von einer Entstehung im unteren Mantel ausgegangen wurde.

Die folgenden beiden Beiträge befassen sich mit Schmelzprozessen im tiefen Erdmantel. In der ersten Arbeit wird versucht, die Zusammensetzung wasserhaltiger Schmelzen zu bestimmen, die bei geringfügigen Aufschmelzgraden an der Basis des oberen Erdmantels entstehen. In mehreren seismischen Studien werden solche Partialschmelzen als Ursache für relativ geringe

Erdbebenwellengeschwindigkeiten in dieser Tiefe angesehen. Es ist sehr schwierig, die Zusammensetzung solcher Schmelzen exakt zu bestimmen, aber letztlich gelang es, eine typischen Mantelzusammensetzung mit einer wässerigen Schmelze zu sättigen. Die Kenntnis der Zusammensetzung der Schmelze ist auch deshalb wichtig, weil sie die Dichte bestimmt. Relativ dichte Schmelzen würden sich in dieser Tiefe ansammeln, während weniger dichte Schmelzen aufsteigen würden. In einem nächsten Schritt wird deshalb die Dichte solcher Schmelzen untersucht werden. Die zweite Studie, die sich mit Schmelzbildung beschäftigt, hat zum Ziel, ein thermodynamisches Modell für Schmelzbildung im unteren Erdmantel zu erstellen. Solche Modelle sind u. a. notwendig um die Kristallisation eines tiefen Magmaozeans während der Bildung der Erde zu verstehen. In der Studie wurde experimentell die Zusammensetzung der ersten Schmelze im einfachen MgO-SiO_2 System bei Bedingungen untersucht, die dem unteren Erdmantel entsprechen, aber dennoch gut kontrolliert werden können. Die Zusammensetzung der entstandenen Schmelze gibt wichtige Hinweise in Bezug auf die Thermodynamik der Mischprozesse in Silikatschmelzen, was wiederum zur Konstruktion von Phasendiagrammen über einen Druckbereich verwendet werden kann, in welchem experimentelle Resultate mit einer großen Unsicherheit behaftet wären.

In den nachfolgenden zwei Beiträgen wird der Zusammenhang zwischen der Sauerstoff-fugazität und dem Oxidationszustand von Eisen in Mantelmineralen untersucht. Die Bestimmung von Redoxbedingungen ist nicht nur deshalb wichtig, weil sie die Zusammensetzung von Mantelmineralen steuert, sondern auch die Mobilität von Kohlenstoff und Schwefel beeinflusst. Im ersten Beitrag wurde der Oxidationszustand von Eisen in Bridgmanit – dem dominierenden Mineral im unteren Erdmantel – als Funktion der Sauerstofffugazität und der chemischen Gesamtzusammensetzung untersucht. Mehrere frühere Studien kamen zu gegensätzlichen Schlüssen in Bezug auf den Oxidationszustand von Eisen in Bridgmanit sowie in Bezug auf das Fraktionierungsverhalten von Eisen zwischen Bridgmanit und Ferroperiklas – dem zweithäufigsten Mineral des unteren Erdmantels. Die Resultate dieser Studie zeigen, dass das Fraktionierungsverhalten von Eisen stark von der Sauerstofffugazität abhängt und dass die unterschiedlichen Ergebnisse früherer Studien auf ein Fehlen der Kontrolle dieses Parameters zurückzuführen sind. Der zweite Beitrag befasst sich mit dem Oxidationszustand von Eisen im wasserhaltigen Mineral Serpentin, welches als der wichtigste Träger von Wasser in Subduktionszonen angesehen wird. Bei der Bildung von Serpentin wird offenbar durch Oxidation von Fe^{2+} zu Fe^{3+} der Sauerstoffgehalt der ozeanischen Kruste erhöht. Der Sauerstoffgehalt der Kruste ist seinerseits wichtig, weil er die Stabilität und Mobilität volatiler Elemente kontrolliert. Die Resultate führen zu einem ersten thermodynamischen Modell, mit dessen Hilfe der Redox-Zustand subduzierter serpentinitisierter Lithosphäre simuliert werden kann. Es zeigt sich erstaunlicherweise, dass das Gesamtgestein während der Subduktion relativ reduziert bleiben kann, auch wenn der Serpentin selbst oxidiert und eine erhebliche Menge an Fe^{3+} enthält. Serpentin kann somit durch die Oxidation von Eisen kontinuierlich Sauerstoff von anderen Mineralien absorbieren. Beispielsweise kann umgebendes Karbonat zu Graphit umgewandelt werden, was zur Erhaltung von Kohlenstoff in der subduzierenden Platte und dessen Rückführung in den Erdmantel beiträgt.

Die nächste Studie handelt von der geochemischen Signatur des Inselbogenvulkanismus. Mit Hilfe von sogenannten Diamantfallen-Experimenten wird untersucht, ob eine solche Signatur von subduzierten Sedimenten herrühren kann. Zu diesem Zwecke wurde 30-40 Gew. % Fluid zu einer metapelitischen Ausgangszusammensetzung zugegeben und das Ganze bei Bedingungen equilibriert, die unterhalb des Schmelzpunkts liegen. Die Resultate zeigen, dass chlorhaltige Fluide durchaus eine geochemische Signatur annehmen können, die derjenigen von Inselbogenvulkanen ähnelt, während in der Vergangenheit angenommen wurde, dass dies nur bei einer Aufschmelzung der Sedimente der Fall ist.

Die letzten beiden Beiträge stehen im Zusammenhang mit der Bildung von Erzlagerstätten. Im ersten Beitrag wurde die Diffusion von Kupfer in Amphibolen untersucht um zu klären, ob Kupfergehalte dieses Minerals und darin enthaltene Schmelzeinschlüsse dazu benutzt werden können, um den Kupfergehalt früherer Schmelzen zu rekonstruieren, aus denen die Amphibole kristallisiert sind. Es stellt sich heraus, dass die Diffusionsrate von Kupfer in Amphibolen sehr hoch ist, weshalb von dieser Anwendung abgeraten werden muss. Der zweite Beitrag befasst sich Amphibol-reichen Xenolithen aus der Erdkruste, welche durch Magmen an die Oberfläche befördert wurden, die mit Kupfer- und Goldlagerstätten in Tongling im Südosten Chinas im Zusammenhang stehen. Anhand petrologischer und geochemischer Daten wird die Auswirkung von Amphibol-Kristallisation und damit einhergehender Sulfid-Ausfällung auf das Mineralisationspotential der Magmen untersucht. Obwohl die erzbildenden Magmen nachweislich erhebliche Mengen an Kupfer und Gold in der Tiefe verloren haben müssen, waren sie trotzdem noch in der Lage, reiche Lagerstätten zu bilden. Dies impliziert, dass der Metallgehalt des Magmas nicht der Hauptfaktor ist, der das Mineralisationspotential bestimmt, sondern eher andere Faktoren wie zum Beispiel der Wassergehalt der Magmen.

3.3 Mineralogie, Kristallchemie und Phasentransformationen

Mineralogie mit all ihren verschiedenen Aspekten – angefangen von der Untersuchung von Kristallstrukturen von Mineralen bis zur Bestimmung ihres Stabilitätsbereiches und ihrer Phasenübergänge sowie der Charakterisierung ihrer mikroskopischen Eigenschaften – ist ein essentielles Werkzeug, um die Prozesse in der Erde zu verstehen.

Während des vergangenen Jahres haben sich eine Reihe von Projekten am BGI auf das mögliche Verhalten von Fe-haltigen Verbindungen unter hohen Drucken und Temperaturen konzentriert. Die Kristallstrukturen von zwei neuen Eisenoxiden wurden erstmals bestimmt (erster Beitrag) und zeigten die Möglichkeit einer homologen Serie von Fe-Oxiden auf, die durch die gemeinsame chemische Formel $n\mathrm{FeO}\cdot m\mathrm{Fe_2O_3}$ charakterisiert sind. Die Stabilitäts-felder von zwei weiteren, erst kürzlich entdeckten Eisenoxiden, $\mathrm{Fe_4O_5}$ and $\mathrm{Fe_5O_6}$, wurden unter hohen Drücken und Temperaturen mithilfe der *in situ* Röntgenbeugung in einer Laser-beheizten Diamantstempelzelle (LHDAC) untersucht (zweiter Beitrag). Die dritte Studie in diesem Kapitel berichtet über den Substitutionsmechanismus von oxidiertem Eisen ($\mathrm{Fe^{3+}}$) in Bridgmanit bei den p,T-Bedingungen des äußersten unteren Erdmantels. Die Resultate zeigen,

dass für sehr geringe Mengen von Fe die Substitution mithilfe von Sauerstoffleerstellen der dominante Mechanismus zur Aufnahme von Fe^{3+} in einer MgO-gesättigten Umgebung ist. Der vierte Beitrag beschreibt, wie der Fe^{3+}-haltige Jeffbenit (ein Mineral, das als Einschluss in ultratiefen Diamanten gefunden wurde) erstmalig in einer Multianvilpresse synthetisiert und seine Kristallstruktur im Detail charakterisiert wurde.

Eine wichtige Klasse der Fe-Verbindungen stellen die Eisenhydroxide dar. Insbesondere FeOOH ist ein weit verbreitetes Oxyhydroxid an der Erdoberfläche. Von dort kann es durch die Subduktion von Sedimenten bis hinunter in den Erdmantel transportiert werden und es wird angenommen, dass es in der Tiefe eine Mischkristallreihe mit AlOOH bildet. Die fünf folgenden Beiträge berichten über die Synthese und das Hochdruck- und Hochtemperatur-verhalten von Proben, die zur Mischkristallreihe δ-AlOOH – ε-FeOOH gehören. Große Einkristalle mit drei verschiedenen Zusammensetzungen der Reihe ε-(Fe,Al)OOH wurden erfolgreich synthetisiert (fünfter Beitrag) und strukturell charakterisiert, während Proben mit höherem Al-Gehalt in der sechsten Studie bei hohen Temperaturen und Drücken in der LHDAC untersucht wurden. Dabei wurde gezeigt, dass diese wasserhaltigen Verbindungen bei Drücken des unteren Erdmantels bis zu einer Temperatur von 1850 K stabil sind. Im siebten Beitrag wird über die Änderungen der Kristallstruktur und der Gitterparameter berichtet, die mit der Symmetrisierung der Wasserstoffbindungen und dem Spinübergang von Fe in δ-$Al_{0.89}Fe_{0.11}OOH$ unter ansteigendem Druck verbunden sind. Der Übergang von high-spin zu low-spin verursacht dabei eine relative Verringerung der Elastizitätsparameter der Kristallstruktur. Derselbe Spinübergang in Fe scheint auch einen starken Effekt auf die thermische Leitfähigkeit des Kristallgitters von δ-(Al,Fe)OOH auszuüben, die mithilfe von ultraschneller Zeitdomänen-Thermoreflektanz untersucht wurde (achter Beitrag). Auf physikalischen Grundprinzipien beruhende Berechnungen wurden im folgenden Beitrag genutzt, um das Protonenpotential zu charakterisieren und so die Natur der Wasserstoffordnung und -symmetrisierung in reinem δ-AlOOH aufzuklären.

Akkurate Phasengleichgewichtsexperimente sind essentiell für die korrekte Bestimmung von seismischen Diskontinuitäten im Erdmantel. Im zehnten Beitrag dieses Kapitels wurde die Clapeyron-Steigung des Phasenübergangs von Pyrop zu Bridgmanit mithilfe von *in situ* Röntgenbeugung in Kombination mit einer Multianvilpresse bestimmt. Diese neuen Resultate ergeben einen konkaven Verlauf der Clapeyron-Steigung als Funktion der Temperatur, was zu einem komplexeren Einfluss dieses Phasenübergangs auf geodynamische Prozesse im Erdmantel führt als bisher angenommen.

Meteoritische und lunare Proben spielen eine grundlegende Rolle für unser Verständnis der Prozesse, die zur Bildung und Entwicklung unseres Sonnensystems beitrugen. Die sorgfältige Untersuchung von durch Impakte verursachten texturellen Merkmalen in einer Mondprobe der Apollo 15-Mission wird im elften Beitrag beschrieben. Sie ergab den erstmaligen Nachweis einer natürlich aufgetretenen inkongruenten Schmelze von Olivin, was darauf hindeutet, dass diese Probe einen völlig anderen Druck-Temperatur-Pfad durchlaufen hat als meteoritische Proben.

Die letzten vier Beiträge demonstrieren, wie die Charakterisierung der mikroskopischen Struktur von Mineralen zum besseren Verständnis ihres makroskopischen Verhaltens und ihrer Bildungsgeschichte beiträgt. Zum Beispiel können die Grenzen zwischen Antiphasendomänen in Magnetit ein Schlüsselhinweis auf ansonsten nicht detektierbare Eisenoxide mit gemischten Valenzen sein, die bei hohen Drücken und Temperaturen stabil waren (zwölfter Beitrag). In Omphazit dagegen bieten die Grenzen zwischen Antiphasendomänen die Möglichkeit, die Kinetik von metamorphen Prozessen in Eklogiten zu beschreiben, die während der Subduktion einer Hoch- oder Ultrahochdruckmetamorphose ausgesetzt waren (dreizehnter Beitrag). Dauphiné-Zwillinge in Quarz wurden im darauffolgenden Beitrag erstmals mit dem sogenannten electron channeling contrast imaging (ECCI) Verfahren in deformiertem Quarzit abgebildet, um die Deformationsmechanismen in diesem Mineral besser verstehen zu können. Transmissionselektronenmikroskopie wurde in der letzten Studie dieses Kapitels dazu verwendet, um den diffusiven Austauschprozess von Fe, Mg und Ca zwischen Ortho- und Klinopyroxenen im Detail zu untersuchen. Die Resultate zeigen ein komplexes Verhalten, das aus einem mehrstufigen Zusammenspiel von Rekristallisation, Diffusion und Kristallwachstum besteht.

3.4 Physikalische Eigenschaften von Mineralen

Schallwellen, die sich durch das Erdinnere fortpflanzen, liefern Schlüsseldaten für die Mineralphysik, da seismische Beobachtungen das wichtigste Werkzeug zur Bestimmung der thermochemischen Struktur des Erdinneren sind. Seismische Wellengeschwindigkeiten hängen von den elastischen Modulen und der Dichte des Materials ab, das die Wellen durchqueren. Beide Eigenschaften hängen wiederum von der Kristallstruktur und chemischen Zusammensetzung der gesteinsbildenden Minerale ab sowie von Druck und Temperatur. Darüber hinaus sind die elastischen Eigenschaften auch von der Kristallorientierung abhängig.

Die Messung der Wärmeleitfähigkeit von Mineralen ist eine komplementäre Methode, um den Wärmetransport in dem weiten unzugänglichen Bereich in der Tiefe unseres Planeten zu erkunden. Magnetische und elektronische Eigenschaften von Materialien unter hohem Druck (und hoher Temperatur) sind nützlich für die Untersuchung des Magnetismus von planetaren Kernen sowie der Phasenstabilität in Super-Erden als auch der Supraleitfähigkeit bei hohen Temperaturen, die alle nur durch Experimente bei extremen Bedingungen oder computergestützte Berechnungen verstanden werden können.

Die ersten vier Beiträge beschreiben Untersuchungen der Abhängigkeit der seismischen Wellengeschwindigkeit von der Kationen-Substitution in den Mischkristallserien von Bridgmanit, Akimotoit und dichten wasserhaltigen Magnesiumsilikaten. Experimente, bei denen die Wellengeschwindigkeiten direkt bestimmt werden, wurden entweder mit Laserlicht (Brillouin-Streuung) oder Ultraschallwellen mit simultanen Dichtebestimmungen als Funktion des Drucks (und der Temperatur) durchgeführt. Die Kombination der Geschwindigkeiten mit präzisen Dichtewerten aus der Einkristall-Röntgenbeugung ergeben elastische Module, die mit

seismischen Beobachtungen abgeglichen werden können. Die erstmalige direkte Eingrenzung der p-Wellengeschwindigkeit von $MgSiO_3$-Bridgmanit bei Drücken des tiefen unteren Erdmantels zeigt, dass die Schallwellengeschwindigkeiten einer vereinfachten, Al-freien Peridotit-Zusammensetzung das vorläufige seismische Referenzmodell des Erdinneren (PREM) mit einer Unsicherheit von nur 1 % abbilden. Die elastischen Eigenschaften von Akimotoit, dem Mineral der Mantelübergangszone mit der höchsten Anisotropie, können die seismisch beobachteten, anisotropen Merkmale eines Harzburgit-reichen Plattenmaterials erklären. Das Auftreten von Fe- und Al-haltigem Akimotoit in einer harzburgitischen Lithologie erhöht die P- und S-Wellengeschwindigkeiten des Gesamtmaterials so, dass sie zu denen des PREM an der Basis der Übergangszone passen. Die Substitution von Al-Fe in der sog. Phase H [$MgSiO_2(OH)_2$] hat dagegen unter Raumbedingungen nur geringe Auswirkungen auf die Komponenten des Elastizitätstensors.

Die nächsten beiden Beiträge konzentrieren sich auf die Gitterwärmeleitfähigkeit von wasserhaltigem Ringwoodit und die Kompressibilität von Fe-haltigen Kalzium-Aluminaten. Die Aufnahme von Wasser in die Ringwoodit-Struktur reduziert die thermische Leitfähigkeit signifikant bei Drücken der Mantelübergangszone im Vergleich zu nominell trockenen Proben und zeigt, wie Wasser im Kernbereich von subduzierenden Platten erhalten werden kann, so dass wasserführende Minerale tatsächlich den unteren Erdmantel erreichen könnten. Die Stabilität von Kalzium-Aluminaten bei hohen Drücken bedeutet, dass sie als Träger von Aluminium bis in den unteren Erdmantel dienen könnten.

Die letzten vier Beiträge beschäftigen sich mit magnetischen und elektronischen Eigenschaften bei hohem Druck. Eine kombinierte Untersuchung einer Invar-legierung bei hohem Druck mit nuklearer Magnetresonanz (NMR) und Mössbauer Spektroskopie zeigt, bei welchen Bedingungen der Magnetismus verloren geht und könnte so Kontroversen über das Verhalten der Invar-Legierung auflösen. Gitterdynamikberechnungen mit einer stochastischen, selbstkonsistenten harmonischen Annäherung ergeben ein verbessertes Verständnis des B1-B2 Phasenübergangs in MgO unter den extremen Bedingungen im Inneren von Planeten, und vermitteln eine bessere Einsicht in die Phasenübergänge bei der Zerfallssequenz von $MgSiO_3$ Post-Perovskit. Die Kombination von Hochdruck-NMR Messungen und *ab initio* Berechnungen erlaubt die Untersuchung der elektronischen Eigenschaften von Wasserstoff-atomen unter extremen Bedingungen und zeigt die Übergangstemperaturen zur Supraleit-fähigkeit in wasserstoffreichen Metallhydriden. Messungen mithilfe der dynamischen Diamantstempelzelle schließlich lösen Ordnungs-Unordnungsübergänge in Eis auf, die eine wichtige Rolle in der Entwicklung der großen Eisplaneten spielen könnten.

3.5 Fluide, Schmelzen und ihre Wechselwirkung mit Mineralen

In Subduktionszonen werden flüchtige Bestandteile wie Wasser, Kohlenstoff und Stickstoff in den Erdmantel zurückgeführt. Ein großer Teil dieser Komponenten wird bereits in einer Tiefe

von weniger als 150 km von der subduzierten Platte wieder abgegeben und findet den Weg zurück zur Erdoberfläche, entweder durch Entgasung oder durch magmatische Aktivität. Nur der in der Platte verbleibende Anteil gelangt in den tieferen Teil des Mantels. Die Quantifizierung dieser Prozesse ist wichtig für die Modellierung der tiefen Kohlenstoff- und Wasserkreisläufe in der geologischen Vergangenheit. Diese Kreisläufe regulieren den Meeresspiegel und die Zusammensetzung der Atmosphäre im Verlauf der Erdgeschichte. Ein wichtiges Problem ist hier der Mechanismus der Fluid-Mobilität in Subduktionszonen – diffundieren die Fluide durch das gesamte Gestein oder fließen sie in engen Kanälen oder nur in bestimmten Richtungen, die durch das Gefüge des Gesteins vorgegeben sind? Der erste Beitrag in diesem Teil des Jahresberichts beschäftigt sich mit diesem Problem. Ein natürlicher Serpentinit mit starker Schieferung wurde in einem Multianvilexperiment entwässert. Die Untersuchung der Versuchsprodukte zeigte, dass der Fluid-Verlust tatsächlich weit überwiegend in Richtung der Schieferung erfolgte. Neben Wasser und Kohlenstoff transportieren subduzierte Sedimente auch Stickstoff zurück in den Mantel. Dies beruht vorwiegend auf der Substitution von Ammonium (NH_4^+) für Kalium in bestimmten Schichtsilikaten. Der zweite Beitrag in diesem Kapitel untersucht, wieviel Stickstoff in diesen Mineralen maximal gelöst werden kann. Im Gleichgewicht mit einer Stickstoff-reichen Fluidphase können die Minerale bis über 2 Gew. % Stickstoff aufnehmen und die isotopische Zusammensetzung verschiebt sich zu höheren $\delta^{15}N$-Werten relativ zum Fluid. Wenn diese Minerale in einer Subduktionszone instabil werden und sich zersetzen, wird ein großer Teil des Stickstoffs entweder durch Wasser-reiche Fluide oder durch Silikatschmelzen zur Oberfläche zurückgeführt. Um abzuschätzen, wie effektiv dieser Prozess ist, werden Daten über die Löslichkeit von Stickstoff in Silikatschmelzen benötigt. Entsprechende Messungen enthält der nächste Beitrag. Die Stickstoff-Löslichkeit steigt linear mit dem Druck bis mindestens 2 GPa. In SiO_2-reichen Schmelzen – wie sie oft in Subduktionszonen vorkommen – ist Stickstoff sehr viel stärker löslich als in basaltischen MORB-Schmelzen. Nur wenige Phasen können flüchtige Komponenten tief in den Mantel transportieren, jenseits der Tiefe, in der die meisten wasserhaltigen Minerale instabil werden. Die δ-H-Phase, ein Mischkristall von AlOOH und $MgSiO_4H_2$ ist ein möglicher Kandidat für die tiefe Subduktion von Wasser in den unteren Mantel. Die Phasenbeziehungen von δ-H im System $MgSiO_3$-Al_2O_3-H_2O wurden in einem weiteren Beitrag untersucht. Interessanterweise bevorzugen sowohl H als auch Al sehr stark die δ-H-Phase, so dass der koexistierende Bridgmanit praktisch wasserfrei ist.

Der Mechanismus der Wasser-Speicherung im Erdmantel wird nach wie vor intensiv untersucht. Während in einigen Publikationen vorgeschlagen wurde, dass im obersten Mantel der größte Teil der OH-Gruppen im Mineral Olivin zu einem Defekt gehört, der Ti^{4+} enthält, zeigt eine neue Untersuchung in diesem Jahresbericht, dass bei 2-3 GPa OH-Defekte oft an Al^{3+} gekoppelt sind. Die Abhängigkeit der Wasser-Löslichkeit im Olivin von der Sauerstoff-Fugazität wird in einem weiteren Beitrag untersucht. Wasser aus der tiefen Erde kann durch Magmen wieder zur Erdoberfläche gebracht werden. Eine wichtige Frage ist hier, unter welchen Bedingungen wasserhaltige Silikatschmelzen leichter sind als das umgebende Gestein und daher im Mantel aufsteigen. Diese Fragestellung wurde mit molekular-dynamischen Simulationen untersucht.

Die Daten zeigen, dass Schmelzen mit mehr als 4 Gew. % Wasser versuchen würden, zur Erdoberfläche aufzusteigen. Interessanterweise ist ein großer Teil des Wasserstoffs in diesen Schmelzen gebunden als O-H-O-Brücken. Im Gegensatz zu Silikatschmelzen sind Wasser-reiche Fluide im Mantel relativ selten; sie kommen wahrscheinlich nur in Bereichen vor, die durch Wasser aus subduzierten Platten beeinflusst wurden. Hier können solche Fluide jedoch einen wichtigen Beitrag zu chemischen Transportprozessen leisten und aufgrund ihrer hohen elektrischen Leitfähigkeit können sie eventuell mit magnetotellurischen Messungen nachgewiesen werden. Die elektrische Leitfähigkeit dieser Fluide ist oft durch gelöstes NaCl und KCl erhöht. In Ergänzung zu früheren Untersuchungen im H_2O-NaCl-System wurde die elektrische Leitfähigkeit von H_2O-KCl-Fluiden bis 4 GPa gemessen. Hierzu wurde eine verbesserte Messzelle für die Piston-Cylinder-Apparatur entwickelt. Aufgrund der verstärkten Dissoziation von KCl steigt die Leitfähigkeit mit dem Druck stark an.

Im Vergleich zum Erdmantel ist die Speicherung leichter, flüchtiger Elemente im Erdkern sehr viel weniger untersucht. Das Dichte-Defizit des Kerns im Vergleich zu reinem Eisen oder einer Eisen-Nickel-Legierung deutet auf das Vorhandensein eines leichten Elementes hin. Es ist grundsätzlich denkbar, dass bei der Bildung der Erde Wasserstoff zusammen mit anderen leichten Elementen im Kern angereichert wurde. Ein Beitrag in diesem Teil des Jahresberichts untersucht die Eigenschaften von in flüssigem Eisen gelöstem Wasserstoff unter hohem Druck mit Hilfe von *ab initio* molekular-dynamischen Simulationen. Die Berechnungen zeigen, dass der Diffusionskoeffizient von Wasserstoff in flüssigem Eisen anomal hoch ist, was möglicherweise die Gleichgewichtseinstellung zwischen dem Kern und dem Magmenozean bei der Entstehung der Erde begünstigt hat. Der letzte Beitrag in diesem Kapitel beschäftigt sich mit dem Einfluss von Spin-Fluktuationen auf die elektronischen Transporteigenschaften von flüssigem Eisen, die möglicherweise die Entstehung des Erdmagnetfeldes beeinflussen.

3.6 Rheologie

Die Rheologie beschreibt, wie sich Materialien als Reaktion auf eine angelegte Spannung deformieren und fließen. Die Rheologie des Erdmantels ist eine fundamentale Eigenschaft, die die Natur und die Geschwindigkeit der Festkörperkonvektion und damit Prozesse wie die Plattentektonik und den Wärmetransport im Erdinneren kontrolliert. Aufgrund ihrer Wichtigkeit für das Verständnis der Prozesse in der Erde ist die Rheologie von Erdmaterialien schon seit vielen Jahren untersucht worden. Normalerweise geschieht dies mithilfe von Deformationsexperimenten durchgeführt, bei denen Gesteins- oder Mineralproben kontrolliert deformiert werden, indem man sie einer bekannten Spannung aussetzt; Verformungsraten werden dann als Funktion von Variablen wie Druck, Temperatur oder Mikrostruktur gemessen. Ein signifikantes Problem dieses Ansatzes ist, dass die experimentellen Verformungsraten um mehrere Größenordnungen höher sind als die Verformungsraten in der Erde. Das bedeutet, dass die experimentellen Ergebnisse sehr stark extrapoliert werden müssen, um auf die Prozesse in der Erde anwendbar zu sein. Die Zuverlässigkeit solcher Extrapolationen kann oft fraglich sein.

Experimentelle Deformationsstudien der Rheologie von Olivin haben gezeigt, dass im atomaren Gitter gelöstes Wasser die Festigkeit stark reduziert. Daher wird von diesen Studien ausgehend angenommen, dass die Viskosität des oberen Erdmantels auch mit zunehmendem Wassergehalt signifikant abnimmt. Der obere Erdmantel verformt sich wahrscheinlich überwiegend durch den Mechanismus des Versetzungskriechens, der durch die Geschwindigkeit kontrolliert wird, mit der Versetzungen vernichtet werden. Die erste Studie untersucht dieses Phänomen mit einem anderen Ansatz, indem nämlich der Effekt von Wasser auf die Rheologie von Olivin über die damit verbundene Ausheilungsrate von Versetzungen analysiert wird. Es wurde beobachtet, dass der Wassergehalt eine sehr geringe Auswirkung auf die Ausheilung von Versetzungen und somit auch auf die Mantelrheologie hat. Diese neuen Resultate stellen daher die Bedeutung von Deformationsstudien mit hohen Verformungsraten in Frage.

Die Korngröße eines Materials ist ein wichtiger Parameter, der den Deformationsmechanismus bestimmt. Bei geringer Korngröße ist der dominante Deformationsmechanismus Diffusionskriechen, während bei höherer Korngröße Versetzungskriechen vorherrschend ist. Kornwachstum spielt sich unter statischen Bedingungen bei hoher Temperatur ab und wird durch die Reduktion der Korngrenzflächen und somit der Korngrenzenergie angetrieben. Studien der Kornwachstumsrate in Olivin wurden bisher nur bei niedrigen Drücken ($\leq$1 GPa) durchgeführt. Der zweite Beitrag beschreibt Resultate, die bei wesentlich höheren Drücken von 1-12 GPa erzielt wurden. Sie zeigen, dass hoher Druck einen signifikanten Effekt hat, indem er das Kornwachstum verlangsamt und so dazu führen könnte, dass Diffusionskriechen der vorherrschende Deformationsmechanismus im Erdmantel bei Tiefen größer als 200 km ist.

Quantitative Deformationsexperimente von Mineralen der Übergangszone und des unteren Erdmantels sind aufgrund der erforderlichen hohen Drücke technisch sehr anspruchsvoll. Das rheologische Verhalten kann jedoch abgeschätzt werden, wenn die Diffusionsraten von Silizium und Sauerstoff bekannt sind, da die Diffusion dieser Elemente die Rheologie kontrolliert. Im dritten Beitrag wurden daher die Diffusionsraten von Silizium und Sauerstoff in Einkristallen von Mg_2SiO_4 Wadsleyit bei 1300-1600 °C als Funktion von Wassergehalt und kristallographischer Orientierung gemessen. Wasser erhöht in diesem Mineral die Diffusionsraten signifikant, im Gegensatz zu Olivin. Bei Wasserkonzentrationen < 1000 ppm ist Silizium die Spezies mit der geringsten Diffusionsrate, während bei höheren Konzentrationen Sauerstoff die am langsamsten diffundierende Spezies ist.

Der untere Erdmantel besteht hauptsächlich aus Bridgmanit (Silikatperovskit) plus einem relativ geringen Anteil von (Mg,Fe)O Ferroperiklas. Letzterer ist deutlich deformierbarer als Bridgmanit und es wurde bisher angenommen, dass sein Vorhandensein die Gesamtrheologie des unteren Erdmantels nur dann beeinflusst, wenn die Ferroperiklas-Körner miteinander verbunden sind. Das vierte Projekt ist eine rechnerbasierte Studie der Rheologie von Bridgmanit-Ferroperiklas-Aggregaten als Funktion des Ferroperiklas-Anteils, dem Viskositätskontrast zwischen beiden Phasen und des Ausmaßes, bis zu dem die Ferroperiklas-Körner

gelängt werden können. Die Resultate zeigen, dass die Auslängung der Ferroperiklas-Körner zu einer signifikanten Reduzierung der Mantelviskosität führt, selbst dann, wenn die Körner nicht mehr miteinander verbunden sind.

Der letzte Beitrag in diesem Kapitel stellt vorläufige Resultate einer experimentellen Studie vor, die die Rolle des Olivin-Spinell-Phasenübergangs bei der Erzeugung von tiefen Erdbeben erhellen soll und wie stark dieser Vorgang durch die Korngröße beeinflusst wird. Deformationsexperimente wurden mit Proben aus Mg_2GeO_4 Olivin durchgeführt, der als Analogmaterial für den Silikat-Olivin dient und sich schon bei deutlich niedrigeren Drucken in Spinell umwandelt.

3.7 Materialwissenschaften

Kompression stellt eine Möglichkeit dar, einem chemischen System große Mengen an Energie zuzuführen. Dies kann bei Festkörpern zu Phasenübergängen und Änderungen in physikalischen Eigenschaften führen, die bei Normaldruck nicht zugänglich sind. Das Bayerische Geoinstitut ist mit einer einzigartigen Kombination aus Hochdruck-Apparaten und analytischen Methoden – sowohl *in situ* als auch für dekomprimierte Proben – ausgestattet, die die Messung physikalischer und chemischer Eigenschaften von so gewonnenen Proben ermöglicht. Bei der methodischen Entwicklung stand in den vergangenen Jahren die Möglichkeit im Vordergrund, Einkristall-Röntgenbeugung bei Drücken von mehr als 100 GPa durchzuführen. Diese Methode wird auch in einigen der in diesem Kapitel vorgestellten Arbeiten angewandt.

Durch die starke sp^3-Bindung zwischen den Kohlenstoff-Atomen ist Diamant bis heute das härteste bekannte Material, und verschiedene Syntheseansätze für die Bildung von sp^3-gebundenen Kohlenstoffsystemen wurden verfolgt, ausgehend von unterschiedlichen sp^2-gebundenen Allotropen. Der erste Beitrag in diesem Kapitel verfolgt diesen Ansatz weiter, mit C_{60} als Ausgangsmaterial. Das Syntheseprodukt – gewonnen bei 30 GPa und dann zu Normalbedingungen gebracht – ist sp^3-gebunden und weist Ordnung auf mittleren Längenskalen aus, zwischen der Kurzordnung in amorphen und der Fernordnung in kristallinem Diamant.

Stickstoff-basierte Verbindungen haben ein großes Potential als Materialien mit interessanten Eigenschaften, die von Schleifmitteln mit großer Härte bis zu Sprengstoffen mit einer hohen Energiedichte reichen. Durch die Vielfältigkeit seines Auftretens in Festkörpern – isolierte N^{3-} als Nitride, als N_2^{2-} Pernitrid-Moleküle sowie verschiedene N_m^{-n} Anionen – ist Stickstoff ein besonders interessantes Legierungselement in der Festkörpersynthese. Zusätzlich zu konventionellen chemischen Verfahren bei Normal- oder niedrigem Druck, bietet hoher Druck die Möglichkeit, stickstoffhaltige Verbindungen mit ungewöhnlichen Eigenschaften zu

synthetisieren. Drei Beiträge in diesem Kapitel untersuchen stickstoffhaltige Systeme auf der Basis von Rhenium und Magnesium. Die vorgestellten Hochdruckuntersuchungen beschreiben die Bildung eines neuartigen Materials, in dem Stickstoff sowohl isoliert und als Pernitrid vorkommt, die Beobachtung einer chemischen Reaktion zwischen Rhenium und Stickstoff bei einem Druck im TPa Bereich, sowie die Bildung der Salze MgN_4 und Mg_2N_4, beide mit einer hohen Energiedichte. In Mg_2N_4 liegt Stickstoff als N_4^{4-} Anion vor, das auch zu Normalbedingungen gebracht werden kann, und damit ein bisher unbekannter Baustein zur Materialsynthese ist. Die dann folgende Arbeit an Rheniumkarbiden ergänzt die Untersuchung zu den Rhenium-Stickstoff-Verbindungen und zeigt Ähnlichkeiten und Unterschiede beider Systeme auf.

Mit der Entdeckung von Hochtemperatur-Supraleitung im Schwefelwasserstoff-System bei hohem Druck wurden Hydride von großem Interesse in der Hochdruckphysik. Deren Untersuchung wurde auch durch die Entwicklung von Protonen-Magnetresonanzspektroskopie in der Diamantatempelzelle am Bayerischen Geoinstitut ermöglicht. Zwei Beiträge zu Hydriden werden im vorliegenden Kapitel vorgestellt. Der erste Beitrag nimmt das Schwefel-Wasserstoff System genauer unter die Lupe und beschreibt, dass im Druck-Bereich, in dem Supraleitung vorliegt, nicht eine, sondern zwei Schwefelhydride auftreten; dies kann die starke Fluktuation in Materialeigenschaften (z. B. der kritischen Temperatur für Supraleitung) zwischen verschiedenen Untersuchungen erklären. Magnetresonanz-Messungen in der Diamantstempelzelle benötigen eine Kupferspule in der Probenzelle, und eine mögliche Reaktion zwischen Kupfer und Wasserstoff zu einem Kupferhydrid könnte die Messungen an anderen Metallhydriden beeinflussen. In einem entsprechenden Experiment werden im Druckbereich von 35 bis 150 GPa zwei Kupferhydrid-Phasen gefunden und charakterisiert, sodass deren möglicher Einfluss auf andere Experimente erkannt werden kann.

Auf ähnliche Weise hat die Synthese von Eisenoxiden mit ungewöhnlichen Zusammensetzungen bei hohem Druck im Verlauf der vergangenen Dekade – einschließlich zahlreicher Arbeiten am Bayerischen Geoinstitut – das Interesse am Hochdruck-Verhalten von Übergangsmetalloxiden erneuert. Hier wird die Hochdruckphase von Mn_3O_4 und deren physikalischen Eigenschaften untersucht; dabei zeigt sich, dass Mn_3O_4 – unerwartet – zu einem Halbleiter mit kleiner Bandlücke wird. In einer wasserhaltigen Umgebung bilden Übergangsmetall-Anionen Hydroxide oder Oxyhydroxide. Für Eisen ist dies FeOOH Goethit, ein wichtiges Erz. Die Möglichkeit, dass mit dieser Phase Wasser – oder Wasserstoff – in den tiefen Erdmantel transportiert werden kann, verleiht ihr geophysikalische und geochemische Signifikanz. In Experimenten in der Diamantstempelzelle werden Proben oft zusammen mit Salzen in die Probenkammer gegeben, wobei das Salz als Druck-übertragendes Medium eingesetzt wird, auch unter der Annahme, dass es nicht mit der Probe reagiert. Der letzte Beitrag dieses Kapitels zeigt, dass die Annahme chemischer Trägheit für NaCl mit FeOOH so nicht richtig ist und sich im Experiment ein komplexes Reaktionsprodukt bildet, womit die Ergebnisse bisheriger Untersuchungen in Frage gestellt werden.

3.8 Methodologische Entwicklungen

Der Auftrag des Bayerischen Geoinstitutes (BGI) ist es, die Struktur, Dynamik und Entwicklung des Inneren der Erde und anderer Planeten mithilfe von experimentellen, analytischen und theoretischen Methoden zu untersuchen. Methodologische Entwicklung ist dabei essentiell für Fortschritte in jedem Bereich der Wissenschaft, und daher investiert das BGI stark in die Entwicklung neuer Forschungstechnologien.

Diamantstempelzellen (DAC) sind derzeitig die einzigen statischen Druckapparate, die höhere Drücke erzeugen können als im Zentrum der Erde herrschen. Am BGI wurde die sog. Doppelstempel-Technik entwickelt, die zum weltweit erstmaligen Erreichen eines Druckes von 1 TPa genutzt wurde. Im letzten Jahr untersuchten Krupp und ihre Mitarbeiter verschiedene Formen von Sekundärstempeln und zeigten, dass alle getesteten Stempelformen bei hohem Druck eine Druckintensivierung mit einem Faktor von 2.5~3.0 erzeugten.

Die Transparenz von Diamant erlaubt es, Laser-Heizungen und verschieden Techniken der *in situ* Beobachtung anzuwenden. In der zweiten Studie in diesem Kapitel wurde eine neue Methode zur Detektion von Schmelzen in laser-geheizten Proben mithilfe von *in situ* Röntgen-Transmissionsmikroskopie entwickelt. Im dritten Beitrag wurde ein neues Hochtemperatur- und Hochdruck-Einkristall-Röntgenbeugungssystem an der Diamantstempelzellen-Strahllinie des Deutschen Elektronensynchrotrons (DESY) installiert. Mit diesem System können Daten zur Einkristall-Röntgenbeugung schrittweise mit einem zeitaufgelösten Hochgeschwindigkeits-Röntgendetektor (LAMBDA) synchronisiert mit einem gepulsten Laserheizungssystem aufgenommen werden. Das BGI hat in den letzten drei Jahren ein NMR-Spektrometer aufgebaut, das bis zu Megabar-Drücken anwendbar ist. Im letzten Jahr lag der Fokus der Entwicklung auf der Verbesserung der Auflösung der NMR-Spektren sowie auf der Kombination von NMR mit einem Laser-Heizungssystem. Der vierte und fünften Beitrag von Meier *et al.* berichten über die Fortschritte in diesen Bereichen der Entwicklung. Kurnosov *et al.* beschreiben Elastizitätsmessungen mit Brillouinspektroskopie bei Hochdruck- und Hochtemperaturbedingungen ebenfalls mithilfe einer Laserheizung. Die letzte Studie zu der Fortentwicklung von Experimenten mit Diamantstempelzellen befasst sich mit der Messung der Sauerstofffugazität in Diamantstempelzellen mithilfe einer Fe-Ir-Legierung.

Großvolumige Multianvilpressen werden ebenfalls am BGI für Hochdruck- und Hochtemperatur-Untersuchungen eingesetzt. Eine der Nutzungen dieser Apparate ist die Abschreckung und Erhaltung von Proben, die nur bei hohen Drücken und Temperaturen stabil sind, bis zu Raumbedingungen, um sie dann *ex situ* zu analysieren. Schmelzen und Fluide sind dabei besonders schwierig zu erhalten.

Bondar *et al.* haben ein Kühlungssystem zum Abschrecken einer Schmelze in ein Glas entwickelt und damit erfolgreich mafische Silikatschmelzen bei Drücken bis zu 6 GPa abgeschreckt. Rustioni *et al.* haben mit flüssigem Stickstoff eine Probenkapsel abgeschreckt,

und konnten so erfolgreich Festkörper, die aus einem Fluid beim schnellen Abkühlen kristallisierten, mit einem Laserablations-ICP-Massenspektrometer analysieren. Eine weitere Studie wurde durchgeführt, um eine Multianviltechnik zu entwickeln, die bei Drücken über 6 GPa reduzierte Fluide und Fluideinschlüsse für *ex situ* Analysen mit Ramanspektroskopie und Gaschromatographie produziert, um die Rolle von volatilen Komponenten in Mantelprozessen zu verstehen. Der letzte Beitrag zu experimentellen Entwicklungen berichtet über die Erzeugung von Ultrahochtemperaturen in Multianvilpressen. Obwohl die simultane Erzeugung von Ultrahochdruck und Ultrahochtemperatur sehr anspruchsvoll ist, gelang es Xie und seinen Mitarbeitern Temperaturen von 3000 K in einem Aufbau mit gesinterten Diamantstempeln in einer Multianvilpresse zu erzeugen, die so einen Druck von 80 GPa erreichen kann.

Die letzten drei Beiträge sind der Entwicklung der numerischen Modellierung gewidmet. Die zwei Studien von Eichheimer *et al.* untersuchten den Fluidtransport durch poröse Medien. Ein solcher Durchfluss wird durch die Permeabilität der Gesteine bestimmt, die im Mikrobereich mit einem nichtlinearen Fluid modelliert werden muss. Obwohl Berechnungen für nichtlineare Fluiddynamik numerisch aufwendig sind, gelang es, die Genauigkeit der Simulationen trotz niedriger rechnerischer Kosten zu erhöhen. In einer weiteren Studie wurden Permeabilitäts-messungen durchgeführt und das poröse Medium mit Bildanalysemethoden analysiert, um Beziehungen zwischen Permeabilität und effektiver Porosität zu bestimmen. Im letzten Beitrag dieses Kapitels wurde die rechnerische Auflösung für die Modellierung plattentektonischer Prozesse getestet, in denen eine stark temperaturabhängige Rheologie essentiell ist; es wurde aufgezeigt, dass eine hohe Auflösung unabdingbar ist, um die dünne Abdeckung der Lithosphäre in den Modellen darstellen zu können.

3. Research Projects

3.1 Earth and Planetary Structure and Dynamics

Planetesimals and planets formed rapidly in the nascent solar system. Records of condensation started ≈ 4.57 billion years ago in the solar system when refractory calcium-aluminium inclusions (CAIs) formed. The CAIs serve as the start of the chronology of planetary formation. Meteorite studies provide evidence that many parent bodies differentiated into a core, mantle and crust rapidly, before the end of formation of chondrules and thus chondrites. Models based on Hf-W and Fe-Ni short-lived isotope systematics propose that Mars had reached 90 % of its final mass within 5 million years after CAIs. Earth had a more protracted accretion history lasting up to 100 Myrs with the Moon-forming event known as the giant impact delivering about 10 % of its current mass. After core formation, the late accretion of the terrestrial planets occurred over 100s of Myrs after that. It was the last key period of Earth's formation as the final accreted materials brought siderophile and possibly volatile elements which remained in the Earth's outer silicate layers.

Astrophysical theories and thermal modelling of meteorite parent bodies indicate that planetesimals had sizes ranging from a few dozen to hundreds of kilometers. The decay of short-lived radiogenic isotope ^{26}Al (half-life 0.708 Myrs) was the primary heat source for these planetesimals. Radiogenic heating due to the decay of ^{26}Al and the potential energy release powered the formation of magma oceans on early formed planetesimals and protoplanets. Fewer constraints exists for planetary bodies of the outer solar system which are not as easily accessible. The first contribution describes numerical models treating the thermal evolution of early cometary objects called cometesimals. The study considers their size and timing of accretion which are critical parameters influencing their temperature evolution and thus controlling whether and where highly volatile compounds like CO can be preserved or are lost to space. The results suggest that only small or late-formed cometesimals are able to retain these highly volatile compounds.

The differentiation of planetary interiors and homogeneity in mass-independent stable isotopic compositions (*e.g.*, O, Cr, Ti) of most achondrite meteorite groups and terrestrial samples suggest that their parent bodies underwent a magma ocean stage. The crystallization mechanisms and dynamics of the cooling of magma oceans are not well constrained for planetary bodies. For example, the fate of carbon in a magma ocean expected to be present during terrestrial planet accretion is currently under debate. Previous studies suggested that the majority of the carbon would enter the Earth's core as a light alloying element. Keppler and Golabek discuss in their contribution whether some of the carbon could instead form graphite. Their results show that under reducing conditions this could be the case for about half of the carbon. Due to its low density the graphite could be prone to rise towards the planetary surface and to form a graphite-rich layer. Analytical calculations indicate that graphite ascent is most viable on small terrestrial planets like Mercury. This is supported by observations by NASA's MESSENGER mission suggesting the presence of a graphite-enriched layer at its surface.

Secondary processes related to the re-processing of planetary crust caused by planetary impacts further modified the evolution and composition of planetesimals. Frossard and colleagues investigated the elemental composition of pyroxene and plagioclase of a unique ungrouped achondrite named NWA 8486 which formed in the inner Solar System. They found that large positive anomalies in Sr and Eu in these two mineral phases and whole-rock could only have formed by partial melting of an anorthositic crust. Dynamical modeling supports that plagioclase floatation could occur on small planetesimals within short timescales < 1 Myrs. So far, anorthositic crust was only observed on the Moon, or in large igneous intrusions on Earth, while anorthosite is absent in meteorite collections.

By the end of planetary formation Earth had a differentiated structure featuring a silicate mantle and an iron core, both cooling over time. Earth's molten core is expected to be mostly a Fe-Ni alloy with probably several additional light elements as minor contributions. Based on seismic velocities and the density of Earth's solid inner core, it is expected that some of these light alloying elements enter the Earth's inner core as it crystallizes with one of the candidates being silicon. Measuring both seismic velocities and density for an iron-nickel-silicon alloy at high-pressure conditions, Dominijanni and colleagues determine that silicon is indeed a viable light alloying element in Earth's solid inner core.

The timing and origin of volatile elements delivery to terrestrial planets is a key question yet to be answered. Either volatile elements were delivered during the accretion phase with the building blocks, or the terrestrial planets accreted largely from dry material. This would require that volatile-rich material was added after core formation ceased during a late accretion phase bringing siderophile elements in order to explain the Earth's mantle budget. This topic is investigated by two studies using experimental and sample analysis constraints on elemental and isotopic behaviour for Earth and numerical modeling for Venus, respectively.

The study by Blanchard and Shcheka with colleagues at IPG Paris investigated the behaviour of Sn isotopes in multianvil apparatus experiments to determine the elemental behaviour of Sn and isotopic fractionation factor during core–mantle equilibration. They investigated the relative influence of temperature, pressure, oxygen fugacity, and metal and silicate composition on the metal–silicate partitioning behaviour of Sn. Using geochemical core-mantle modelling, they suggest that Earth's Sn budget and isotope composition can be explained if volatiles were added during late accretion by carbonaceous chondrite-like material and 2 to 4 wt. % S resides in Earth's core.

Since Venus probably never featured liquid water at its surface, its atmospheric evolution is expected to be simpler than Earth's since water can be delivered by impacts or outgassed from the interior, but it cannot be recycled back into the planet's interior. Using dynamical models of late accretion and modelling mantle and atmosphere evolution over 4.5 Gyrs, Golabek and colleagues' study different late accretion scenarios and compositions. This way they are able to determine whether a wet or a dry composition of late accretion is in agreement with the present-day volatile content of the Venus atmosphere. The results indicate that Venus experienced a preferentially dry late accretion.

In the final contribution, Zhang and colleagues investigate the planetary impact records of lunar Apollo 17 impact melt breccias. Because of their field relationships, these breccias have been regarded as a product of the Serenitatis basin-forming impact. They found that the micro-zircons have a Pb-Pb age (3921 ± 14 Ma), texture, and trace-element concentrations that are similar to the zircons from some of the Imbrium-originated breccias (Fig. 3.1-8). These results support that the spike of ≈ 3.9 Ga ages in Apollo sample suites may be overprinted by the Imbrium impact crater ejectas that were spread over the near-side of the Moon.

a. *Thermomechanical evolution of cometesimals (V. Szlachta, G.J. Golabek and M. Thielmann, in collaboration with M. Jutzi/Bern)*

Cometesimals (comet nuclei) are porous, low-density, km-sized objects found in the outer Solar System composed of rock and volatile ice. The thermomechanical evolution of these primitive objects is governed by heating from the radioactive decay of short-lived radioisotopes found in silicate rock such as ^{26}Al. This heating results in the sublimation of volatiles such as CO, CO_2, and NH_3. These volatiles are present at large heliocentric distances beyond 35 au and sublimate at temperatures between 40-140 K. The literature reports that meteorite parent bodies will not experience widespread thermal processing if they accreted > 2 Myr after the formation of the Solar System due to the decreased abundance of ^{26}Al present.

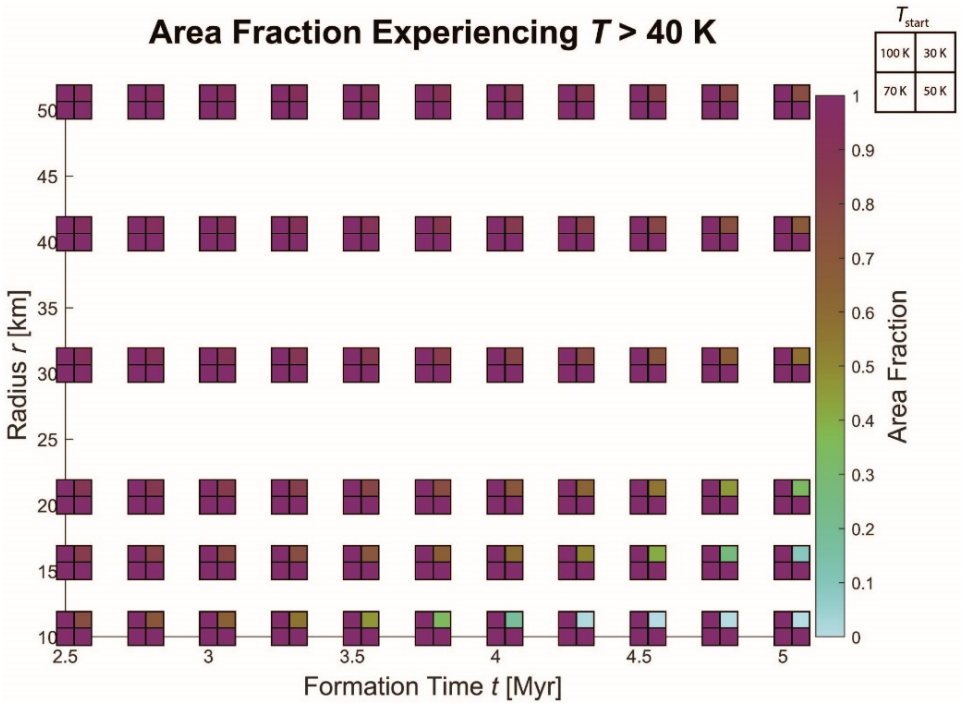

Fig. 3.1-1: Area fraction scatter plot for all models with starting temperatures of 30 K, 50 K, 70 K, and 100 K and a rock volume fraction of 0.6. Each small square shows the area fraction of the cometesimal that experiences temperatures greater than 40 K at the various starting temperatures. The starting temperatures represent the ambient temperature of the outer Solar System.

In this study, we investigated the formation time, radius, starting temperature, and rock fraction of cometesimals in order to determine under which conditions they retain the highly volatile species. The results can be used to constrain the formation time and size of bodies in the Solar System. For this purpose, we employed 2D numerical simulations using the finite difference code I2MART. We find that the radius and formation time have the greatest effect on the models compared to the other parameters. Small cometesimals with radii below 15 km cool efficiently, while large comets which form shortly after calcium-aluminium-rich inclusions (CAIs) are the most processed. Comet nuclei with radii of 10 km which form at least 4 Myr after CAIs will not sublimate CO and remain pristine (Fig. 3.1-1).

b. *Graphite floatation on a magma ocean and the fate of carbon during core formation (H. Keppler and G.J. Golabek)*

The fate of carbon in a young planet is a subject of considerable scientific interest, as the distribution of carbon between atmosphere, mantle, and core has a strong effect on the potential habitability of a planet. CO_2 and CH_4 are important greenhouse gases that may help to stabilize surface temperatures above the freezing point of water. Additionally, the availability of carbon in some reactive form is essential for the abiotic synthesis of early biomolecules. Current models of the fate of carbon in an early terrestrial planet, however, usually assume that most of the carbon would be sequestered in the core, leaving a carbon-depleted surface behind. However, as we will show in this contribution, it is possible that under certain conditions the evolution of a terrestrial planet after magma ocean solidification starts with a graphite-enriched surface.

Chondritic meteorites mostly contain carbon in the form of some organic, graphite-like material. During accretion of terrestrial planets, very commonly a magma ocean forms. Accreting chondritic material will disintegrate during impact. As the density of graphite is lower than those of a peridotitic melt, we investigated the dynamic stability of graphite near the surface of a magma ocean, testing two analytical expressions (Fig. 3.1-2). The calculations show that mm to cm-sized graphite particles likely accumulate of the surface of a magma ocean. In such a situation the composition of the primordial atmosphere is controlled by the equilibria:

$$C\ (graphite) + \tfrac{1}{2}\ O_2 = CO$$

$$C\ (graphite) + O_2 = CO_2$$

During early accretion, the oxygen fugacity of the magma ocean was likely very low, ranging from five to two log units below the Fe-FeO (iron wustite) buffer. Under these conditions, the CO and CO_2 fugacities are buffered to very low values, which in turn cause only trace amounts of carbon to be dissolved in a magma ocean (Fig. 3.1-3). These low carbon concentrations in the silicate melt limit the amount of carbon that could be sequestered into the metal phase during further impact events. If a planet grows through N impact events of equal mass, one may show by mass balance that the final concentration c_m of carbon in the metal phase of the core is

$$c_m = c_s\ (N+1)\ (1-f)\ /\ f$$

where f is the metal fraction in the impactors and c_s is the carbon concentration in the silicate melt (Fig. 3.1-3). This model predicts that for a plausible range of up to 200 impact events, less than half of the total carbon in the planet will be sequestered in the core, if the oxygen fugacity remained at IW-3 or below during accretion. Since the solubility of carbon in the silicate phase of the magma ocean is very low, this implies that terrestrial planets that accreted under rather reducing conditions may have developed a graphite-enriched surface layer. Indeed, there is very strong evidence for such a graphite-enriched layer on Mercury. Moreover, the ureilite meteorites, a class of carbon-rich achondrites, may be the remnants of a graphite-enriched surface layer on an asteroid. If a similar graphite-enriched surface layer had formed on Earth, the low albedo of graphite would have helped to stabilize clement surface temperatures.

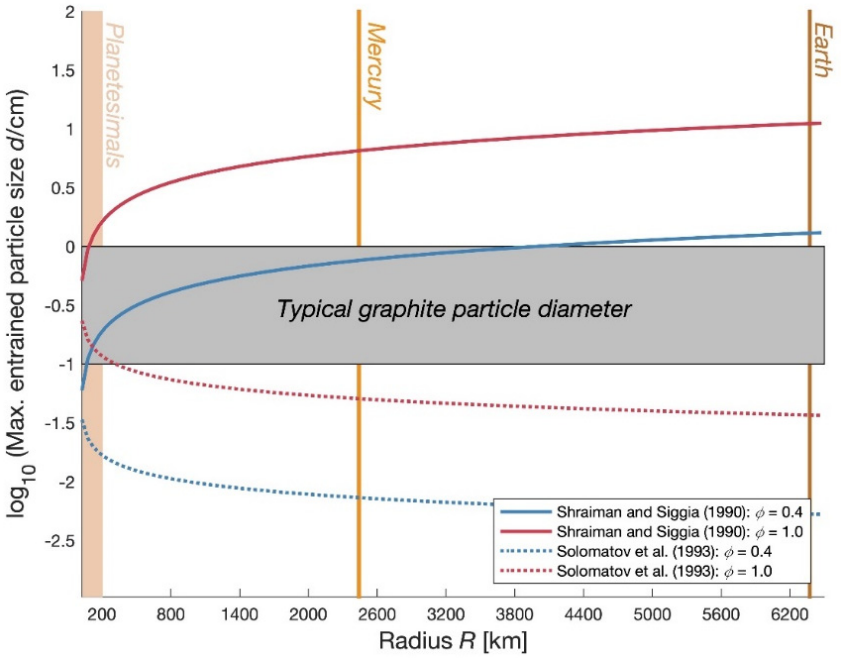

Fig. 3.1-2: Critical size for the entrainment of graphite particles on the surface of a vigorously convecting magma ocean. Calculations are based on the models of Shraiman and Siggia (1990; Phys Rev A 42: 3650) and Solomatov *et al.* (1993; EPSL 120: 387). The latter model predicts that graphite will always accumulate near the surface, while in the former model, this occurs only in relatively small plants. ϕ is the fraction of melt in the convecting mantle.

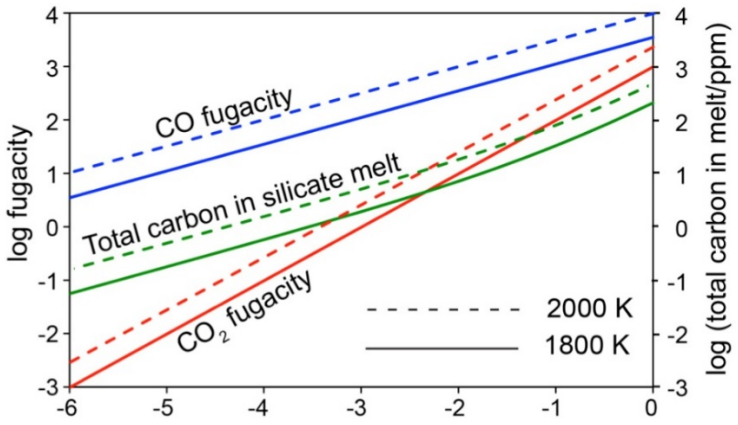

Fig. 3.1-3: Calculated CO and CO_2 fugacity and bulk carbon solubility in a peridotite melt in equilibrium with graphite at various oxygen fugacities.

c. *Evidence for anorthositic crust formed on an inner solar system planetesimal (P. Frossard and M. Boyet/Clermont-Ferrand; A. Bouvier; T. Hammouda and J. Monteux/Clermont-Ferrand)*

During the first million years of solar system history, planetesimals experienced extensive melting powered by the radioactive decay of ^{26}Al. To date, the only known anorthositic crust on a solar system body is that of the Moon, formed by plagioclase flotation on top of the magma ocean. In this study we show evidence from the elemental composition of the ungrouped achondrite meteorite Northwest Africa (NWA) 8486 that an anorthositic crust formed on a planetesimal very early in solar system history (< 1.7 Ma).

In the past 20 years, over 80 ungrouped achondrites have been found, enriching our collections with new types of meteoritic samples. NWA 8486 is one of several paired stones, along with the ungrouped achondrites NWA 7325 and 8014, that have been found in the Sahara Desert. They are plagioclase-rich cumulative gabbros that experienced remelting and fast cooling, with a very peculiar calcic and magnesian mineralogy. NWA 8486 formed under reduced conditions, with an oxygen fugacity (fO_2) of 3.2 log units below the iron wustite (IW) buffer, and therefore likely originates from the inner solar system. Based on Cr, Ti and O isotopic compositions, NWA 7325/8486 have affinities with both acapulcoite-lodranite and ureilite groups. The Pb-Pb isochron age of 4563.4 ± 2.6 Ma, Al–Mg age of 4563.09 ± 0.26 Ma and initial Mg isotopic composition for NWA 7325 indicate that the parent material of this meteorite had to be formed within 1-2 Myr after Solar System formation.

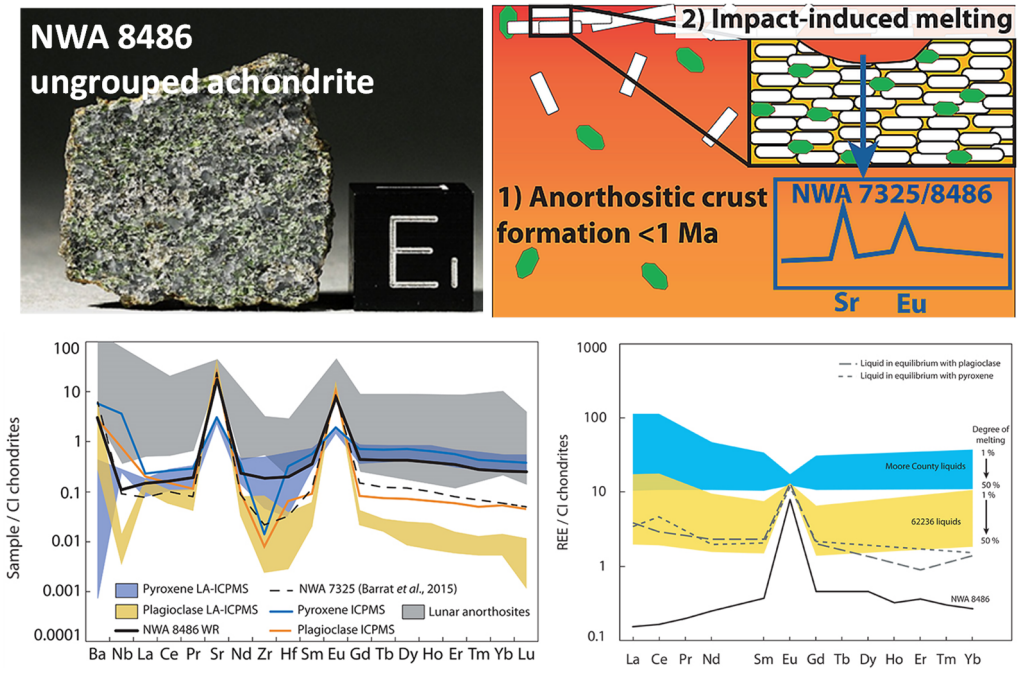

Fig. 3.1-4: A piece of the NWA 8486 ungrouped achondrite meteorite. A scenario is proposed for the origin of this meteorite parent body by impact melting of anorthositic crust on reduced planetesimal formed within 1 Ma after the start of the Solar System. The melt in equilibrium with the measured compositions of NWA 8486 minerals can be produced by 20-50 % melting of a pyroxene-rich anorthosite such as Apollo 62236.

We found that NWA 8486 displays the highest anomalies in Eu and Sr of all achondrites measured so far (Fig. 3.1-4). For the first time, positive Eu and Sr anomalies are also identified in meteoritical clinopyroxene and are of much higher amplitude compared to those of lunar anorthosites. Elemental modelling, together with calculated timescales for crystal settling, show that only the melting of a pyroxene-rich anorthosite such as Apollo 62236 can produce the composition of NWA 8486 within the first 5 million years of solar system history. Our results indicate that such a differentiation scenario was achievable over short timescales within the inner solar system, and must have contributed to the formation and elemental budget of the terrestrial planets.

d. *High-pressure sound velocity and density measurements of bcc-(Fe,Ni,Si) alloy using inelastic X-ray scattering: Implications for Earth's core composition (S. Dominijanni and C.A. McCammon; E. Ohtani, D. Ikuta and T. Sakamaki/Sendai; T. Ishii)*

Earth's inner core likely consists of Fe-Ni alloy(s) plus a minor fraction of light element(s) to match the density and sound wave velocities of seismological models such as the preliminary reference Earth model (PREM). Among possible alloying light elements (*e.g.*, Si, O, H, S, C), silicon is a popular candidate based on its cosmochemical abundance and potential involvement in chemical reactions at the core-mantle boundary. Previous work has shown that the solubility of Si in *hcp*-(Fe,Ni) alloy increases the stability field of the *bcc*-phase at high pressure. Comparison of sound velocity and density data of Fe-Ni-Si alloys with geophysical observations and theoretical predictions provide important constraints on the structure and dynamics of Earth's inner core. However, knowledge of the high-pressure and high-temperature behaviour and properties of Fe-Ni alloys that contain light elements is limited. We therefore investigated *bcc*-$Fe_{0.78}Ni_{0.07}Si_{0.15}$ alloy to compare its sound velocity and density with *ab initio* calculations and PREM in order to clarify the role of Si as a light element in Earth's inner core.

We measured sound velocities and densities of *bcc*-$Fe_{0.78}Ni_{0.07}Si_{0.15}$ alloy using inelastic X-ray scattering (IXS) and powder X-ray diffraction at the SPring-8 synchrotron facility (BL35XU beamline). High pressure was generated using a BX90-type diamond anvil cell. The metal alloy sample was loaded together with Ne (pressure medium) in a Re sample chamber and was mechanically compressed to 75 GPa through steps of 10 GPa at room temperature. IXS data were acquired at each pressure point in the range of momentum transfer of 4.24 to 7.63 nm^{-1}. To determine density, we collected X-ray diffraction patterns of the sample before acquisition of each IXS spectrum using a flat panel detector installed in the optical system. All IXS spectra were fitted using Lorentzian functions (Fig. 3.1-5, left). The dispersion relationship between energy (E) and momentum transfer (Q) was obtained by fitting all data with the following equation:

$$\mathrm{E\ (meV)} = 4.192 \times 10^{-4}\ v\mathrm{p}\ (^{\mathrm{m}}/_{\mathrm{s}}) \times \mathrm{Q_{max}}\ (\mathrm{nm^{-1}}) \times \sin\left(\frac{\pi}{2}\ \frac{\mathrm{Q(nm^{-1})}}{\mathrm{Q_{max}\ (nm^{-1})}}\right), \quad (1)$$

where *v*p is the sound velocity of the sample.

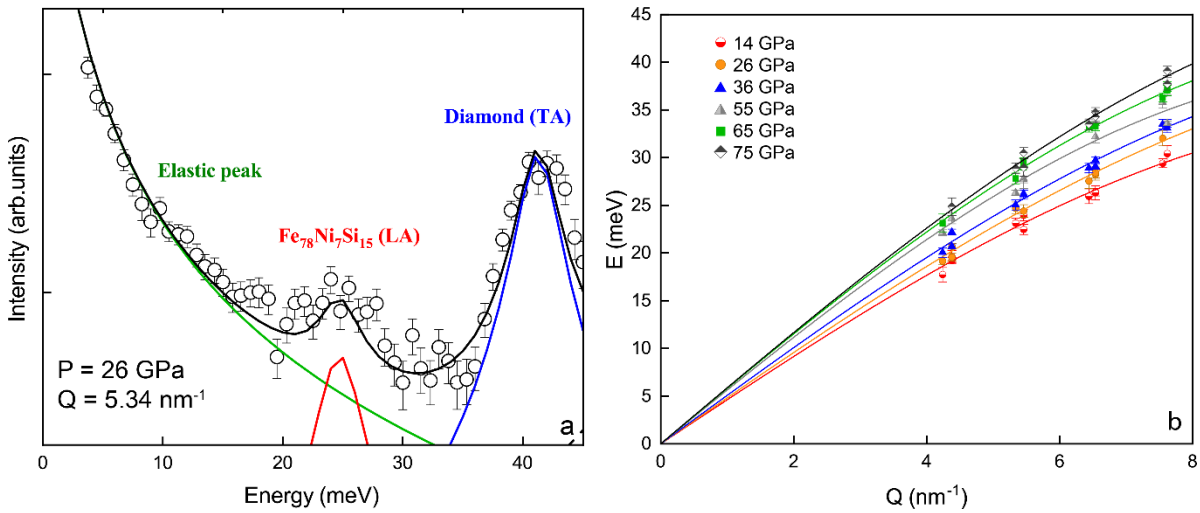

Fig. 3.1-5: (left) Room temperature IXS spectrum of bcc-$Fe_{0.78}Ni_{0.07}Si_{0.15}$ alloy at 26 GPa. Solid curves show individual contributions to the total spectrum (black): elastic peak (green), longitudinal acoustic (LA) phonon mode of the sample (red), and transverse acoustic (TA) phonon mode of the diamond (blue). Lorentzian functions were used to fit the data. (right) Dispersion curve of bcc-$Fe_{0.78}Ni_{0.07}Si_{0.15}$ alloy at room temperature and different pressures. Solid curves indicate fits of the longitudinal acoustic phonon energies to Eq. 1.

Preliminary results for *bcc*-$Fe_{0.78}Ni_{0.07}Si_{0.15}$ show that the energy of the longitudinal acoustic phonon increases with increasing pressure (Fig. 3.1-5, right). Additionally, we found that *vp* follows Birch's Law, *i.e.*, there is a linear relationship between density and sound velocity. Based on the comparison of our results and those for *hcp*-Fe and Fe-Si alloys reported previously with PREM, we propose that *bcc*-$Fe_{0.78}Ni_{0.07}Si_{0.15}$ alloy is a viable candidate as a component of Earth's inner core.

e. *Tracing Earth's volatile delivery with tin (E. Kubik, J. Siebert, B. Mahan and J. Creech/Paris; I. Blanchard and S. Shcheka; A. Agranier/Brest and F. Moynier/Paris)*

The habitability of our planet depends intrinsically on the presence of volatile elements. The timing and origin of volatile elements delivery on Earth is a key question yet to be answered. The two most extreme accretion scenarios propose either that volatile elements were delivered during the main phases of Earth's accretion and differentiation, or that the Earth accreted largely from material devoid of volatiles with late addition of volatile-rich material after core formation ceased. The study of the partitioning and isotopic behaviour of elements that are both volatile and siderophile can help discriminate between these two scenarios by isolating the effect of siderophile processes, such as the Earth's differentiation, from the effect of volatile processes.

Tin is a moderately volatile and moderately siderophile element which is only slightly depleted in the mantle with respect to lithophile elements of similar volatility. However, its metal–

silicate partitioning behaviour is poorly constrained and how the present abundance of Sn in the mantle can be linked to the signature of core–mantle equilibration is currently unclear. In addition, existing measurements of Sn isotopic composition in natural samples (*i.e.*, terrestrial rock, chondrites) can provide an additional independent constrain of the origin of Earth's mantle volatiles but require the determination of Sn isotopic fractionation during core–mantle equilibration. In this work, we have performed a series of thirty high-pressure and high-temperature experiments in a piston-cylinder press at IPGP and in multianvil apparatus at Bayerisches Geoinstitut from 2 to 20 GPa and 1700 to 2573 K, and systematically investigated the relative influence of temperature, pressure, oxygen fugacity, and metal and silicate composition on the metal–silicate partitioning behaviour of Sn. Elemental measurements include EPMA (Camparis, Université Pierre et Marie Curie, Paris) and LA-ICPMS (IUEM, University of Brest) analyses. Our results indicate that Sn siderophility noticeably decreases with increasing temperature and S content of the liquid metal but increases dramatically with pressure (Fig. 3.1-6). These results can be used to remark on the conditions of Earth's formation.

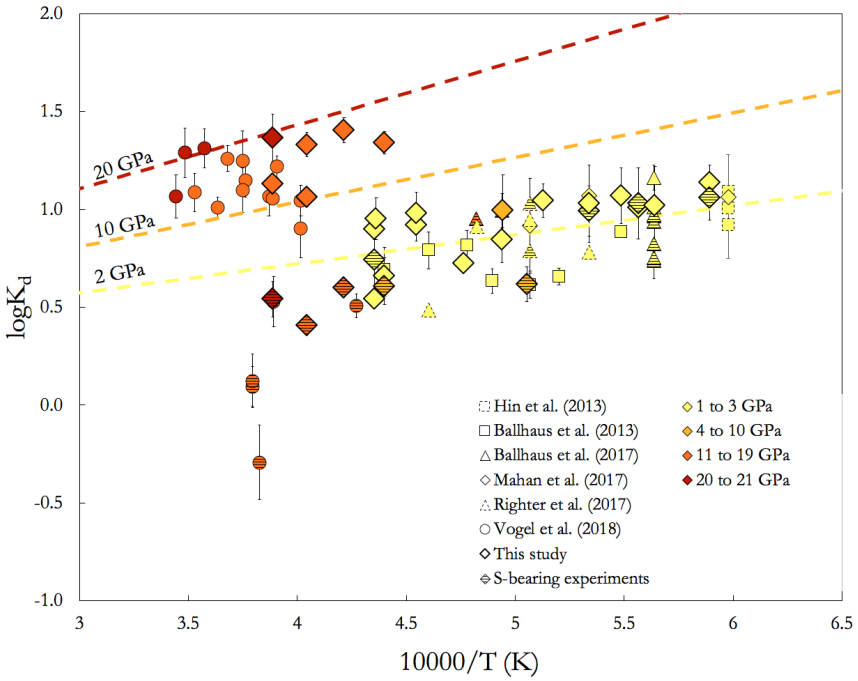

Fig. 3.1-6: Exchange coefficient $\log K_D$ plotted as a function of reciprocal temperature for all experiments of this study and data compiled from the literature (Ballhaus *et al.* 2017, 2013; Hin *et al.* 2013; Mahan *et al.* 2017; Righter *et al.* 2017; Vogel *et al.* 2018). Errors correspond to 1 standard deviation (σ) and were propagated from EPMA and LA-ICPMS measurements of this study and from the literature. Experiments containing more than 1 mol. % of S in the metal part are represented with a horizontal lines pattern. All experiments are color-coded according to their pressure: 1-3 GPa in yellow, 4-10 GPa in orange, 10-19 GPa in light red, > 19 GPa in dark red. Multilinear regression fits are also displayed at IW-2 in several conditions: 2 GPa, 10 GPa, and 20 GPa with no S in the metal. Sn partitioning is affected by temperature, Sn becoming less siderophile as the temperature increases. Pressure has a positive and strong effect on partition coefficients. S also presents a notable effect on $\log K_D$ which tends lower the partitioning as the S content of the metal phase increases.

Tin isotope measurements were performed using a Neptune Plus MC-ICP-MS (IPGP, Paris). A resolvable isotopic fractionation factor between metal and silicate was also measured on these experiments indicating that core–mantle equilibrium temperatures (~ 3000 K) could potentially generate a Sn isotopic composition of the mantle lighter than the core by 150-200 ppm per amu. Core formation modelling shows that the reduced depletion of Sn in the bulk silicate Earth can only be produced if volatiles were added late in the accretion history, namely during the last 10 % of Earth's accretion, from equilibration with a sulfide "matte" that segregated to the core. Consequently, a final core containing roughly 2 to 4 wt. % S is required. Further, modelling of the final Sn isotopic composition of the BSE argues for a late Sn accretion delivery on Earth during the last stages of core formation with carbonaceous chondrite-like material as the most likely source of volatiles for our planet.

f. *Dry late accretion inferred from Venus' coupled atmosphere and interior evolution (G.J. Golabek, C. Gillmann/Brussels and S. Raymond/Bordeaux; M. Schönbächler and P.J. Tackley/Zurich; V. Dehant and V. Debaille/Brussels)*

The composition of meteoritic material delivered to the terrestrial planets after the end of core formation as late accretion remains contentious. Numerical models demonstrate that the composition and mass of late accretion, including the amount of water, delivered to both Earth and Venus were comparable. On Earth water transport into the planetary interior by plate recycling limited the water loss and modified the water distribution between mantle and surface. On Venus, however, the absence of standing water prevented its recycling into the mantle and escape mechanisms were more efficient. This implies that the evolution of Venus' atmospheric composition is less intricate, which provides the opportunity to test implications of wet and dry late accretion compositions by using present-day atmosphere measurements.

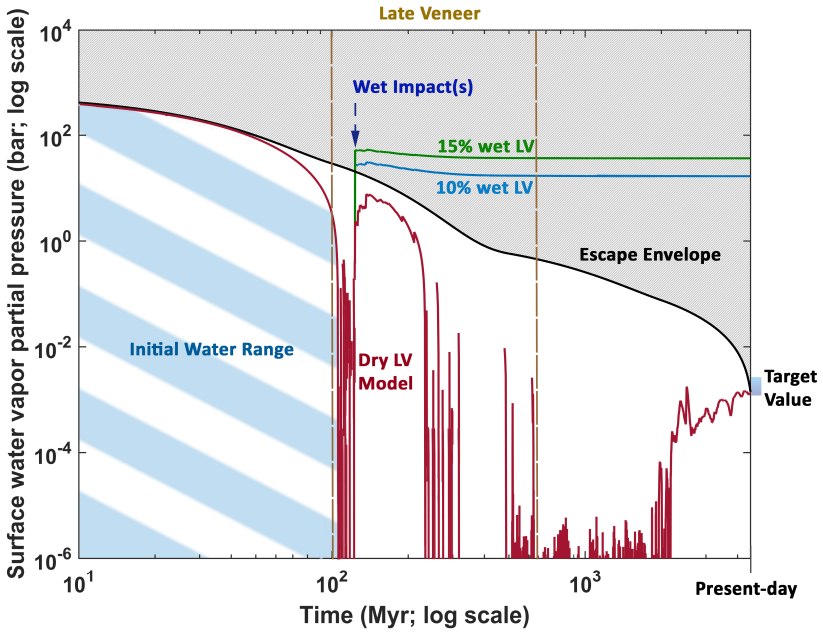

Fig. 3.1-7: Time evolution of H_2O abundance in the Venus atmosphere for three different impactor compositions.

We investigated the long-term evolution of Venus using self-consistent numerical models of global thermochemical mantle convection coupled with both an atmospheric evolution model and a late accretion N-body volatile delivery model (Fig. 3.1-7). Performing a systematic study of both the composition and size distribution of the late accretion, we demonstrate that a preferentially wet composition of the late accretion impactors is in disagreement with available observational data on H_2O, CO_2 and N_2 in Venus' present-day atmosphere. Our study suggests that the late accretion material delivered to both Earth and Venus was mostly dry and therefore the majority of Earth's water must have been delivered already during planet formation.

g. *Imbrium age for zircons in Apollo 17 South Massif Impact Melt Breccia 73155 (B. Zhang/London (Ontario, CA), Y. Lin/Beijing, D. Moser/London (Ontario, CA), J. Hao/Beijing, S. Shieh/London (Ontario, CA) and A. Bouvier*

Mare Serenitatis is one of the largest basins on the near side of the Moon, and its age is important for calculating lunar impact intensity over the ~ 600 million years after Solar-System formation. The poikilitic impact melt breccias brought back to Earth by the Apollo 17 mission have been widely seen as ejecta from the Serenitatis impact basin and have been used to date its formation. In this study, we found that zircons in Apollo 17 poikilitic impact melt breccia 73155,69 have age, textural and geochemical characteristics linked to the younger, 3.9 billion-year-old Imbrium basin. We propose that at least some components of the Apollo 17 site are Imbrium ejecta. Our findings further highlight the necessity to re-visit the Serenitatis origin for the Apollo 17 poikilitic breccias.

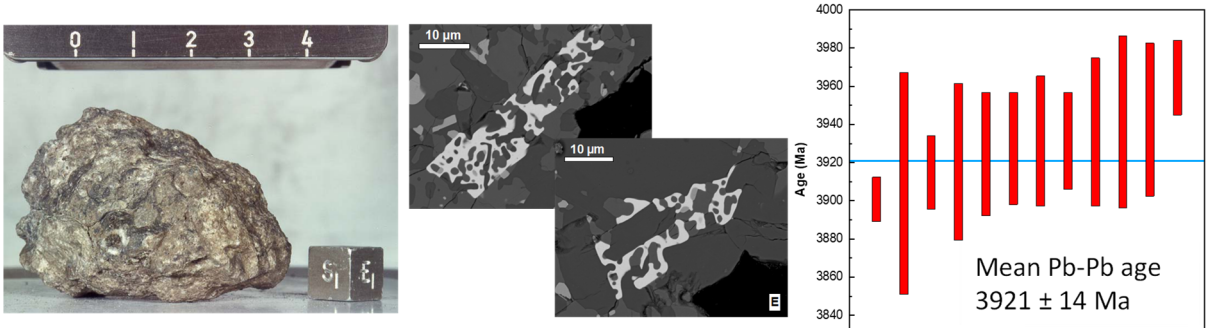

Fig. 3.1-8: NASA Apollo 73155 breccia and scanning electron microscope images of micro-zircons characterized and analysed for their elemental and U-Pb isotopic compositions in this study.

We carried out petrological, geochemical and U-Pb geochronological investigations of the poikilitic impact melt of Apollo 73155,69 which was sampled from the South Massif of the Taurus Littrow valley. Nanoscale secondary ion mass spectrometry (NanoSIMS at CAS Beijing) analyses of well-preserved poikilitic zircons from sample 73155,69 yield a uniform

age population with a weighted mean $^{207}Pb/^{206}Pb$ age of 3921 ± 14 Ma (Fig. 3.1-8). The zircons have distinctly high concentrations of Y (3279−6347 ppm) and Th (254−302 ppm) compared with other Apollo 17 zircons. These characteristics, together with their texture, are remarkably similar to zircons from high-Th melt breccias from Apollo 12 samples and lunar meteorite Sayh al Uhaymir 169 attributed to the formation of the high-Th deposits of the Imbrium basin. We, therefore, propose an Imbrium provenance for the zircons found in 73155,69. Our results provide new evidence for components of Imbrium ejecta occurring among the South Massif breccias. Consequently, the Apollo 17 poikilitic impact melt breccias may not represent Serenitatis ejecta.

3.2 Geochemistry

The majority of geological processes cannot be directly observed and their nature is obscured either by immense time or by the fact that they occurred deep within the Earth or other planetary interiors. These mechanisms leave behind evidence as to how they operated, however, in the chemical compositions of resulting rocks and minerals. Many of the studies in this section seek to provide the experimental data through which to interpret these geochemical signals to provide information on the causes and conditions of the events that have shaped the Earth and planets.

The first three contributions in this section examine the processes involved in planetary core formation. Rare meteorites, called pallasites, contain silicate minerals surrounded by iron metal that have been considered to be sections of the core–mantle boundaries of small planetesimals. In the first study chemical analyses on pallasites and deformation experiments on similar materials were performed in order to explore whether some of the metal may have been added through an impact shortly before the entire body solidified. While the textures obtained in the experiments support the impact hypothesis, the geochemical data apparently do not show evidence for the addition of external metallic liquid. In the next study laser-heated diamond anvil cell experiments have been performed to determine how carbon would have partitioning between the silicate mantle and core-forming metal as the core separated. It is found that under conditions compatible with the Earth's lower mantle carbon partitions considerably less strongly into liquid iron than at lower pressures, which helps to explain why carbon was not completely extracted from the Earth's outer layers. In the following study experiments have been performed to examine how much sulphur can dissolve in silicate melts at high pressures and temperatures. To date no experiments had examined this maximum sulphur content for a silicate melt composition compatible with melting of the entire silicate portion of the Earth. The results show that this sulphur content is much higher than previously predicted, which is important when modelling how much sulphide may have separated into the core from the molten mantle.

The following three contributions examine aspects related to the capture of mineral inclusions in diamonds, which provide the only sample we have from the deep mantle. In the first study the concentration of oxygen in iron sulphide melts, which form the most common inclusions in diamonds, is used to determine the temperature at which diamonds are produced in the lithosphere. The results show that diamonds are formed over quite wide temperature ranges, spanning those expected for incoming melts from the hot underlying mantle down to those more typical of the thick cratonic lithospheric mantle. Diamonds from the deeper convecting mantle are rare but their most common inclusions are of the oxide ferropericlase. Investigations of ferropericlase inclusions show that they often contain ferric iron rich oxides, which have separated out from the host mineral. In the following study the phase relations of these oxide phases are examined in order to understand the conditions at which this separation occurs. The most likely explanation is that while the diamonds were formed in the deep convecting mantle, after formation they became entrained in the subcratonic lithosphere where cooler temperatures

led to the oxides separating. In the final study on diamond formation and their inclusions, experiments were performed to partially melt carbonate and silicate assemblages at transition zone conditions. One of the most important findings is that magnesiowustite inclusions can form from such carbonate assemblages at transition zone conditions, whereas in the past such assemblages have been proposed to have formed in the lower mantle.

The next two studies continue the theme of deep mantle melting. The first attempts to determine the composition of a small degree hydrous melt at the base of the upper mantle, where a number of seismic studies have proposed that such melts may be the cause of low seismic wave velocities. There are a host of difficulties in determining such melt compositions, but in this study, it was ultimately possible to saturate a mantle assemblage with a hydrous melt. The composition of the melt is important because of its influence on the density. Dense melts might accumulate at this depth due to neutral buoyancy and the next step will be to test this by measuring the density of the melt at these conditions. The second melting study aims to constrain a thermodynamic model for melting in the Earth's lower mantle. Such models are important for determining how a deep magma ocean on Earth would have crystallised. In this study the composition of the first melt produced in a simple MgO-SiO_2 system is determined experimentally at a pressure compatible with the lower mantle but at conditions that can still be well controlled. This composition places important constraints on the thermodynamics of mixing in silicate melts that can then be used to construct melting phase diagrams over much wider ranges of pressure, where experiments would involve large uncertainties.

The following two studies examine the relationship between the oxidation state of iron in mantle minerals and the oxygen fugacity. Determining such redox relations is important because they not only control the compositions of minerals in the mantle but also influence the redox states and mobility of other elements such as carbon and sulphur. In the first study the redox state of iron in the dominant lower mantle mineral bridgmanite has been determined as a function of oxygen fugacity and bulk chemical composition. Many previous studies have disagreed on the oxidation state of iron in bridgmanite and on the extent to which iron partitions between bridgmanite and ferropericlase, the other dominant lower mantle mineral. The results of this study show that inter phase iron partitioning is strongly dependent on the oxygen fugacity and the large variations within and between all previous studies can be easily explained by their lack of control over this parameter. The second study examines the oxidation state of iron in the hydrous mineral serpentine, which is considered to be the main carrier of water into subduction zones. As serpentine forms it also raises the oxygen content of the oceanic crust through the oxidation of iron from the ferrous to the ferric state. Understanding the redox state in subduction zones is important as it influences the stability and mobility of volatile element-bearing phases. The results provide the first thermodynamic model through which the redox conditions of subducting serpentinized lithosphere can be determined. It shows quite surprisingly that although serpentine may be highly oxidised and contain a significant proportion of ferric iron, redox conditions during subduction remain relatively reduced. In fact, serpentine would continue to absorb oxygen from other minerals through the oxidation of iron.

Surrounding carbonate rocks, for example, would be reduced to graphite, which may help to preserve carbon within the subducting slab such that it enters the deep mantle.

The following study examines how magmas produced by island arc volcanism may obtain a geochemical signature inherited from subducted sediments. In order to determine the nature of metasomatic fluids emanating from cold subduction zones, diamond trap experiments were performed using metapelitic sediment starting materials, to which 30-40 wt. % fluid was added. The experiments were then equilibrated at conditions below the melting point of this assemblage where only fluids would be mobilised. The results show that chlorine-bearing fluids can attain arc-like trace element signatures, where as in the past it had been assumed that this signature resulted from melting of the sediments.

The final two contributions in this section are related to economic geology and both involve studies on the mineral amphipole. In the first contribution experiments were performed to examine the diffusion of copper in amphibole to investigate whether this mineral can reliably record the copper content of the silicate melts from which it crystallised. It turns out that copper diffusion in amphiboles is very fast, which casts doubts on the use of amphiboles and the melt inclusions contained within them, as a proxy for magmatic copper contents. In the second contribution amphibole-rich cumulate xenoliths from the mid to lower crust are examined that were brought to the surface by ore-related magmas in the Tongling copper-gold mining district in SE China. Analysis of these rocks, which formed through crystallisation of the ore-related magmas at depth, allow the effects of amphibole crystallization and associated sulphide precipitation on the magma mineralization potential to be explored. Although the magmas from which the metal ores were derived clearly lost significant amounts of copper and gold at depth, they were still able to produce extensive metal ores, which suggests that magma metal content is not the primary factor determining the mineralization potential. Factors such as the presence of water, which helps to concentrate the metal ores, may be more important.

a. *Petrological and geochemical study of the Seymchan pallasite meteorite, and experimental constraints on the formation of pallasites (D. Souza, A. Bouvier and G.J. Golabek, in collaboration with N. Walte/Garching)*

Pallasites are stony-iron meteorites composed of 55-75 vol. % olivine embedded within 20-40 vol. % of Fe-Ni metal alloy, along with minor phases such as pyroxene, phosphate and troilite. The olivine crystals occur as clusters, aggregates, or isolated crystals in the metal matrix. Past studies on pallasite formation models are divided in two main hypotheses: (1) Pallasites formed near the core-mantle boundary (CMB) of planetesimals during extensive fractional melting. (2) Pallasites formed by a non-destructive impact that introduced and mixed metal from an impactor with the mantle of the target body. Previous studies proposed that pallasites with rounded and fragmental olivines could have formed inside small planetesimals, through an impact event followed by convection. Past experimental simulations of angular pallasites indicated that these textures might preserve a two-stage evolution of a parent body, consisting

of inefficient differentiation and a later collision. In this model, olivine clusters may retain up to 15 % of primordial metallic melt from the parent body. Hence, metal inside olivine clusters and in the matrix of pallasites may differ in terms of mineralogy and/or chemistry.

In order to test these models, two pieces of Seymchan pallasite were characterized in terms of texture and chemistry. The samples consisted of one piece of metal matrix devoid of olivine, and one olivine-bearing slice of Seymchan. Chemical analyses were conducted with electron microprobe and Laser Ablation Inductively Coupled Plasma Mass Spectrometry (LA-ICP-MS) at BGI. In order to understand the controlling factors of pallasitic texture formation, deformational experiments were also performed, using the 6 Piston Mavo press in BGI and the SAPHiR press in Garching. The confining pressure was 1 GPa, and deformation temperature was ~ 1300 °C, with varied strain rates and deformation geometry. The starting material for the deformation experiments was a mixed powder of 80 % grinded San Carlos olivine and 20 % of synthetic FeS. To simulate influx of additional metallic melt during the experiments, pieces of solid gold or FeS powder (~ 5-10 vol. % of the capsule) were placed in the center of the capsule. The assembly consists of a pyrophyllite cube with 12 mm edge-length, a furnace and capsule made of Re-foil, mounted in a symmetrical geometry.

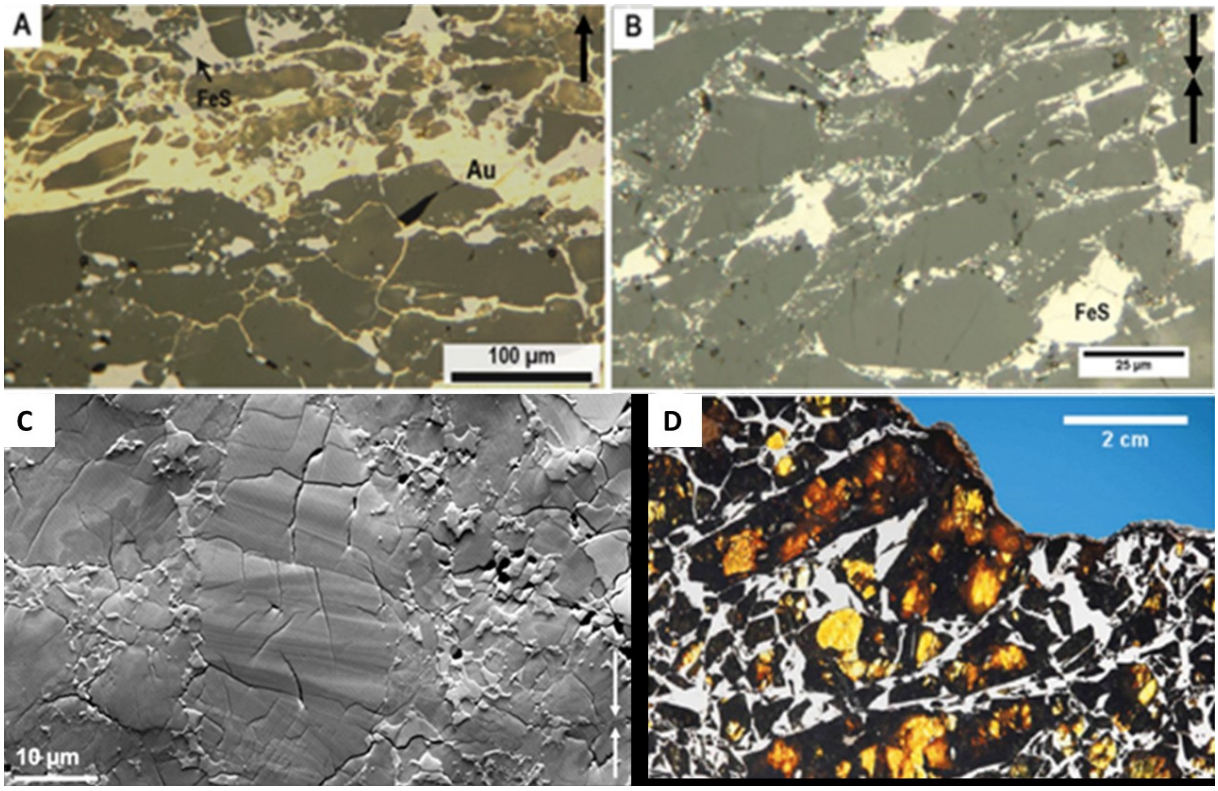

Fig. 3.2-1: Deformation experiments performed using the Mavo 6 piston press at BGI. Experiments M715 (A) and M726 (B) (reflected light) with strain rates of 2.0×10^{-3} s^{-1} produced textures with fragmental olivines, similar to those observed in Admire pallasite (D). Arrows on the top right indicate deformation axis direction. Experiment M719 (C) (orientation contrast image-EBSD detector) with final strain rates of 5.3×10^{-4} s^{-1} generated internal deformation of olivine grains, and clusters of round olivine with melt, which textures are not observed in pallasites.

The results of the natural samples showed that Seymchan pallasite contains angular and fragmental olivines with an average composition of $Fa_{11.1\pm0.3}$, which are not oriented or internally deformed. Metallic matrix and pools contain kamacite ($Fe_{92.7\pm0.2}Ni_{6.6\pm0.3}$) and taenite ($Fe_{76.0\pm2.3}Ni_{23.6\pm2.4}$), with schreibersite $(Fe,Ni,)_3P$ as a minor phase. The mineralogy and chemistry of metallic phases does not suggest different sources for matrix versus pools. Further isotopic (*e.g.*, Fe, Ni, and Cu) analyses would be useful to establish their respective origin. The minor phases are stanfieldite ($Ca_{3.99}Mg_{4.42}(PO_4)_6$), whitlockite ($Ca_{7.86}Mg_{0.86}(PO_4)_6$), and troilite (FeS). Deformation experiments in the brittle domain generated textures with fragmental olivines similar to textures observed in Admire pallasite, while others developed more angular textures, resembling those of Seymchan or Imilac pallasites (Figs. 3.2-1 and 3.2-2). One experiment performed at a lower strain rate resulted in brittle-ductile microstructures including internal deformation of olivine grains, which is not observed in pallasites. Hence, pallasite textures are produced under high strain-rate conditions in the brittle deformation regime, which supports the impact models. The formation of angular olivine is favored by extensional strain and a pre-existent partial melt phase that weakens the grain boundaries and facilitates intergranular fracturing.

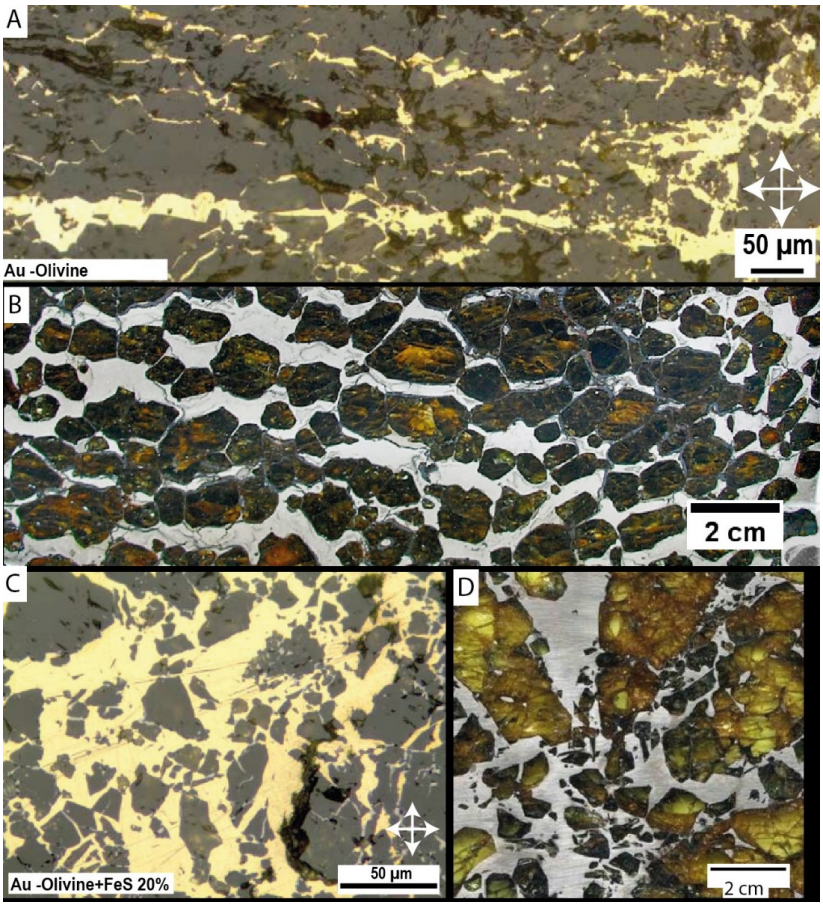

Fig. 3.2-2: A) Experiment SA176 performed with SAPHiR press in Garching (reflected light). Arrows indicate the extension directions. This experiment produced a texture similar to Mt. Vernon pallasite shown in B. C) In experiment SA177 (reflected light), the presence of FeS melt pockets in the matrix creates planes of weakness which favored the formation of angular olivines similar to those observed in Esquel pallasite (D).

b. *The fate of carbon during Earth's core-mantle differentiation (I. Blanchard, E.S. Jennings/London, I.A. Franchi and X. Zhao/Milton Keynes, S. Petitgirard/Zurich, N. Miyajima, S.A. Jacobson/Michigan and D.C. Rubie)*

Carbon is an essential element for the existence and evolution of life on Earth. It constitutes up to 50 % of dry biomass and its presence is a likely requirement for all life in the universe. Its high abundance in Earth's crust and mantle (the Bulk Silicate Earth, BSE) is surprising because carbon is strongly siderophile (metal-loving) and should have segregated almost completely into Earth's core during accretion. Estimates of the concentration of carbon in the BSE lie mostly in the range 80-120 ppm, which is much higher than expected based on simple models of core-mantle differentiation. Here, we performed experiments at the likely conditions of core-mantle segregation using state of the art laser-heated diamond anvil cells. Our samples were subsequently analysed using an electron microprobe for major elements and nanoSIMS for carbon in the silicate melt. We show through experiments at 49-71 GPa and 3600-4000 K that carbon is significantly less siderophile at such conditions than at the low pressures (≤ 3 GPa) of previous studies. We derived a new parameterization of the pressure-temperature dependence of the metal-silicate partitioning of carbon and applied this in a combined model of planet formation and core-mantle differentiation that is based on astrophysical N-body accretion simulations. We first assume that carbon is accreted to Earth only in bodies that originate beyond 4.5 AU and that their average C concentration is 1.6 wt. % (an approximately mean carbonaceous chondrite (CI, CM, CO and CV) value). This model successfully reproduces the BSE amount of carbon (red line in Fig. 3.2-3). However, in this model the final concentration of C in the core is 47 ppm which means that the carbon concentration of the bulk Earth is only 83 ppm, *i.e.*, far below the lowest estimate of 520 ppm. We have therefore developed a scenario that results in a bulk concentration of ~ 520 ppm. We assume that bodies from beyond 4.5 AU contain on average 1.6 wt. % carbon and that C concentrations in bodies originating at < 4.5 AU decrease along a linear gradient to reach a value of zero at a heliocentric distance of 1.88 AU. The model then predicts a final mantle C concentration of 314 ppm (black line in Fig. 3.2-3), a core concentration of 950 ppm and a bulk Earth concentration of 518 ppm.

The combined accretion/differentiation model predicts that much more carbon is retained in the mantle than is suggested by simple core-formation models. There are two reasons for this major difference: (1) When fully-oxidized bodies are accreted to Earth in our model, there is no core-formation event because such bodies do not contain metal. Thus, carbon and other volatiles cannot be transported to the core and are retained in the mantle. (2) When metal-bearing differentiated bodies are accreted, their metal only equilibrates with a small fraction (< 10 %) of the magma ocean/mantle and thus the removal of C to the core is very inefficient.

A BSE carbon concentration of > 200 ppm is considerably higher than the estimated value of about 100 ppm. If the 100 ppm value is correct, an additional process that is not included in our model, may have transported excess carbon to the core. There is experimental evidence that the pressure-induced disproportionation of $Fe^{2+} \rightarrow Fe^{3+} + Fe$ in deep magma oceans causes the

formation of dispersed Fe metal droplets. The gravitational segregation of these metal droplets could have transported the excess carbon to the core, leaving ~ 100 ppm in the mantle and resulting in a low concentration (*e.g.*, 0.14 wt. %) of C in the core. In conclusion, our results show that BSE carbon concentrations increase strongly starting at a very early stage of Earth's accretion and, depending on the concentration of carbon in accreting bodies, can easily reach or exceed estimated BSE values.

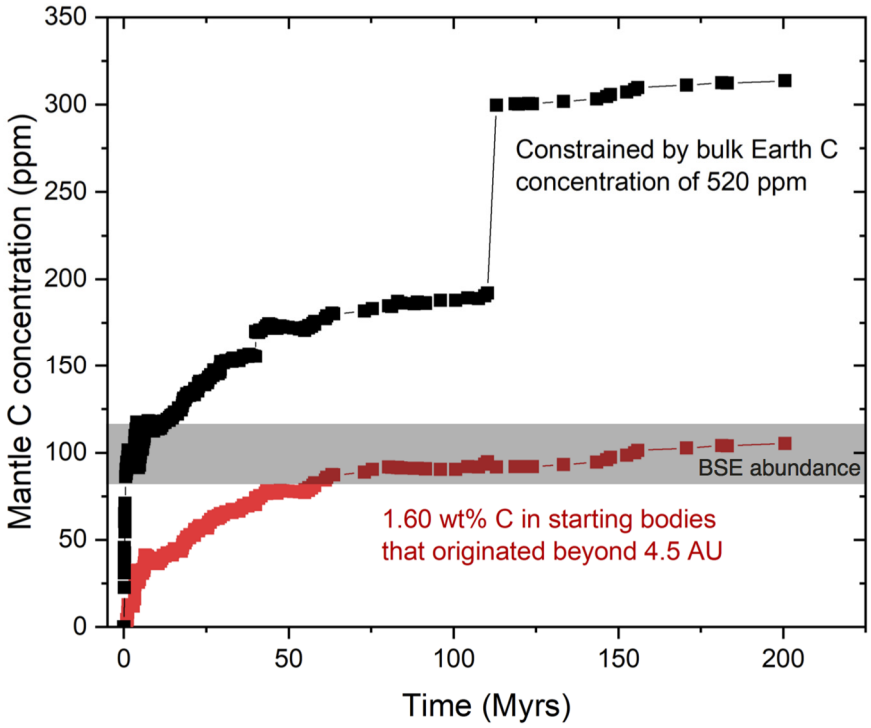

Fig. 3.2-3: Mantle C concentration during accretion as a function of time based on a combined accretion/differentiation model. The red symbols show the evolution of mantle carbon concentration assuming that all starting planetesimals that originated from beyond 4.5 AU contained an average of 1.6 wt. % C; bodies originating at heliocentric distances < 4.5 AU are assumed to contain zero C. The black symbols show the evolution when the average carbon concentration in starting bodies originating from beyond 4.5 AU is 1.6 wt. % and C concentrations in bodies originating at < 4.5 AU decrease along a linear gradient to reach a value of zero at a heliocentric distance of 1.88 AU. The prominent jump at 110 Myrs is caused by the final giant impact. Estimates of the BSE concentration range from 100±20 ppm, as shown, to 765 ± 300 ppm.

c. *The effects of pressure and temperature on the sulphur content at sulphide saturation of peridotitic liquid (I. Blanchard, S. Abeykoon, D.C. Rubie and D.J. Frost)*

The amount of sulphur that can be dissolved in a silicate liquid is of fundamental importance because it is closely related to several major Earth related processes such as the formation of magmatic sulphide deposits, volcanic degassing during eruptions, core-mantle differentiation and late-accretion scenarios. Considerable effort has been made to understand the interplay

between the effects of silicate melt composition and the melt's capacity to retain sulphur, but the dependence on pressure and temperature for a given melt composition is still quite poorly constrained. Here we conducted a systematic study of the effects of pressure and temperature on sulphur content at sulphide saturation (SCSS) for a peridotitic liquid.

We equilibrated a peridotitic melt with sulphide melt at various conditions of pressure and temperature. We performed multianvil experiments from 7 to 23 GPa and 2073 to 2623 K and analyzed the recovered runs using both electron microprobe and laser ablation ICP-MS. We highlight in this study the systematic decrease of the amount of sulphur in the silicate melt with increasing pressure and its increase with increasing temperature over the range of pressures and temperatures studied here (Fig. 3.2-4). We used our data to propose a new model of the dependence of sulphur content of peridotitic melt on pressure and temperature that for the first time encompasses the entire range of upper mantle pressure and temperature.

We observe that for silicate containing > 18 wt. % MgO at a given P-T, the SCSS is much higher than concentrations that have been predicted from experiments performed at concentrations < 18 wt. %. Consequently, an MgO-rich magma ocean in equilibrium with sulphide will become sulphide undersaturated during its adiabatic ascent towards the surface. It has been proposed that komatiites and their associated ore deposits acquired sulphur and chalcophile elements by crustal contamination instead of reaching sulphur saturation. Our study confirms this hypothesis indirectly – *i.e.*, that ultramafic magmas such as komatiite were likely not sulphur saturated when they reached the surface, and acquired their high sulphur content by contamination through interaction with the surrounding crust.

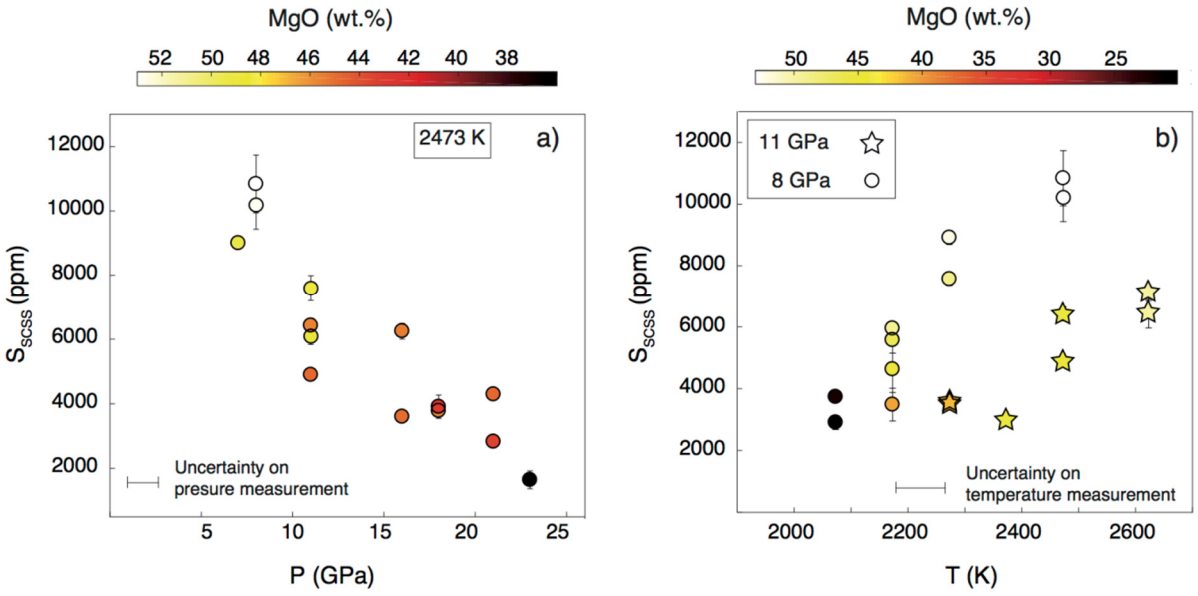

Fig. 3.2-4: Experimental results on the effects of pressure and temperature on SCSS. In (a) data obtained at constant temperature of 2473 K are plotted as a function of pressure. In (b) data obtained at constant pressure of 8 GPa (circles) and 11 GPa (stars) are plotted as a function of temperature and are colour coded according to their MgO content.

d. *A new geothermometer based on the oxygen content of sulphide inclusions in diamonds (S. Abeykoon, D.J. Frost, V. Laurenz and N. Miyajima)*

Sulphides are the most common type of inclusion found in diamonds and are widely used to determine the timing and lithology of diamond formation. Sulphide inclusions are generally trapped as melts which crystallise initially to form Fe-Ni rich monosulphide solid solutions (mss). Upon cooling below ~ 1000 °C these inclusions recrystallize again to pyrrhotite, $Fe_{(1-x)}S$ (x = 0 to 0.2), and pentlandite, $(Fe,Ni)_9S_8$, and sometimes pyrite (FeS_2), depending on the bulk composition. The presence of oxygen as oxides, or even hydroxides, associated with sulphide inclusions in mantle xenoliths is usually interpreted as being a result of low temperature sulphide alteration. Previous experimental studies, however, show that some oxygen should partition into sulphide melts, particularly at high temperatures. Most importantly measurements of natural sulphide inclusions in diamonds indeed show measurable oxygen concentrations, which are unlikely to be caused by alteration. If the parameters that control sulphide oxygen concentration can be determined then they could be potentially used to understand the formation conditions of diamonds.

We performed a series of high-pressure (3-15 GPa) and high-temperature (1473-2023 K) multianvil experiments to understand the factors that influence the oxygen contents of sulphide melts. A fertile peridotite (KLB-1) mixture was equilibrated with molten sulphide (FeS) in graphite capsules. The effects of pressure, temperature, oxygen fugacity and composition (both silicate and sulphide) have been investigated. We also investigated the effect of Ni is sulphide on the oxygen content as it is a major element in most mantle suphides. Ir was added in sufficient quantities to saturate the sulphides and form an Fe-Ir alloy from which the oxygen fugacity could be accurately determined. Run products that contained mantle silicate minerals and quenched sulphide melts were analysed using the electron microprobe. The results are used to parameterize the oxygen content in sulphides in equilibrium with a mantle peridotite assemblage at conditions relevant to diamond formation.

We measured up to 16 mol. % of FeO in our experimental sulphide melts at mantle conditions. Moreover, the content of oxygen in the sulphide is found to be relatively independent of fO_2 or fS_2 over the range investigated. This is in contrast to previous experimental studies conducted at ambient pressure conditions. The experimental results indicate that the oxygen concentration is mainly controlled by the FeO activity in coexisting silicate phases and the temperature. In order to fit the data and to account for the observed FeO dependence, we developed a thermodynamic model using an end-member equilibrium involving FeO dissolved in the sulphide melt, *i.e.*,

$$\underset{\text{olivine}}{Fe_2SiO_4} = \underset{\text{orthopyroxene}}{FeSiO_3} + \underset{\text{sulphide melt}}{FeO}$$

The standard state Gibbs free energy change (ΔG^0) at the pressure and temperature of interest is calculated from the activates of the components *i.e.*,

$$\Delta G^0 = -RT \ln \frac{a_{FeO}^{sulphide} a_{FeO}^{opx}}{a_{FeO}^{olivine}}$$

Where R is the gas constant and T is temperature. Well known activity-composition relations for the silicates are used and an activity composition model to describe activities in the FeS-FeO-NiS system is derived from the experimental data. Figure 3.2-5 shows values of ΔG^0 calculated as a function of temperature. The effect of Ni has been well accounted for because the Ni-bearing and Ni-free samples plot along the same line. The strong temperature dependence of the equilibrium and the apparent lack of a pressure influence mean that it is a potentially very useful thermometer.

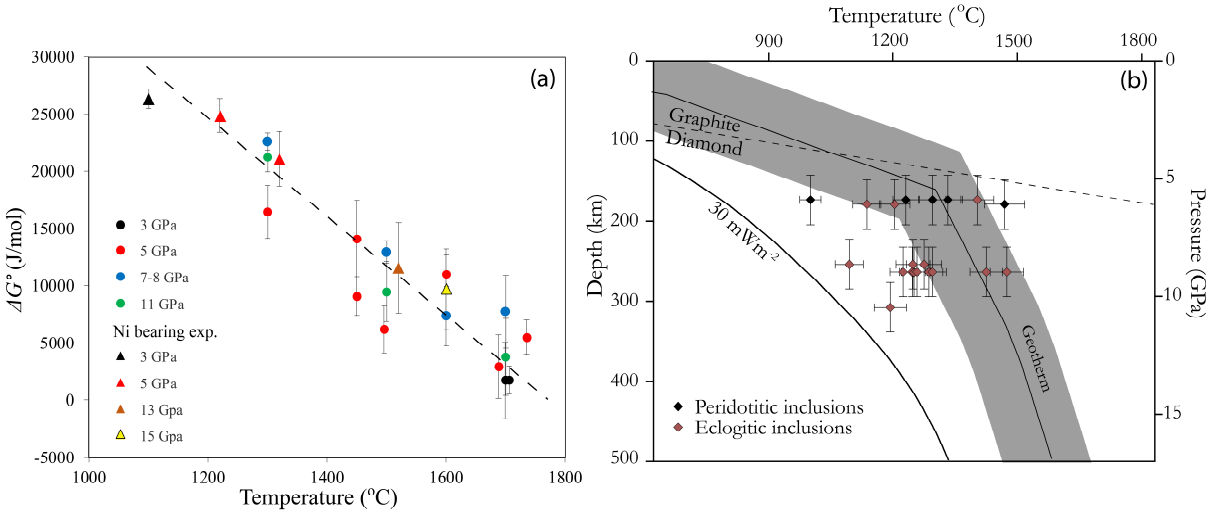

Fig. 3.2-5: (a) The ΔG^0 for FeO dissolution in sulphide melt determined from individual experiments, plotted as a function of the temperature. The dashed line shows the fit used to describe the temperature dependence of the equilibrium. Errors were propagated from 1σ standard deviation in the sulphide oxygen concentrations. (b) Temperatures determined using oxygen contents of sulphide inclusions in diamonds from the Slave craton, Canada. Depth estimates are made using compositions of garnets found as inclusions in the same diamonds. The peridotite or eclogite distinction is based on the Ni content of the sulphides

With the resulting relationship and assuming a typical mantle olivine composition, measurements of oxygen in natural sulphide inclusions in diamonds from the Slave craton, Canada, are used to determine temperatures for lithospheric diamond formation, as shown in Fig. 3.2-5. Temperatures are found to be in the range 1140-1510 °C. The pressures of formation are determined from the majorite contents of garnet inclusions found in the same diamonds. Low Ni content sulphide inclusions are generally proposed to come from eclogitic protoliths, whereas high Ni contents are associated with peridotites. We plot temperatures for such eclogitic inclusions using the same model although experiments are currently underway to examine sulphide oxygen contents coexisting with eclogitic and pyroxenitic assemblages,

where the FeO activity will likely be more variable. None the less, the results indicate the feasibility of determining pressures and temperatures of diamond formation with this methodology.

e. *The conditions of sub-lithospheric diamond formation constrained from ferric iron-rich exsolution in ferropericlase inclusions in diamond (C. Melai, D.J. Frost, T. Boffa Ballaran and C.A. McCammon)*

The rocks-salt structured Mg-Fe oxide, ferropericlase, is one of the most common minerals found as an inclusion in sub-lithospheric diamonds, where it appears with a wide range of Fe/(Fe+Mg) ratios. It is important to be able to understand the formation conditions of such inclusions as they provide some of the only direct evidence for processes that are part of the deep mantle carbon cycle. In a number of TEM investigations exsolution of Fe^{3+}-rich phases, normally described as being part of the magnetite-magnesioferrite solid solution, have been identified within such ferropericlase inclusions. This is somewhat surprising because it implies that ferropericlase becomes saturated in Fe_2O_3. At low pressures this would indeed result in the exsolution of magnetite-magnesioferrite solid solution but this only occurs at oxygen fugacities that are higher than those at which diamond or graphite would be stable. At pressures > 8 GPa, however, experiments have shown that other mixed valence iron oxide phases with the stoichiometries Fe_4O_5 and Fe_5O_6 are stable, which may well cause a decrease in the maximum Fe_2O_3 content of coexisting ferropericlase. In order to understand the exsolution of Fe_2O_3-bearing oxides from ferropericlase inclusions in diamonds and to determine the conditions or the changes in conditions required for this to occur, it is essential to be able to describe phase relations in the FeO-MgO-Fe_2O_3 system at high pressures and temperatures. This information will not only allow the oxygen fugacity of diamond formation to be assessed but can potentially provide information on the post entrapment conditions experienced by diamonds.

In this project we examine the conditions at which mixed valence iron oxides become stable and determine the maximum $Fe^{3+}/\Sigma Fe$ ratio of coexisting $(Fe,Mg)_{1-x}O$ ferropericlase using both experimental measurements and thermodynamic modelling. Multianvil experiments have been performed between 6-25 GPa and 1200-1800 °C using a starting composition of $(Mg_{86}Fe_{14})O$ and $(Mg_{50}Fe_{50})O$ plus varying amounts of Fe_2O_3 (20 %, 10 %, 5 %). Pt powder was added to the experiments to act as a redox sensor and minor amounts of Ni, Cr, Mn and Na were also added. Samples were then analysed using scanning electron microscopy, the electron microprobe, Mössbauer spectroscopy and X-ray diffraction.

In the recovered experiments, ferropericlase was found to coexist with magnetite-magnesioferrite solid solution up to 12 GPa and $Mg_2Fe_2O_5$-Fe_4O_5 solid solution at higher pressures. At 25 GPa a phase along the $Mg_3Fe_2O_6$-Fe_5O_6 solid solution was formed. In all experiments the oxygen fugacities could be determined from three different equilibria simultaneously, and in the calculation of the oxygen fugacity a ferropericlase model in the FeO-$Fe_{2/3}O$-MgO system was employed and exchange of Mg and Fe^{2+}in magnetite was accounted for.

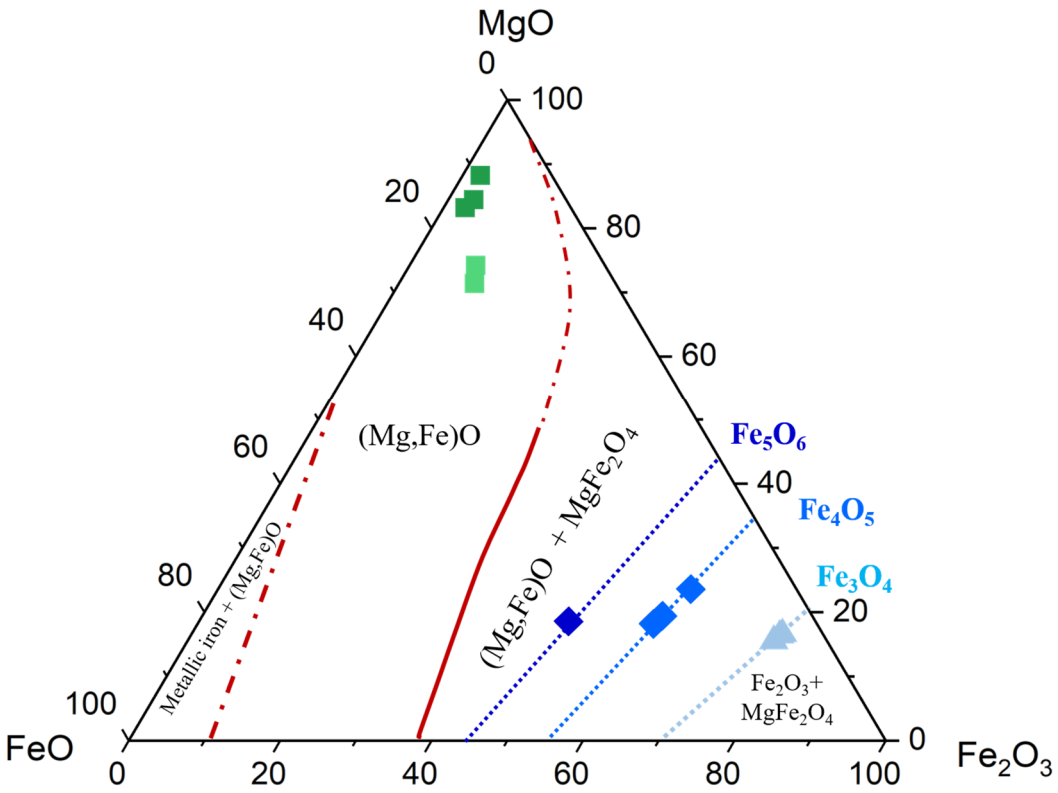

Fig. 3.2-6: Mineral analyses from the present study are plotted in the ternary system in wt. % at 1200 °C. Green squares denote the ferropericlase data where the light green ones represent low pressure experiments (6-12GPa) and the darker ones the higher pressures (16-25 GPa). Light blue triangles are the magnetite phases coexisting in the low-P experiments, light blue diamonds are $(Fe,Mg)_4O_5$ phases coexisting in the higher-P experiments and the dark blue diamond is for $(Fe,Mg)_5O_6$ observed in a 25 GPa experiment. The red curves show the phase boundaries of $(Mg,Fe)_{1-x}O$ at room pressure.

The compositions of coexisting phases are plotted in Fig. 3.2-6, where a comparison can also be made with the phase relations at room pressure. It can be seen that even at conditions where ferropericlase (light green squares) coexists with magnetite-magnesioferrite solid solution (Fe_3O_4-$MgFe_2O_4$) at 6-12 GPa, the Fe_2O_3 content of ferropericlase is significantly lower than expected at room pressure. As pressures increase, however, and higher pressure mixed valence iron oxides become stable, the Fe_2O_3 content of ferropericlase decreases further. Only at pressures above 16 GPa would the oxygen fugacity of $(Fe,Mg)_4O_5$ exsolution be compatible with the diamond stability field. As it is likely that the exsolution observed in natural ferropericlase inclusions occurred after entrapment in the diamond, it must have occurred either as pressures increased after entrapment or temperatures decreased. The first scenario might imply that the diamonds were then further subducted after formation, while the second scenario might arise if the diamonds were then later stored in the subcontinental lithosphere. From precise determinations of the $Fe^{3+}/\Sigma Fe$ ratios of ferropericlase inclusions coexisting with

exsolved mix valence iron oxides and through characterisation of the exsolved oxides themselves, it should be possible to differentiate between these scenarios.

f. *Experimental study of melting relations in the multicomponent MgO – FeO – SiO_2 – Na_2O – CaO – K_2O – CO_2 system at 14 GPa (A. Spivak, E. Zakharchenko and Y. Litvin/ Chernogolovka; I. Koemets and L.S. Dubrovinsky)*

The study of melting relations in multicomponent magmatic and diamond-forming systems makes it possible to investigate the physicochemical mechanisms of deep mantle melting and the nature of the prevailing minerals. In assessing the overall chemical and phase composition of diamond-forming environments in the mantle transition zone, the mineralogical data of syngenetic inclusions in diamonds, whose genesis is associated with the corresponding depths of the Earth's mantle, are of particular importance. In inclusions of natural diamonds (formed at the depths of the border of the upper mantle and transition zone) the main minerals are represented by wadsleyite, ringwoodite, retrograde olivine, and majoritic garnet. Oxide minerals such as magnesiowustite (Fe,Mg)O, stishovite SiO_2, and Na-, Mg-, Fe-, Ca-, and K-carbonates are also found. The aim of this work is to investigate the melting relations in the diamond-forming system SiO_2-FeO-MgO-CaO-Na_2O-K_2O-CO_2

Experimental studies on the melting phase relations in this system were carried out at 14 GPa and 1000-1800 °C using a multianvil apparatus. Starting materials were homogenous gel mixtures of Mg_2SiO and Fe_2SiO_4 plus Na_2CO_3 – $CaCO_3$ – K_2CO_3 carbonates. Phase identification was carried out using the electron microprobe and Raman spectroscopy. Olivine, wadsleyite, ringwoodite, enstatite, clinopyroxene, magnesite, carbonates (magnesite, Ca-magnesite, Ca, Na, K-carbonates) plus melt were detected in the samples after the experiments (Fig. 3.2-7). The Mg# of olivine is 0.74-0.98, while that of wadsleyite is 0.57-0.65, and 0.49-0.42 for ringwoodite. Magnesiowustite is present only in samples with relatively high iron contents. The Fe# of magnesiowustites reaches an average of 0.95. Among the carbonate phases, magnesite and Ca-magnesite are formed at high temperatures, then Ca,K-carbonate and Ca,K,Na-carbonates join them with decreasing temperature.

In the preliminary partial melting experiments in the Mg_2SiO_4 – Fe_2SiO_4 – $CaCO_3$ – Na_2CO_3 – K_2CO_3 system at 14 GPa the coexistence of the three $(Mg,Fe)_2SiO_4$ polymorphs was observed – olivine, wadsleyite and ringwoodite. It was previously shown that the presence of olivine is only possible near the Mg_2SiO_4 boundary of the Mg_2SiO_4 – Fe_2SiO_4 system at a pressure of 15 GPa. It should be noted that a mineral phase with the composition of olivine $(Mg,Fe)_2SiO_4$ was found among micro-inclusions in superdeep diamonds, in association with inclusions of bridgmanite and Ca-perovskite. The Mg# of this phase varies over a wide range, including ferrous compositions 0.79-0.89 that are unusual for mantle olivine. The formation of these "olivines" may be associated with the retrograde transformation of higher-pressure phases or with the retrograde reaction of ferropericlase + ferrobridgmanite = olivine.

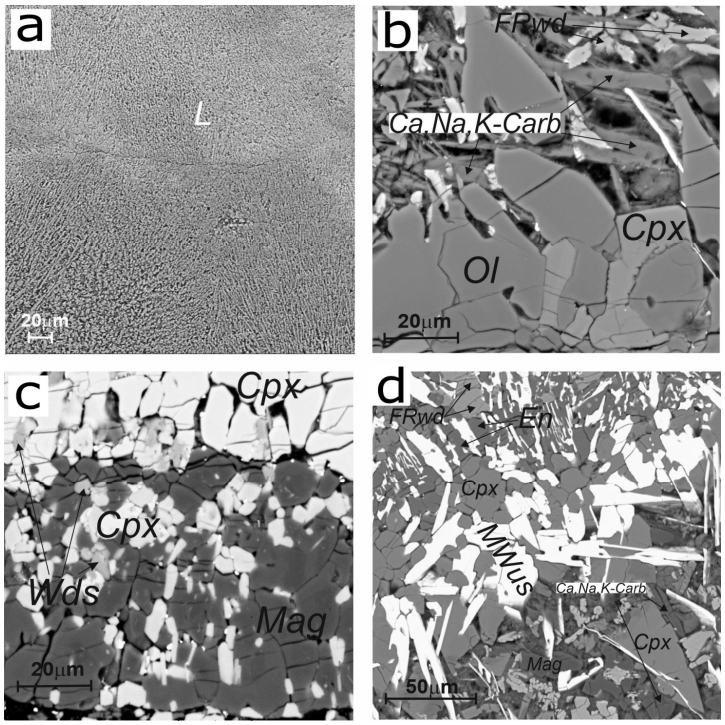

Fig. 3.2-7: SEM images of the experimental samples of from a polythermal section $(Mg_2SiO_4)_{70}Carb_{30}$ – $(Fe_2SiO_2)_{70}Carb_{30}$ at 14 GPa after quenching: (a) $(Mg_2SiO_4)_{49}(Fe_2SiO_4)_{21}(Carb)_{30}$ at 1500 °C; (b) $(Mg_2SiO_4)_{28}(Fe_2SiO_4)_{42}(Carb)_{30}$ at 1300 °C; (c) $(Mg_2SiO_4)_{56}(Fe_2SiO_4)_{14}(Carb)_{30}$ at 1300 °C; (d) $(Mg_2SiO_4)_{28}(Fe_2SiO_4)_{42}(Carb)_{30}$ at 1300 °C. Symbols: *L* – melt, *Ol* - olivine, *Wds* – wadsleyite, *FRwd* – Fe-rich ringwoodite, *Cpx* – clinopyroxene, *Mag* – magnesite, *Ca,Na,K-Carb* – carbonate, *MWus* – magnesiowustite.

g. *Partial melts at the base of the upper mantle (V. Szlachta and D.J. Frost)*

Reductions in seismic velocities above the 410 km discontinuity are proposed to be a result of partial melts forming a low shear wave velocity layer. These low-degree melts may form as a result of dehydration melting due to the difference in water storage capacity between minerals in the transition zone (*i.e.*, wadsleyite) and the upper mantle (*i.e.*, olivine). The density of the melt compared to the surrounding mantle depends on its chemical composition, which is important to determine.

Knowing the composition and liquidus temperatures of partial melts is important to understand their buoyancy above the mantle transition zone. For this purpose, we performed multianvil experiments at pressure-temperature conditions of the 410 km discontinuity. Experiments were performed at 14 GPa and 1500 °C using KLB-1 peridotite and an initial guess melt composition in a 14/8 assembly with a lanthanum chromite heater. Iterative crystallization experiments were used to determine a melt composition in equilibrium with the typical peridotite assemblage found in subsolidus experiments. Melt water contents were determined using mass balance calculations in experiments that generated a large volume of melt. Mass balance results and disequilibrium in several experiments suggests that iron is oxidized due to water loss through

sample capsules in some experiments. Figure 3.2-8 shows an experiment with a well separated melt composition that contained approximately 13.5 wt. % H_2O based on a mass balance. This melt coexists with a complete peridotite assemblage at conditions compatible with the 410 km discontinuity.

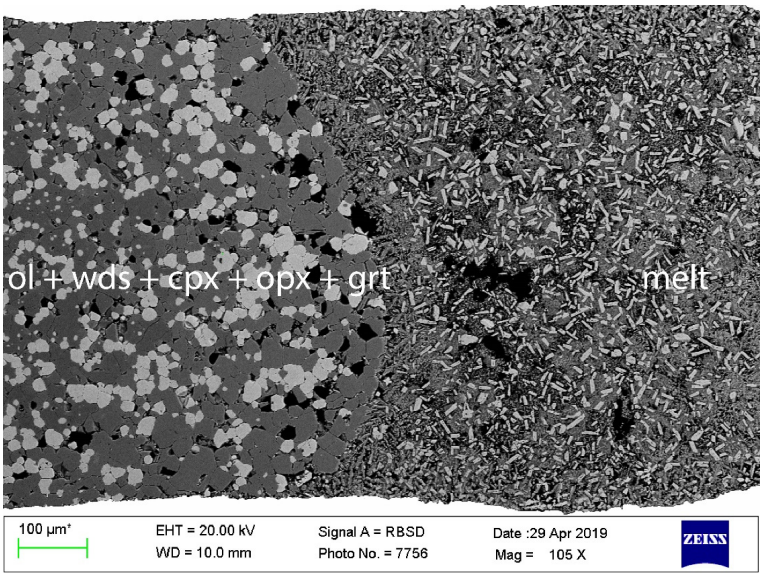

Fig. 3.2-8: Backscattered electron image showing an experiment that generated melt coexisting with olivine (ol), wadsleyite (wds), garnet (grt), clinopyroxene (cpx), and orthopyroxene (opx).

h. *Melting relations in the MgO-SiO_2 system at lower mantle conditions from multianvil experiments (J. Yao, D.J. Frost and G. Steinle-Neumann)*

Giant impact events in the early Earth's history led to large-scale melting, potentially resulting in the entire planet being molten. Some highly fractioned residual melt may have persisted at the base of the mantle contributing to the existence of the ultra-low velocity zone (ULVZ) and possibly even the large low shear velocity province (LLSVP). Crystallization of silicate melt from the magma ocean – or in residual reservoirs – therefore provides an important constraint on the chemical differentiation and stratification in the Earth.

The MgO-SiO_2 system serves as the first-order approximation of a mantle composition and melting relations along this join inform us about the crystallizing sequence in the magma ocean. A lot of work has focused on the MgO-rich side of this join (MgO-$MgSiO_3$) as model compositions for both the modern and primordial mantle are in this range of MgO/SiO_2 ratio. Experiments and thermodynamic modelling on this system have helped to constrain the liquidus phase over a wide range of pressure (P), including conditions of the uppermost lower mantle and have constrained peritectic and eutectic compositions in the system. At the eutectic near $XSiO_2$=0.43 (at $P \sim 25$ GPa), the liquidus phase shifts from MgO to $MgSiO_3$ bridgmanite. However, for a full description of the thermodynamics of the MgO-SiO_2 system, the SiO_2-rich side also needs to be considered. At lower mantle pressures, a second eutectic must exist, where SiO_2 stishovite becomes the phase to crystallize on the liquidus. While some efforts have been made to estimate the composition of this eutectic, it has not been experimentally determined, although thermodynamic models of melting relations at lower mantle P would be significantly improve by such a constraint.

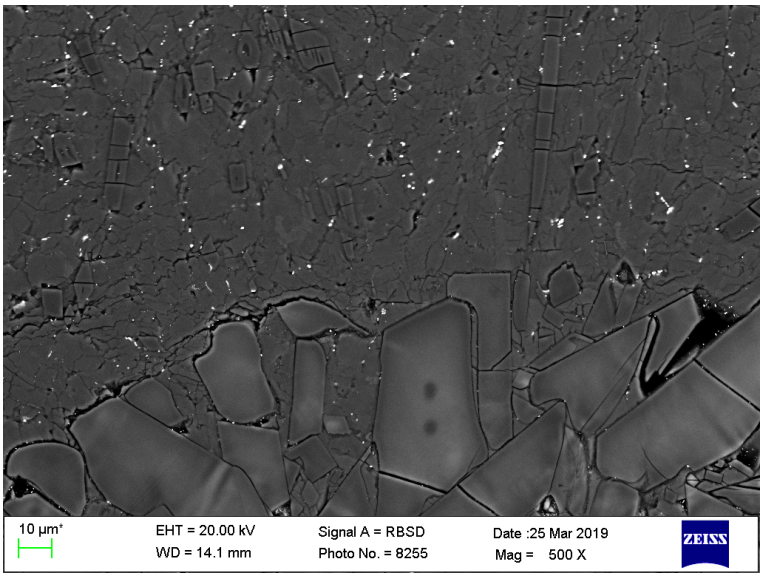

Fig. 3.2-9: SEM image of the $Mg_{0.4}Si_{0.6}O_{1.6}$ composition at 24 GPa and 2800 K shows that the sample is above the solidus, with stishovite (bottom) coexisting with a liquid phase.

We have performed a multianvil experiment with a $Mg_{0.4}Si_{0.6}O_{1.6}$ composition at 24 GPa and 2800 K using a 7/3 cell assembly and a rhenium capsule. The texture of the run product was analysed with the scanning electron microscope (Fig. 3.2-9) and the chemical composition was examined with the electron microprobe. Large subsolidus stishovite crystals coexisted with the liquid. These crystals have settled at the bottom of the capsule and the liquid evolves towards a silica poorer composition compared to the starting material ($XSiO_2$=0.60). The liquid composition is determined to be $XSiO_2$=0.54(±0.02), tightly constraining the eutectic. Based on the chemical analysis of the residual melt and constraints provided by previous determinations of the more Mg-rich eutectic, the MgO-SiO_2 phase diagram has been calculated at 24 GPa (Fig. 3.2-10) by equating the chemical potentials of the MgO and SiO_2 components between the solid and liquid phases. This provides excellent constraints on the thermodynamic mixing properties of the silicate melt at high pressures.

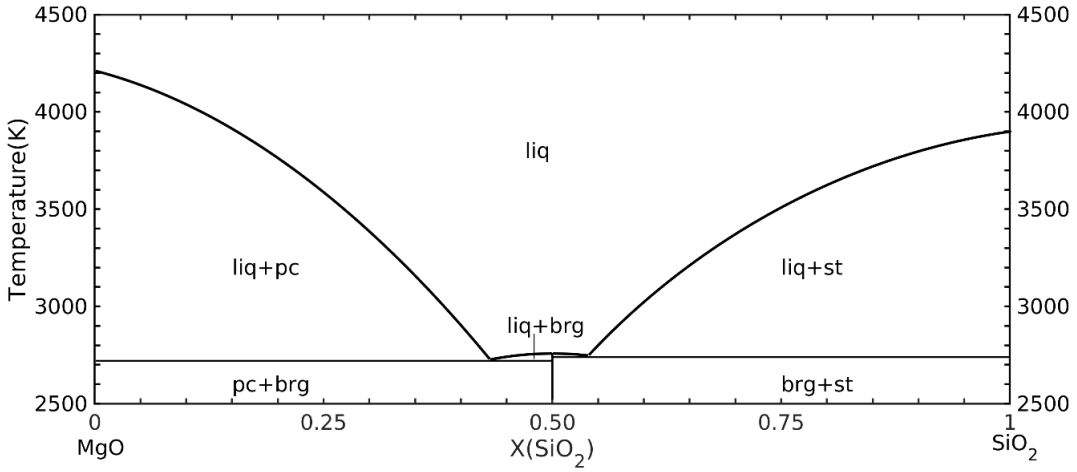

Fig. 3.2-10: Computed phase diagram of the MgO-SiO_2 solid solution at 24 GPa showing two eutectic points at $xSiO_2$=0.43 and $xSiO_2$=0.54 with the liquidus phases shifting from periclase to bridgmanite and then to stishovite, with increasing melt SiO_2 content.

i. *The ferric iron content of bridgmanite and the Fe distribution in the lower mantle (R. Huang, T. Boffa Ballaran, C.A. McCammon, N. Miyajima, D.J. Frost)*

Whether Earth's lower mantle is isochemical with the upper mantle has important implications for the formation and evolution of the Earth as well for understanding the style of mantle convection, mantle heat flux and volatile content of the Earth's interior. A plausible way to determine this is to examine whether a mineral model for a specific chosen bulk composition can reproduce the seismic velocities observed in the lower mantle. In order to do this, we need to know the elastic properties of specific minerals at pressure and temperature conditions corresponding to that of the lower mantle. More importantly, however, it must be possible to determine the chemical compositions and proportions of minerals in the lower mantle for a given bulk composition, mainly because the compositions of minerals will influence their elastic properties. In this study, the compositions of bridgmanite (Brg) and ferropericlase (Fp) were examined at 25 GPa and 1973 K, and the factors that govern the speciation of Fe and Al in Brg were explored. A thermodynamic model was developed to describe this behaviour.

Samples of $(Mg,Fe)(Si,Al)O_3$ bridgmanite with different Al and Fe contents were synthesized in multianvil runs at a pressure of 25 GPa and a temperature of 1973 K. The oxygen fugacity was controlled or determined by adding different oxygen buffers such as Fe metal, hematite, Ru-RuO_2 and PtO_2 or redox sensors such as Pt or Ir metal. The experimental oxygen fugacities varied between IW-1 and IW+8. The compositions of the run products were measured using the electron microprobe and the $Fe^{3+}/\Sigma Fe$ ratios in Brg were determined using Mössbauer spectroscopy.

In Figure 3.2-11 (a), the $Fe^{3+}/\Sigma Fe$ ratio of Brg is plotted against the fO_2. The $Fe^{3+}/\Sigma Fe$ ratio of Brg increases with the Al content but is also strongly dependent on fO_2. The nature of this relationship, however, apparently changes with Al content. For Al-bearing samples, $Fe^{3+}/\Sigma Fe$ also increases with fO_2 but the slope is less steep. The Brg composition can be described as a function of fO_2 using a thermodynamic model if the model also accounts for the inter-site partitioning of 3+ cations. The model shown in Fig. 3.2-11 (a) employs two equilibria to define the inter-site partitioning of Al and Fe^{3+} and one to describe the variation in Fe^{2+} and Fe^{3+} as a function of fO_2. As all interactions are considered to be ideal, the model, which fits the entire data set very well, has only three equilibrium coefficients that are adjustable parameters at a given P and T.

Using the developed model combined with a mass balance calculation, the composition and proportion of coexisting Brg and Fp were calculated for a pyrolite bulk composition at different oxygen fugacities Fig. 3.2-11 (b). The results show that K_D (app) (*i.e.*, the Mg-Fe exchange coefficient between Brg and Fp that assumes all iron is Fe^{2+}) is a strong function of oxygen fugacity due to the variation of the Brg Fe^{3+} content with fO_2. The model can reproduce the apparent K_D and the $Fe^{3+}/\Sigma Fe$ ratio reported in previous studies if an oxygen fugacity of IW + 1.5 is assumed. This is a quite reasonable assumption for these experiments that employed carbon capsules. Previously this change in K_D was attributed to an iron spin transition.

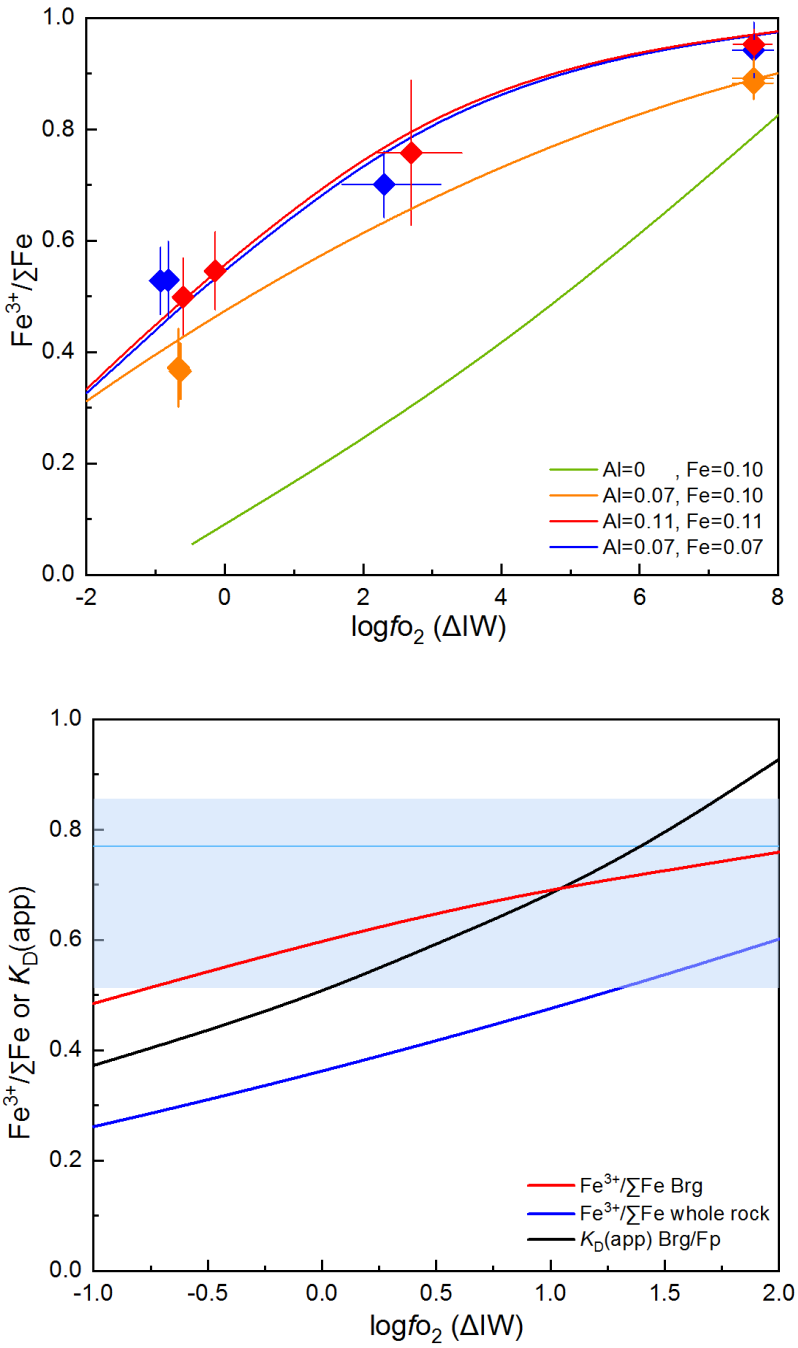

Fig. 3.2-11: (a; top) Calculated model curves predicting the $Fe^{3+}/\Sigma Fe$ ratio in Fe and Al-bearing Brg for a given oxygen fugacity and bulk Al and Fe contents at 25 GPa and 1973 K. The experimental data used to calibrate the model are also plotted and are in good agreement. For Al-free Brg only the model is plotted. (b; bottom) Model results for K_D *(app)* describing the Fe-Mg exchange between Brg and Fp (where *app* refers to the apparent iron content where all iron is assumed to be Fe^{2+}) and the $Fe^{3+}/\Sigma Fe$ ratio of both Brg and the whole rock calculated for a pyrolite composition as a function of oxygen fugacity. The blue shaded region shows the range in K_D(app) reported from a previous study for a pyrolite composition between 28.7 and 47.4 GPa, with the solid horizontal line showing the value at 28.7 GPa. Small changes in fO_2 can easily explain the range in K_D(app) previously reported.

The absence of fO_2 measurements in almost all previous experimental determinations of K_D (app) for Brg-Fp at deep lower mantle conditions almost certainly explains the large variations observed between studies. The calculated models for a pyrolite composition show that ferric Fe on the Brg A site increases with oxygen fugacity causing Al to be pushed from A site to B site. Moreover, the oxygen vacancy component in Brg decreases with increasing oxygen fugacity. At low oxygen fugacities, which are more realistic for the bulk of the lower mantle, the main 3+ cation components are $AlAlO_3$ and $(Mg,Fe)AlO_{2.5}$, which may be important for Brg transport properties and lower mantle transport properties in general.

j. *A thermodynamic model describing the ferric iron content of serpentine and its influence on redox processes in subduction zones (L. Eberhard, D.J. Frost and C.A. McCammon)*

Serpentine is one of the main hosts responsible for transporting H_2O into the interior in subduction zones. Serpentinization, however, also raises the oxygen content of the oceanic lithosphere through the formation of ferric iron in both magnetite and serpentine minerals themselves. $Fe^{3+}/\sum Fe$ ratios in serpentinites range from 0 to almost 1. It is therefore important to understand the oxygen buffering capacity of serpentinized lithosphere, particularly, given that serpentinized rocks also transport C and S into the mantle, the fate of which will be dependent on the oxygen fugacity. To date, the examination of the redox state of serpentinized rocks has focused on equilibria involving silicate minerals and magnetite. Serpentine minerals themselves can also contain significant ferric iron, however, but their role in governing the redox state of subducting lithosphere and their influence on fluid speciation has never been examined. Using analyses of experiments performed on serpentine minerals at either buffered or measured redox conditions, we have determined a thermodynamic expression to describe the $Fe^{3+}/\sum Fe$ ratio of serpentine as a function of oxygen fugacity.

Experiments were performed on two natural serpentinites where the serpentine minerals had high and low $Fe^{3+}/\sum Fe$ ratios of 0.7 and 0.3. Experimental conditions ranged over the stability field of serpentine minerals. In all experiments the fO_2 was either buffered, using metal oxide mixtures such as Re and ReO_2 added directly to the samples, or monitored using a noble metal redox-sensor. This approach allowed a large range in fO_2 to be covered from ΔFMQ+1 to >ΔFMQ+10. The initial and final Fe^{3+} content of the serpentine minerals and the site occupancy of Fe^{3+} in the structure were analysed with Mössbauer spectroscopy.

Although temperatures were very low in the experiments (< 700 °C) it was possible to change the $Fe^{3+}/\sum Fe$ ratios of serpentine using the redox buffers. Ferric iron was found to partition into the serpentine octahedral site. With increasing temperature, the $Fe^{3+}/\sum Fe$ ratio at a given fO_2 was found to drop strongly. This is observed over the entire range of fO_2 investigated.

In the samples investigated Fe^{3+} appears to form a Tschermak's-substitution and is charge balanced by Al on the tetrahedral site. This can be described using a ferri-Tschermak's-

endmember component $Mg_2Fe^{3+}|AlSi|O_5(OH)_4$. The activity of the ferric endmember can be described in terms of the mole fractions of cations on the two sites, *i.e.*, $a_{ferri\text{-}serpentine} = (X_{Mg})^3(X_{Fe}3+)^3[X_{Al}]^2$. In the experiments, serpentine coexists with either magnetite at lower fO_2 or hematite at higher fO_2. Therefore, the following equilibria can be employed to determine the standard state Gibbs free energy of $Mg_2Fe^{3+}|AlSi|O_5(OH)_4$ using the experimental data set and assuming ideal mixing.

$$2\ Fe_3O_4 + 0.5\ O_2 + 3\ Mg_5Al_2Si_3O_{10}(OH)_8 \rightarrow 1.5\ Mg_2Si_2O_6 + 6\ Mg_2Fe^{3+}|AlSi|O_5(OH)_4 \quad [1]$$

magnetite — serpentine — enstatite — chlorite

$$Fe_2O_3 + Mg_5Al_2Si_3O_{10}(OH)_8 \rightarrow 0.5Mg_2Si_2O_6 + 2Mg_2Fe^{3+}|AlSi|O_5(OH)_4 \quad [2]$$

hematite — serpentine — enstatite — chlorite

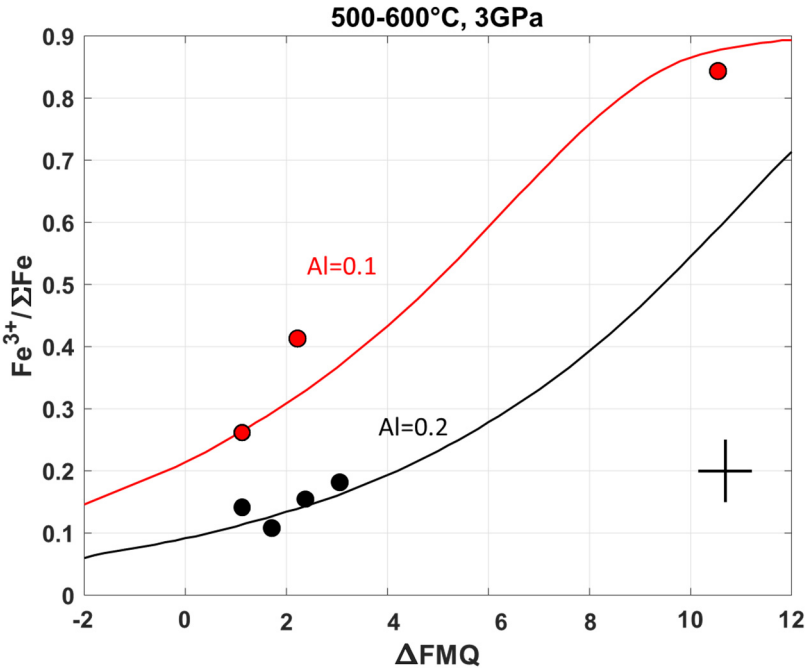

Fig. 3.2-12: The ferric iron over total iron ratios of serpentine samples equilibrated as a function of oxygen fugacity, relative to the fayalite-magnetite-quartz oxygen buffer at approximately 500 °C and 3 GPa. Red symbols show serpentine samples containing approximately 0.1 Al cations per 2 silicon cations. Black symbols are for samples with 0.2 Al cations coexisting. The results of the thermodynamic model plotted for the two Al contents are also shown.

In agreement with the resulting model the serpentine $Fe^{3+}/\sum Fe$ ratio is found to be a strong function of the Al content, which in turn is found to increase with increasing temperature. Figure 3.2-12 shows experimental data collected between 500-600 °C for samples that contained different Al contents, which are fit very well by the resulting thermodynamic model, which is also shown. The decrease in $Fe^{3+}/\sum Fe$ ratio with increasing temperature for a given fO_2 can be explained by the increase in Al content with temperature. As temperature increases

during subduction the fO_2 for a fixed $Fe^{3+}/\sum Fe$ ratio will increase. This is shown in Fig. 3.2-13 using the predictions of the derived thermodynamic model. At low temperatures, during the early phases of subduction, the serpentinite fO_2 would be relatively reducing regardless of the $Fe^{3+}/\sum Fe$ ratio. This implies that S would form sulphides and C graphite, which would tend to immobilise these components within the slab. Local carbonates, for example, would be reduced with a consequent increase in the $Fe^{3+}/\sum Fe$ ratio of serpentine. At conditions, however, closer to the dehydration of serpentine (600-700 °C) the fO_2 is predicted to be above the level where sulphides would be oxidised to produce sulphate components that would dissolve in the released H_2O. In this way, redox reactions involving serpentine would result in a relatively reducing fore arc but an oxidised sub arc.

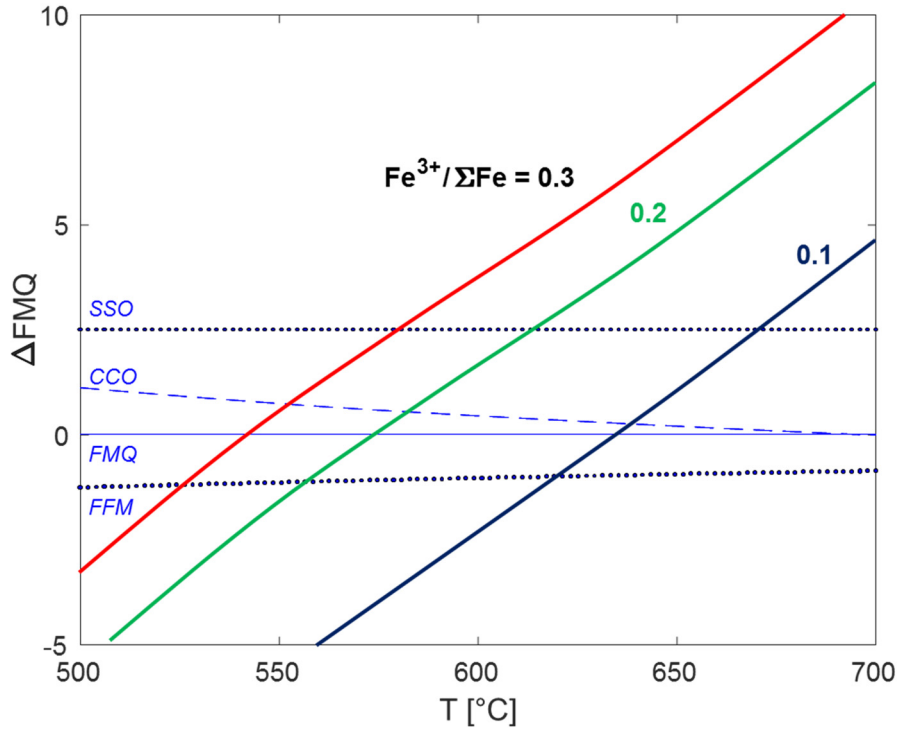

Fig. 3.2-13: The oxygen fugacity (relative to the fayalite-magnetite-quartz, FMQ, buffer) of a serpentinite bearing assemblage as a function of temperature for different serpentine $Fe^{3+}/\sum Fe$ ratios. Horizontal lines show the approximate oxygen fugacity at which sulphide species would be oxidised to sulphate (SSO), graphite to carbon dioxide (CCO), and the ferrosilite-fayalite-magnetite (FFM) oxygen buffer.

k. *Trace element transport by saline aqueous fluids in cold subduction zones (M. Putak Juriček and H. Keppler)*

High concentrations of LILE and LREE in arc magmas are features inherited from slab-derived metasomatic fluids that infiltrate the mantle wedge. Various types of high-pressure fluids have been proposed as suitable metasomatic agents, ranging from saline aqueous solutions to supercritical fluid-melt mixtures and silicate melts.

The nature of metasomatic fluids largely depends on the thermal structure of subduction zones. Predictions of slab geotherms by different numerical modelling approaches vary by several hundred degrees Celsius at constant depth. Since both H_2O-saturated and dry solidi of slab-surface lithologies lie within the predicted range of temperatures, numerical models alone cannot resolve the nature of slab-derived metasomatic fluids. As a result, considerable experimental efforts have been made in recent decades to constrain slab-surface P-T conditions by studying trace element partitioning between various high-pressure fluids and metamorphic slab lithologies.

The role of subducted sediments in the production of characteristic arc magma trace element signatures is of particular interest. The volume of subducted sediments is small compared to the bulk of underlying basalts, but they are enriched in certain trace elements relative to average MORB and may significantly contribute to the total trace element flux in subduction zones. Reported geochemical similarities between trace element and isotope ratios of arc magmas and sediments deposited in adjacent trenches seem to support this claim.

At sub-arc depths, the slab is mostly dehydrated and eclogites with basaltic protoliths are not expected to melt under these conditions. Additionally, melting relationship studies of sediment bulk compositions with varying H_2O contents indicate that even metapelites may not produce a melt at sub-arc conditions. In cold subduction zones partial melting is expected only if considerable fluid fluxing from underlying lithologies occurs. The aim of this study is to investigate the scenario in which no slab melting takes place and trace elements are mobilized from metapelitic assemblages by aqueous fluids of varying salinity.

We performed several two-week piston cylinder experiments at 3.5 GPa and 600 ^{o}C using a starting material with a major element composition similar to GLOSS (GLObal Subducted Sediments). The GLOSS starting material was mixed with 2 wt. % of doped diopside glass to introduce trace elements. For capturing and separating aqueous fluids from the solid residue, we employed the diamond trap method. The diamond trap was located in the center of the capsules, sandwiched between two GLOSS layers. The fluid content was by necessity of the experimental method high, between 30 and 40 wt. %, and the starting fluid composition varied from distilled H_2O to brines containing 10 wt. % NaCl. After the experiments, the fluids trapped in pore space between diamonds were analyzed in frozen state by LA-ICP-MS using a sample stage equipped with a Peltier element. The capsules were afterwards embedded in epoxy and mineral compositions were measured by electron microprobe and LA-ICP-MS to determine major and trace element concentrations, respectively.

All fluids were found to have been in equilibrium with a metamorphic assemblage consisting of clinopyroxene, lawsonite, phengite, coesite and accessory rutile. Mass fractions and $D_{fluid/mineral}$ for all major solid phases were determined from fluid and mineral compositions. Bulk $D_{fluid/GLOSS}$ trace element partition coefficients were then calculated from the fluid/mineral partition coefficients (Fig. 3.2-14).

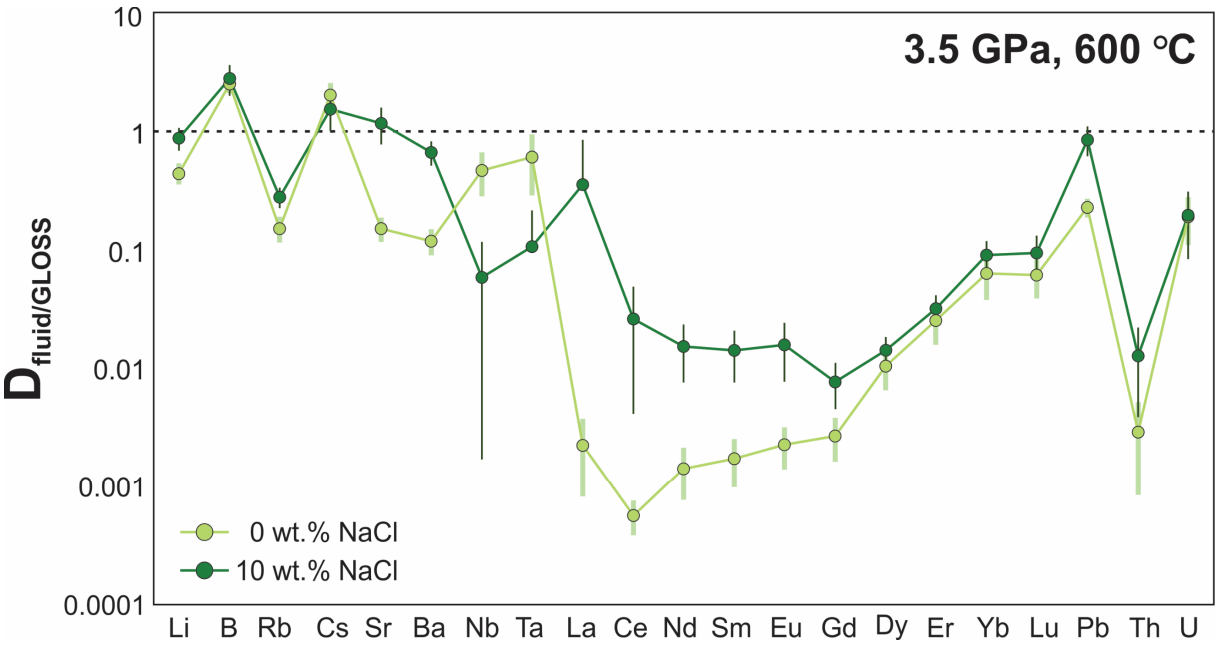

Fig. 3.2-14: Fluid/rock trace element partition coefficients ($D_{fluid/GLOSS}$) for metapelites in equilibrium with non-Cl-bearing and Cl-bearing aqueous fluid.

Previous work has demonstrated that the addition of chlorine increases the solubility of certain trace elements in aqueous fluids. This is entirely consistent with our preliminary results. Fluids that had initially contained 10 wt. % NaCl were able to mobilize considerably more LILE and LREE than distilled H_2O, as evidenced by one to two orders of magnitude higher calculated $D_{fluid/GLOSS}$ for some trace elements (Fig. 3.2-14). Moreover, the effect of chlorine on trace element solubility is apparent even though the experimental mineral assemblage contained phases that reportedly control LILE and LREE partitioning (*i.e.*, phengite and lawsonite).

Based on literature data, the solidus of metapelites with bulk compositions similar to GLOSS is thought to be around 750 °C at 3.5 GPa in the presence of several wt. % of H_2O. Even in numerical models predicting the highest slab-surface temperatures, 700 to 750 °C at 3.5 GPa is representative of cold subduction geotherms. Though our experiments had to be performed at lower temperatures to ensure that no partial melting occurs, the presented fluid/rock partition coefficients indicate that Cl-bearing aqueous fluids may mobilize certain LILE elements (Rb, Cs, Sr and Ba), as well as LREE (La) and Pb to some degree. This may provide a plausible explanation for the transport of the Pb and Sr isotopic signal from the sediment to arc source, without requiring sediment melting.

I. *Cu diffusion in amphiboles (N. Ma and A. Audétat)*

Most of the world's Cu supply stems from porphyry Cu deposits, which form through a sequence of magmatic to hydrothermal processes. An important question is whether ore-

forming magmas are enriched in Cu relative to non-mineralizing magmas. Unfortunately, whole rocks cannot be used to answer this question because their Cu content likely became modified through fluid exsolution, magma degassing, and potentially through later Cu mineralization. For this reason, efforts have been made to characterize the Cu content of magmas indirectly via melt inclusion compositions or the Cu content of silicate minerals.

Amphibole is a common mineral in magmas associated with porphyry Cu deposits and contains easily detectable amounts of Cu (typically on the order of tens of ppm), which makes it a potential candidate to be used as a proxy of the Cu content of the parental silicate melt.

However, it is not known whether amphibole reliably records original, magmatic Cu contents, or whether this mineral, similar to plagioclase, is susceptible to diffusive re-equilibration of Cu concentrations.

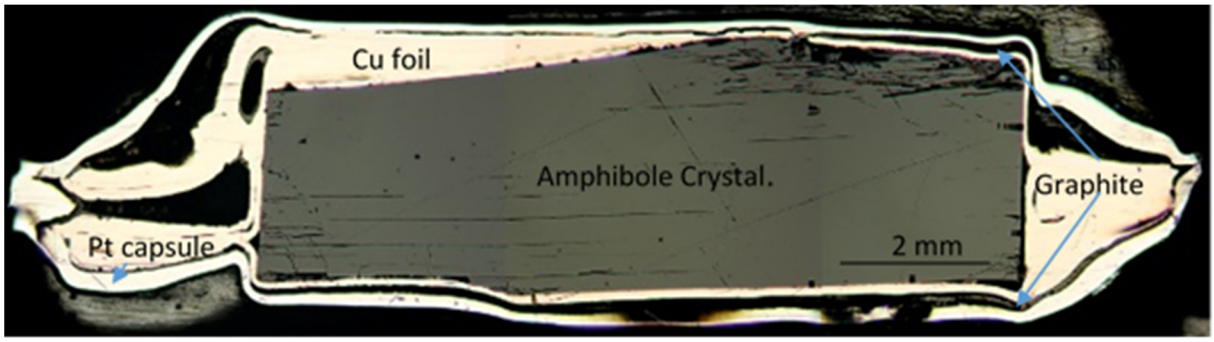

Fig. 3.2-15: Reflected-light image of a polished sample after the experiment. The cm-sized amphibole crystal was first wrapped in a Cu foil, then a thin graphite layer was painted onto the Cu foil, and finally the package was welded into a Pt capsule. The graphite layer served to avoid alloying of the Cu foil with the Pt capsule during the experiment.

To test this, Cu diffusion rates in amphiboles as a function of temperature, amphibole composition and crystallographic orientation were experimentally determined out by equilibrating pieces of gem-quality amphibole crystals wrapped in Cu foils in externally-heated cold-seal pressure vessels at 1 kbar, 850-950 °C. A typical view of the sample after the experiment is shown in Fig. 3.2-15. About one-third of the amphibole crystal was removed by polishing. Copper contents of the amphibole was measured by LA-ICP-MS along several profiles oriented along two different crystallographic directions (parallel and perpendicular to the c-axis; the first termed direction C; the latter termed direction A) and then fitted manually through a diffusion equation to calculate the diffusion coefficient D (Fig. 3.2-16).

The obtained data demonstrate that Cu diffusion in amphibole is very fast (typically on the order of log D = -14.0 m^2/s parallel to the c axis, and log D = -15.0 m^2/s perpendicular to this axis, at 950 °C), which is not surprising given the small ionic radius of Cu^+. A fairly consistent

temperature dependency of the diffusion coefficients and a relatively weak amphibole composition effect allows to extrapolate our data to lower temperatures.

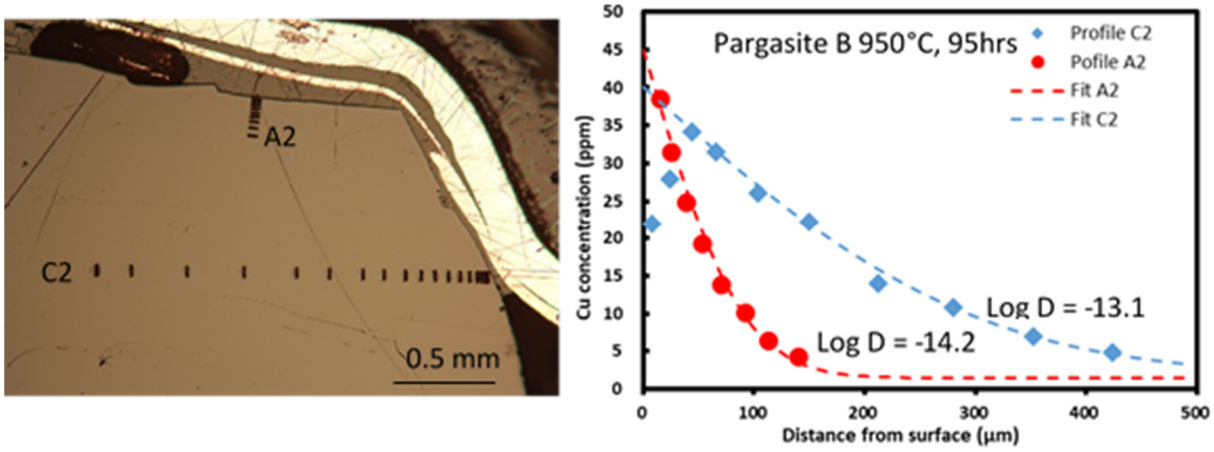

Fig. 3.2-15: Reflected-light image (left) of part of an amphibole crystal after LA-ICP-MS measurements (small, rectangular pits are laser spot). A2 and C2 stands for diffusion profiles measured parallel to the c-axis of the crystal (C2) and approximately perpendicular to the c-axis (A2), respectively. The corresponding data points and fitted diffusion equation trends are shown on the right.

Numerical modelling indicates that at 900 °C a silicate melt inclusion hosted in the center of a 20-times larger amphibole crystal can re-equilibrate with the external silicate melt within a few hundreds of days. Similarly, the Cu content of amphibole crystals can change within relatively short time scales: the half-concentration distance calculated at 850 °C for 10 years is on the order of millimeters, which casts doubts of the reliability of using the Cu content of amphibole crystals as a proxy of the Cu content in ore-related parental magmas. The could anyway be constrained only for magmas that are sulfide-undersaturated, as the amount of Cu hosted in magmatic sulfides can usually not be constrained. Therefore, caution has to be taken when using Cu content of amphiboles or amphibole-hosted melt inclusions to reconstruct the Cu content of parental magmas.

m. *Early sulfide saturation is not detrimental to porphyry Cu-Au formation: Evidence from Tongling, China (J. Du/Beijing and A. Audétat)*

The Tongling mining district in south-central China hosts 19 dioritic to granodioritic intrusions of early Cretaceous (137-145 Ma) age that are associated with numerous porphyry Cu-Au deposits with a combined resource of 3.3 Mt Cu and 160 t Au. A few slightly younger (121-137 Ma) and more mafic intrusions carried up amphibole- rich cumulate xenoliths (Figs. 3.2-16 A, B) that have been dated at the same age as the ore-forming intrusions. This situation offers a unique opportunity to study the effect of high-pressure crystal fractionation on the mineralization potential of arc-like magmas.

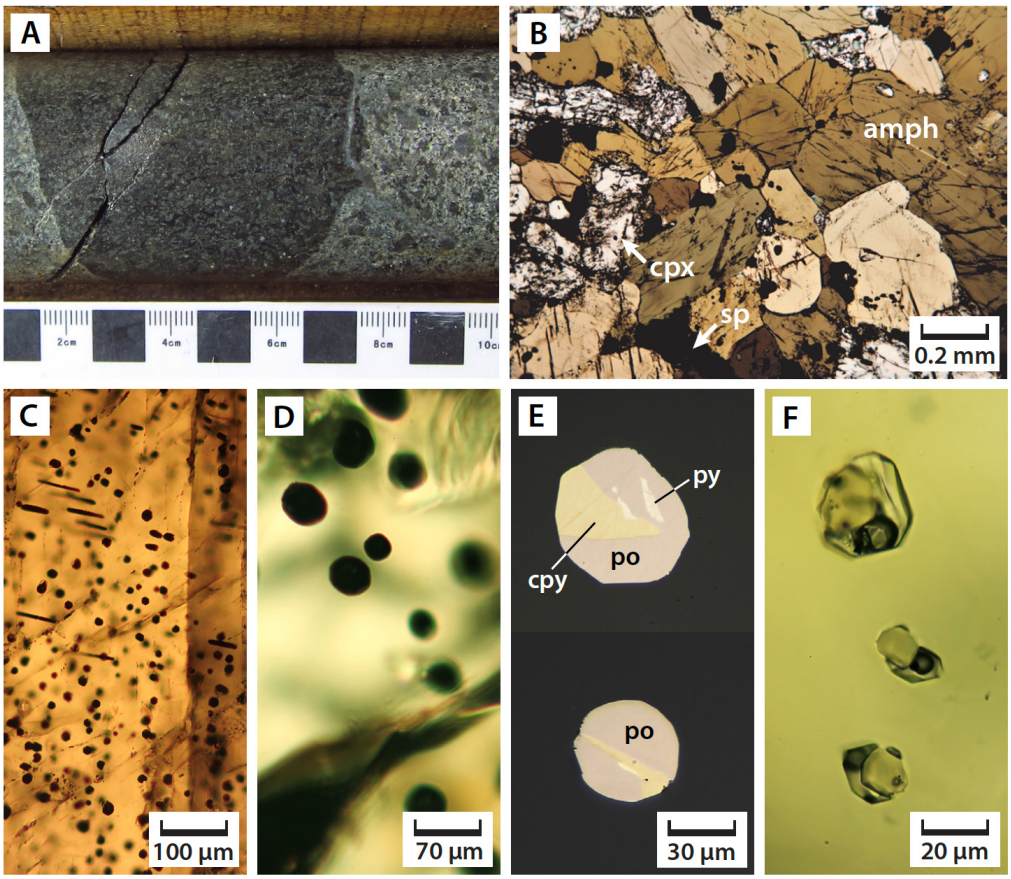

Fig. 3.2-16: Petrography of amphibole-rich cumulate xenoliths. (A) Typical xenolith in a drill core. (B) Microscopic view of a thin section. (C) Sulfide inclusions in an amphibole megacryst. (D) Sulfide (originally monosulfide solid solution) inclusions in clinopyroxene. (E) Exposed sulfide inclusions in amphibole (top) and clinopyroxene (bottom). (F) Crystallized melt inclusions in clinopyroxene. Images b, c, d, f were taken in transmitted light; image e in reflected light.

Notably, the cumulates contain abundant magmatic sulfide inclusions (Figs. 3.2-16 C, D, E), testifying to substantial loss of chalcophile elements during magma fractionation. It is thus critical to explore whether the ore-forming magmas represent residual liquids after cumulate formation, or separate, metal-undepleted magma batches. Whole-rock data of the intrusions and LA-ICP-MS analyses of silicate melt inclusions (Fig. 3.2-16 F) in the cumulates define regular fractionation trends that are very similar to those obtained in experimental studies of hydrous arc magmas (Figs. 3.2-17). This, together with the age data, thermobarometric studies, trace elements and Nd- and Sr-isotopes, suggests that the mineralizing magmas represent residual liquids after significant amphibole and clinopyroxene fractionation in the middle crust (960-1000 °C, 3.8-5.6 kbar). A quantitative fractionation model based on experimental temperature-crystallinity relationships, sulfide-silicate melt partition coefficients, sulfur contents of melt inclusions, and LA-ICP-MS analyses of sulfide inclusions reproduces the compositional trends observed in the sulfide inclusions and predicts that after 20 wt. % crystallization already ~ 75 % of the Cu and ~ 33 % of the Au originally present in the magma were stored in sulfides.

That the residual silicate liquids at Tongling nevertheless were able to produce major Cu-Au deposits implies that the formation of metal-rich cumulates at depth was not detrimental to their fertility. On the contrary, the common association of porphyry Cu (-Au) deposits with high Sr/Y magmas suggests that amphibole fractionation at depth even promotes the mineralization potential, despite the associated loss of metals. This implies that it is not the metal content that determines the mineralization potential, but other factors such as the magma water content, for example.

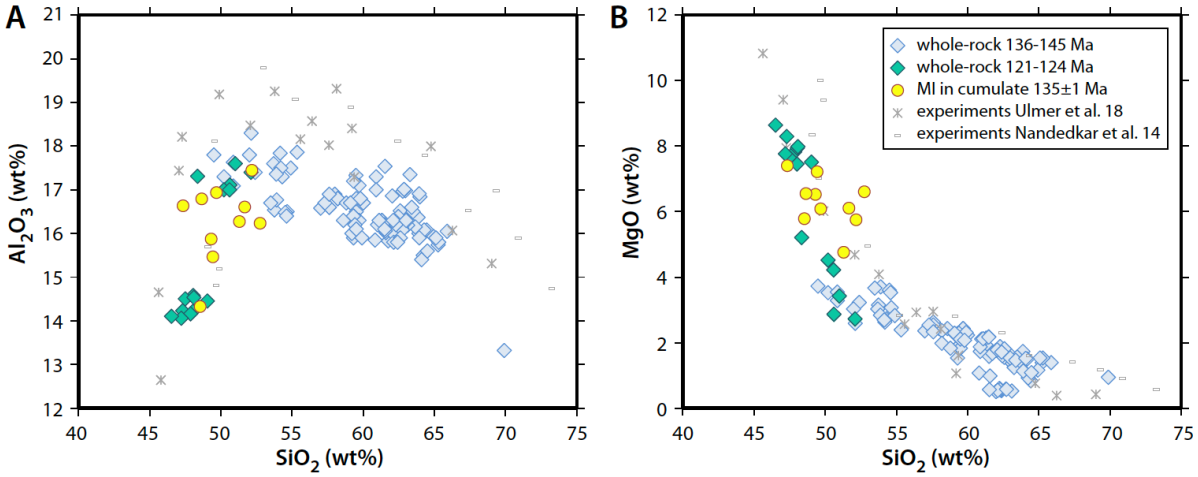

Fig. 3.2-17: Major element composition of whole-rocks and melt inclusions of Tongling, compared to experimentally derived fractional crystallization trends of hydrous arc magmas.

3.3 Mineralogy, Crystal Chemistry and Phase Transformations

Mineralogy, in all its diverse aspects from the study of the crystal structure of minerals to the determination of their phase stability and transformations and to the characterization of their microscopic properties, is an essential tool for understanding the processes occurring inside the Earth.

During the last year, many studies have focused on understanding the possible behaviour of Fe-bearing compounds at high pressures and temperatures. The crystal structures of two new oxides have been resolved (first contribution) and have been used to suggest the possibility of a homologous series of iron oxides described by the common formula $n\mathrm{FeO}\cdot m\mathrm{Fe_2O_3}$. The stability fields of two other recently discovered iron oxides, $\mathrm{Fe_4O_5}$ and $\mathrm{Fe_5O_6}$, have been investigated at very high pressures and temperatures by means of *in situ* X-ray diffraction using a laser heated diamond anvil cell (second contribution). The third study in this chapter reports on the ferric iron substitution mechanism in bridgmanite under p,T conditions of the top of the Earth's lower mantle. The results show that for very small amounts of Fe oxygen vacancy substitution is the dominant mechanism to incorporate Fe^{3+} in a MgO-saturated environment. The fourth contribution describes how the Fe^{3+}-bearing jeffbenite (a mineral which has been found as an inclusion in deep and ultra-deep diamonds) has been synthetized for the first time in a multianvil apparatus and its crystal structure has been characterized in detail.

An important class of Fe compounds is represented by Fe hydroxides. In particular, FeOOH is a common oxyhydroxide at the Earth's surface. It may be transported down into the mantle by subduction of sediments and it is thought to be present at depth in a solid solution with AlOOH. Five contributions report about the synthesis and high-pressure and -temperature behaviour of samples belonging to the δ-AlOOH – ε-FeOOH solid solution. Large single crystals of three different compositions of ε-(Fe,Al)OOH have been successfully synthetized (fifth contribution) and structurally characterized, whereas samples having an Al-richer composition have been investigated at high temperatures and pressures using laser heated diamond anvil cells (sixth contribution) showing that this hydrous compound is stable up to 1850 K at pressures of the lower mantle. The changes in crystal structure and lattice parameters associated with hydrogen bond symmetrisation and Fe spin transition in $\delta\text{-Al}_{0.89}\mathrm{Fe}_{0.11}\mathrm{OOH}$ are reported in the seventh contribution. The high-spin to low-spin transition gives rise to softening of the unit-cell lattice parameters. The same spin transition also appears to have a strong effect on the lattice thermal conductivity of δ-(Al,Fe)OOH investigated by means of ultrafast time-domain thermoreflectance (eighth contribution). First principle calculations have been used in the following contribution to characterize the proton potential and, thus, to shed light on the nature of hydrogen disorder and symmetrisation in pure δ-AlOOH.

Accurate phase-equilibria experiments are essential for correctly characterize mantle seismic discontinuities. In the tenth contribution of this chapter the Clapeyron slope of the pyrope to bridgmanite phase transition has been determined by means of *in situ* X-ray diffraction coupled

with a multianvil apparatus. These new results show a concave curvature of the Clapeyron slope as a function of temperature suggesting a more complex influence of this transition on mantle dynamics than previously thought.

Meteoritic and lunar samples play an essential role in understanding the processes responsible for the formation and evolution of our solar system. The careful investigation of impact-induced textural features in an Apollo 15 sample conducted in the eleventh contribution resulted in the first report of a naturally occurring incongruent melt of olivine and suggest that this lunar sample recorded a pressure-temperature path very different from those of other meteoritic samples.

The last four contributions show how the characterization of the microscopic structure of minerals allows us to better understand their macroscopic behaviour and formation history. The antiphase domain boundary in magnetite, for example, can be a key feature of unseen mixed valence iron oxides stable at high pressures and temperatures (twelfth contribution), whereas the study of antiphase domain boundaries in omphacites (thirteenth contribution) allows to elucidate the kinetics of metamorphic processes in exhumed high-pressure and ultra-high-pressure eclogites. Dauphiné twins in quartz have been characterised by electron channeling contrast imaging in deformed quartz crystals for the first time, as reported in the fourteenth contribution, in order to better constrain the deformation mechanism of this mineral. Transmission electron microscopy has been used as well in the last contribution of this chapter to determine the exchange process of Fe, Mg and Ca between ortho- and clino-pyroxenes. The results show a complex behaviour involving a multi-step process of recrystallisation, diffusion and growth.

a. *A new series of homologous compounds in the Fe-O system (E. Bykova/Hamburg, M. Bykov, E. Koemets, I. Koemets, N.A. Dubrovinskaia/Bayreuth, L.S. Dubrovinsky; K. Glazyrin and H.-P. Liermann/Hamburg, M. Mezouar/Grenoble and V.B. Prakapenka/Argonne)*

The structure, properties and high-pressure behaviour of compounds in the Fe–O system have been extensively investigated because of their high importance in Earth sciences, solid state physics, and technology. Recent high-pressure studies revealed a variety of new phases belonging to the Fe-O system, that are either high-pressure polymorphs of conventional iron oxides (FeO, Fe_3O_4 or Fe_2O_3) or compounds with completely new stoichiometries (like Fe_4O_5, Fe_5O_6, Fe_5O_7, Fe_7O_9, Fe_9O_{11}, Fe_5O_7, $Fe_{13}O_{19}$ *etc*). Many of these compounds have similar structures formed by two building blocks, FeO_6 octahedra and trigonal prisms (Fig. 3.3-1). Prisms connect to each other through triangular faces arranging in rods, while octahedra share only edges and form ribbons. Rods and ribbons are extended in the same direction, so when they connect to each other by sharing common edges, they form various quasi-two-dimensional structures. We can combine such structures in a homologous series, similar to those observed in lillianite (compounds in the PbS-Bi_2S_3 system), calcium thallates and calcium titanates.

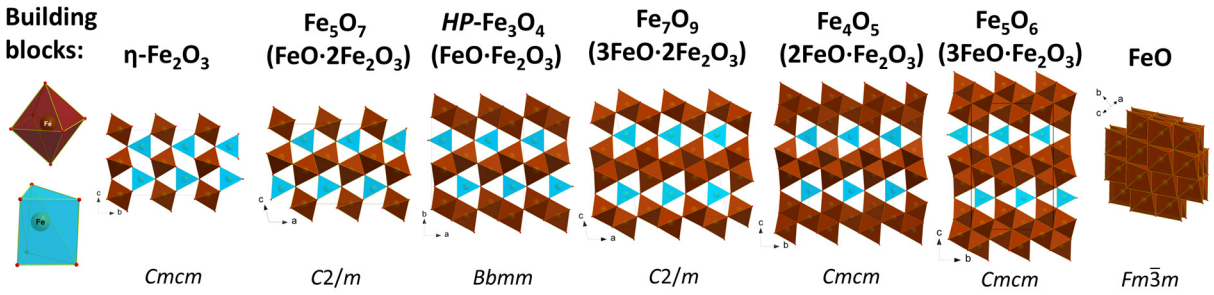

Fig. 3.3-1: Homologous series of iron oxides described by the common formula nFeO·mFe$_2$O$_3$. The structures may be described as constructed from two building blocks, FeO$_6$ octahedra and trigonal prisms (prisms could be two-capped but they are not shown for simplicity). Prisms connect to each other through triangular faces, while octahedra share only edges.

Here we report the synthesis and structural characterization of two iron oxides, Fe$_{16}$O$_{21}$ and Fe$_{25}$O$_{32}$. Their structural similarity allows us to propose another class of homologous compounds in the Fe-O system. Both compounds were synthesized at high-pressure and high-temperature conditions in laser-heated diamond anvil cells (DACs) and characterized by single-crystal X-ray diffraction. Fe$_{25}$O$_{32}$ was identified among the products of a thermal decomposition of Fe$_3$O$_4$ at 80 GPa. It crystallizes in the hexagonal unit cell (sp. gr. $P\bar{6}2m$) with unit-cell parameters a = 13.4275(16) and c = 2.6289(4) Å. In the same DAC we could find another hexagonal phase with unit-cell parameters a = 10.7563(8), c = 2.6247(8) Å (sp. gr. $P\bar{6}2m$). Based on the crystal structure solution, the chemical composition of this phase was determined to be Fe$_{16}$O$_{21}$. We also observed Fe$_{16}$O$_{21}$ in a separate experiment, among the products of a thermal decomposition of Fe$_2$O$_3$ at 106 GPa.

One can notice drastic similarities between the crystal structures of Fe$_{16}$O$_{21}$ and Fe$_{25}$O$_{32}$ (Fig. 3.3-2). In both compounds the iron atom located in the 1a position (0, 0, 0) is surrounded by a trigonal prismatic arrangement of six oxygen atoms. Similarly to compounds in the lillianite series, prisms are packed along the c-direction by sharing common triangular faces, each trigonal prism has three additional neighbors formed by FeO$_7$ one-capped prisms. These assemblages are connected to each other through 2- (in case of Fe$_{16}$O$_{21}$) or 3-membered (in Fe$_{25}$O$_{32}$) ribbons formed by edge-sharing octahedra. In the cavities formed by the ribbons, one can find either 3 or 9 rods formed by face-sharing FeO$_6$ prisms. The members of the proposed homologous series would then differ by the number of the rods located in the cavity and by the width of the octahedral slabs. As a result, the common structural formula would be Fe$_{7+9n}$O$_{10+11n}$, where Fe$_{16}$O$_{21}$ and Fe$_{25}$O$_{32}$ are the 2nd and the 3rd members of the series, respectively. We can also expect that other members of this series (for example with n = 0 or n > 2) are yet to be discovered.

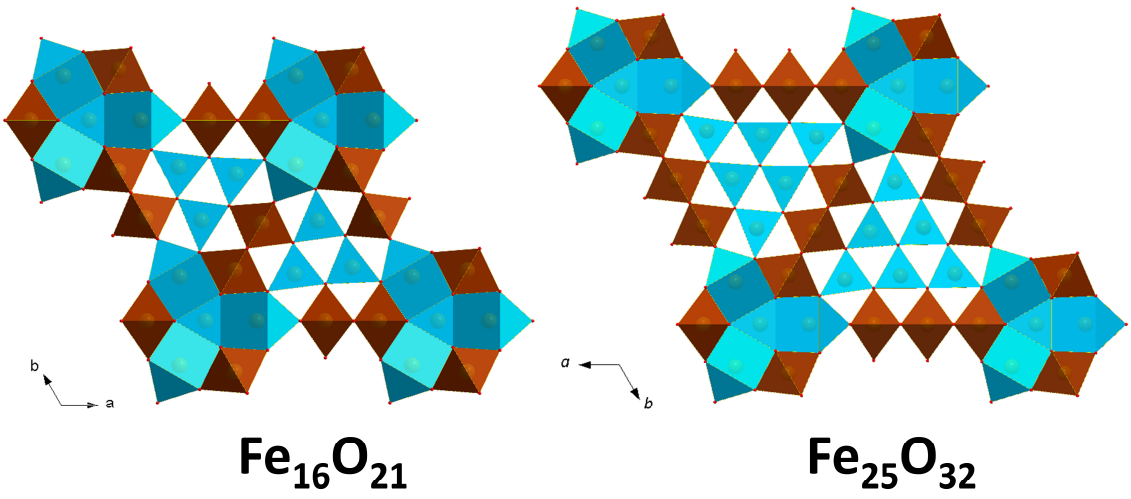

Fig. 3.3-2: Crystal structures of $Fe_{16}O_{21}$ and $Fe_{25}O_{32}$. Both structures are members of the new series of homologous compounds and consist of FeO_6 octahedra (brown), trigonal prisms and one-capped trigonal prisms (blue).

b. *The stability of Fe_5O_6 and Fe_4O_5 at high pressure and temperature (K. Hikosaka, R. Sinmyo and K. Hirose/Tokyo, Y. Ohishi/Hyogo and T. Ishii)*

It has been suggested that Earth's deep mantle may have a wide variation in oxygen fugacity, which is largely controlled by iron-bearing minerals. Over the past few years, various studies have reported iron oxides with chemical compositions between FeO and Fe_3O_4 at pressures above ~ 10 GPa. However, there is a lack of data concerning the stabilities of these high-pressure iron oxides. This study was conducted with the aim of determining the stability of Fe_5O_6 and Fe_4O_5 at high P-T conditions.

In situ X-ray diffraction measurements in a laser-heated diamond anvil cell were performed in order to determine the phase relations in both Fe_5O_6 and Fe_4O_5 bulk compositions up to 61 GPa and 2720 K. The results show that Fe_5O_6 is a high-temperature phase which is stable above 1600 K and ~ 10 GPa, while FeO + Fe_4O_5 is more stable at comparatively lower temperatures (Fig. 3.3-3). At pressures above 38 GPa, we observed both the decomposition of Fe_5O_6 into 2FeO + Fe_3O_4 and the decomposition of Fe_4O_5 into FeO + h-Fe_3O_4. The coexistence of FeO and Fe_3O_4 indicates that none of the recently discovered compounds between FeO and Fe_3O_4 (*i.e.*, Fe_5O_6, Fe_9O_{11}, Fe_4O_5, and Fe_7O_9) are formed beyond ~ 40 GPa at 1800 K, corresponding to conditions in the shallow lower mantle. Since it is plausible that magnesiowustite + Fe^{3+}-rich phases found as inclusions in some superdeep diamonds are relics of these high-pressure iron oxides, these results give constraints on pressure and temperature conditions of their formation. Additionally, we observed a distinct volume contraction for Fe_4O_5 at around 50 GPa, which could possibly be due to the spin transition of Fe^{3+}.

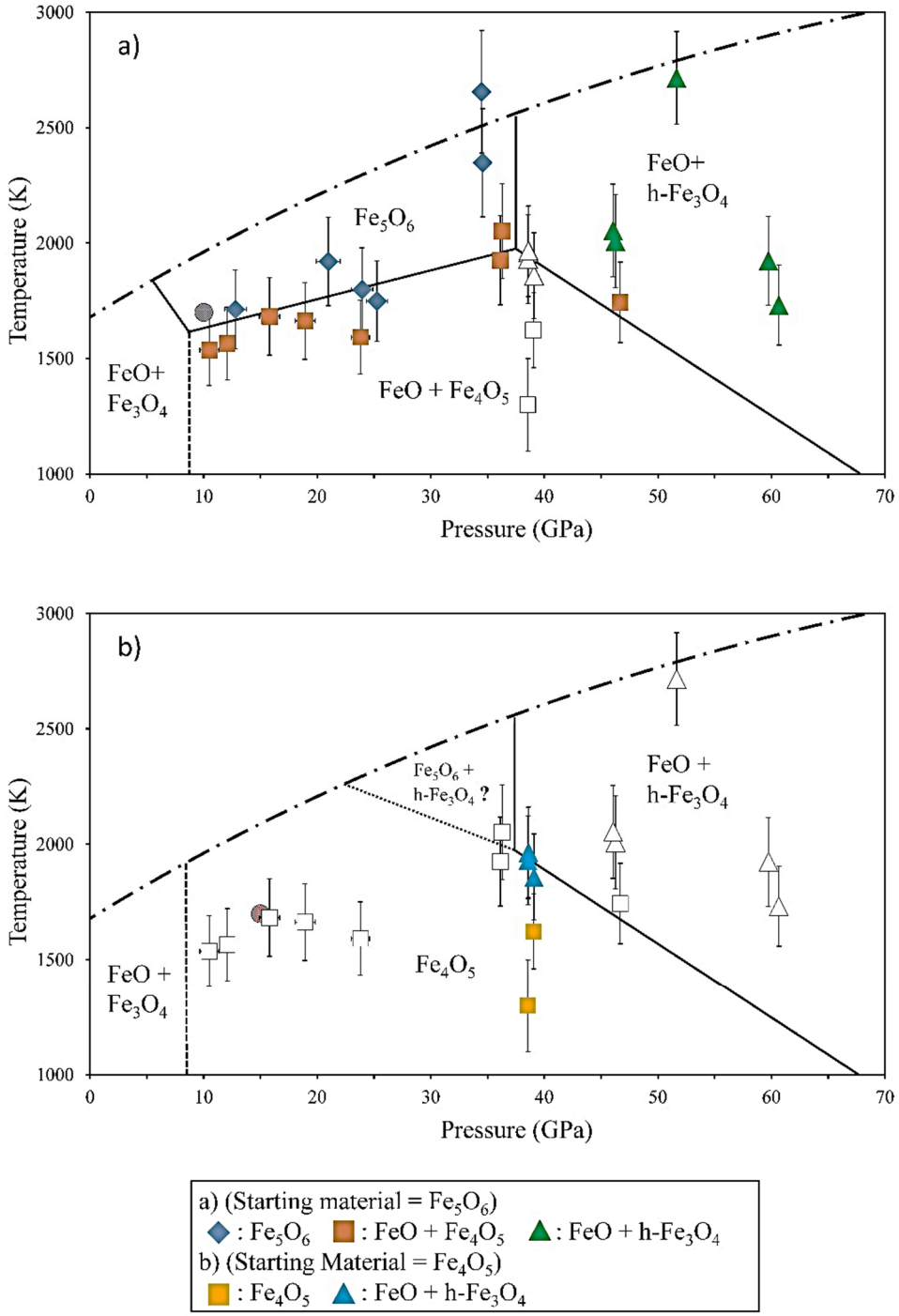

Fig. 3.3-3: Phase relations in (a) Fe_5O_6 and (b) Fe_4O_5 bulk compositions. The data points indicate conditions where the relevant phases were observed to be stable. In a) open squares and triangles are relevant data from a run with an Fe_4O_5 starting composition. In b) open symbols are relevant data from runs with an Fe_5O_6 starting composition. The purple and red circles indicate the condition where the Fe_5O_6 and Fe_4O_5 starting materials were synthesized respectively . The Fe_5O_6 + h-Fe_3O_4 region is supposed to exist, although not observed in this study. The dashed line is based on Myhill *et al.* (Contrib. Mineral. Petrol., 171:51, 2016). The chain curve shows the melting curve of FeO (Fischer and Campbell, Am Min, Volume 95, pages 1473-1477, 2010), which can be a guide for melting temperatures of Fe_5O_6 and Fe_4O_5.

c. *Ferric iron substitution mechanisms in bridgmanite under the topmost lower mantle conditions (H. Fei, Z. Liu, C.A. McCammon and T. Katsura)*

Bridgmanite comprises 80 vol. % of the Earth's lower mantle and therefore it dominates its physical and chemical processes. Due to its variable valence, iron is the most important element that affects the properties of bridgmanite and thus mantle dynamics. Generally, iron incorporates into the crystal structure of bridgmanite in the Mg site with the ferrous valence state. However, it is also known that a large amount of iron in bridgmanite can be in the ferric valence state. With Fe^{3+} substitution, the $MgFeO_{2.5}$ and $FeFeO_3$ components, respectively, will be formed through the reactions,

$$Si_B^{\times} \rightarrow Fe_B' + \frac{1}{2}V_O^{\bullet\bullet} \qquad (MgSiO_3 + \frac{1}{2}Fe_2O_3 \rightarrow MgFeO_{2.5} + SiO_2) \qquad (1)$$

$$Mg_A^{\times} + Si_B^{\times} \rightarrow Fe_A^{\bullet} + Fe_B' \qquad (MgSiO_3 + Fe_2O_3 \rightarrow FeFeO_3 + MgSiO_3) \qquad (2)$$

A critical question is how much Fe^{3+} in bridgmanite is stored as $MgFeO_{2.5}$ and/or $FeFeO_3$ components in the lower mantle. If a large proportion of $MgFeO_{2.5}$ is present, the concentration of oxygen vacancies will be high, which is expected to lower the viscosity of lower mantle. In contrast, $FeFeO_3$ component would not enhance the plastic deformation of bridgmanite significantly. To constrain the $MgFeO_{2.5}$ and $FeFeO_3$ concentrations under lower mantle conditions, we determined chemical compositions of bridgmanite coexisting with and without MgO (hereafter MgO-saturated and MgO-undersaturated, respectively) synthesized from an oxide mixture of MgO, SiO_2, and Fe_2O_3 at 27 GPa and 1700-2300 K using a multianvil apparatus. The total Mg, Fe and Si contents were measured using a microprobe (EPMA). The absence of ferrous iron was confirmed by Mössbauer spectroscopy.

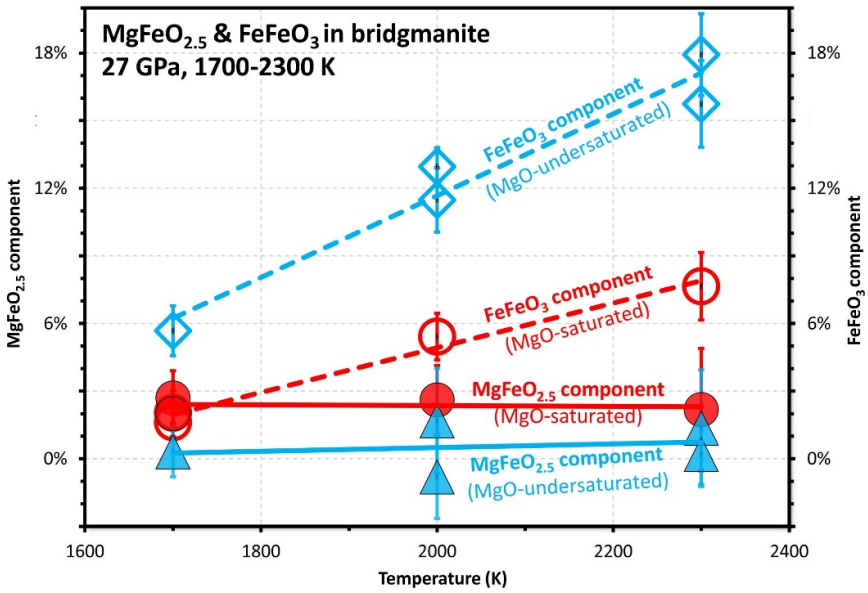

Fig. 3.3-4: Atomic concentrations of $MgFeO_{2.5}$ and $FeFeO_3$ in bridgmanite recovered from MgO-saturated (red) and -undersaturated (blue) synthesis runs.

With increasing temperature from 1700 to 2300 K, the concentration of $FeFeO_3$ increases systematically for both MgO-saturated and -undersaturated samples (Fig. 3.3-4). In contrast, the concentration of the $MgFeO_{2.5}$ is independent of temperature. It is generally zero in MgO-undersaturated samples, whereas it is 2-3 mol. % under MgO-saturated conditions. As enhanced by MgO saturation, the maximum solubility of $MgFeO_{2.5}$ in bridgmanite is about 2.5 mol. % (Fig. 3.3-4). The variation of Mg and Si contents with Fe^{3+} content for MgO-saturated samples crossover the pure oxygen vacancy substitution mechanism at an Fe^{3+} content of 0.025 pfu. Therefore, when Fe^{3+} < 0.025 pfu, the majority of Fe^{3+} in bridgmanite should follow the $MgFeO_{2.5}$ substitution mechanism under MgO-saturated condition (Fig. 3.3-5).

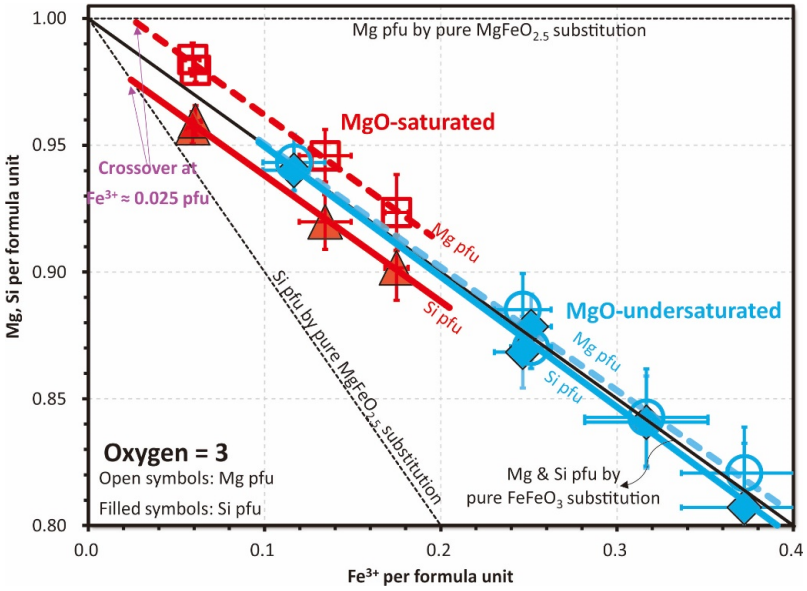

Fig. 3.3-5: Mg and Si per formula unit in bridgmanite (oxygen = 3) as a function of Fe^{3+} content. The thin solid and dashed lines indicate the theoretical concentrations of Mg, Si per formula unit for the pure $FeFeO_3$ and $MgFeO_{2.5}$ substitutions, respectively.

With the presence of (Mg,Fe)O in the lower mantle, the concentration of $MgFeO_{2.5}$ component should be maximized. By considering ΣFe = 0.1 pfu for bridgmanite in the MgO-SiO_2-FeO-Fe_2O_3 system at the topmost lower mantle, we have $Fe^{3+}/\Sigma Fe \approx 0.2$. Therefore, the Fe^{3+} concentration is about 0.02 pfu, which is below the solubility of $MgFeO_{2.5}$ in bridgmanite. Thus, oxygen vacancy substitution should be the dominant mechanism for Fe^{3+} incorporation in Al-free bridgmanite under the topmost lower mantle conditions, rather than the $FeFeO_3$ substitution as proposed previously.

d. *Ferric-iron-bearing jeffbenite synthesized at 15 GPa and 1200 °C (J.R. Smyth/Boulder, S.D. Jacobsen/Evanston and E. Posner)*

Jeffbenite is a mineral recently named and described as inclusions in diamonds thought to be of deep (transition zone) or ultra-deep (lower mantle) origin. Previously termed TAPP (for

tetragonal almandine-pyrope phase), the composition of the natural crystals closely resembles that of Al-rich garnet. The occurrence of this phase was also reported in laser-heated diamond anvil cell experiments at pressures of 6 to 10 GPa and 1300 to 1700 °C, but it has not previously been reported from multianvil experiments.

Exploratory multianvil experiments were conducted in the forsterite-fayalite-magnetite field under slightly hydrous conditions. The objective was to explore whether there might be complete solid solution between the wadsleyite field at 13-18 GPa and a ferric-iron-rich spinelloid III on the fayalite-magnetite join at 6 GPa. One such experiment at 15 GPa and 1200 °C produced an unrecognized Fe-rich silicate phase co-existing with what appeared to be a quenched liquid and a Ca-free clinopyroxene. Single-crystal X-ray diffraction experiments were carried out to characterize the iron silicate phase. Three of the crystals gave a body-centered tetragonal unit cell with cell parameters a = 6.6 Å and c = 18.4 Å.

Single crystal X-ray diffraction was carried out on a Bruker P4 four-circle X-ray diffractometer with an APEX II detector system at the University of Colorado. The X-ray source was a Bruker 18KW rotating Mo-anode generator operated at 50 KV and 250 mA with incident graphite monochromator. Five crystals were examined and all gave similar body-centered tetragonal unit cells with a = 6.6449 Å and c = 18.4823 Å. A data collection out to 75° 2θ was measured yielding 12871 intensities, of which 1061 were unique. Systematic absences were consistent with the acentric space group $I\bar{4}2d$.

The composition appears to nearly overlap that of a garnet and it has been pointed out also that the Raman spectrum is very similar to that of garnet. The density of jeffbenite of composition $(Mg_{0.60}Fe_{0.40})_4\,(Mg_{0.36}Fe_{0.64})_8\,(Mg_{0.65}Fe_{0.35})_8\,Si_4\,(Si_{0.94}Fe_{0.06})_8O_{48}$ is calculated to be 3.93 g/cm^3, whereas that of a skiagite garnet of a similar composition $(Mg_{0.87}Fe_{0.13})_3Fe_2Si_3O_{12}$ is estimated to be 3.95 g/cm^3 based on an estimated garnet unit-cell edge of 11.468Å, cell volume of 1508.3 Å^3 and formula weight of 473.15 g. These are essentially indistinguishable, so that there is no clear density difference between jeffbenite and garnet. The main difference is in the ratio of trivalent to divalent cations. Moreover, the crystal structure of jeffbenite (Fig. 3.3-6) does not closely resemble garnet or the tetragonal garnet, majorite nor it appears to be a simple pressure polymorph of garnet. The unit cell appears to bear a strong relationship to that of zircon with body-centered tetragonal symmetry, a similar a-axis, and a tripled c-axis.

There are two tetrahedral sites, T1 (four per cell) and T2 (eight per cell). T1 appears to be completely occupied by Si, whereas T2 appears to be occupied by Si plus about 6 percent ferric iron. There are three cation sites of higher coordination, M1, M2, and M3. The M1 site (four per cell) may be seen as a tetrahedron, with four near oxygens at 2.14 Å, but with four other oxygens at 2.58 Å and is somewhat analogous to the Zr site in zircon. The site occupancy appears to be 60 % Mg and 40 % ferrous iron. Due to the large distances, the site might be able to accommodate larger-radius cations such as rare earths, Zr, or U. The M2 site (eight per cell) is a small, but fairly regular octahedron. The occupancy appears to be 36 % Mg plus 64 % iron,

presumably ferric. The M3 site (eight per cell) is also a fairly regular octahedron and slightly larger than M2. Occupancy modelled with Mg and Fe scattering factors and assuming no vacancy gives 65 % Mg and 35 % Fe.

Because synthesis was carried out at 15 GPa and 1200 °C, it seems unlikely that the phase is a metastable retrograde inversion from a higher pressure phase such as bridgmanite. It appears that this phase has a true stability field within the Earth's transition zone at depths near 450 km in Al-rich or under oxidizing and Fe-rich conditions despite its very close compositional overlap with garnet.

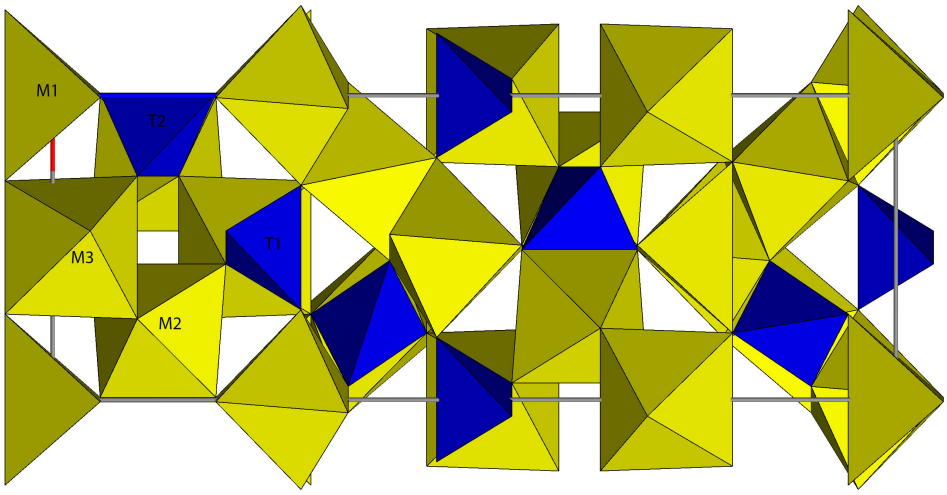

Fig. 3.3-6: Polyhedral representation of the crystal structure of jeffbenite, *c*-horizontal.

e. *Synthesis of ε-(Fe,Al)OOH single crystals (T. Ishii, G. Criniti, T. Boffa Ballaran and T. Katsura, in collaboration with J. Liu and X. Su/Beijing)*

FeOOH is a common oxyhydroxide at the Earth's surface, which can be transported into the mantle by subduction of sediments and can be formed in the mantle by reactions between iron and water. Therefore, this component can play an important role on oxygen and hydrogen cycles in the Earth's interior. ε-FeOOH, which is a high-pressure polymorph of FeOOH, is stable under deep mantle conditions. It is reported that this phase forms solid solutions with δ-AlOOH, which is an isostructural phase stable down to the lowermost mantle. Therefore, high-pressure behaviour of the ε-δ solid solutions should provide better understanding of the hydrogen and oxygen cycle. In this study, we attempted to synthesize single crystals of ε-(Fe,Al)OOH.

We prepared starting materials with $(Fe_x,Al_{1-x})OOH + H_2O$ compositions (x=0.9, 0.7, 0.5) using mixtures of $Al(OH)_3 + Fe_2O_3$ with distilled water for x = 0.9 and $Al(OH)_3$ + α-FeOOH for x = 0.7 and 0.5. Single crystals of Al-bearing ε-FeOOH with dimensions up to ~ 200 μm were synthesized at 21 GPa and 1473 K for 5 h in a 1200-ton multianvil high-pressure apparatus. We recovered ε-phases with Fe/(Fe+Al) ratios up to 0.6 (Fig. 3.3-7). Single crystal X-ray diffraction

showed that unit-cell volumes of ε-(Fe,Al)OOH almost linearly decreased with increasing Al content, in agreement with a previous study. The present syntheses of ε-(Fe,Al)OOH single crystals will be used in future studies such as P-T phase equilibrium experiments and physical property measurements (*e.g.*, elasticity and thermal conductivity) to improve understanding of hydrogen and oxygen cycles in the Earth.

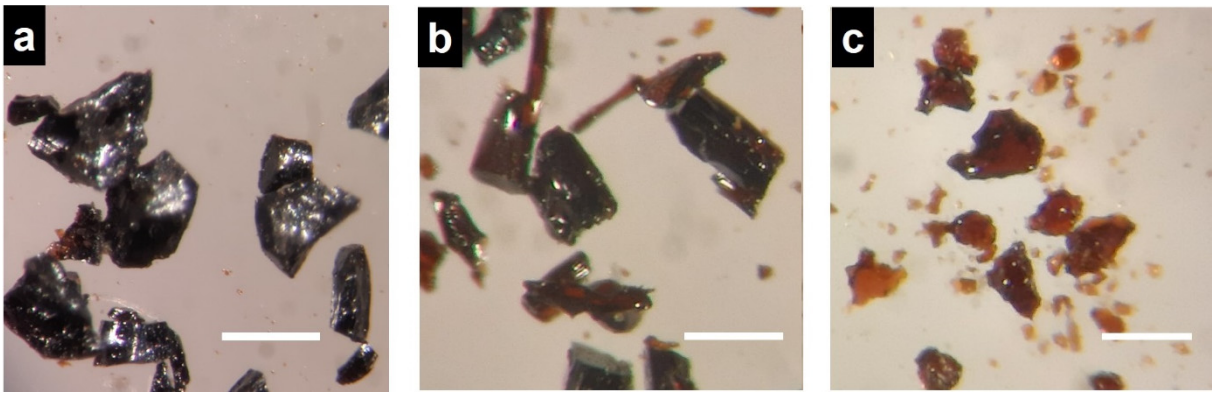

Fig. 3.3-7: Photographs of (a) ε-$Fe_{0.9}Al_{0.1}OOH$, (b) ε-$Fe_{0.7}Al_{0.3}OOH$, and (c) ε-$Fe_{0.6}Al_{0.4}OOH$ single crystals. The length of the scale bar is 200 μm.

f. *High-pressure high-temperature X-ray diffraction on δ-(Al,Fe)OOH: Defining the geophysical signature of hydration in Earth's lower mantle (J. Buchen, B. Strozewski and J.M. Jackson/Pasadena, T. Ishii)*

Even small degrees of hydration can significantly alter physical properties of rocks in Earth's upper mantle and transition zone. How hydration changes the physical properties, such as seismic wave velocities and density, of the lower mantle remains largely unknown. Solid solutions between phase H and δ-phase in the system $MgSiO_2(OH)_2$-AlOOH-FeOOH have been observed to coexist with bridgmanite in experiments and might store H_2O as hydroxyl groups in Earth's lower mantle. To evaluate how the presence of these hydrous phases might affect geophysical observables, we performed X-ray diffraction experiments on δ-(Al,Fe)OOH at combined high pressures and high temperatures.

Solid solutions of δ-(Al,Fe)OOH were synthesized from powders of $Al(OH)_3$ and Fe_2O_3 at 21 GPa and 1470 K using a multianvil press at BGI, Bayreuth. Individual grains of δ-(Al,Fe)OOH with Al/(Al+Fe) = 0.87(2) were selected from the synthesis run product and crushed between a pair of diamond anvils. The resulting powder was loaded into a diamond anvil cell together with gold powder as pressure marker. To prevent dehydration of δ-(Al,Fe)OOH at high temperatures, we used $Al(OH)_3$ powder as pressure-transmitting medium and thermal insulation. After cold compression to pressures in excess of 40 GPa, DAC loadings were heated simultaneously from both sides using the double-sided laser heating setup at beamline 12.2.2 of the Advanced Light Source (ALS), Berkeley, CA. Temperatures were determined from thermal emission spectra. In addition, the pyrometry setup at beamline 12.2.2 allows to map the

temperature distribution across the heated sample area. We recorded X-ray diffraction patterns before, during, and after laser heating in order to detect any reversible or irreversible changes of δ-(Al,Fe)OOH at high temperatures.

Figure 3.3-8 shows X-ray diffraction patterns recorded before, during, and after laser heating together with temperature maps of the hot spot. Before and after laser heating, the pressure as derived from gold was around 71 GPa. Taking into account the temperature effect on the equation of state of gold suggests a pressure of about 78 GPa during laser heating. The evaluation of thermal emission spectra and maps yields a mean temperature of about 1850 K while temperatures on the downstream side appeared to be about 300 K lower than on the upstream side. On both sides, peak temperatures in excess of 2000 K decay along steep thermal gradients to temperatures below the emissivity threshold within a distance of about 20 µm. In all diffraction patterns, the most intense X-ray reflections can be allocated to δ-(Al,Fe)OOH and gold. Minor diffracted intensity arises from diffraction of X-rays on the rhenium gasket and potentially from corundum, Al_2O_3, that may have formed by partial dehydration of $Al(OH)_3$ and δ-(Al,Fe)OOH during laser heating. Note that we did not observe X-ray reflections from $Al(OH)_3$, which is expected to amorphize above 30 GPa. Since we did not observe a significant change in relative diffracted intensities upon laser heating, we conclude that δ-(Al,Fe)OOH remained stable at 78 GPa and 1850 K. Together with results of future laser heating experiments, X-ray diffraction patterns recorded at combined high pressures and temperatures will be used to derive a thermal equation of state for δ-(Al,Fe)OOH.

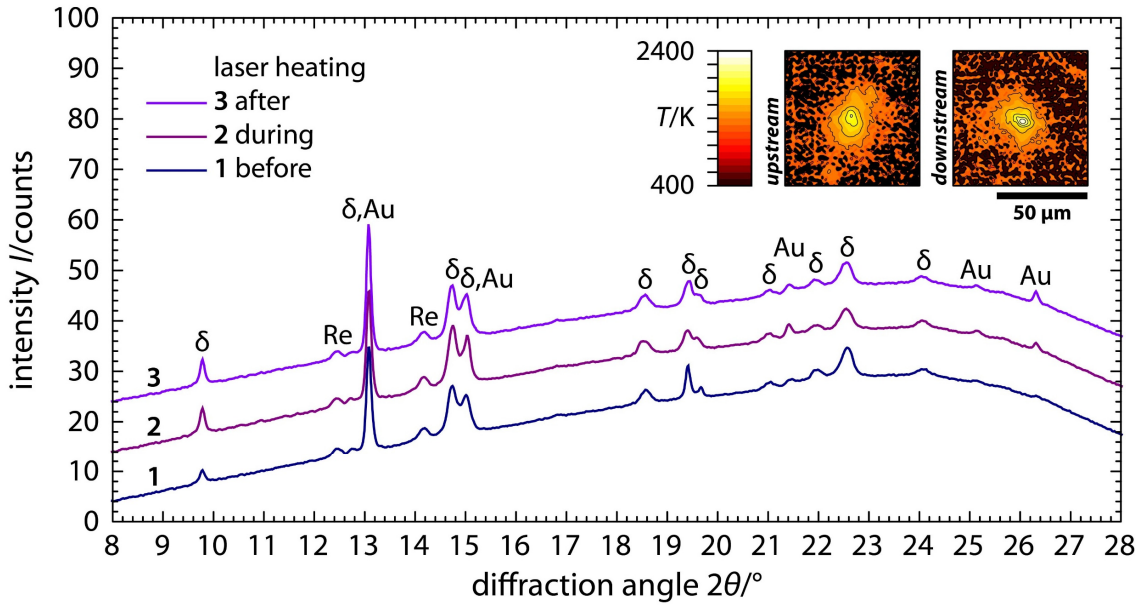

Fig. 3.3-8: X-ray diffraction patterns of δ-(Al,Fe)OOH and gold powder before (1), during (2), and after (3) laser heating in a diamond anvil cell. X-ray reflections are labeled according to the contributing phases δ-(Al,Fe)OOH (δ), gold (Au), and rhenium (Re). Upon heating, pressure increased from 71 GPa at room temperature to 78 GPa at about 1850 K. The inset in the upper right corner shows temperature maps of the hot spot viewed from the upstream (left) and downstream (right) side. Note the steep thermal gradients around the temperature peak.

g. *Hydrogen bond symmetrization and spin crossover in (Fe,Al)OOH upon compression at ambient temperature (I. Koemets, E. Koemets, T. Ishii and L.S. Dubrovinsky)*

The presence of water can strongly affect physical and chemical properties of mineral assemblages in the Earth's interior. For example, water incorporation into minerals leads to decreases in viscosity, melting temperature, and impacts melt composition. Water is present in minerals as H^+ and OH^- groups, and recent reports suggest that oxyhydroxides (goethite, diaspore and their high-pressure polymorphs) could transport water into the Earth's mantle within subducting slabs. Therefore, the behaviour of oxyhydroxides at extreme conditions is of great importance for understanding the evolution and dynamics of the Earth and the deep water cycle. In this project we investigated hydrogen bond symmetrisation and the impact of spin crossover on (Fe,Al)OOH elasticity during compression of the material at ambient temperature up to ~ 67 GPa.

We used a sample from the AlOOH–FeOOH solid solution synthesized in a multianvil apparatus as a starting material. A high-quality single crystal with dimensions of about 20x10x5 μm^3 was selected for a DAC experiment and contained ~ 11 % of iron (as was determined based on structure refinement at ambient conditions). The sample was placed in a pressure chamber made in a Re gasket; Ne was used as pressure-transmitting medium and a ruby chip was used for pressure determination. *In situ* single-crystal X-ray diffraction data were collected on the beamline P02.2 at DESY.

Analysis of systematic absences reveals a symmetry change from space group $P2_1nm$ to $Pnnm$ between 5 and 12 GPa. In the case of the low-pressure $P2_1nm$ structure the MO_6 octahedra have three long (1.942(3) Å) and three short (1.886(3)-1.875(3) Å) M-O distances (occupancy $M=Fe_{0.11}Al_{0.89}$). The longer M-O bonds correspond to the covalently bound oxygen of the hydroxyl, while the other oxygens are weakly bound to H of the nearest hydroxyl group. At 12 GPa all M-O bonds become similar, suggesting that symmetrisation of the hydrogen bonds occurred (Fig. 3.3-9).

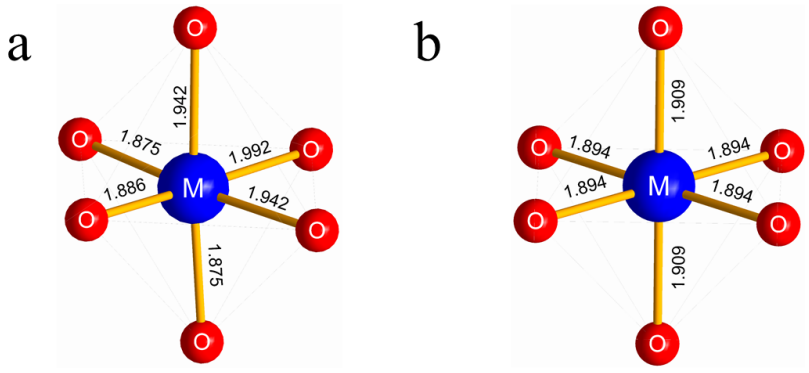

Fig. 3.3-9: Selected MO_6 ($M=Fe_{0.11}Al_{0.89}$) octahedron for $P2_1nm$ **(a)** and $Pnnm$ **(b)** (Fe,Al)OOH. In case of $P2_1nm$ structure one can distinguish three long (1.942(3) Å) and three short (1.886(3)-1.875(3) Å) M-O distances. The longer M-O bonds correspond to the covalently bound oxygen of the hydroxyl, while the other oxygens are weakly bound to H of the nearest hydroxyl group. Under compression the M-O bonds become similar, which indicates that hydrogen bonds symmetrize.

At pressures of 35-40 GPa we observed a softening of the lattice parameters which is related to a spin crossover in Fe^{3+} occupying the octahedral site and could be clearly observed on the F-f plot obtained from the P-V data (Fig. 3.3-10). The fitting of the experimental data points with a second-order Birch-Murnaghan equation of state resulted in $K_0 = 212(5)$ GPa and $V_0 = 56.7(1)$ $Å^3$ for the high spin state, and $K_0 = 240(12)$ GPa and $V_0 = 55.4(3)$ for the low spin state.

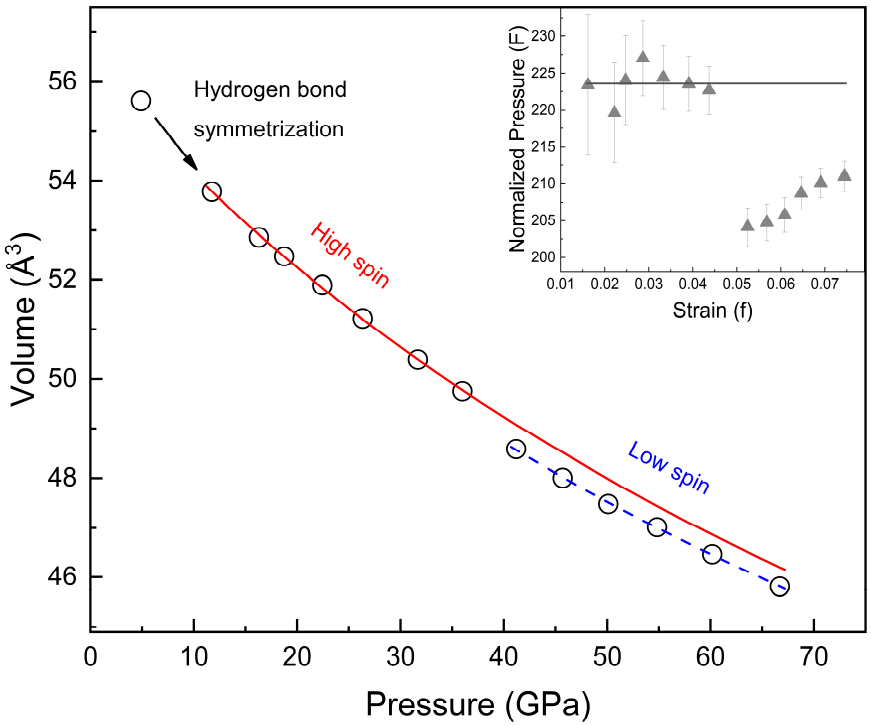

Fig. 3.3-10: Compression behaviour of (Fe,Al)OOH. The red solid line represents the fit of the experimental data in the pressure range between 10 and 35 GPa using a second-order Birch-Murnaghan equation of state. The blue dashed line represents the fit of data at pressures above 35 GPa. The softening between 35 and 40 GPa is related to the high spin to low-spin crossover in octahedral Fe^{3+}. Inset: Normalized pressure versus Eulerian strain plot.

h. *Spin transition of iron in δ-(Al,Fe)OOH induces thermal anomalies in Earth's lower mantle (W.-P. Hsieh and K.-H. Chao/Taipei, J. Tsuchiya/Matsuyama, F. Deschamps/Taipei, E. Ohtani/Sendai and T. Ishii)*

Transport of water from Earth's surface to its interior via subduction of hydrous minerals within a slab can play a critical role in affecting the physical and chemical properties, as well as the evolution of the Earth's mantle. Mineral physics experiments showed that δ-AlOOH is stable under lower mantle pressure-temperature conditions, making it a key water-carrier to the deep mantle. Though many physical properties of δ-AlOOH under extreme conditions have been extensively investigated, its thermal conductivity at relevant deep mantle conditions, in particular, through the spin transition of iron, has never been measured. Given the large amounts

of iron in the Earth's mantle, thermal conductivity of hydrous δ-(Al,Fe)OOH is critically needed since it would bring important insight into the thermal states in subduction zones and surrounding mantle in the Earth's deep interior, as well as potential impacts of the water cycle on the deep mantle structure and geodynamics.

Here we used ultrafast time-domain thermoreflectance coupled with a diamond anvil cell to study the lattice thermal conductivity of δ-AlOOH and δ-(Al,Fe)OOH phases to Megabar pressures at room temperature. We found that the thermal conductivity of δ-(Al,Fe)OOH varies drastically by a factor of 2-3 across the spin transition of iron (Fig. 3.3-11). We also observed an enhanced iron substitution effect in its low-spin state, causing an exceptionally lower thermal conductivity than the surrounding mantle at lowermost mantle conditions, which would in turn induce local temperature and heat flux anomalies above the core-mantle boundary, and alter the route of the deep water cycle.

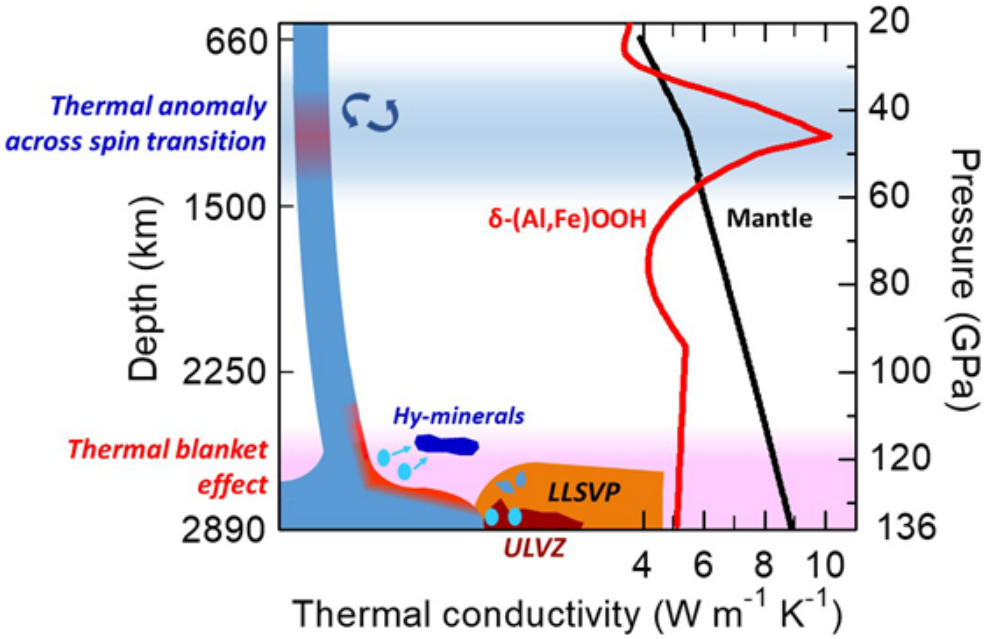

Fig. 3.3-11: Modeled thermal conductivity of δ-($Al_{0.85}Fe_{0.15}$)OOH (red curve) and pyrolitic mantle (black curve) along a representative geotherm (mantle potential temperature of 2000 K). A schematic illustration of δ-(Al,Fe)OOH in an oceanic crust of a slab subducted to the bottom of the mantle is also shown. A thermal anomaly and small-scale convection (illustrated by rotating arrows) due to heterogeneous density distribution could be induced by the spin transition of iron (~ 30-60 GPa, blue shaded area), where the thermal conductivity of δ-(Al,Fe)OOH varies drastically, resulting in an anomalous temperature distribution within the slab (slab temperature is higher below the region with higher δ-(Al,Fe)OOH thermal conductivity). At the lowermost mantle (pink shaded area), the exceptionally low thermal conductivity of δ-(Al,Fe)OOH creates a thermal blanket effect that promotes heating (thin red faded area with higher temperature at the top layer of the slab) and consequently enhances dehydration. The large amounts of water (light blue droplets) released from δ-(Al,Fe)OOH facilitate partial melting of minerals for seismic ULVZ, and also serve as a water source to form deep-mantle hydrous minerals (dark blue lobe), *e.g.*, hydrous Al-bearing bridgmanite.

i. *High-pressure behaviour of δ-AlOOH from first-principles simulations (B. Wang, F. Trybel and G. Steinle-Neumann)*

The high-pressure polymorph of diaspore and boehmite, δ-AlOOH, shows one of the highest pressure (*P*) stability of a hydrous mineral that can potentially be subducted into the deep Earth. Aside from this important geophysical and geochemical role, δ-AlOOH is of significant crystalchemical interest due to a subtle structural transition expected at *P*~8 GPa from the $P2_1nm$ to the Pnnm structure, the nature and origin of hydrogen disorder, the symmetrization of the O-H…O hydrogen bond, and their interplay.

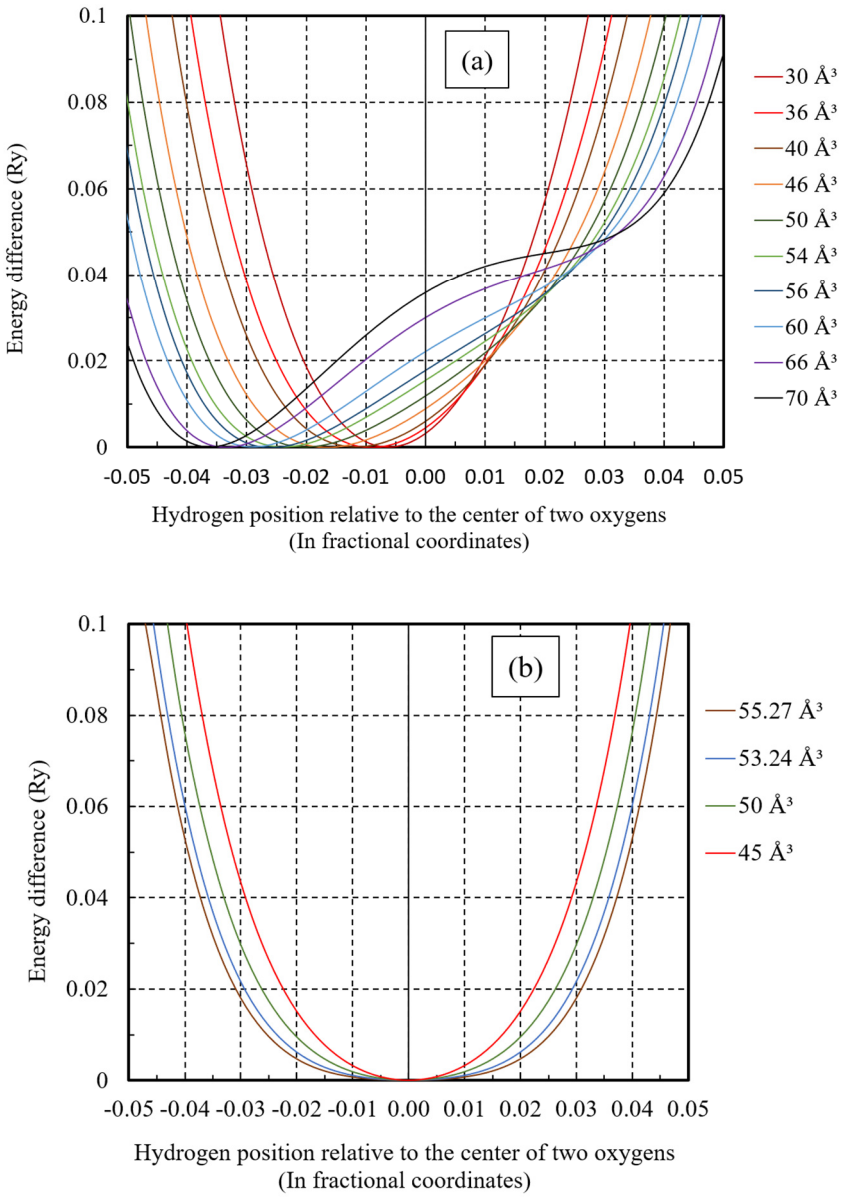

Fig. 3.3-12: (a) Evolution of the H potential between O1 and O2 at different volume (for $P2_1nm$ δ-AlOOH) and (b) Evolution of the H potential between two oxygens at different volume (for Pnnm δ-AlOOH).

While a significant number of experimental and computational studies have been performed to address these questions, no consensus has emerged. We perform a series of density functional theory-based simulations on both the $P2_1nm$ and Pnnm structures of δ-AlOOH, with the goal to better characterize the proton potential and therefore the nature of hydrogen disorder. In this context, it is particularly important to establish the shape of this potential that helps to understand whether proton disorder stems from tunneling between different hydrogen positions (double-well potential) or is of thermal origin (wide anharmonic potential).

From the simulation results we infer for $P2_1nm$ δ-AlOOH that the potential is asymmetric at low *P*, without a second minimum (not even local) for the H…O branch, ruling out disorder by tunneling. The potential remains asymmetric to the highest compression investigated here, well beyond the transition pressure (Fig. 3.3-12a). The O-H and H…O bond lengths determined at ambient pressure-volume are in close agreement with data from neutron experiments for δ-AlOOH. By contrast, for the high-*P* Pnnm structure of δ-AlOOH we find a symmetric but wide potential for the proton (Fig. 3.3-12b), suggesting that disorder in this phase is caused by thermal activation. Equation-of-state (EoS) parameters determined for the two structures when using the computationally optimized H-positions are in reasonable agreement with previous estimates. However, the transition *P* we determine from our EoS fits to both phases is in the range of 2-3 GPa, *i.e.*, lower than experimental data suggest (8 GPa).

j. *Drastic change with temperature in Clapeyron slope of the post-garnet transition in* $Mg_3Al_2Si_3O_{12}$ *by accurate phase-equilibrium experiment with* in situ *X-ray diffraction in a multianvil press (T. Ishii, D.J. Frost, A.D. Chanyshev, K. Nishida, L. Xie, R. Ban/Sendai, X. Su/Beijing, Y. Higo/Kouto, Y. Tange/Kouto and T. Katsura)*

Understanding of mantle seismic discontinuities is key to understanding the structure and dynamics of the Earth's mantle. Our previous study raised a serious problem with previous high-pressure phase-equilibrium experiments: pressure drops upon heating and sluggish transition kinetics hamper accurate determination of transition pressures. Thus, phase-equilibrium experiments with a right procedure are required to obtain accurate phase boundaries.

Garnet (Gt) is the second and most abundant mineral in peridotite and basalt, respectively, in the deep upper mantle, and transforms to bridgmanite (Brg) in the upper part of the lower mantle (post-garnet (pGt) transition). This transition should provide hints to understand the structure and dynamics of the lower mantle. In this study, the pGt (Gt to Brg + corundum (Crn)) phase boundary in the pyrope composition was determined by *in situ* X-ray diffraction in combination with a multianvil press. The starting material was a sintered mixture of Brg + Crn and Gt with a molar ratio of 1:1 in the bulk composition of pyrope. A stable phase was judged by observing change in relative intensity of coexisting Brg, Crn and Gt to exclude kinetic effects (Fig. 3.3-13). We successively determined transition pressures by bracketing the phase boundary with increasing temperature from 1400 to 2000 K in 100-K intervals to suppress a pressure drop.

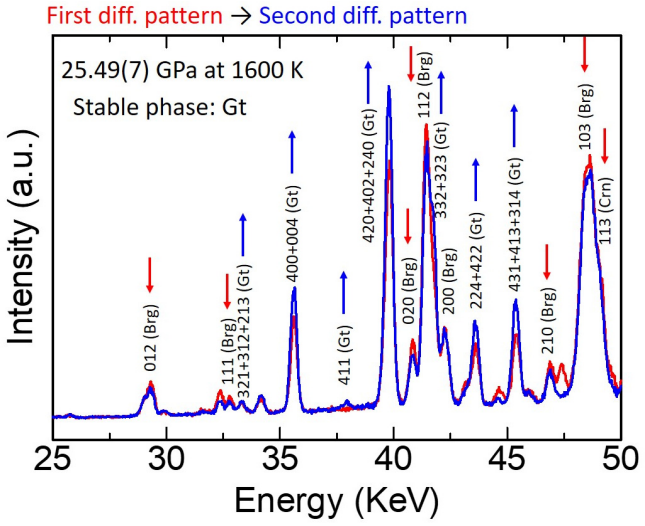

Fig. 3.3-13: An example of change in intensity ratio between Gt, Brg and Crn. Compared with the first diffraction shown in red, the second diffraction shown in blue shows that the Gt peaks became stronger whereas those of Brg and Crn became weaker, identifying Gt as the stable phase.

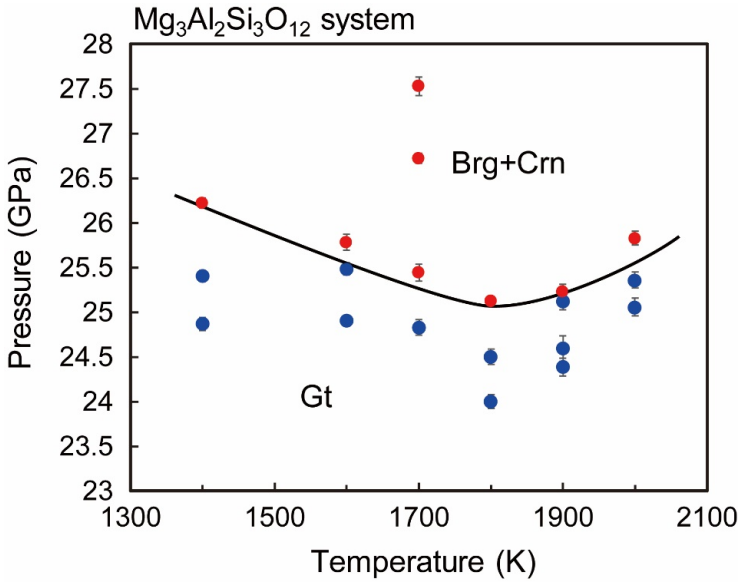

Fig. 3.3-14: Phase boundary of the pGt transition in $Mg_3Al_2Si_3O_{12}$. Blue solid circles indicate the stable phase of Gt. Red solid circles indicate the stable phase of Brg + Crn. Pressures were determined based on the Tange MgO scale [Tange *et al.*, J. Geophys. Res., 114, B3, 2009].

The present phase boundary is found to be located at pressures of 25-26.5 GPa in the investigated temperature range (Fig. 3.3-14). One remarkable feature of the phase boundary is its downward concave curvature, where the Clapeyron slope increases from the negative value of -3 MPa/K to the positive value of +3 MPa/K with increasing temperature from 1400 to

2000 K. This observation suggests that, although the pGt transition will impede subduction due to the negative slope at lower temperatures, it will enhance plume ascendance due to the positive slope at higher temperatures. We suggest the necessity of redetermination of phase boundaries of all important mantle phase-transitions by the right experimental procedure demonstrated in this study for a correct understanding of mantle dynamics.

k. *Apollo 15 sample provides the first natural observation of incongruent melting of olivine (N. Satta, M. Miyahara/Hiroshima, S. Ozawa/Sendai, H. Marquardt/Oxford and E. Ohtani/Sendai)*

Collisions between rocky bodies play an integral role in the formation and evolution of planetesimals and planets in the inner Solar System. During an impact event, shock waves propagate through the unshocked material causing temporary and sharp increases in pressures (P) and temperatures (T). Large impact events can expose rocks to P-T conditions comparable to those of deep planetary interiors, and thereby drive melting, amorphization and phase transitions in rock-forming minerals. Shock related features, including mineralogical and textural aspects, in impact-induced shocked rocks can provide important insights on the P-T conditions triggered by impact events. Therefore, the study of shocked natural samples allows to understand cosmic processes in the inner Solar System.

Olivine is the most abundant mineral of the Earth's upper mantle by volume. Olivine transforms into wadsleyite and ringwoodite at transition zone P-T conditions, and dissociates into ferropericlase (Fe,Mg)O plus bridgmanite (Mg,Fe)SiO_3 at lower mantle conditions (> 23 GPa and > 1900 K). Moreover, at relatively low pressures and high temperatures (~ 10 GPa, ~ 2200 K) olivine can melt incongruently, forming ferropericlase plus liquid. Phase transitions and dissociation of olivine have been widely observed in natural impact-shocked samples, and hence have been crucial to delineate the P-T conditions triggered by impact events. However, incongruent melting of olivine has never been observed in any natural samples investigated so far, thus remaining a process confined to experiments.

The geological quiescence of the Moon allowed the preservation of a cratering record and shocked rocks on its surface, thus making it the best place to collect large quantities of shocked natural samples. The Apollo missions returned several regolith breccias to the Earth – typical lunar rocks fragmented and lithified by impact events. In this study, we investigated a platelet obtained from the Apollo sample 15299, a regolith breccia collected during the Apollo 15 mission. We employed Scanning Electron Microscopy (SEM), Focused Ion Beam (FIB) sample preparation and Transmission Electron Microscopy (TEM) to detail a series of impact-induced textural features. We found evidence that strongly suggest that olivine underwent incongruent melting (Fig. 3.3-15). This documents the first naturally occurring example of incongruent melting of olivine due to a shock event.

Our finding implies that the Apollo 15299 sample recorded a P-T path that is very different from those of other meteoritic samples. We infer that such a unique P-T path can only be the

result of a collision between a projectile and the porous lunar regolith. This discovery opens new scenarios in the study of shocked natural samples, and further remarks the importance of exploring our natural satellite to understand solar system dynamics.

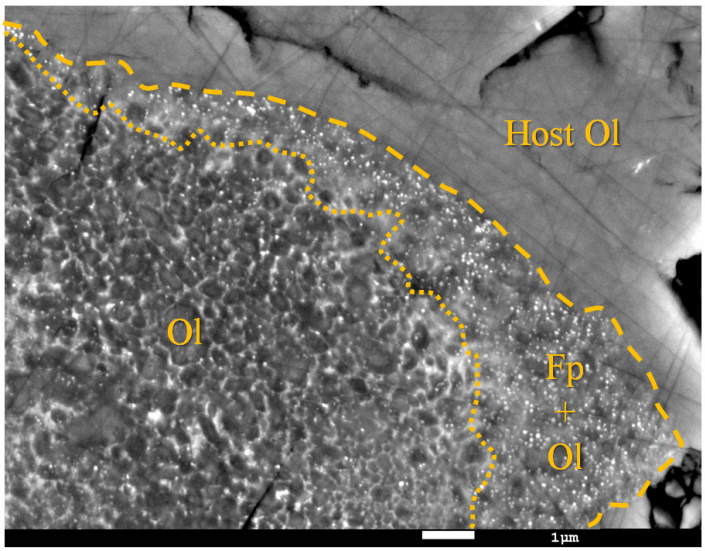

Fig. 3.3-15: High magnification SEM image of the studied shock melt pocket in the Apollo 15 sample. The large dashed line outlines the boundary between the host olivine crystal and the shock melt pocket. The small dashed line defines the boundary between the two distinct mineral assemblages coexisting within the shock melt pocket. Fp = ferropericlase, Ol = olivine.

I. *Antiphase domain boundaries in magnetite: A key feature of unseen high-pressure mixed-valence iron oxides (N. Miyajima; L. Uenver-Thiele and A.B. Woodland/Frankfurt; T. Boffa Ballaran and D. J. Frost)*

Antiphase domain boundaries (APBs) and the APB structures in epitaxial magnetite films grown on MgO substrates are known to have a strong influence on the magnetic properties. However, no APBs in natural magnetite have been reported so far. Recently new mixed valence iron oxides, *e.g.*, Fe_4O_5 and Fe_5O_6 in a homologous series of $CaFe_{n+2}O_{n+4}$ compounds (n = an integer), were reported to reflect the redox state in the interior of the Earth. The stability of the mixed-valance iron oxides in the Mg-Fe-Si-O system can give a wide variation to the phase relations in the Earth's mantle, while the polymorphs of $Fe_{1-x}O$, Fe_3O_4 and Fe_2O_3 are stable at ambient conditions. Along with these studies, unusual {113} twins in magnetite were reported as a characteristic record of back-transformation from unseen high-pressure phases in the deep mantle. The twin microstructures can be related to the crystal structure of precursors at high pressure and high temperature. We report here preliminary results based on transmission electron microscopy (TEM) studies of the APB structures in magnetite which is one of the decomposition phases from a mixed valence iron-magnesium oxide (Fig. 3.3-16). The rock-salt structured phase was also intergrown with magnetite, displaying diffuse scattering intensities

related with the defect cluster distribution (Inset in Fig. 3.3-16). TEM observations confirmed the existence of APBs in magnetite which we suspect may be a key feature of unseen mixed valent iron oxides.

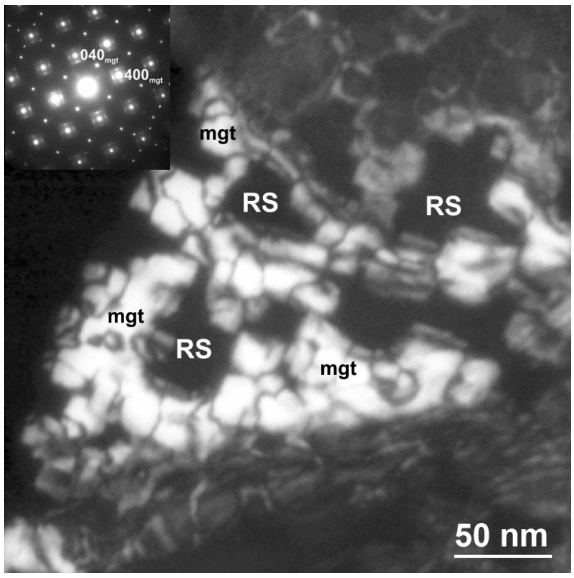

Fig. 3.3-16: Dark-field TEM image of an intergrowth of magnetite (mgt) and rock-salt phase (RS) in the decomposition from a mixed valance iron-magnesium oxide.

m. *Reappraisal of natural omphacite: To see a world in a nanoscale domain (T. Tsujimori and R. Fukushima/Sendai, N. Miyajima)*

Omphacitic pyroxene, with compositions close to $Ca_{0.5}Na_{0.5}(Mg,Fe^{2+})_{0.5}Al_{0.5}Si_2O_6$, is ubiquitous in a variety of high-pressure (HP) and ultrahigh-pressure (UHP) metamorphic rocks of basaltic protoliths. Its parageneses and major-element compositions have been commonly used to characterize subducted oceanic crusts in the HP–UHP metamorphic belts. In our project, we explore the potential of nanoscale properties of omphacite to understand the kinetics of metamorphic processes in exhumed HP–UHP rocks.

Omphacite at high temperature has disordered *C*2/*c* symmetry. At temperature recorded in blueschist and most orogenic eclogites, however, the difference in space-group symmetry between ordered (*P*2/*n*) omphacite and disordered (*C*2/*c*) diopsidic pyroxene allows the miscibility regions between jadeitic pyroxene (*C*2/*c*)–omphacite (*P*2/*n*) and augitic pyroxene (*C*2/*c*)–omphacite (*P*2/*n*). The solvus between the ordered *P*2/*n* omphacite and other *C*2/*c* pyroxenes becomes wider with decreasing temperature. Consequently, the two solvus as a function of temperature have been considered for numerous thermodynamic modelling/analyses of metamorphic phase equilibria for blueschist and eclogites.

The cation ordering in omphacite has been investigated in numerous transmission electron microscopic studies. As shown in Fig. 3.3-17, natural omphacite shows nanoscale antiphase

domain (APD) boundaries, which is the planar crystallographic defects in the lattice structure. It forms via the phase transition from *C*2/*c* omphacite to *P*2/*n* omphacite. Previous work suggests that the APDs coarsen with increasing time at a given temperature: $\delta^8 = 4.8 \times 10^{36} \exp(-75{,}000/RT)t$, where δ is the mean APD size and t the time. Evidence includes numerous observations of APD in different temperature range of blueschist and eclogites in different localities; note that the observed APD in some low-temperature *P*2/*n* omphacites might have formed from metastable *C*2/*c* omphacite. However, the systematics are not as simple as they have been simplified in the above equation. For example, a process like deformation (or multiple deformations) leads to recrystallization easily.

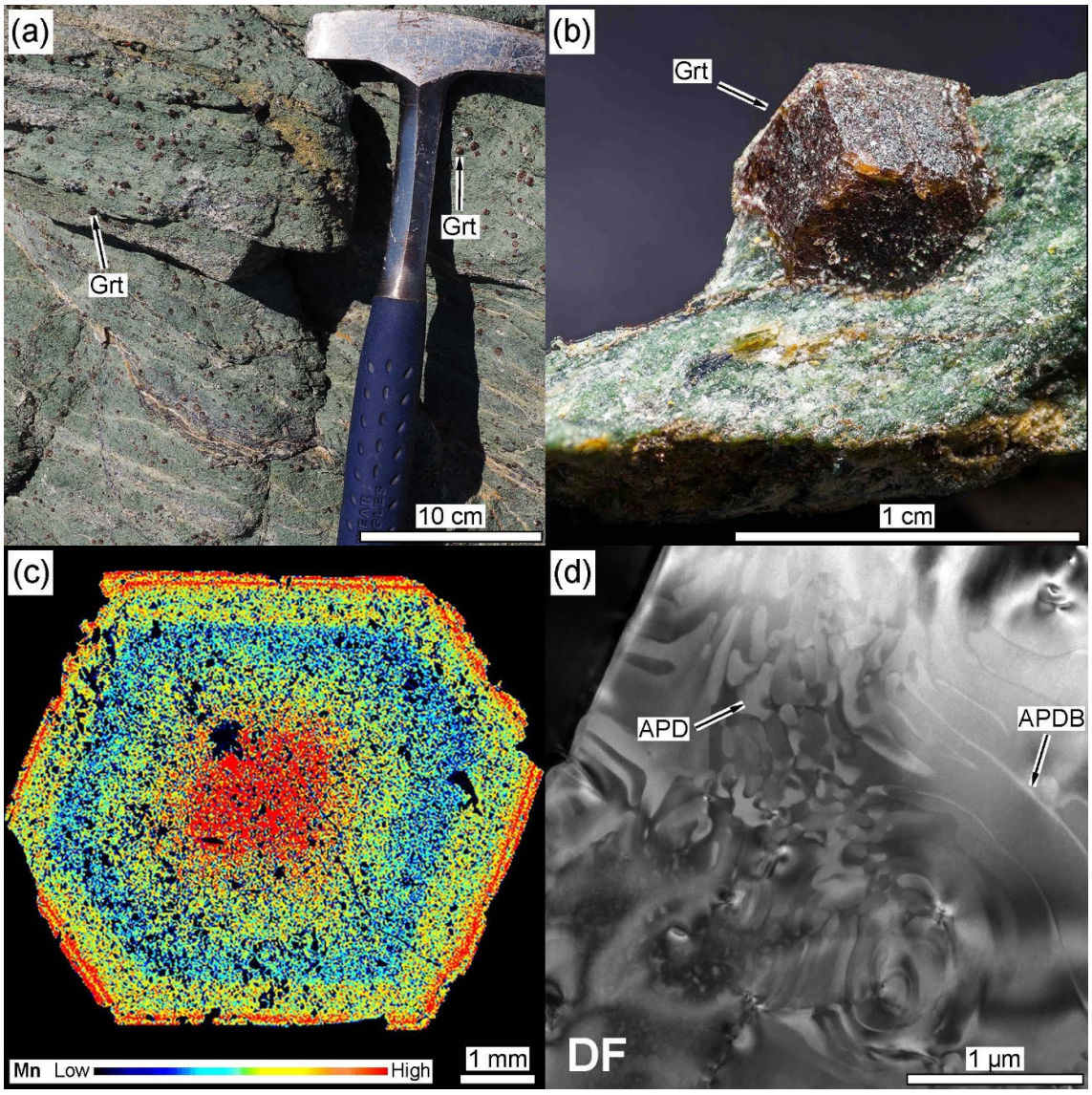

Fig. 3.3-17: (a) Low-temperature eclogite on the island of Syros showing abundant garnet porphyroblasts in a foliated matrix. (b) The investigated euhedral garnet with rhombic dodecahedron shape. (c) Electron microprobe X-ray mapping of a center-cut euhedral garnet extracted from a sample shown in (b). Raw intensity data was processed using R version 3.5.3. (d) Dark field TEM image of omphacite within garnet in (c) showing antiphase domain (APD) and antiphase domain boundary (APDB).

Through our preliminary research, we have realized that omphacite hosted in garnet is the best target for APD studies. Omphacite hosted by prograde-zoned garnet in low- to medium-temperature eclogite, which can be formed during progressive subduction, is the key to decipher systematics among omphacite APD and kinetics of metamorphic processes. To understand kinetics of metamorphic processes from nanoscale texture of omphacite, we are undertaking a collaborative project to answer the above questions. We intend to apply our extensive experiences in the study of HP–UHP eclogites, combining it with nanoscale mineral characterization at BGI.

n. *Dauphiné twin in a naturally deformed quartz: Characterization by electron channelling contrast imaging and large-angle convergent-beam diffraction (N. Miyajima, D. Souza and F. Heidelbach)*

Dauphiné twinning occurs when high-temperature quartz (α-Qtz) transforms back to low-temperature quartz (β-Qtz) or α-Qtz is subjected to high shear stress. Dauphiné twins (DTs) are related to each other by a 2-fold symmetry operation about the [001] direction, this being the very symmetry lost when [001] transforms from a 6-fold to a 3-fold axis. The intergrowth of the transformation twins appears to have a symmetry equal to that of the high-temperature form. Origin and role of DTs in a naturally deformed Qtz affect the fabric development in plastic deformation. For the interpretation of quartz deformation mechanisms, it is important to identify DTs and slip systems with transmission electron microscopy (TEM). DTs are not visible in polarized light optical microscopy and conventional SEM. Dark-field (DF) TEM imaging is the best technique to investigate DTs at the nanoscale. However, DTs in deformed Qtz have not yet been unequivocally characterized in TEM due to the interference with high density of dislocations and misoriented subgrain boundaries in DTs.

In the current project we successfully identified DTs in a deformed Qtz by electron channelling contrast imaging (ECCI) in a field emission scanning electron microscopy (FESEM) assisted with electron backscattering diffraction (EBSD). The DTs were then examined by using large-angle convergent-beam diffraction (LACBED) in TEM. TEM foils were prepared from Dauphiné twin boundaries (DTBs) characterized by ECCI, by using the site-specific focused ion beam (FIB) sampling. The DF-TEM images with diffraction vectors of rhombohedral planes, *e.g.*, $\boldsymbol{g} = 30\bar{3}1$ revealed that the twin domains have different patterns of the thickness contour fringes reflected with the differences of the structure factors of negative and positive rhombohedral planes in the electron diffraction at 200 kV acceleration voltage (Fig. 3.3-19 left). The LACBED pattern from the boundary indicates no mis-orientation between the twin domains (Fig. 3.3-19 right). These results support that the different ECCI contrasts from the twin domains do not originate from the mis-orientation across the DTBs but from the differences of the structure factors of positive and negative rhombohedral planes in electron diffraction at 20 kV in FESEM. The visualization mechanisms of DTs in Qtz with ECCI, for the first time, are clarified by LACBED analysis in TEM. Combining ECCI and FIB milling techniques to prepare site-specific TEM foils provide a robust approach to investigate DTs in Qtz at the nanoscale.

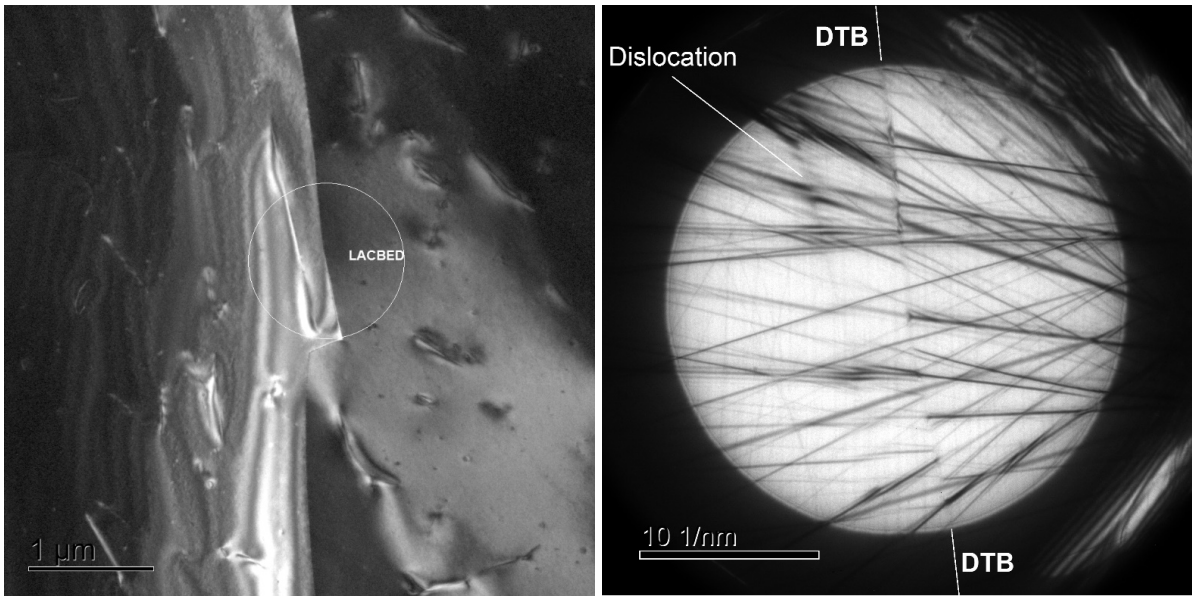

Fig. 3.3-19 left: Dark-field micrograph of a Dauphiné twin boundary (**g** = $30\bar{3}1$). The white circle indicates the area of LACBED on the right showing the effect of Dauphiné twin boundary (DTB). Some Bragg lines are not affected by the boundary, while some other lines disappear or undergo a visible change of intensity at the boundary.

o. *Implications of chemically induced stresses in the mechanisms of element exchange between minerals – an experimental study based on pyroxenes (J. Primocerio, S. Chakraborty and T. Fockenberg/Bochum, K. Marquardt)*

Exchange of elements or isotopes between minerals forms the basis of geothermometry and other applications of element partitioning. In the absence of direct observations, it has been implicitly assumed that purely diffusive exchange between contacting mineral phases allows grains of two minerals to attain the equilibrium compositions at any given condition. Recent advances in experimental and analytical methods allow the exchange process to be tracked as crystals evolve from the initial to the equilibrium state. In this study we want to determine the process of exchange of Fe, Mg and Ca in the system of pyroxenes by using ortho- and clinopyroxene pairs. Our experimental results reveal a multi-step process involving recrystallization to minimize defect concentrations coupled with diffusion and grain growth.

We used mixtures of pre-synthesized crystals of opx and cpx with different Fe/Mg ratios as starting materials. Syntheses were carried out in a gas mixing furnace (1000-1250 °C, fO_2 ~ IW+1) or in a piston cylinder apparatus (15 kbar, 1200 °C, graphite capsule). Exchange experiments were performed at 1 bar, 1000-1200 °C (fO_2 ~ IW+1) in a gas mixing furnace with variable durations and in a piston cylinder apparatus at 15 kbar and 900-1200 °C in multi-chamber graphite capsules. Starting materials and run products were characterized using X-ray diffraction (XRD), electron microprobe (EMP) and transmission electron microscopy (TEM) analysis of foils produced by focused ion beam (FIB) thinning.

In our experiments, grains equilibrate stepwise along two different paths, depending on whether the T-X combination crosses the pyroxene miscibility gap or is located outside it (Fig. 3.3-20). Different stages of evolution toward equilibrium are observed in a single sample (Fig. 3.3-21). Grains with initial compositions usually have a high density of dislocations. Furthermore, lamellae and pores are related to chemically induced stresses during element partitioning. This process is repeated until grains with final equilibrium compositions (unzoned or only weakly zoned), and usually with low defect densities, are obtained. This stage is followed by pure grain growth.

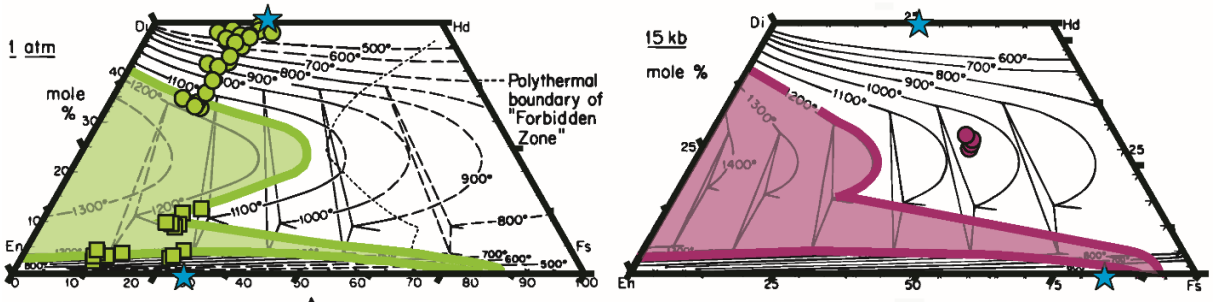

Fig. 3.3-20: Analytical points from two different experiments with appropriate starting compositions (blue star); green: 1 bar, 1150 °C, 120 h; red: 15 kbar, 1200 °C, 168 h; coloured areas represent appropriative miscibility gaps; circles show pyroxenes with high Ca-content and squares low Ca-content; miscibility gaps drawn after literature data.

Inferences based on the observation of the final frozen compositions without an understanding of the underlying mechanism of element exchange may lead to incorrect interpretations of temperatures from geothermometry or timescales from diffusion modelling.

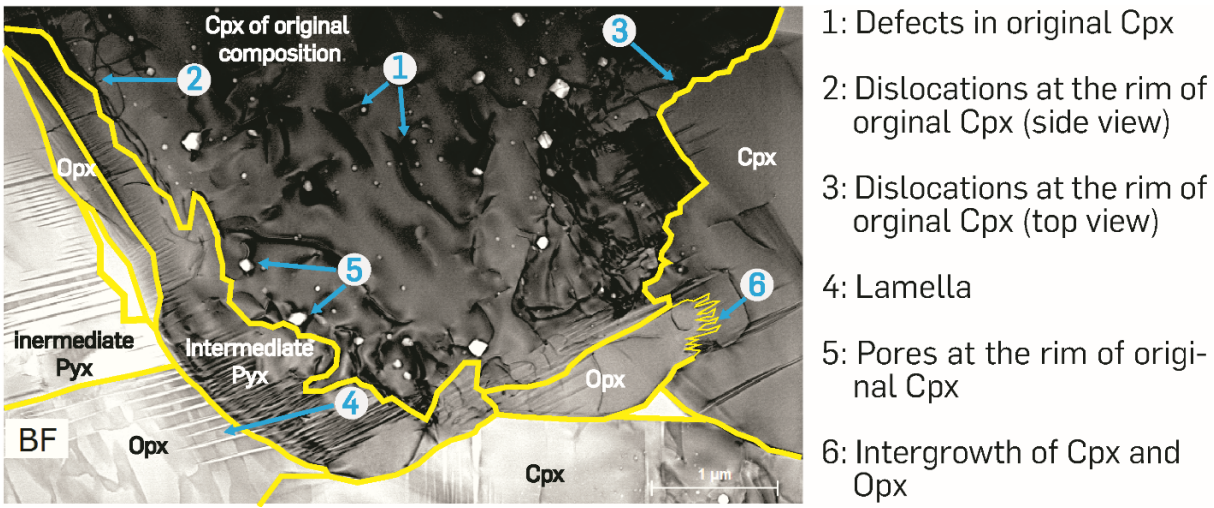

Fig. 3.3-21: BF-image (TEM) of the same experiment shown in Fig. 3.3-20 (left side); yellow lines represent grain boundaries, blue arrows show different structural features which are described in the legend on the right of the figure.

3.4 Physical Properties of Minerals

Sound waves passing through Earth's deep interior provide key data for mineral physics, since seismic observations are a primary tool for constraining the thermochemical structure of Earth's interior. Seismic wave velocities depend on the elastic moduli and density of materials through which waves propagate. Both properties depend in turn on the crystal structure and chemical composition of constituent minerals as well as on pressure and temperature. Elastic moduli further depend on crystal orientation. Measurement of lattice thermal conductivity of minerals is a complementary probe for investigating heat transport in the vast yet inaccessible interior of our planet. Magnetic and electronic properties of materials at high pressure (and high temperature) are useful for investigating magnetism in planetary cores and phase stability in rocky super-Earths as well as superconductivity at high temperatures, all of which can only be understood through experiments at extreme conditions or by computational studies.

The first four contributions describe investigations of the dependence of seismic wave velocity on cation substitution in solid solutions of bridgmanite, akimotoite, and dense hydrous magnesium silicates. Experiments that directly constrain wave velocities were conducted using either laser light (Brillouin scattering) or ultrasonic sound waves with simultaneous density measurements as a function of pressure (and temperature). Combination of velocities with precise density data from single-crystal X-ray diffraction yields elastic moduli that can be compared with seismic observations. The first direct constraint on the compressional velocity of $MgSiO_3$ bridgmanite at pressures of the deep lower mantle shows that sound velocities of a simplified, Al-free peridotite composition matches the preliminary Earth reference model (PREM) within 1 %. Properties of akimotoite, the most anisotropic mineral in the transition zone, can explain anisotropic features of seismic observations of harzburgite-rich slab material. The formation of Fe- and Al-bearing akimotoite in a harzburgitic lithology increases bulk compressional and shear wave velocities to match those of PREM at the base of the transition zone. However, Al-Fe substitution in phase H [$MgSiO_2(OH)_2$] has only a weak effect on components of the elastic stiffness tensor at ambient conditions.

The next two contributions focus on lattice thermal conductivity of hydrous ringwoodite and compressibility of Fe-bearing calcium aluminates. The incorporation of water in ringwoodite reduces thermal conductivity significantly at mantle transition zone pressures compared to a nominally dry sample and shows how water can be preserved in subducting slab cores, allowing hydrated minerals to reach the lower mantle. The stability of calcium aluminates at high pressures reveals potential carriers of aluminium to the deep mantle.

The final four contributions highlight magnetic and electronic properties at high pressure. A combined magnetic remanence and Mössbauer study of an Invar alloy at high pressure reveals conditions under which magnetism is lost and may resolve controversies regarding Invar alloy behaviour. Density functional theory-based lattice dynamics calculations with the stochastic self-consistent harmonic approximation show improved calculation of the B1-B2 phase transition in MgO at extreme conditions of planetary interiors, and provide insight into phase

transitions in the $MgSiO_3$ post-perovskite breakdown sequence. The combination of high-pressure nuclear magnetic resonance measurements and *ab initio* calculations overcomes challenges of investigating electronic properties of hydrogen atoms at extreme conditions and shines light on superconducting transition temperatures in hydrogen-rich metal hydrides. Finally, measurements conducted in a dynamic diamond anvil cell resolve order-disorder transitions in ice that may play a significant role in the evolution of ice giant planets.

a. *Sound wave velocities in Earth's mid-lower mantle (G. Criniti, A. Kurnosov, T. Boffa Ballaran and D.J. Frost)*

Seismic observations are a primary tool for constraining the thermochemical structure of Earth's interior. However, lack of experimental studies on the compressional and shear wave velocities of lower mantle minerals at high pressure and temperature limits the resolution of mineral physics models that are essential for interpreting seismological data. Here, the single-crystal elastic tensor (c_{ij}) of $MgSiO_3$ bridgmanite, the most abundant mineral of the lower mantle, was determined using Brillouin spectroscopy and single crystal X-ray diffraction in a diamond anvil cell (DAC) up to 78 GPa.

Two crystals of $MgSiO_3$ bridgmanite with different orientations, one each parallel to (*100*) and (*011*), were loaded into the same DAC for measurements up to 30 GPa using Ne as a pressure transmitting medium. For measurements at higher pressure, the two crystals were loaded in two individual DACs and He was used as a pressure medium. In order to determine the compressional velocity (v_P) of both crystals at high pressure, the in-plane orientation of the platelets was carefully chosen. In particular, the maximum of v_P in the (*100*) plane was matched with the minimum of the shear wave velocity (v_S) of diamond, while the minimum of v_P in the (*011*) plane was matched with the maximum of v_S of diamond. In this way, we predicted that v_P in the (*100*) plane would be visible at approximately 50 GPa at higher frequency than diamond v_S, while v_P in the (*011*) plane would still be visible at pressures in excess of 30 GPa at lower frequency than diamond v_S. The crossover between the diamond v_S and v_P in the (*100*) plane was observed at 55 GPa (Fig. 3.4-1), providing the first direct constraint on v_P of $MgSiO_3$ bridgmanite at pressures corresponding to the deep lower mantle.

Using a global fit of all elasticity data, the c_{ij} values, the bulk and shear moduli as well as aggregate velocities were computed as a function of pressure. The elastic moduli at ambient conditions are consistent with previous studies, while the pressure derivatives of adiabatic bulk and shear moduli are respectively smaller and larger than previously reported. Our results can be used to update already existing internally consistent thermodynamic databases and compute sound wave velocities of candidate mantle rocks at pressures and temperatures of Earth's lower mantle. For instance, it is seen that for a simplified, Al-free peridotite composition (80 % bridgmanite, 13 % ferropericlase, 7 % Ca-perovskite) along an adiabatic temperature profile, the deviation from the preliminary Earth reference model is always smaller than 1 % in compressional and shear wave velocities throughout the entire lower mantle.

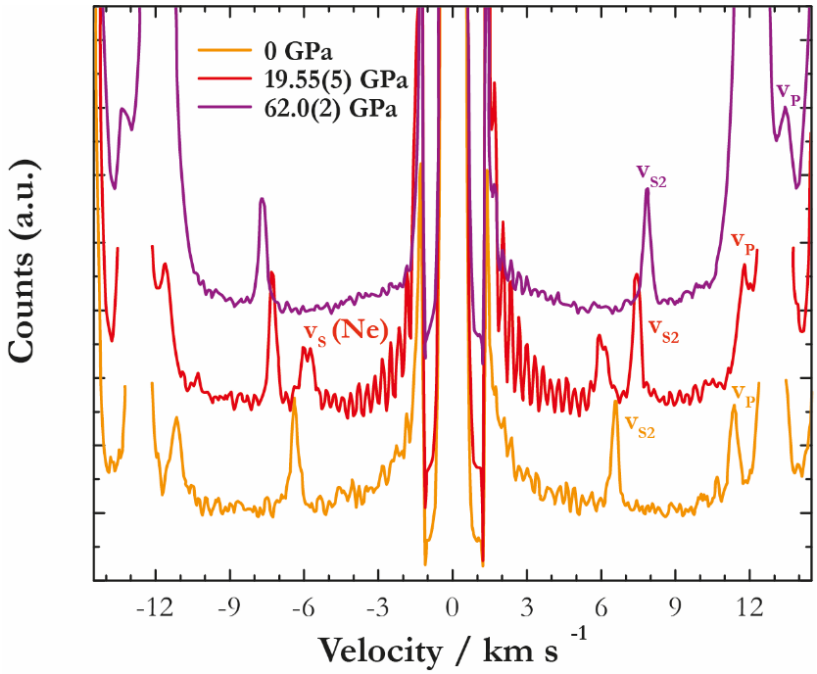

Fig. 3.4-1: Pressure evolution of Brillouin spectra of a platelet of $MgSiO_3$ bridgmanite cut parallel to (*100*). At ambient conditions the maximum of v_P of bridgmanite is still slower than v_S of diamond (orange line). With increasing pressure, v_P of bridgmanite starts to overlap with v_S of diamond and eventually disappears (red line). At pressures exceeding 55 GPa, a crossover between the two peaks occurs and v_P of bridgmanite becomes visible again at higher velocity relative to diamond (purple line).

b. *Wave velocities and anisotropic behaviour of $MgSiO_3$ akimotoite at transition zone pressures (N.C. Siersch, A. Kurnosov, G. Criniti, T. Boffa Ballaran, T. Ishii and D.J. Frost)*

Akimotoite is a high-pressure $MgSiO_3$ polymorph that replaces garnet at the base of the transition zone, particularly in subducting slabs, where temperatures are lower than the average mantle geotherm, and in Al-poor harzburgitic protoliths. The presence of akimotoite in the mantle might provide an explanation as to why seismic wave velocities are faster at the base of the transition zone than can be accounted for with a typical mantle peridotite assemblage which is not expected to contain akimotoite. Its presence may also explain anisotropic features and multiple discontinuities that occur near 660 km depth. The elastic properties of akimotoite have been studied previously using ultrasonic interferometry and indeed were found to increase the modelled wave velocities when incorporated in the mineralogical models of the transition zone. However, in order to interpret the anisotropy observed at the base of the mantle transition zone knowledge of the full elastic tensor at high pressure is needed.

High-quality single-crystals of $MgSiO_3$ akimotoite were synthesised in the multianvil apparatus at 22 GPa and 1500 °C. Three single crystals were oriented, double-sided polished and cut into half-circles that were loaded together into a diamond anvil cell and pressurised under quasi-

hydrostatic conditions using neon as pressure-transmitting medium. In order to investigate the full elastic tensor of $MgSiO_3$ akimotoite, Brillouin spectroscopy measurements in combination with single-crystal X-ray diffraction were conducted at eleven pressure points up to 25 GPa, *i.e.*, to pressures at the base of Earth's transition zone.

Knowledge of the elastic tensor and density of akimotoite allows the determination of the elastic properties, *e.g.*, bulk and shear moduli and consequently the compressional and shear wave velocities at each pressure point. Moreover, the absolute pressure inside the diamond anvil cell can be obtained without having to rely on a secondary pressure gauge such as ruby. The compressional wave velocities obtained from previous ultrasonic measurements performed on polycrystalline akimotoite are slightly faster than the aggregate wave velocities determined in this study and have a much steeper slope with pressure, whereas the aggregate shear wave velocities, v_S, are in very good agreement between both acoustic velocity methods.

The anisotropic behaviour of akimotoite can be determined from the full elastic tensor. The velocity distribution for $MgSiO_3$ akimotoite at 25 GPa shows that the fastest wave velocities do not follow any specific direction along the crystallographic axes of akimotoite, and only the slowest v_{S2} travels along the *c*-axis. Both the compressional wave anisotropy, v_P, and the S-wave polarisation anisotropy were found to decrease with pressure (Fig. 3.4-2); however, both are still significant in comparison to lower transition zone minerals such as ringwoodite and majoritic garnet. Akimotoite, being the most anisotropic mineral in the transition zone, can therefore explain observations of seismic anisotropy and may imply the presence of harzburgite-rich subducted lithosphere.

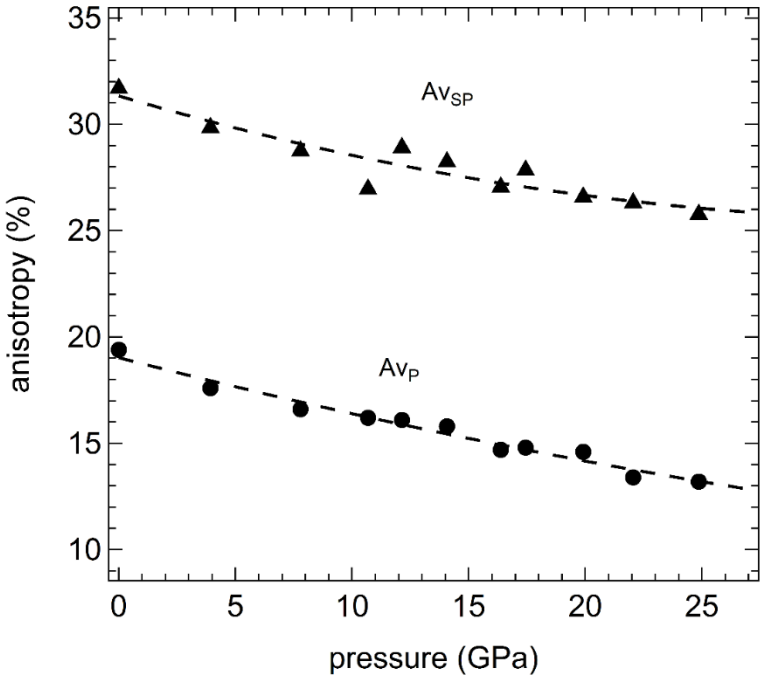

Fig. 3.4-2: Gradual decrease of P-wave anisotropy and S-wave polarisation anisotropy of $MgSiO_3$ akimotoite with increasing pressure.

c. *Effect of Fe- and Al-bearing akimotoite on seismic wave velocities of harzburgite at transition zone pressures (N.C. Siersch, T. Boffa Ballaran, Z. Liu, T. Ishii, D.J. Frost and T. Katsura, in collaboration with Y. Wang and T. Yu/Argonne)*

Akimotoite is a $MgSiO_3$ polymorph with a limited stability field in fertile peridotite compositions, but it has been synthesised from harzburgitic compositions at conditions of the lower transition zone. Faster compressional and shear wave velocities observed in end-member $MgSiO_3$ akimotoite (this Annual Report) suggest that the presence of akimotoite may improve agreement with seismic reference models between 600 and 660 km depth, where mineralogical models excluding the presence of this mineral give velocities that are too slow. Harzburgitic compositions also contain Fe and Al, which can substitute into the akimotoite structure and affect its elastic properties. In this study we report acoustic wave velocities of Fe-bearing akimotoite, construct a thermodynamic model to determine the proportion of akimotoite in a harzburgitic composition at transition zone conditions, and estimate densities and seismic wave velocities at these depths.

Akimotoite containing 10 mol. % $FeSiO_3$ was synthesised at 25 GPa and 850 °C for 1 hour in the IRIS-15 multianvil apparatus installed at BGI. The recovered sample was carefully analysed using a micro-focus X-ray diffractometer equipped with a Co tube (λ= 1.79026 Å) to confirm the formation of pure akimotoite. Grain size and chemical composition were further analysed using the scanning electron microscope and the electron microprobe. Ultrasonic experiments were performed on a polished sample with perfectly parallel faces inside a modified 10/4 assembly equipped with a Re foil heater with laser cut windows. This allows the *in situ* measurement of akimotoite density using synchrotron X-ray diffraction and of sample length using X-ray radiography. A piezoelectric $LiNbO_3$ transducer was glued with epoxy onto a truncation of an TF05 WC anvil polished to mirror quality in order to produce and detect P- and S-waves simultaneously. Compressional and shear wave velocities of Fe-bearing akimotoite were collected up to 27 GPa and 800 K at the 13 ID-D beam line of the Advanced Photon Source using an ultrasonic system.

The incorporation of Fe into the akimotoite structure reduces both compressional and shear wave velocities relative to the $MgSiO_3$ akimotoite end-member. The elastic properties of fictive $FeSiO_3$ and Al_2O_3 akimotoite end-members were refined by fitting simultaneously the wave velocities of the $MgSiO_3$ akimotoite end-member determined by Brillouin spectroscopy (see this Annual Report), of Al-bearing akimotoites determined in a previous study (see BGI Annual Report 2018) and of Fe-bearing akimotoite investigated in this study. The resulting elastic properties of the fictive end-members were then used to determine the mineral proportions in a harzburgitic composition at pressures of the basal transition zone along a mantle adiabat. It was then possible to calculate the compressional and shear wave velocities of harzburgite and compare them to those of seismic reference models (Fig. 3.4-3). The mineral model shows that formation of Fe- and Al-bearing akimotoite in a harzburgitic lithology increases bulk compressional and shear wave velocities to match those of the seismic reference models at the base of the transition zone. The presence of a harzburgitic layer on top of the 660 km

discontinuity is plausible on a regional scale due to stagnation of subducting lithospheric mantle as shown by tomographic models. Furthermore, the garnet-akimotoite transition was found to occur over a narrow depth range (~ 24 km) potentially explaining shallower discontinuities compared to the global 660 km-discontinuity found in subduction zone settings between 610-640 km depth.

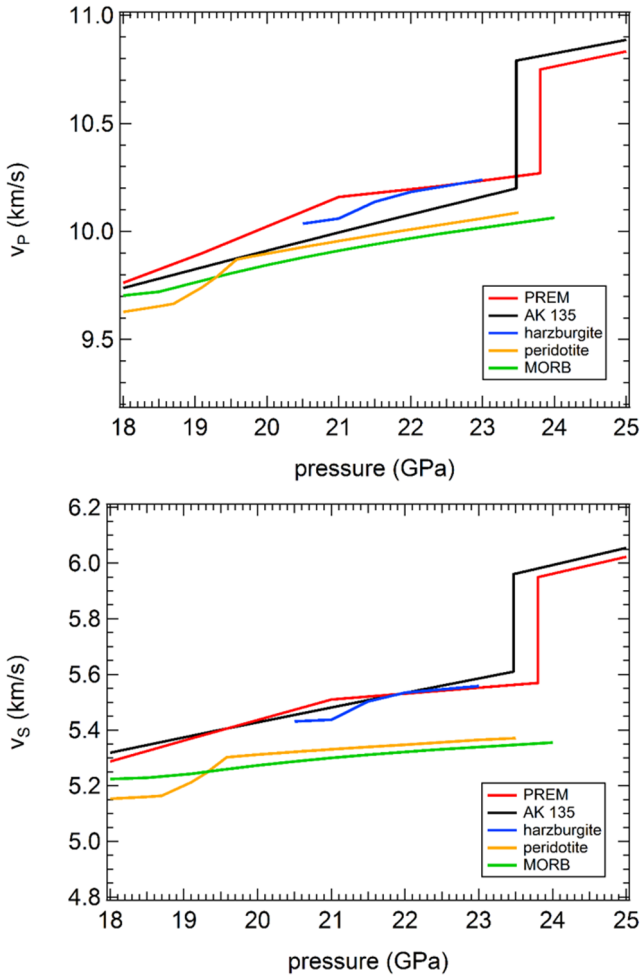

Fig. 3.4-3: Calculated wave velocities of harzburgite, containing Fe- and Al-bearing akimotoite compared with with peridotite and MORB lithologies. Calculations assume a mantle adiabat at lower transition zone conditions and are compared with seismic reference models. The formation of akimotoite from majoritic garnet causes a strong change in the slope of seismic wave velocity with pressure, which might potentially be detected as a discontinuity.

d. *Effect of Al-Fe substitution on the elastic properties of δ-(Al,Fe)OOH (N. Satta, G. Criniti, T. Ishii, A. Kurnosov, T. Boffa Ballaran, J. Buchen/Pasadena and H. Marquardt/Oxford)*

Earth's deep water cycle potentially plays a pivotal role in the dynamic evolution of our planet. The input of water into Earth's interior is controlled by subduction of hydrated oceanic lithosphere. Experimental investigations have revealed that dense hydrous magnesium silicates (DHMS) are efficient hosts of water in large parts of Earth's mantle, ranging from the upper mantle to the core-mantle boundary. In particular, solid solutions between δ-AlOOH, ε-FeOOH and phase H [$MgSiO_2(OH)_2$] are thought to be integral to stabilising water reservoirs in the deep mantle. Exploring elasticity of members of the δ-AlOOH - ε-FeOOH - $MgSiO_2(OH)_2$ solid solution is crucial to mapping water in Earth's lower mantle through interpretation of seismological observations. The high-pressure elastic properties of δ-(Al,Fe)OOH remain

largely unknown, and in particular the full elastic tensor of δ-(Al,Fe)OOH has not yet been determined.

In this study, we investigated the single-crystal elastic properties of two different members of the δ-(Al,Fe)OOH solid solution by Brillouin spectroscopy and X-ray diffraction. δ-($Al_{0.97}$,$Fe_{0.03}$)OOH and δ-($Al_{0.94}$,$Fe_{0.06}$)OOH single crystals were synthesised in a multianvil apparatus and characterised by electron microprobe, Mössbauer spectroscopy and single-crystal X-ray diffraction. Optically clear crystals were selected, double-side polished and investigated with Brillouin spectroscopy at ambient conditions, providing the first experimental elastic stiffness tensor for δ-(Al,Fe)OOH solid solutions. Our results show that Al-Fe substitution has a weak effect on the components of the elastic stiffness tensor at ambient condition (Fig. 3.4-4). Future experiments will explore elastic properties of different members of the δ-(Al,Fe)OOH solid solution at high pressure.

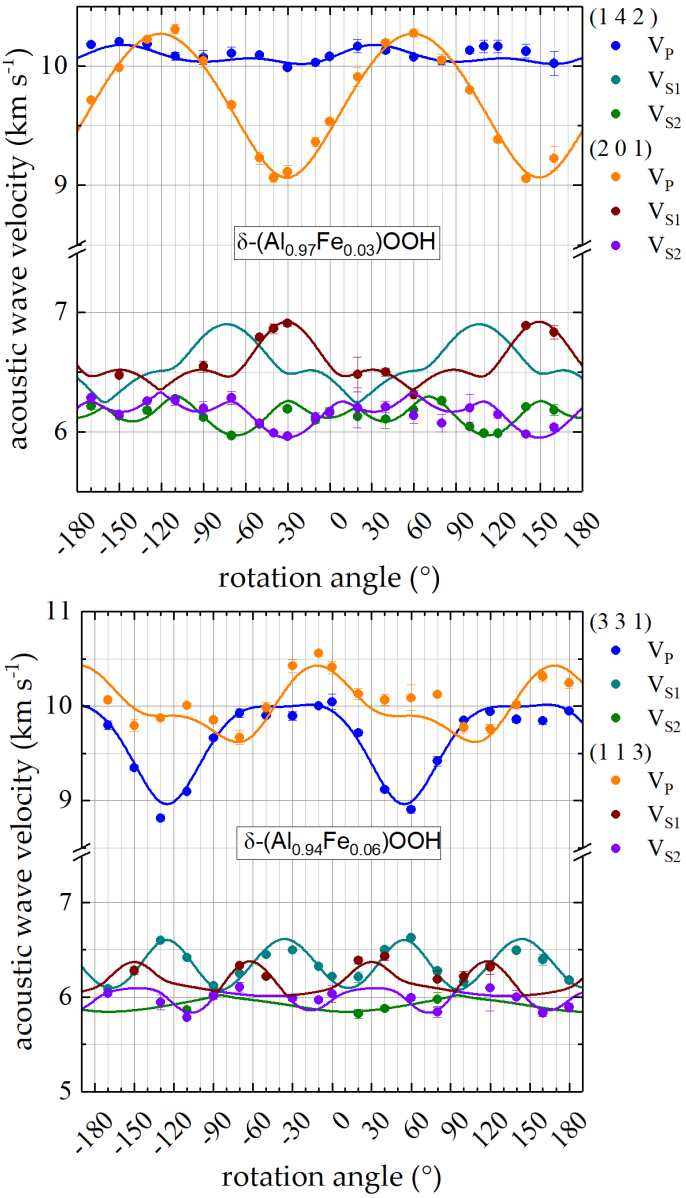

Fig. 3.4-4: Measured (circles) and calculated (curves) acoustic wave velocities as a function of rotation angle for the two investigated δ-(Al,Fe)OOH compositions.

e. *Effect of water on lattice thermal conductivity in ringwoodite and implications for thermal evolution of stagnant slabs (E. Marzotto, W.-P. Hsieh/Taipei, T. Ishii, K.-H. Chao/Honolulu, G.J. Golabek, M. Thielmann and E. Ohtani/Sendai)*

Measurements of lattice thermal conductivity, Λ, are fundamental to constraining the thermal state of cold slabs that stagnate in the mantle transition zone (MTZ). Since the oceanic lithosphere is mainly composed of depleted mantle (20-100 km thickness), the most abundant minerals in the slab are olivine or its high-pressure polymorphs. Ringwoodite is the olivine high-pressure polymorph that is stable in the lower MTZ (17-25 GPa). Moreover, it has been shown that ringwoodite can store up to 2-3 wt. % water in its structure. The presence of water in the crystal lattice might reduce Λ, thus helping to maintain a cold slab core. This mechanism could preserve water in the slab core, allowing hydrated minerals to reach the lower mantle.

In our study we combined diamond anvil cell (DAC) experiments with time-domain thermo-reflectance (TDTR) measurements in order to study the thermal conductivity, Λ_{Rw}, of ringwoodite samples with different water contents. Ringwoodite samples were synthesised starting from San Carlos olivine powder using a multianvil apparatus with a 4/10 assembly. Distilled water (3-10 wt. %) was added in order to grow hydrous crystals. Fourier-transform infrared spectroscopy measurements showed that the synthesised samples contained approximately 1100, 4700, and 17 300 ppm of water.

Each sample was coated with a ~ 90 nm thick Al film as a thermal transducer for TDTR measurements. Crystals were loaded into a DAC, along with a ruby sphere for pressure determination. We employed diamonds with 400 µm culet diameter, a Re gasket, and silicone oil as the pressure medium. Measurements were performed at room temperature and high pressure up to 25 GPa. The incorporation of 17300 ppm (1.73 wt. %) water in ringwoodite results in a ~ 40 % reduction of the thermal conductivity at MTZ pressures, with respect to the nominally dry sample (1100 ppm) (Fig. 3.4-5).

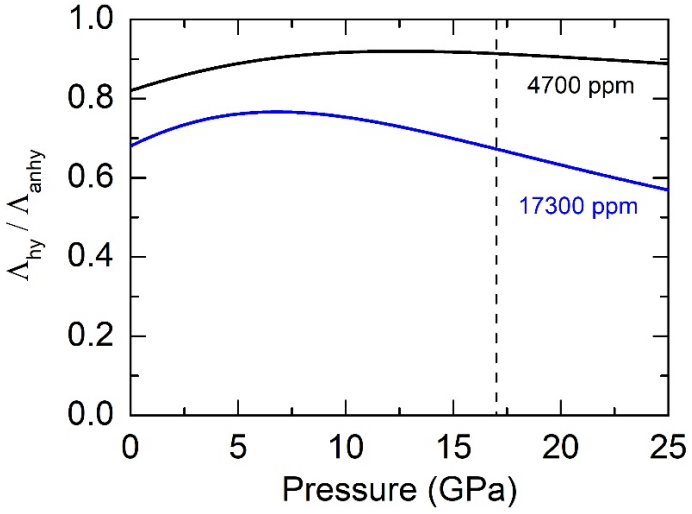

Fig. 3.4-5: Effect of pressure on lattice thermal conductivity of ringwoodite with water contents of 17 300 ppm (blue curve) and 4700 ppm (black curve). $\Lambda_{hy}/\Lambda_{anhy}$ was obtained by taking the ratio of the parameterised curves obtained from our measurements. The uncertainties are typically 10-15 %. The vertical dashed line indicates the pressure range where ringwoodite becomes stable (17 GPa).

f. *Synthesis, crystal structure and equation of state of calcium aluminates at conditions of Earth's transition zone and lower mantle (A. Iskrina/Moscow, A. Spivak/Chernogolovka, A. Bobrov, N. Eremin and E. Marchenko/Moscow, L.S. Dubrovinsky)*

In Earth's crust aluminium is the most abundant metal and the third most abundant element after oxygen and silicon. The concentration of aluminium, according to various researchers, reaches 16.4 wt. % in Earth's crust. Many scientists assume that aluminates with calcium-ferrite type of structure may host aluminium under conditions of Earth's transition zone and lower mantle. Such Ca-aluminates, which may include cations such as Fe, Mg, Na, influence phase relations in the $CaO–Al_2O_3$ system. It is therefore important to investigate this system and determine phase transitions and the presence of solid solutions between different aluminates under high-pressure and high-temperature conditions.

Experiments were carried out on a 1200-t multianvil apparatus at pressures of 15, 20 and 24 GPa, temperatures of 1100, 1500 and 1600 °C, and run times of one to 1.5 hours. Run products were investigated by optical microscopy, scanning electron microscopy, Raman spectroscopy and microprobe analysis. Crystal structures were identified using single crystal X-ray diffraction. We synthesised $Ca(Al,Fe)_2O_4$ (*Pnma*) and also a new phase $Mg(Al,Cr)_2O_4$ (*Cmcm*) (Fig. 3.4-6). In the former structure, the position of the Ca atom in the tunnel is centred but slightly rotated to nearby tunnels, while in the latter structure with a centred cell, the positions

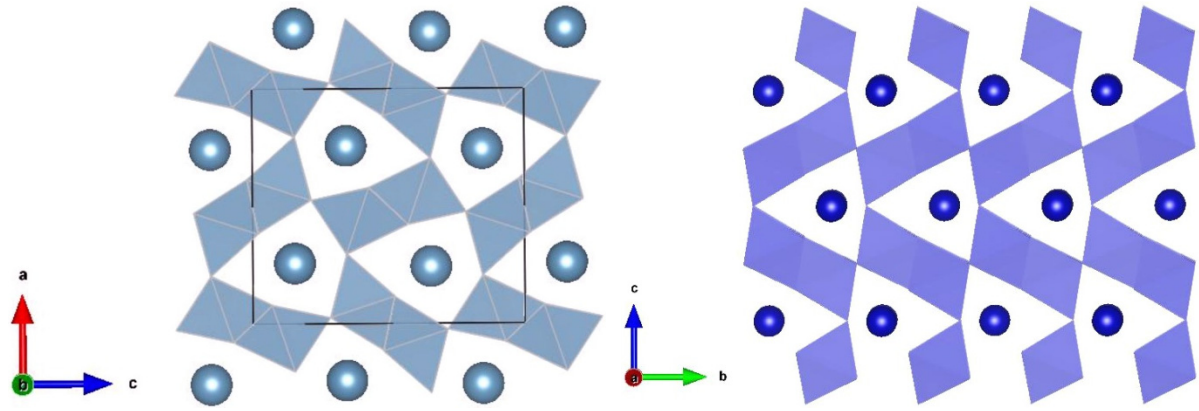

Fig. 3.4-6: Crystal structure of $Ca(Al,Fe)_2O_4$ (left) and $Mg(Al,Cr)_2O_4$ (right).

of the central atoms are aligned. We compressed $Ca(Al,Fe)_2O_4$ stepwise in a diamond anvil cell to ~ 60 GPa and measured the sample using synchrotron radiation (Fig. 3.4-7). No phase transformations were detected in this pressure range except for a spin transition of iron. Our results suggest that both phases that we studied are stable in Earth's transition zone and can be considered to be potential aluminium carriers in the deep mantle.

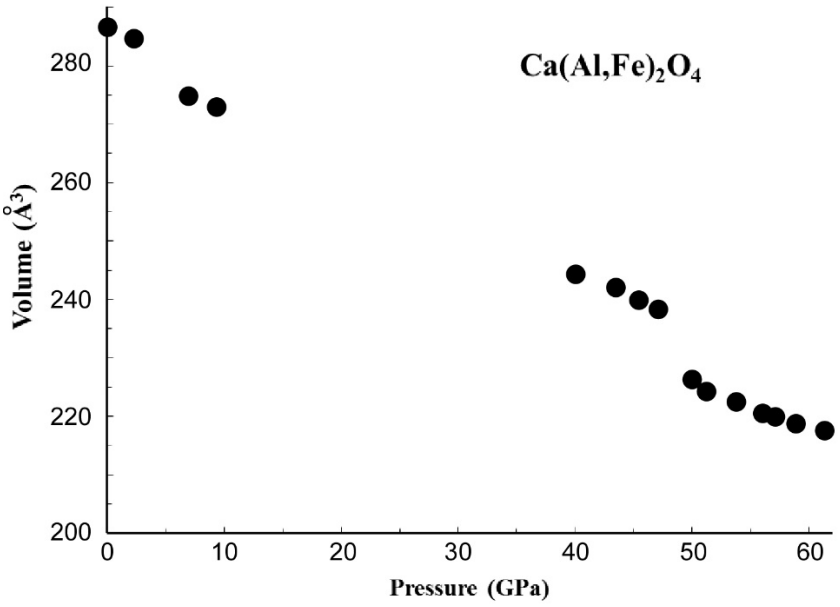

Fig. 3.4-7: Effect of pressure on the unit cell volume of $Ca(Al,Fe)_2O_4$.

g. *Magnetic properties of iron-nickel alloys at high pressure (C.A. McCammon, in collaboration with Q. Wei and S. Gilder/Munich)*

Iron-nickel alloys have been a subject of fascination since 1897 when Charles Edouard Guillaume discovered the near zero thermal expansion of alloys with composition around 36 mol. % nickel. These Invar ("invariable") alloys have many further anomalous properties, all linked primarily to ferromagnetism. Invar compositions may also be found in planetary cores, which may impact planetary magnetism. Despite numerous decades of research, however, many controversies regarding the properties of Invar alloys persist, including the conditions under which magnetism is lost. To address this particular controversy, we undertook a combined magnetic remanence and Mössbauer study of an Invar alloy at high pressure.

We synthesised polycrystalline $^{57}Fe_{62}Ni_{38}$ with *fcc* structure in a one atmosphere gas-controlled furnace. Sample powder was loaded into a Merrill-Bassett-type diamond anvil cell with silica gel as pressure medium and ruby for pressure calibration. We collected high-pressure Mössbauer spectra using a nominal 370 MBq ^{57}Co point source mounted on a spectrometer operating in transmission mode. In parallel the same sample was used to acquire isothermal remanent magnetization at room temperature using a three-axis, superconducting quantum interference device magnetometer in a magnetically shielded room situated in a forest near Landshut, Germany.

Mössbauer spectra of $Fe_{62}Ni_{38}$ collected during stepwise decompression from 20 GPa to room pressure show a clear loss of magnetism (Fig. 3.4-8). Good fits to spectra can be obtained with the traditional approach using a magnetic field distribution, and show that the mean hyperfine

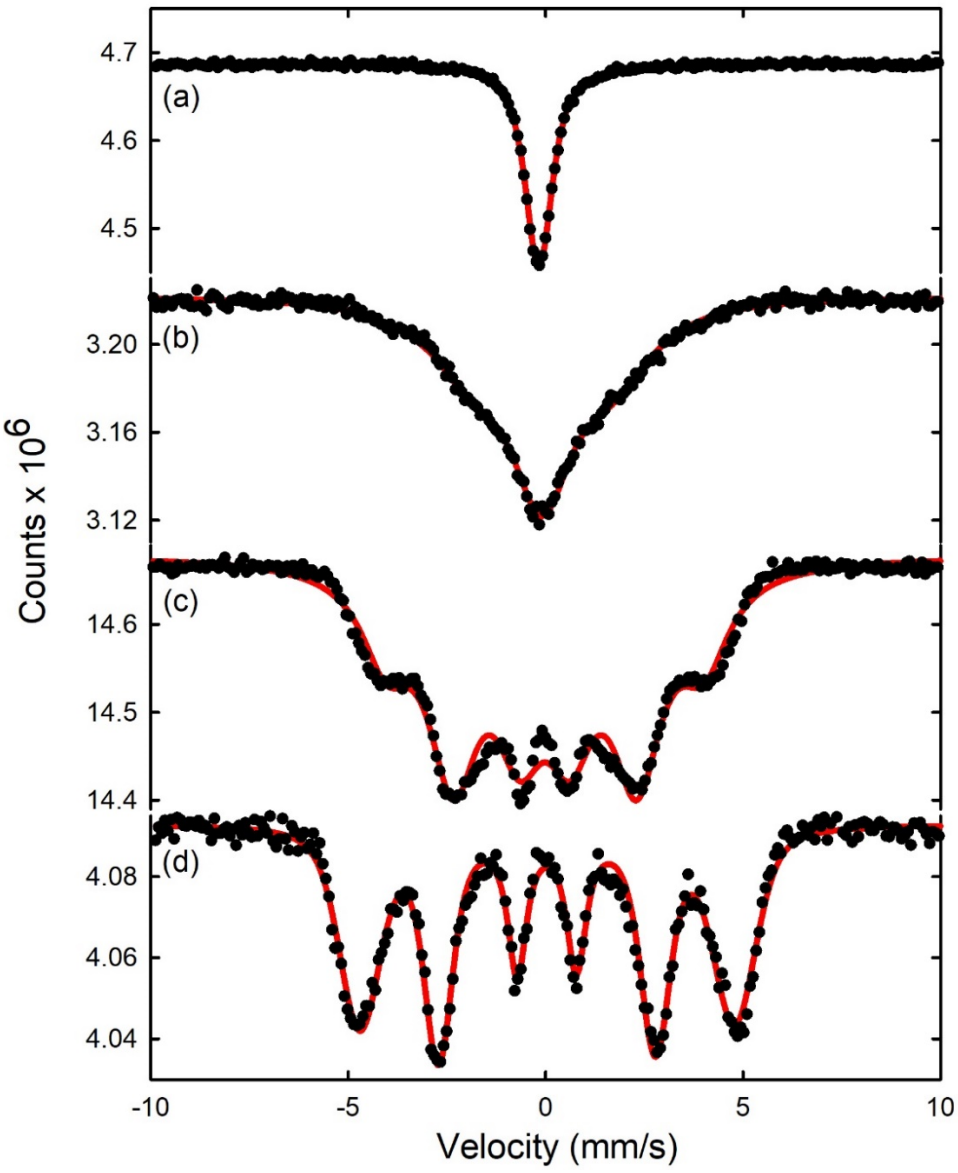

Fig. 3.4-8: Room temperature Mössbauer spectra of $Fe_{62}Ni_{38}$ at (a) 20.3 GPa, (b) 7.7 GPa, (c) 4.4 GPa, (d) 0 GPa. Red lines indicate fits with one subspectrum each: (a) singlet, (b and c) sextet with fluctuating magnetic field, (d) sextet with static magnetic field distribution.

magnetic field decreases rapidly with increasing pressure (grey data points in Fig. 3.4-9). However the implied loss of magnetism between 10 and 15 GPa is inconsistent with our magnetic remanence data that show ferromagnetism to at least 16 GPa. If we instead fit Mössbauer spectra using a simple model proposed many years ago where the magnetic hyperfine field flips with a frequency comparable to the Mössbauer timescale (~ 10^{-8} s), we obtain equally good fits to the Mössbauer spectra (Fig. 3.4-8) and a hyperfine field decrease with pressure (red data points in Fig. 3.4-9) that is consistent with magnetic remanence data (blue region in Fig. 3.4-9). More detailed comparison of Mössbauer and magnetic remanence data is underway to resolve further controversies regarding Invar alloy behaviour.

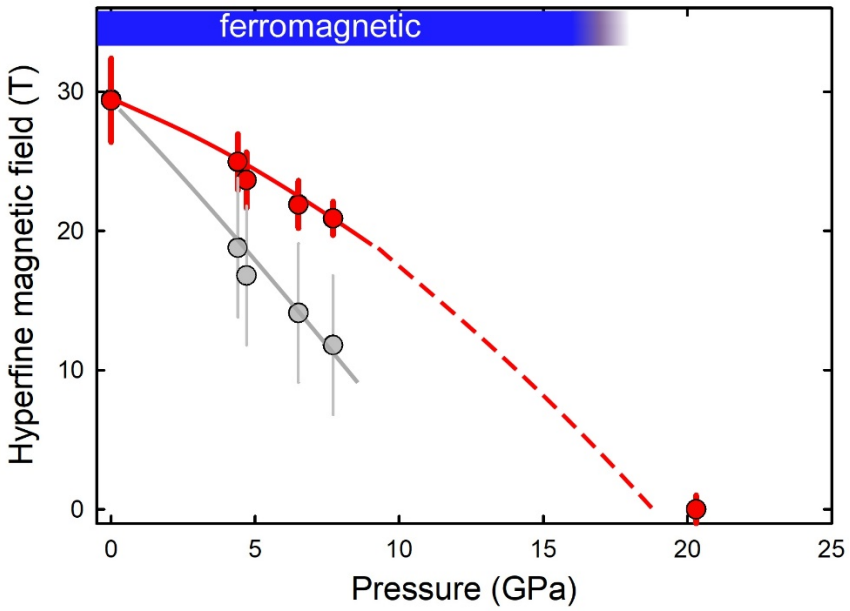

Fig. 3.4-9: Pressure variation of hyperfine magnetic field of $Fe_{62}Ni_{38}$ at room temperature. Data from Mössbauer fits based on a magnetic field distribution are shown in grey, while fits based on a fluctuating magnetic field are shown in red. The trend shown by the red dashed line is consistent with ferromagnetic behaviour to at least 16 GPa seen in magnetic remanence measurements (blue shaded region). Solid lines are guides for the eye.

h. *Anharmonic stabilisation of B2-MgO (F. Trybel, I. Errea/Bilbao, D. Adams/Bern, M. Wenz/Evanston, L. Monacelli/Rome, S. Churakov/Bern, M. Calandra/Paris, F. Mauri/Rome, R. Bianco/San Sebastián, D. Passerone/Dübendorf and G. Steinle-Neumann)*

The explosive growth in astronomical observations has revealed an unexpected variety of planetary bodies in the universe in terms of radius (R), mass (M), Love number k_2 and orbital parameters. In order to characterise these extrasolar planets, especially the M-R relations, it is necessary to investigate phase stability fields of material candidates under conditions significantly exceeding the temperature (T) and pressure (P) range of Earth's interior. We use density functional theory (DFT)-based lattice dynamics to predict phase stability fields and thermodynamic properties at the high P (> 1 TPa) and high-T (> 10000 K) conditions required for modelling planetary interiors. Results also provide a guide for experimental research, *e.g.*, newly established X-ray free electron laser (XFEL) facilities, including the high energy beamline of the European XFEL that recently went online.

An accurate prediction of phase transitions in the $MgSiO_3$ post-perovskite (*ppv*) breakdown sequence is of particular importance as it is expected to dominate the mineralogy of rocky super-Earths. At these extreme conditions the DFT extension to finite T via the quasi-harmonic representation does not describe the system to sufficient accuracy and phase stability fields cannot be predicted with confidence. Therefore, anharmonic vibrational corrections to the energy must be included in the calculations.

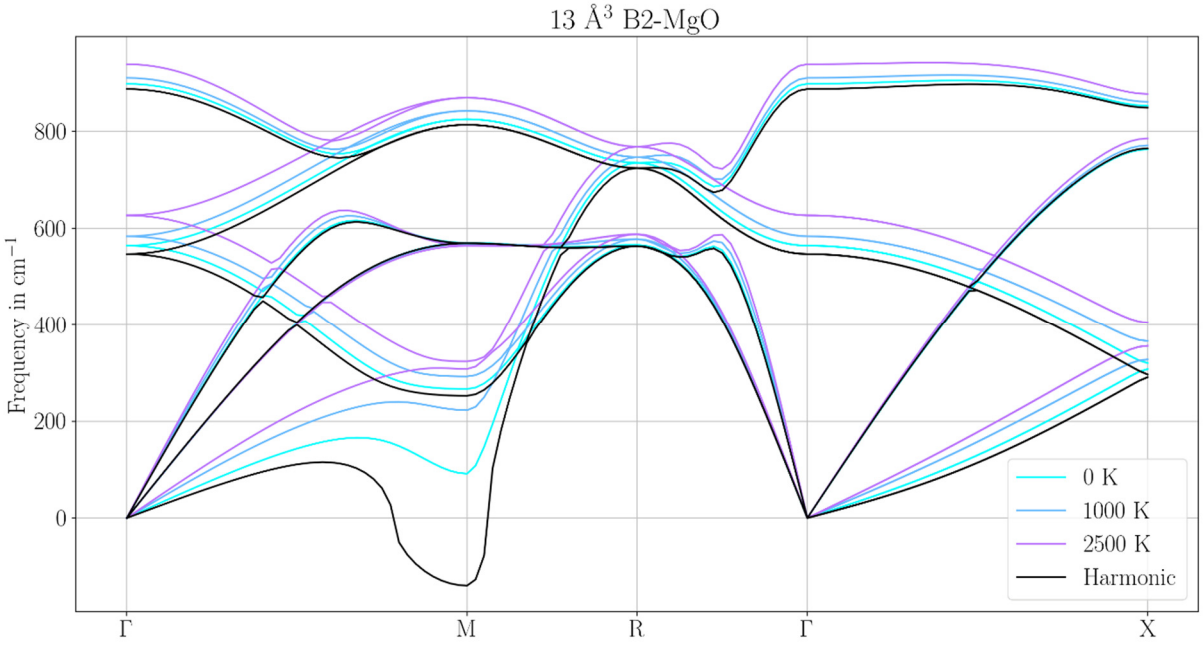

Fig. 3.4-10: Dispersion relation of B2-MgO. It was calculated at a primitive unit cell volume of 13 Å^3 as a function of temperature using the odd3 correction in SSCHA. The negative transverse acoustic mode at the M-point becomes positive when the anharmonic corrections to the zero-point energy are included and is furthermore stabilised with increasing temperature.

The B1-B2 phase transition in MgO can be used as a prototype within the breakdown sequence. The transition is especially interesting because the B2-phase is predicted to be dynamically unstable at primitive unit cell volumes (V) larger than 12 Å^3 (P < 120 GPa) in the quasi-harmonic approximation (Fig. 3.4-10), but may be stabilised by anharmonic effects. We used the stochastic self-consistent harmonic approximation (SSCHA) reported in the literature to include anharmonic corrections in our simulations. The method explores the Born-Oppenheimer energy surface for a given crystal structure to calculate an anharmonic correction to Helmholtz energy as a function of V and T. Calculating the phonon dispersion relation with the SSCHA correction, one can find stabilisation of the B2 phase up to a primitive unit cell V = 14 Å^3 with a remaining soft mode that is further stabilised with increasing temperature as shown in Fig. 3.4-10, providing a more reliable calculation of the B1-B2 phase transition, since additional V,T points increase the accuracy of the equation of state fit to the calculation results.

i. *Electronic properties of metal hydrides (T. Meier, F. Trybel, S. Khandarkhaeva, G. Steinle-Neumann, S. Chariton, G. Criniti, E. Koemets, T. Fedotenko/Bayreuth, S. Petitgirard/Zurich, M. Hanfland/Grenoble, K. Glazyrin/Hamburg, N.A. Dubrovinskaia/Bayreuth and L.S. Dubrovinsky)*

Recent discoveries of superconducting transition temperatures in hydrogen-rich metal hydrides in the range of 260 K sparked a gold rush in metal hydride research in the high-pressure solid-

state physics community. Figure 3.4-11 illustrates the timeline of discovery of several classes of superconductors from 1911 to the present day. Owing to the large number of hydrogen atoms per unit cell, very short H-H distances promote a dissociation of hydrogen molecules and the formation of an intercalating hydrogen sub-lattice. In theory, electron density from the parent metal atoms is transferred to the hydrogen sublattice under increasing pressure, triggering its metallisation. In combination with substantial electron-phonon coupling due to the small mass of the hydrogen atoms, this leads to extremely high superconducting transition temperatures, with Tcs predicted to be well above room temperature in the case of the super-hydride YH_{10}. Up to this point, however, experimental methods probing metal hydrides have been limited to either a structural investigation of the heavy ion parent metal lattice using diffraction techniques or examination of the macroscopic resistivity across the synthesised samples in diamond anvil cells. A detailed investigation of the electronic properties of hydrogen atoms in these compounds was widely believed to be impossible.

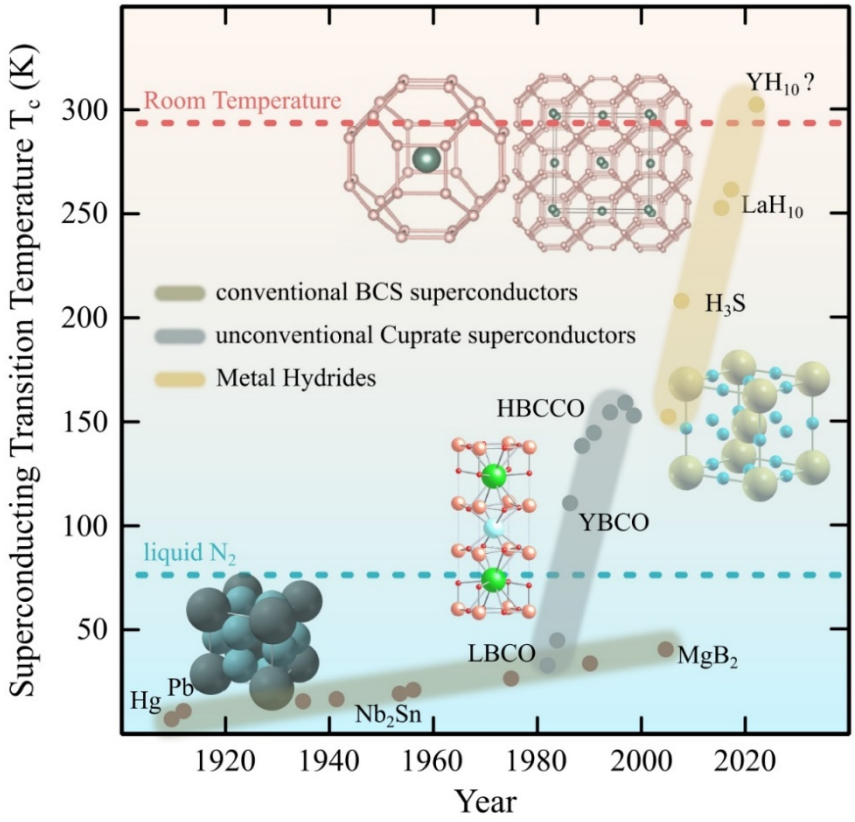

Fig. 3.4-11: Timeline of discovery of various classes of superconductors.

In collaboration with researchers from the synchrotron facilities DESY and ESRF, we were successful in synthesising iron monohydride in diamond anvil cells at pressures of 30 GPa and about 1200 K under double-sided laser heating-assisted synthesis, and investigated the response of the nuclear hydrogen spin system under increasing pressure using nuclear magnetic resonance (NMR). Using this technique, it was possible to observe the onset of electronic interactions between hydrogen atoms at around 100 GPa. Between 80 and 120 GPa, we

observed a significant deviation from the NMR resonance shift expected for Fermi gas-like behaviour of a regular metal. From *ab initio* calculations, it could be demonstrated that electron density from the iron parent metal lattice is transferred to the hydrogen sublattice, leading to an accumulation of conduction electron density in the hydrogen sublattice (see Fig. 3.4-12). Recent ^{1}H-NMR experiments on copper hydrides at pressures up to 90 GPa confirm this conjecture where the formation of the metallic H-sublattice could be observed as well.

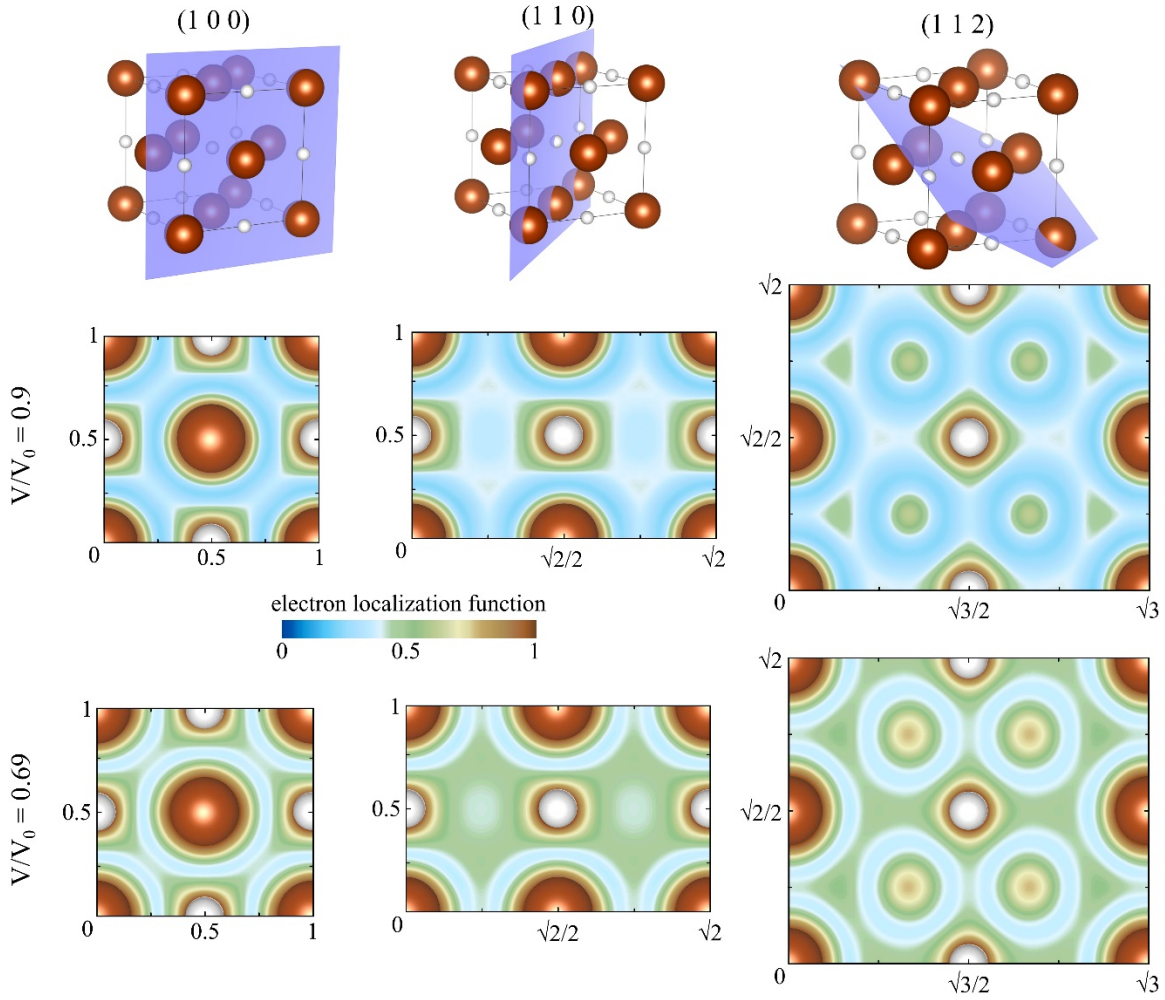

Fig. 3.4-12: Electron localisation function maps in three major crystal planes at compressions of V/V0 = 0.9 and 0.69, corresponding to 30 and 200 GPa, respectively. Brown and white spheres represent iron and hydrogen atoms, respectively. Green areas (ELF ~ 0.5) correspond to Fermi gas-like regions of free electrons.

j. *Effect of proton order-disorder transitions on the compression behaviour of high-pressure ice from time-resolved X-ray diffraction (A.S.J. Méndez/Hamburg, H. Marquardt/Oxford, F. Trybel, M. French/Rostock, G. Steinle-Neumann and H.-P. Liermann/Hamburg)*

High-pressure ice may play a significant role in the evolution of the ice giant planets Uranus and Neptune, as well as in mini-Neptune exoplanets. The high-pressure phases Ice VII and Ice

X, both characterised by cubic crystalline structures, are stable over a large pressure-temperature range, so are potentially the most abundant crystalline ice phases in ice planets. The ice VII - ice X transition is characterised by a sequence of proton order-disorder transitions through which H_2O loses its entity as a molecule and begins to form an atomic solid. Proton order-disorder transitions are continuous and subtly influence the thermodynamic properties of ice. Previous X-ray diffraction studies reported a slight decrease of the unit cell volume of ice VII at pressures from 40-60 GPa, likely associated with a change in proton order towards the formation of ice X. We collected continuous volume compression data, employing a dynamic diamond anvil cell in combination with time-resolved X-ray diffraction measurements at DESY, Hamburg. The unique pressure resolution of our data allows the direct observation of changes in the bulk modulus of ice by differentiating pressure-volume data. The bulk modulus of ice VII shows two main changes at 40 and 60 GPa that may be associated with formation of proton-disordered ice VII and ice X (Fig. 3.4-13). Previous Brillouin scattering experiments using static diamond anvil cells attempted to directly measure the bulk modulus of ice across the ice VII-ice X transition, but results were complicated by overlap of the sample signal with the contribution of diamond anvils in the pressure range from 40-60 GPa.

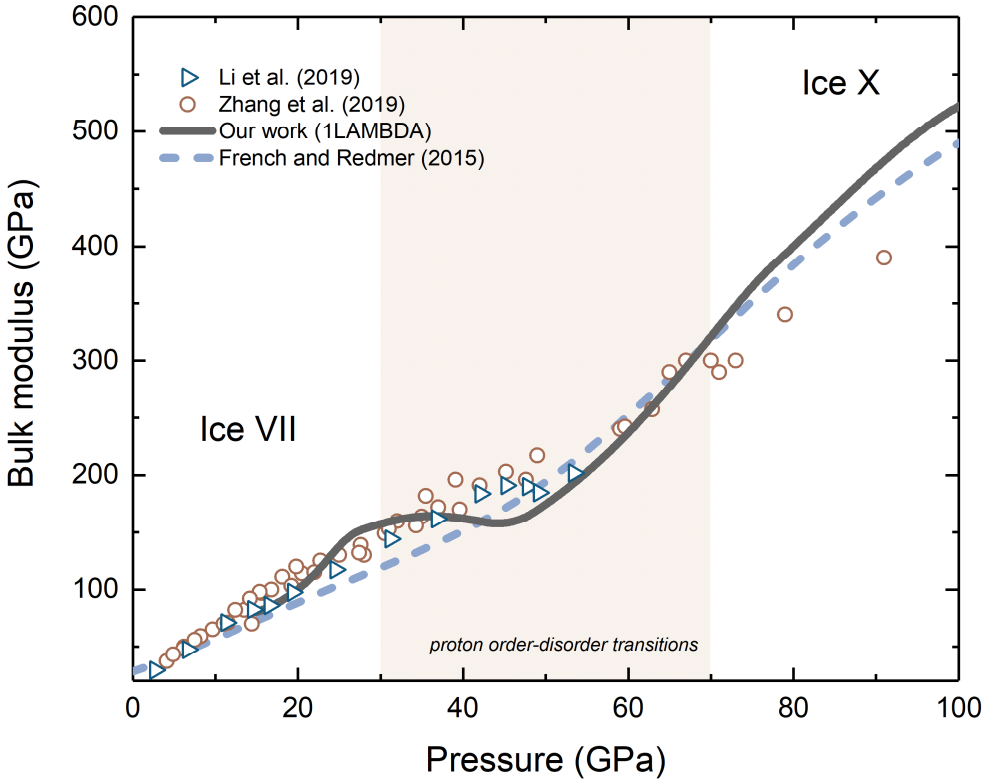

Fig. 3.4-13: Bulk modulus of ice as a function of pressure compared to computations (dashed line) and previous Brillouin scattering data (circles and triangles). Previous data are as follows: Li *et al*. (2019, Amer. Mineral. 104, 1307), Zhang *et al*. (2019, Appl. Phys. Lett. 114, 191903), French & Redmer (2015, Phys. Rev. B 91, 014308).

3.5 Fluids, Melts and their Interaction with Minerals

In subduction zones, volatiles such as water, carbon, and nitrogen are recycled back into Earth's mantle. A significant fraction of these volatiles is released from the subducted slab already at a depth of less than 150 km and returns to the surface by shallow degassing or by arc magmatism. Only the remaining volatile budget may be recycled into the deeper part of the mantle. Quantifying these processes is important for modelling the evolution of the carbon and water cycle in deep geologic time, which controls sea level and atmospheric composition throughout Earth's history. A very important problem here is the mechanism of fluid flow in subduction zones – is this flow pervasive, or is it channeled into narrow zones and certain directions dictated by the fabric of the rock? The first contribution in this section of the annual report addresses this question. A natural serpentinite with strong foliation was dehydrated in a multianvil experiment. Investigation of the run products showed that indeed, fluid loss appears to occur primarily parallel to the direction of foliation. In addition to water and carbon, subducted sediments may also transport nitrogen back into the mantle. The main mechanism for this is the substitution of ammonium (NH_4^+) for potassium in certain sheet silicates. The second contribution of this report investigated the maximum concentration of nitrogen that may be stored in such minerals. In equilibrium with a N-rich fluid phase, they may contain more than 2 wt. % of N and the nitrogen isotopic composition is shifter to higher $\delta^{15}N$ relative to the fluid. When such minerals decompose in a subduction zone, a large fraction of the nitrogen will be carried back to the surface, either by hydrous fluids or by silicate melts. To assess the efficiency of this process, data on nitrogen solubility in silicate melts are required. Such data are provided in the next study. Nitrogen solubility increases nearly linearly with pressure to at least 2 GPa. In silicic melts – as they often occur in subduction zones – nitrogen is much more soluble than in MORB magmas. Only few phases are able to transport volatiles deep into the mantle, beyond the depth where the common hydrous minerals decompose. The δ-H phase, a solid solution of $AlOOH$-$MgSiO_4H_2$ is a candidate phase for the deep subduction of water into the lower mantle. The phase relationships of δ-H in the system $MgSiO_3$-Al_2O_3-H_2O were studied in another contribution. Interestingly, both Al and H partition strongly into δ-H, such that coexisting bridgmanite is nearly dry.

The mechanism of water storage in the mantle is still a subject of intense investigation. While some publications suggested that most of the OH groups in the mineral olivine in the uppermost mantle are related to a defect involving Ti^{4+}, a new study suggests that a 2-3 GPa, defects involving Al^{3+} may be very prominent. The dependence of water solubility in olivine on oxygen fugacity is the subject of another contribution. Water from the deep Earth is brought back to the surface by hydrous silicate melts. An important question here is under which conditions such melts are buoyant, *i.e.*, when to they start to rise to the surface. This question is addressed in a study using first-principle molecular dynamics simulations. The data show that melts with water contents of about 4 wt. % or higher will start to rise to the surface. Interestingly, a large fraction of the hydrogen in these melts is contained in O-H-O bridges. Unlike silicate melts, free aqueous fluids are relatively rare in the mantle and their occurrence is likely limited to

regions affected by water flow from subducted slabs. In these environments, however, aqueous fluids can be very important agents of chemical transport and due to their elevated electrical conductivity, they may be detectable by magnetotelluric observations. The conductivity of these fluids is often increased by dissolved NaCl and KCl. To complement earlier investigations in the H_2O-NaCl system, the electrical conductivity of H_2O-KCl fluids was measured up to 4 GPa using an improved conductivity cell in a piston cylinder apparatus. Increasing pressure strongly enhances conductivity due to a stronger dissociation of KCl in the fluid.

Compared to the Earth's mantle, the mechanisms of volatile storage in the core are much less studied. The density deficit of the core compared to pure iron or iron nickel alloys suggests the presence of some light elements. In principle, it is conceivable that during Earth's formation, some hydrogen partitioned into the core, together with other light elements. One contribution of this section investigates the properties of hydrogen dissolved in liquid iron at high pressures by first-principles molecular dynamics simulations. The study suggests that the hydrogen diffusion coefficient in liquid Fe is anomalously high, which may have helped to achieve an equilibrium distribution of hydrogen between the core and the magma ocean in the very early history of the Earth. Finally, the last contribution of this section of the annual report investigates the possible effects of spin fluctuations on the electronic transport properties of liquid iron, which may affect the generation of Earth's magnetic field.

a. *The P-T dependence of permeability in serpentinites and fluid pathways in subduction zones (L. Eberhard, P. Eichheimer, M. Thielmann, D.J. Frost and G.J. Golabek, in collaboration with A. Suzuki/Sendai)*

The volumes of accessible for fluids released in a subduction zone will be different, depending on whether fluids move pervasively at the grain scale or become channelized. The dissolution of carbonates in aqueous fluids, which is argued to be one of the primary mechanisms for carbon release from slabs, depends strongly on the type of fluid flow. Based on low-pressure measurements it has been proposed that strong foliation of sheared serpentinite units creates anisotropy in fluid permeability that focuses fluids in subduction zones. Even in places where heterogeneities allow fluid to cross the foliation, channelized flow would still be favoured. However, this conclusion is based on permeability experiments performed up to only 50 MPa, because it is extremely challenging to measure permeability at the pressures of serpentine breakdown in a subduction zone.

In this study, a method was developed to examine the consequences of fluid flow anisotropy at high-pressure and -temperature conditions, from which permeabilities can be obtained with the help of numerical simulations. Serpentine minerals dehydrate over a temperature interval, such that water released will still flow through the serpentinite fabric. A serpentinite cylinder was cored from a natural, strongly foliated serpentinite (antigorite) sample in a direction perpendicular to the foliation. The cylinder was placed inside an MgO-sleeve with MgO-discs

on top and bottom (Fig. 3.5-1). This package was then sealed in a gold capsule inside a standard 25/17 multianvil assembly. Experiments were performed at 2 and 2.5 GPa and at temperatures from 500 to 800 °C. Although a piston cylinder press could have been used at these conditions, decompression cracking of the sample during retraction of the piston would have made the interpretation of the experiments more difficult. The run times at temperature were varied between 30 minutes and 24 hours. As the serpentinite decomposes, the cylinder releases water into the surrounding MgO sleeve and formes $Mg(OH)_2$ brucite. The directional flow of H_2O can thus be determined from the amount of brucite produced as water exits the different cylinder surfaces (Fig. 3.5-1).

As shown in Fig. 3.5-1, significantly more brucite was formed in the experiment along the cylinder walls, whereas only minor amounts were formed at the covering discs. The volume of water released in horizontal direction is approximately six times higher than for the vertical direction. This implies that the fluid in the experiment is indeed focused by the preferred orientation of the serpentinite.

The experimental results were compared with those of numerical simulations employing a 3D finite difference code to estimate fluid permeabilities. The results of experiments performed to date indicate strong anisotropy in fluid permeability within serpentine at least up to 2.5 GPa. Above 3 GPa, however, the serpentinite dehydration reaction has a negative P,T slope and thus the volume of the assemblage decreases upon dehydration, which may cause critical changes in permeability. Further experiments are being performed to explore this possibility.

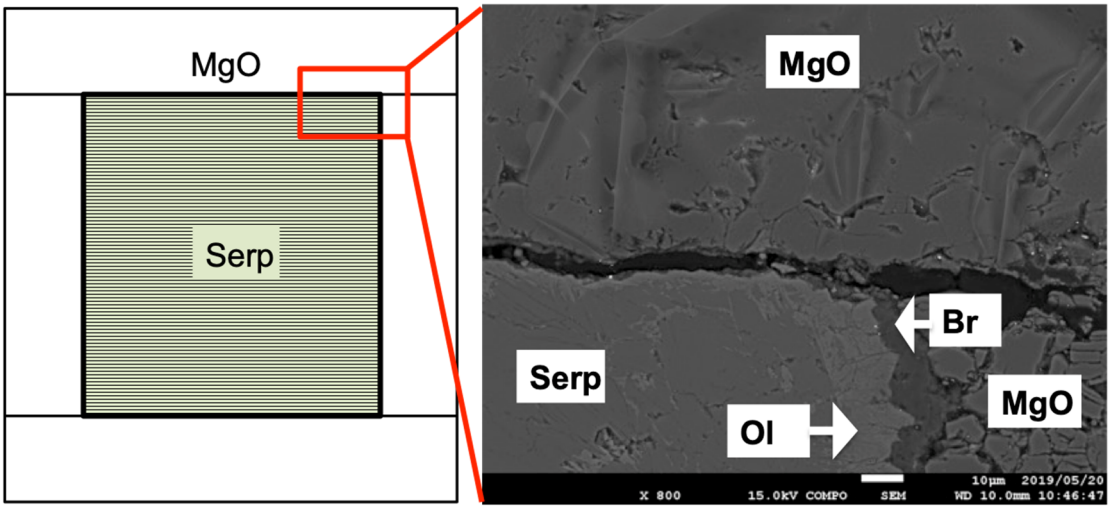

Fig. 3.5-1: The experimental setup (left) and SEM images of a run product (right) from an experiment to determine permeability anisotropy in serpentine at 2 GPa and 700 °C. The cylindrical serpentine (serp) sample is foliated in horizontal direction. Water released from the sample during the experiment transforms MgO surrounding the sample to brucite. As shown (right) the amount of brucite (Br) formed on the side of the sample, which is perpendicular to the foliation, is much greater than that formed on the top of the sample. An olivine layer develops in the serpentine due to reaction with MgO.

b. *Nitrogen solubility in hydrous minerals and nitrogen isotope fractionation in subduction zones (C. Melai and D.J. Frost, in collaboration with Y. Furukawa, A. Ishida and A. Suzuki/ Sendai)*

Subduction zones are sites of material transfer from Earth's surface to the mantle and therefore, they strongly influence the distribution of elements within the Earth. Nitrogen has unique features among volatile elements due to its distinct isotopic composition, which makes it a useful tracer of material exchange between reservoirs. Nevertheless, its abundance in the deep Earth is still not well constrained. Atmospheric di-nitrogen (N_2) is reduced to organic species by biological activity and enters the rock cycle upon decomposition of organic matter, mostly as ammonium ions (NH_4^+). Having similar charge and ionic radius as potassium (K), ammonium may substitute for potassium in clays minerals, micas and other phases. The amount of nitrogen effectively subducted into the mantle has been previously estimated using the flux of N entering at trenches in both sediments and altered oceanic crust and subtracting the nitrogen lost through arc-related volcanic and metamorphic processes. The results indicate that the fraction of N recycled to the surface at arcs is only about 20 % of the amount entering subduction zones. The remaining nitrogen is thought to be further subducted into the mantle. Furthermore, there is an imbalance between the large, isotopically heavy subducted flux as compared to the isotopically light, relatively small outgassing flux. This may suggest that significant amounts of N may have been trapped in the mantle during Earth's history. Adequate characterization of the nitrogen exchange between reservoirs requires data on bulk nitrogen contents, nitrogen distribution, and transport mechanism as a function of pressure, temperature, and fO_2.

The aim of this study is to investigate the partition coefficient of nitrogen, and its isotopic fractionation, between potential N-bearing minerals present within a subduction zone and the melts or fluids that may be formed upon the release of volatiles. Furthermore, the influence of oxygen fugacity on the behaviour of nitrogen is being investigated. Natural samples of montmorillonite, lizardite, antigorite, and phlogopite were loaded into Au capsules together with glycine (NH_2-CH_2-COOH) as organic nitrogen source. Equilibration experiments were conducted in a 1500 ton Kawai type multianvil press at Tohoku University at 3 GPa and 500 °C for a duration of 24 hours. The recovered mineral assemblages were analyzed using an elemental analyzer isotope ratio mass spectrometer (EA-irMS). This provides a bulk analysis of the average isotopic and elemental concentration in the sample of interest. Preliminary measurements yielded information on the solubility of N in subduction zone minerals in the presence of a nitrogen-rich fluid. The amount of nitrogen and the isotopic signature for the mineral assembles from individual experiments are shown in Fig. 3.5-2. The mineral assemblages are plotted on the vertical axis in the sequence in which they break down in a subduction zone.

The minerals initially contained practically no nitrogen, but were all found to have incorporated nitrogen into their structures during the experiment. The amount of nitrogen found in montmorillonite is consistent with observations on some natural clay samples. The solubility of nitrogen is found to decrease in the order in which these hydrous minerals would breakdown

in a subduction zone. The results imply that hydrous minerals have a significant capacity to transport nitrogen into the mantle, although the amounts of nitrogen in subduction zone minerals are unlikely to reach the levels measured in this study. With increasing pressure, dehydration reactions would lead to a decrease in the slab nitrogen content, although it is possible that nitrogen is passed from one mineral to another upon dehydration. To examine this hypothesis, dehydration experiments under both reducing and oxidizing conditions are currently underway.

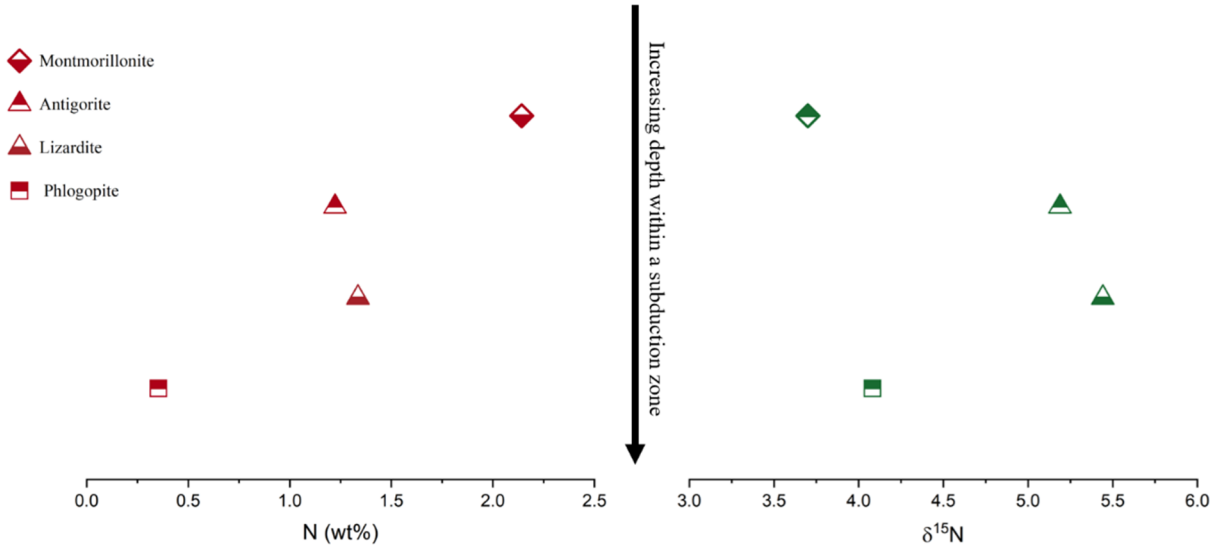

Fig. 3.5-2: The nitrogen concentration (red) and the $\delta^{15}N$ ratio, in per mil, (green) for all minerals recovered from high-pressure experiments. The data are plotted in the sequence in which the minerals would breakdown with increasing depth in a subduction zone: Montmorillonite (diamonds); antigorite and lizardite (triangles); phlogopite(squares).

The measured nitrogen isotopic ratios in the mineral phases, reported as $\delta^{15}N$ in per mil, were in all cases shifted from the starting $\delta^{15}N$ value of approximately 2.2 ‰. The minerals have become enriched in the heavier isotope (^{15}N) due to partitioning of the lighter isotope into a fluid phase, consistent with nitrogen isotope measurements on volatiles released from subduction zones. Interestingly, the serpentine minerals show the largest increase in $\delta^{15}N$. Further experiments are being performed to examine the effect of oxygen fugacity on the nitrogen isotope fractionation and to study the isotopic distribution during dehydration melting of phlogopite.

c. *The solubility of N_2 in silicate melts (L. Cialdella, M. Wiedenbeck/Potsdam and H. Keppler)*

Nitrogen is the main constituent of air. However, in recent years, research at Bayerisches Geoinstitut has shown that the minerals of the mantle may actually store much more nitrogen than is presently contained in the atmosphere. This opens up the possibility of a dynamic exchange of nitrogen between the atmosphere and Earth's interior over geologic time. Nitrogen

is mostly carried to the surface by magmas that degas at shallow depth. Therefore, quantifying the fluxes of nitrogen to the atmosphere requires some data on the solubility of nitrogen in silicate melts. On the modern Earth, the oxygen fugacity of the upper mantle is such that nitrogen will likely be dissolved in silicate melts as N_2 only. Therefore, we carried out a systematic study of N_2 solubility in silicate melts as a function of pressure, temperature and melt composition.

Solubility experiments were carried out of to 5 kbars in an internally-heated gas pressure vessel with rapid-quench device and up to 20 kbar with a piston cylinder press. Starting materials were glasses of haplogranite or MORB compositions and AgN_3 as a source of nitrogen. The AgN_3 was enriched to 99 % with the rare ^{15}N isotope to distinguish nitrogen in the sample from any contamination by air. Nitrogen contents were measured by SIMS (secondary ion mass spectrometry) at GFZ Potsdam.

Preliminary results are shown in Fig. 3.5-3. Nitrogen solubility is nearly proportional to pressure up to 20 kbar (Fig. 3.5-3a). Notably, the solubility in the silicic haplogranite melt is considerably higher than for the more depolymerized MORB melt. This implies that the more

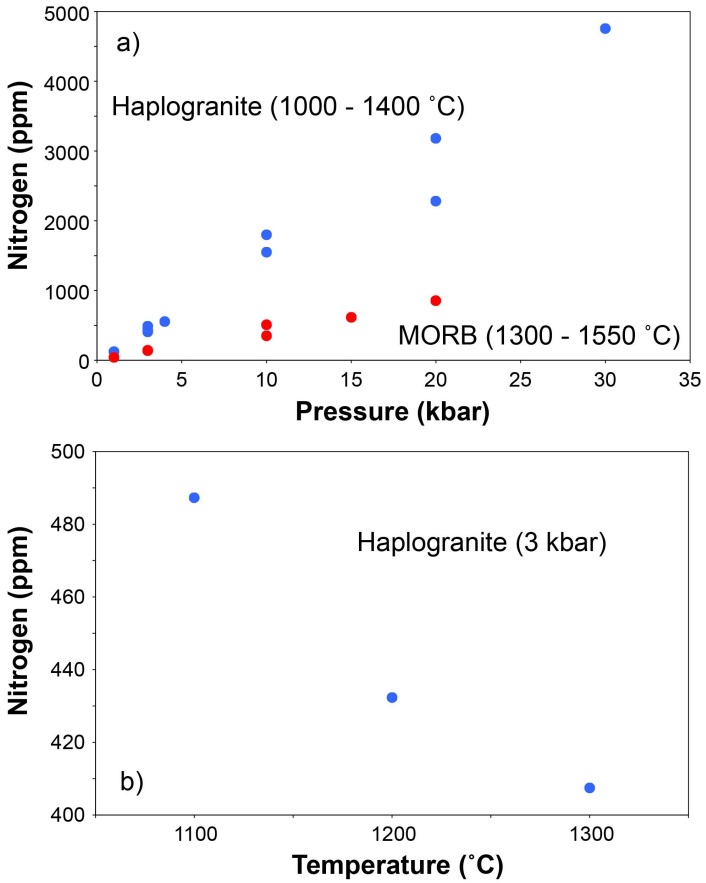

Fig. 3.5-3: Nitrogen solubility (expressed as ppm by weight of ^{15}N) in silicate melts as function of (a) pressure and (b) temperature. Blue data points are for haplogranite, red data points are for MORB.

silicic melts produced in subduction zones are more efficient agents of nitrogen transport back to the surface than the basaltic melts at mid-ocean ridges. The difference in solubility between haplogranite and MORB is likely related to the higher ionic porosity of haplogranite, *i.e.*, a larger number of vacant sites between the silicate units in the more silicic melt. At low pressure, there is a clear decrease of nitrogen solubility with temperature (Fig. 3.5-3b), however, this trend appears to reverse at higher pressures. The data from this study will be used to improve models of nitrogen degassing in subduction zones and at mid-ocean ridges.

d. *Al and H partitioning between bridgmanite and the hydrous phase δ-H, with implications for water transport into the lower mantle (E. Ohtani/Sendai, T. Ishii, T. Katsura, H. Keppler and D.J. Frost)*

The observation of hydrous minerals such as hydrous ringwoodite and phase EGG in natural diamonds suggests that the mantle transition zone is locally hydrated. The subduction of slabs may carry water further into the lower mantle. The δ-H phase, a AlOOH-$MgSiO_4H_2$ solid solution, may be a major candidate for this process. The phase is stable to the bottom of the lower mantle due to a strong O-H bond caused by hydrogen bond symmetrization.

We clarified the phase relations in the $MgSiO_3$-Al_2O_3-H_2O system and the partitioning of aluminium and hydrogen between bridgmanite and hydrous phases at the top of the lower mantle by using a multianvil high-pressure apparatus in the pressure range from 25 to 28 GPa and at temperatures from 1000 to 1600 °C. The recovered samples were polished and investigated by SEM, micro-Raman spectroscopy, X-ray powder diffraction, and EPMA.

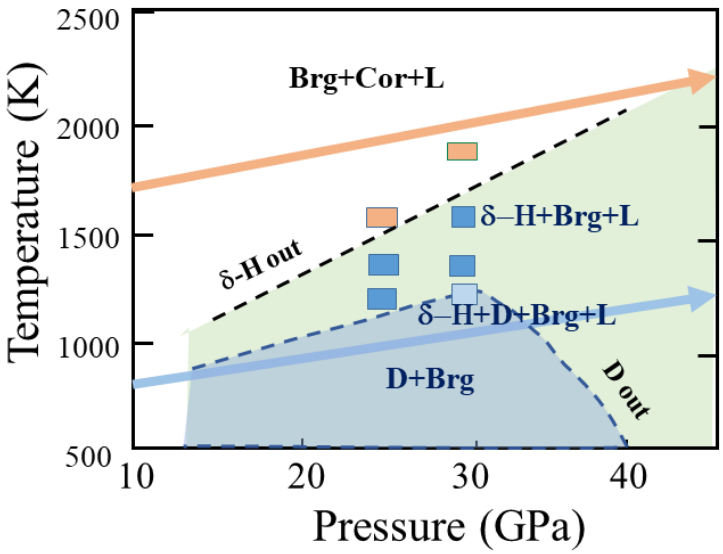

Fig. 3.5-4: Phase relations of the $MgSiO_3$-AlOOH system at high pressure and temperature. Brg = bridgmanite; δ-H = hydrous δ-H solid solution; Cor = corundum; D = hydrous phase D; L = liquid or fluid. The blue and orange arrows show a cold subduction geotherm and an average mantle geotherm.

Bridgmanite coexists with hydrous phase D at around 28 GPa and about 1000 °C, whereas the hydrous phase changes from phase D to phase δ-H for temperatures above 1100 °C at 28 GPa. The phase relations of the system are shown in Fig. 3.5-4. Our experiments revealed that alumina strongly partitions into the δ-H phase and is depleted in bridgmanite, with Al_2O_3 contents in the latter phase being below 1.5 wt. % at 28 GPa and 1100 °C. We also confirmed that bridgmanite coexisting with the hydrous δ-H phase is very dry, with a water content < 10 ppm according to micro-FTIR analysis. The compositions of the coexisting bridgmanite and δ-H solid solution are shown in Fig. 3.5-5. The dry nature of coexisting bridgmanite implies that the δ-H phase is the major carrier of water into the lower mantle.

The coexistence of bridgmanite or post-perovskite and hydrous δ-H solid solution likely decreases the alumina contents in bridgmanite, post-perovskite, and other minerals in the lower mantle. Fluids released at the top of the lower mantle may react with aluminous bridgmanite along the geotherms of the slab and of the normal mantle to create alumina-depleted bridgmanite coexisting with the hydrous phase δ-H. The partition coefficient of alumina $D^{\delta/Brg}$ is about 14 - 26 in a wide pressure and temperature range. The Al_2O_3 contents of bridgmanite in MORB and peridotite under dry condition are ~ 15 wt. % and ~ 5 wt. %, respectively, whereas the Al_2O_3 contents decrease significantly to ~ 3 wt. % and ~ 1 wt. %, respectively, upon addition of water and formation of the hydrous phase δ-H. The depletion of alumina in bridgmanite modifies the phase relations in the lower mantle significantly; the boundaries of the garnet-bridgmanite transition and of the post-bridgmanite transition become shallower and sharpen under wet conditions.

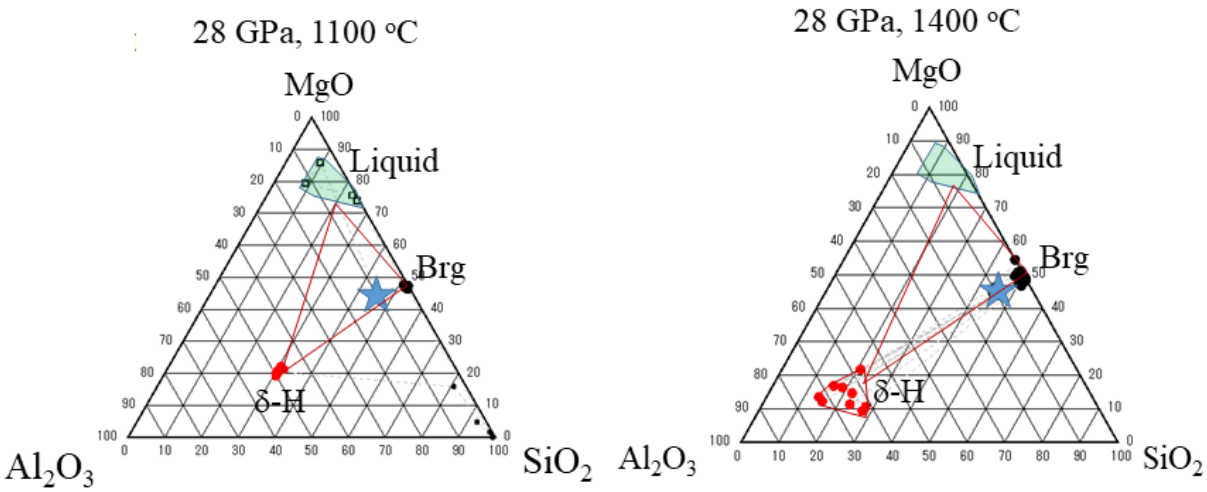

Fig. 3.5-5: Compositions of coexisting bridgmanite and hydrous phase δ-H at 28 GPa and high temperatures. Brg = bridgmanite; δ-H = hydrous phase δ-H solid solution.

e. *Hydrous defects in olivine associated with Al and other trivalent elements (A.C. Withers, in collaboration with J.L. Mosenfelder/Minnesota)*

Hydrogen can be incorporated into olivine in the form of hydroxyl groups when hydrogen atoms attach to oxygen atoms belonging to the silicate framework. Charge balance is achieved by substituting four hydrogen atoms for a silicon atom, two hydrogen atoms for a divalent cation, or by coupled substitutions where titanium plus two hydrogen atoms substitute for three divalent cations, or a trivalent element plus one hydrogen atom substitute for two divalent cations. While all of these substitution mechanisms have been shown to be viable in experiments, natural olivines from mantle xenoliths often show evidence for coupled substitution with titanium. Infrared spectra of olivine synthesized in high-pressure experiments, on the other hand, are often dominated by bands related to a defect complex where hydrogen substitutes for silicon.

Multi-phase experiments in multiple component systems tend to produce small crystals that are analyzed by secondary ion mass spectrometry, which has much greater spatial resolution than infrared spectroscopy, but gives only a bulk analysis of the hydrogen content without providing any information about the structural environment of hydroxyls. Hence, it is assumed that the olivines in such experiments are dominated by the same kind of hydrous defects as in the single-phase experiments. The nature of hydroxyl defect complexes controls the mechanism for hydrolytic weakening of olivine, which in turn may influence the rheology of mantle rocks. Therefore, it is important to be able to predict how hydrogen may be incorporated under different conditions.

We performed piston cylinder experiments in the MgO-Al_2O_3-SiO_2-H_2O (MASH) system at 2-3 GPa and 1400 °C to produce an assemblage of forsterite, enstatite and pyrope, together with a hydrous fluid. Further experiments in the multianvil press at 6 GPa and 1400 °C with bulk compositions of forsterite + Sc_2O_3 or forsterite + Fe_2O_3 + PtO_2 produced 200-400 μm sized olivine crystals. The crystalline phases were identified by Raman spectroscopy, and forsterite crystals were individually oriented by optical microscopy and polished to produce double-sided sections perpendicular to the crystallographic axes. Polarized infrared spectroscopy of the MASH olivines in the OH stretching region shows predominantly bands related to substitution with trivalent elements (Fig 3.5-6a). We use these spectra to determine the minimum number of absorption bands arising from coupled substitution with Al, and to calculate the orientation of the OH dipoles represented by each band (Fig 3.5-6b). This was achieved by simultaneous least-squares fitting of six polarized infrared spectra. The bandwidths are very narrow in this region (Voigt FWHH = 2-7 cm-1), so infrared spectra with a resolution of ≤ 1 cm-1 were used for fitting. The position, width and shape of each peak were constrained to be equal in all six spectra, resulting in well-constrained fits. Six peaks are required between 3300 and 3400 cm^{-1} to fit each spectrum (Fig 3.5-6c). Low-temperature infrared spectra collected at -85 °C resolve five of these six peaks, confirming the results of fitting the room temperature spectra (Fig 3.5-6a). It is not clear how many infrared bands are present in the Fe^{3+}-bearing forsterite, though the spectra are distinct from the MASH forsterites (Fig 3.5-6d). In natural olivines, the peaks

in the 'trivalent region' are significantly broader (with FWHH between 8 and 30 cm^{-1}), making it difficult to distinguish between Al- and Fe^{3+}-related substitutions.

Forsterites from MASH experiments were analyzed by secondary ion mass spectrometry (SIMS). A set of olivine reference materials with H contents between 240 and 1960 ppm H_2O, and whose OH bands have a centroid position of 3566 cm^{-1}, was used to establish the relationship between H concentration and OH/Si count rate.

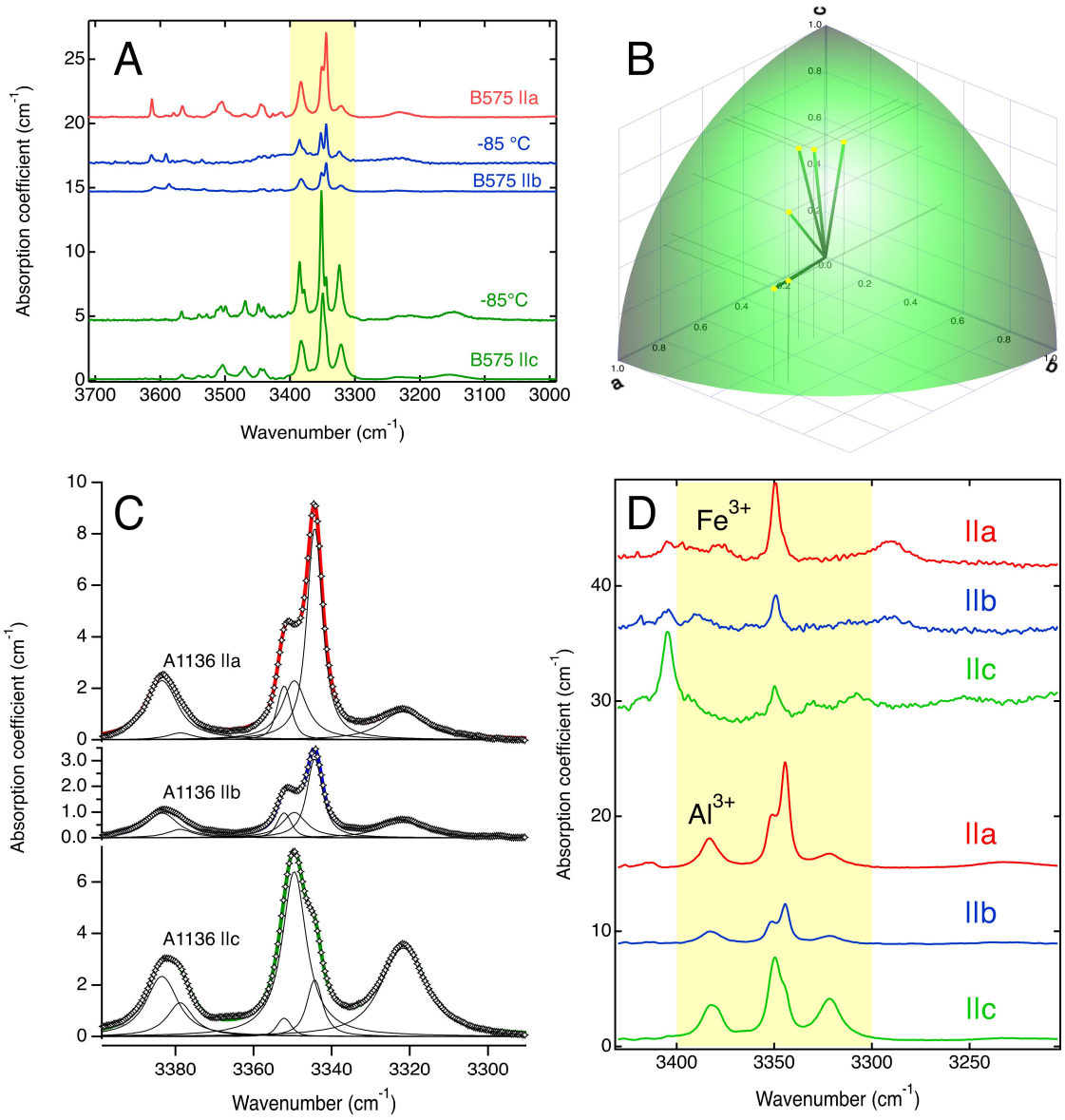

Fig. 3.5-6: (a) Polarized infrared spectra of forsterite synthesised at 2 GPa, 1400 °C. Spectra were collected at room temperature and at -85 °C. Within the shaded region OH stretching bands in olivine are typically ascribed to coupled substitutions with trivalent elements. (b) Orientations for the six OH dipoles associated with Al. (c) Decomposition of polarized spectra into six bands by simultaneous least-squares fitting of six spectra. (d) Comparison of polarized spectra for an Al-bearing forsterite synthesized at 3 GPa and 1400 °C, and an Fe^{3+}-bearing forsterite synthezised at 6 GPa and 1400 °C.

Based on SIMS measurements of 58 and 74 ppm H_2O in the forsterites, the molar absorption coefficient for the Al-related OH stretching bands at around 3350 cm^{-1} should be 25 % greater than that for the higher frequency bands in the reference materials. Such a difference is in agreement with the general sense of frequency dependence of molar absorption coefficient, and means that lower frequency peaks have a greater intensity for the same concentration of OH.

In the presence of garnet, at shallow levels of the upper mantle, coupled substitution of H and Al may contribute significantly to the OH defects in olivine. Under subsolidus conditions the activity of Al_2O_3 is that imposed by the coexistence of garnet and pyroxene, and is greater than that in high-pressure experiments where Al_2O_3 is dilute in a fluid phase. In garnet-bearing experiments in the MASH system, at 2-3 GPa and 1400 °C, Al-bearing defect complexes account for 50-60 % of the H in forsterite.

f. *The effect of oxygen fugacity on water solubility in forsterite (K. Nishida, D. Druzhbin, H. Fei and T. Katsura)*

Olivine is the most abundant mineral in the upper mantle and may store water in the form of hydroxyl groups. The presence of OH in mantle minerals significantly affects a variety of physical and chemical properties, such as the melting temperature, the electrical conductivity, and the rheology of the mantle. Therefore, it is important to clarify the effect of pressure, temperature, composition, and oxygen fugacity on water solubility in olivine. However, the effect of oxygen fugacity (fO_2) on water solubility in olivine is still being debated. Therefore, in this study, we conducted equilibrium experiments on the solubility of water in pure forsterite for a wide range of oxygen fugacities at constant pressure and temperature.

High-pressure experiments were carried out in a Kawai-type multianvil apparatus with the 18/11 BGI standard assembly. Starting material was a powder mixture of MgO, $Mg(OH)_2$ and SiO_2. Oxygen fugacity was controlled by metal/metal-oxide buffers (Hf/HfO_2, Cr/Cr_2O_3, Mo/MoO_2, Pt/PtO_2) using a double capsule technique with an inner Pt capsule containing the charge and an outer Au capsule containing the buffer. Run products were identified by SEM/EDS and XRD. Water contents in forsterite were calculated from unpolarized FTIR spectra.

All run products consisted of forsterite, enstatite and hydrous silicate melt or fluid. Therefore, the compositions of the phases were fixed by the phase rule, which allowed to reliably clarify the effect of fO_2. We also confirmed the coexistence of metal or metal hydride and metal oxide in the recovered sample, which suggests that the fO_2 in sample should be buffered. The experimental results are summarized in Fig. 3.5-7. The water content in forsterite increased with temperature but did not change with oxygen fugacity. Even at subsolidus conditions, the fluid phase contains a large amount of dissolved silicate and cannot be distinguished from a silicate melt at pressures beyond the second critical endpoint. Therefore, the dependence of water solubility in forsterite on oxygen fugacity may be negligibly small regardless of temperature.

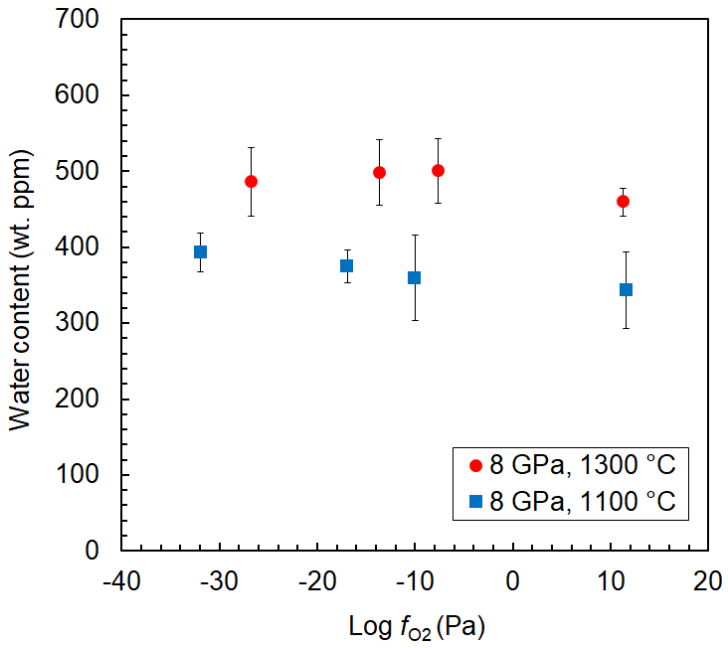

Fig. 3.5-7: Water content of forsterite as a function of oxygen fugacity at 8 GPa. Red circles and blue squares refer to 1100 °C (sub-solidus) and 1300 °C (super-solidus) experiments, respectively. Error bars show one standard deviation.

g. *Structure and density of H_2O-rich Mg_2SiO_4 melts at high pressure from* ab initio *simulations (L. Yuan and G. Steinle-Neumann, in collaboration with E. Ohtani and A. Suzuki/Sendai)*

Water is thought to play an essential role in Earth's dynamics, as it fundamentally alters the physical properties of materials in the planet's interior. Geophysical observations have revealed the existence of low-velocity and high-conductivity layers above the 410-km and below the 660-km discontinuity bracketing the mantle transition zone (MTZ), presumably indicating the occurrence of hydrous silicate melts.

As water preferentially partitions into melts compared to solid peridotite residue, partial melts of hydrous material from the MTZ are expected to be water-rich (probably up to 15 wt. % H_2O), according to observations from melting experiments and insights from thermodynamic modeling. Whether these water-rich melts stay at depth and therefore provide a viable explanation for the geophysical observation is an open question, as they appear to be far too water-rich to be neutrally buoyant. We explore the viability of this hypothesis and report the results of first-principles molecular dynamics simulations of hydrous Mg_2SiO_4 melts with up to 27 wt. % H_2O at pressure-temperature (P-T) conditions relevant to the upper mantle and MTZ. The simulations (Fig. 3.5-8) show that the speciation of hydrogen in the depolymerized silicate melts is dominated by OH hydroxyl groups at low P, but shifts to a significant proportion of bridging hydrogens (-O-H-O-) at high P, particularly for the H_2O-rich compositions. Hydrogen atoms are not only indirectly bonded to the network-forming cation Si

(as Si-O-H) but also to the network-modifier cation Mg. Nevertheless, Mg remains the dominant melt depolymerizer as compared to hydrogen, despite the high water content in the melts considered. The ratio of non-bridging oxygen atoms per silicon (NBO/Si) in the water-poor melt is comparable to that of dry Mg_2SiO_4 melt (NBO/Si = 4), and it increases with water. There is no evidence from the simulation that water causes an increase in melt polymerization for ultramafic magmas, contrary to a hypothesis based on indirect experimental evidence.

Based on the partial molar volume of water in the hydrous melts and those of components of a dry melt assemblage, we examined the densities of hydrous melts in the MTZ and compared them to those of the surrounding mantle (Fig. 3.5-9). The critical water contents at which hydrous peridotite melts have the same density as the surrounding mantle is about 4 wt. % H_2O, much lower than the high water contents (> 10 wt. %) observed for partial melting in experiments and required to thermodynamically stabilize melts in the vicinity of the MTZ. Water may therefore play a significant role in triggering deep plumes ascending from near-MTZ reservoir.

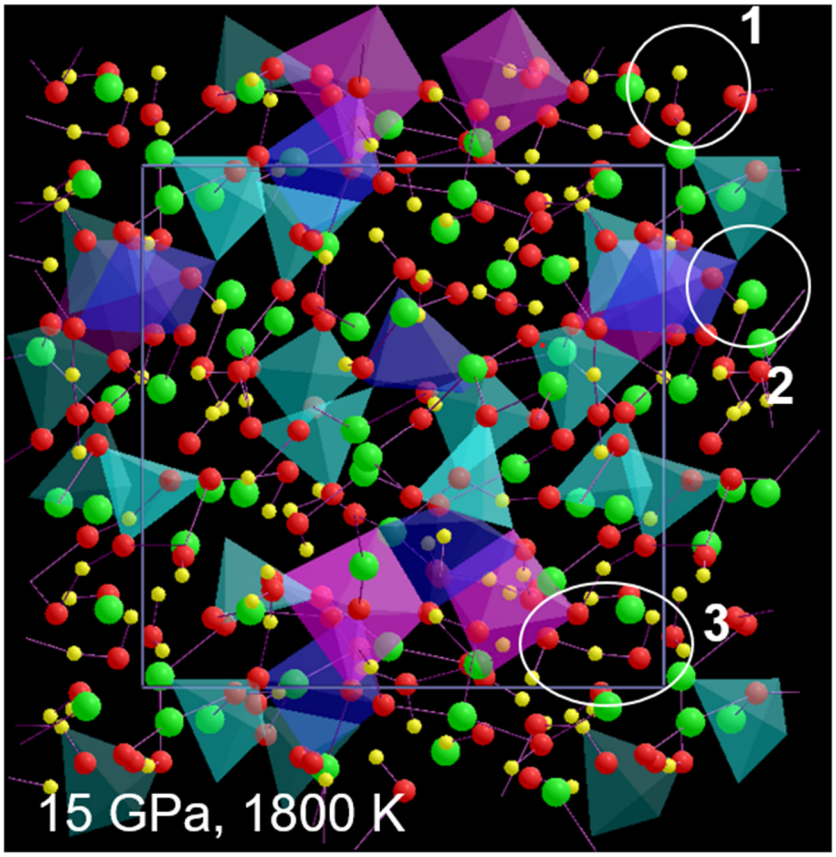

Fig. 3.5-8: Speciation of water dissolved in Mg_2SiO_4 melt. Hydrogen atoms are shown in yellow, oxygen atoms in red, Mg in green; the environments of the silicon atoms are shown as coordination polyhedra. Hydrogen in the silicate melts (at 1800 K and 15 GPa) typically occurs as free H_2O water molecules (marked with 1), OH hydroxyl groups (2) and -O-H-O- bridging hydrogen atoms (3).

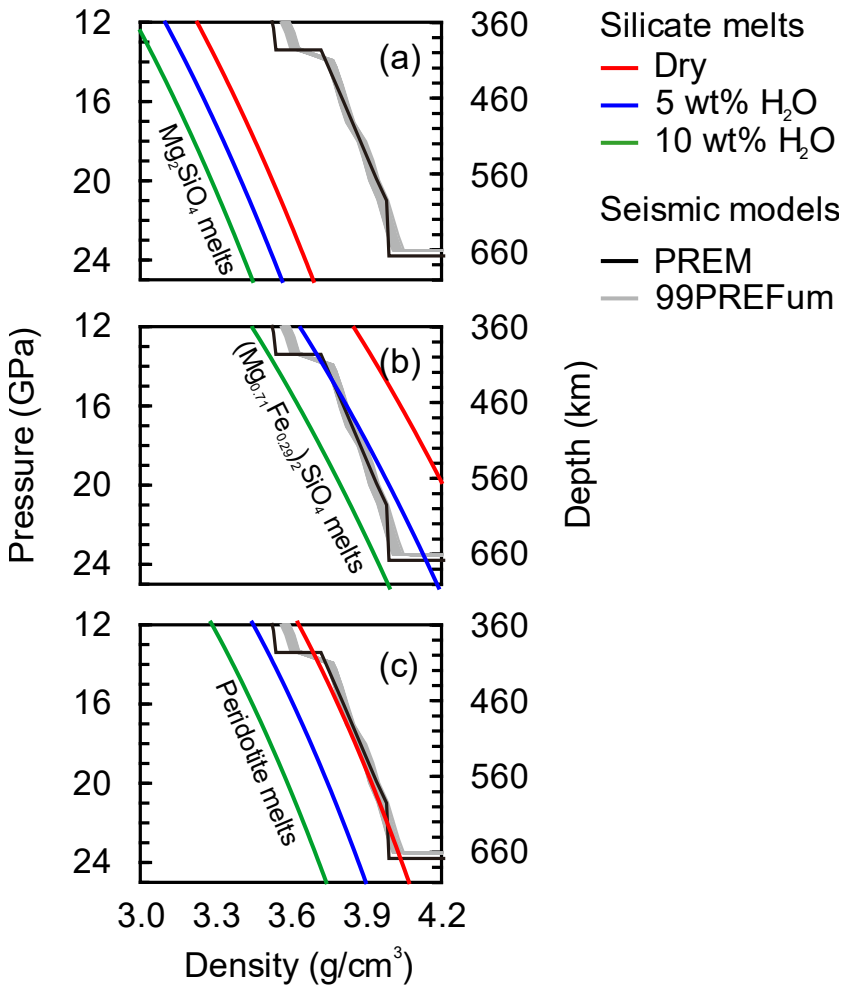

Fig. 3.5-9: (a) Density of silicate melts with idealized compositions of Mg_2SiO_4 (a), $(Mg_{0.71}Fe_{0.29})_2SiO_4$ (b) and a realistic, multicomponent peridotite melt (c). Density of melts with 0 wt. % (red), 5 wt. % (blue), and 10 wt. % H_2O (green) are shown. Mantle density profiles from PREM (black; Dziewonski and Anderson 1981; PEPI 25: 297) and the 99 pyrolite models (99PREFum, grey; Cammarano *et al.* 2005; JGR 110: B01306) are shown for comparison.

h. *Electrical conductivity of H_2O-KCl fluids up to 4 GPa and 900 °C (K. Vlasov and H. Keppler)*

Aqueous fluids occur in Earth's crust and in the mantle above subduction zones. While NaCl is usually the most abundant solute in these fluids, KCl is sometimes the main solute component found in diamond inclusions. This suggests that KCl-bearing aqueous fluids may be rather common in the deep mantle. Electrical conductivity measurements of such fluids have direct geological implications as they may be used for the interpretation of magnetotelluric data, allowing the determination of fluid type and fraction in highly conductive zones of the Earth. They are also essential for improved models of NaCl-KCl-H_2O complex fluids, found in areas of modern ore formation or metamorphic environments. To complement our previous research on the electrical conductivity in the NaCl-H_2O system, we therefore systematically studied the electrical conductivity of KCl-bearing aqueous fluids to upper mantle P, T conditions.

For the measurements, we used an improved piston cylinder cell, in which the fluid is contained in pores of diamond powder between a central electrode and the capsule wall, which served as second electrode. To avoid the possible contamination of the charge by boron, the BN seals of a previous design were replaced by seals made of gold and pyrophyllite (Fig. 3.5-10).

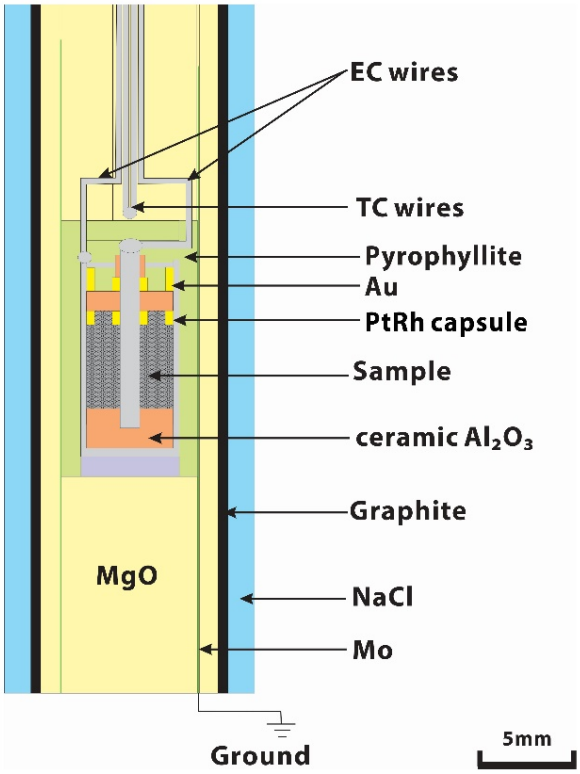

Fig. 3.5-10: An improved piston-cylinder assembly for conductivity measurements of non-corrosive aqueous fluids.

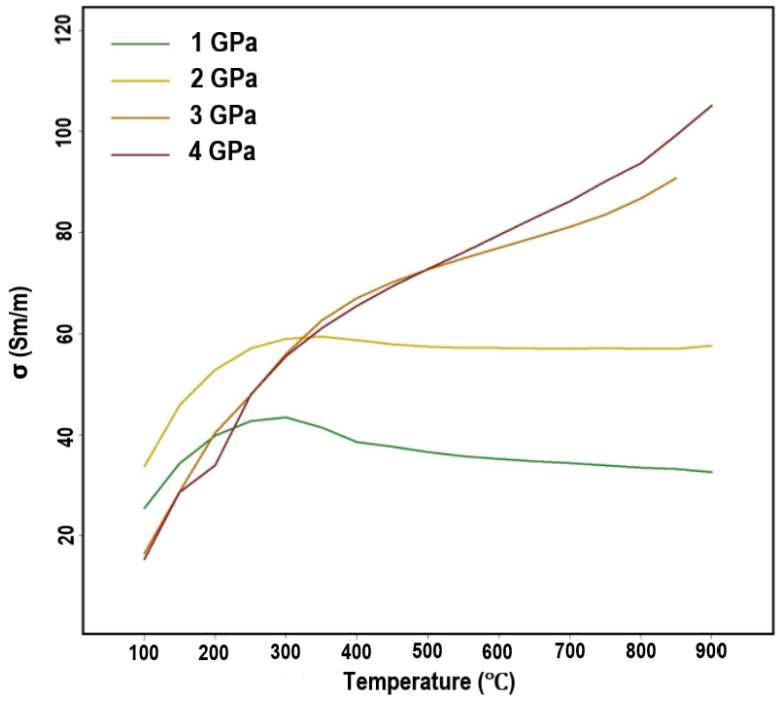

Fig. 3.5-11: Measured conductivities of H_2O-KCl-fluids to 900 °C and 4 GPa. The KCl concentration was equivalent to 1 M = 1 mol/liter at ambient conditions

Cells containing 1 M KCl solution inside the pore space of diamond powder were loaded into a piston cylinder apparatus and compressed to 1, 2, 3, and 4 GPa. Resistances were extracted from impedance measurements from 10 MHz to 1 kHz, during several heating and cooling cycles from 28 to 900 °C at constant pressure. After the run, the fluid fraction was calculated according to the Hashin and Shtrikman upper bound model, based on cell the resistance measured at ambient conditions. Knowing the cell constant, bulk fluid conductivities were then calculated from the resistance values at experimental conditions (Fig. 3.5-11).

The data show a strong enhancement of conductivity by pressure and temperature; with increasing temperature, fluid viscosity decreases, while pressure increases the dielectric constant of the fluid and therefore enhances dissociation of KCl into K^+ and Cl^-. Compared to the NaCl-H_2O system, the observed conductivities tend to be somewhat lower, due to the reduced mobility of K^+ as compared to Na^+.

i. *Anomalous diffusion in the dilute liquid Fe-H system from* ab initio *simulations (E. Posner and G. Steinle-Neumann)*

The Earth's core is composed mostly of an Fe-Ni alloy with substantial, yet unknown concentrations of additional elements. The question of core composition is particularly important because it directly relates to the conditions under which the core formed during Earth's accretion, *e.g.*, pressure (P), temperature (T), and oxygen fugacity (fO_2). The onset and evolution of Earth's geodynamo is also intimately related to the core's light alloy budget owing to the chemical buoyancy associated with fractional crystallization of the inner core. The behaviour of light and alloying elements in iron-rich metallic systems is therefore of great significance for understanding the formation, differentiation, and evolution of the terrestrial planets.

The incorporation of alloying elements in solid metals is well understood to be controlled by the relative radii of an alloying element and that of Fe, which also provide the basis for estimating the coordination number NC. Although liquids lack long-range periodicity, their short-range order can be used to make realistic predictions of "liquid packing structure" – assessing the dominant incorporation mechanism – which affects solubility and partitioning coefficients. The compression behaviour of liquid iron alloys over a planetary-scale P-T range is therefore particularly relevant for estimating alloying element behaviour under conditions beyond those accessible in the laboratory.

The effects of P and T on mass transport properties of alloying elements in liquid iron not only constrain the chemical kinetics of metal-silicate equilibration but also provide insight into structure-property relations. In previous experimental and computational studies, we have explored these aspects for O and Si in liquid Fe. Here, we extend this work by considering another light element candidate, hydrogen, and its incorporation into and diffusion properties in liquid iron. We perform first-principles molecular dynamics simulations on the dilute $Fe_{0.96}H_{0.04}$ composition over a wide P-T range, covering the whole mantle and outer core.

In the $Fe_{0.96}H_{0.04}$ system, hydrogen diffuses faster by approximately one order of magnitude than Fe over the whole P-T range considered (Fig. 3.5-12a), and also significantly faster than the fastest light element we have explored previously (oxygen). This is not surprising given the substantial difference of the average atomic distance between Fe and H (r_{FeH}) and that between the Fe atoms (r_{FeFe}) (Fig. 3.5-12b). It is surprising, however, that in the presence of H, the self-diffusion of Fe is slowed down considerably (by approximately a factor of five; Fig. 3.5-12a) in contrast to simulations in the Fe-H system with higher hydrogen concentrations ($Fe_{0.78}H_{0.22}$, $Fe_{0.69}H_{0.31}$ and $Fe_{0.59}H_{0.41}$; Umemoto & Hirose, 2015, GRL 42: 7153) that find Fe diffusion to be enhanced by hydrogen. This difference can be understood in terms of liquid structure: H is incorporated into the Fe liquid on quasi-interstitial sites with small values of r_{FeH}~1.7–1.5 Å (r_{FeFe}~2.4–2.1 Å; Fig. 3.5-12b) and small NC_{HFe}~4–8, compared with the near-close packing values for NC_{FeFe}~10–13 (Fig. 3.5-12c). By contrast, NC_{FeFe} is strongly reduced for higher H concentrations, representing less dense packing in the liquid, which enhances Fe diffusivity in the Fe-H system. The dense packing of Fe in liquid $Fe_{0.96}H_{0.04}$ and any open space occupied by the fast diffusing hydrogen appear to slow down Fe self-diffusion.

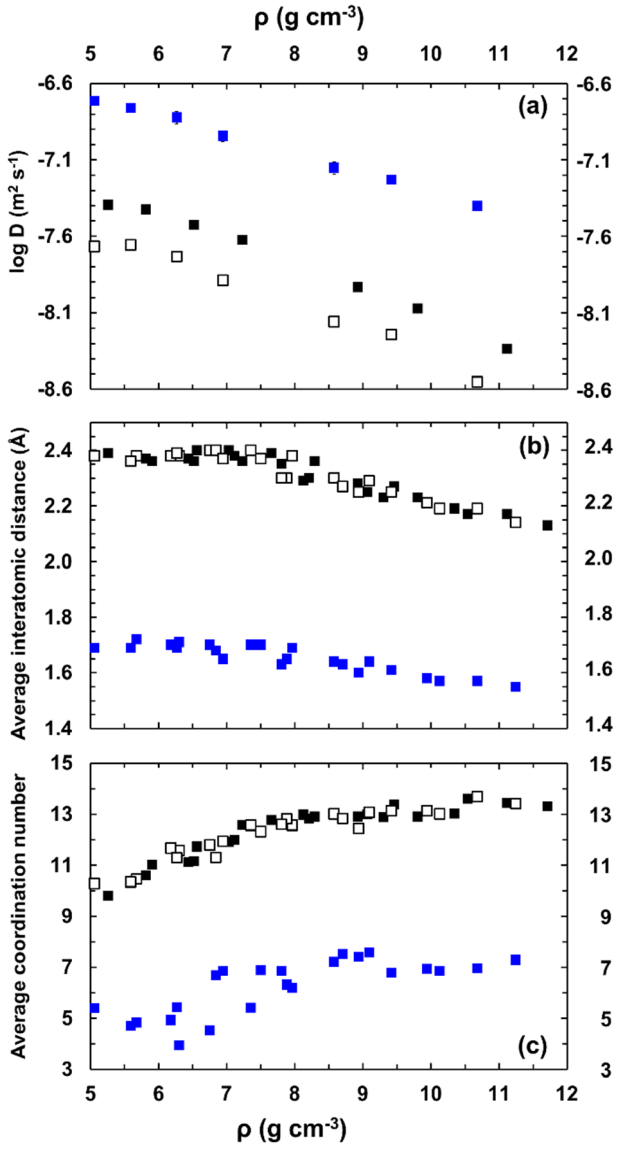

Fig. 3.5-12: Diffusion and structural properties of Fe in pure liquid Fe (black) and liquid $Fe_{0.96}H_{0.04}$ (unfilled) and H in liquid $Fe_{0.96}H_{0.04}$ (blue). (a) Diffusivities at T = 4,500 K over a density range covering pressures of the Earth's mantle and outer core. Hydrogen self-diffusion is approximately one order of magnitude faster than Fe self-diffusion with a larger difference shown for the alloy composition compared with pure liquid Fe. (b) Average distance between Fe atoms in liquid Fe and $Fe_{0.96}H_{0.04}$ and between Fe and H. (c) Coordination number of Fe (NC_{FeFe}) in liquid iron and $Fe_{0.96}H_{0.04}$ and H (NC_{HFe}) in $Fe_{0.96}H_{0.04}$. Results at different T (2,500-6,500 K) are included in panels (b) and (c).

j. *The influence of spin fluctuations on electronic transport properties of liquid iron (J.-A. Korell/Rostock, M. French/Rostock, G. Steinle-Neumann and R. Redmer/Rostock)*

Electrical (σ) and thermal conductivity (λ) of iron and iron alloys at conditions of the Earth's core play a vital role in assessing the efficiency of magnetic field generation and on the thermal evolution of Earth's core. Over the past decade, both simulations and experiments have suggested that their values are significantly higher than geodynamic models had previously assumed, leading to a wide-range of problems in powering the geodynamo. While values from *ab initio* simulations for σ agree with shock wave data at pressure $P > 100$ GPa and are consistent with some static experiments in the diamond anvil cell, at lower and especially at ambient P, computed values for σ and λ are significantly larger than experimental data (Fig. 3.5-13).

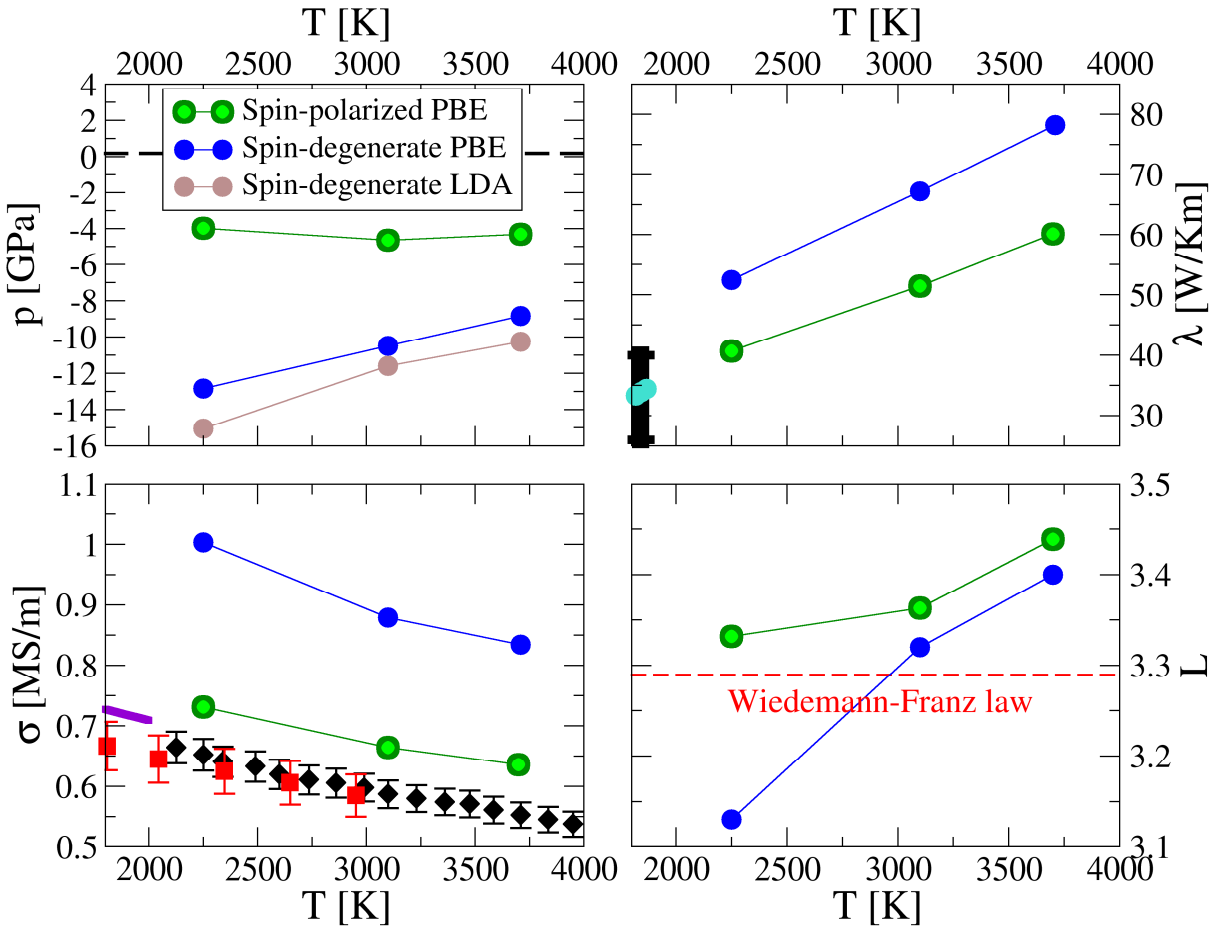

Fig. 3.5-13: Pressure (upper left panel) and transport properties at densities and temperatures of exploding wire experiments (0.2 GPa). Results from our simulations are for spin-polarized and spin-degenerate simulations as indicated in the legend. Measurements for electrical and thermal conductivity at ambient P are included with symbols. The lower right panel shows values computed for the Lorenz number ($L=\lambda/T\sigma$) and compares the results to the Drude-Sommerfeld value of $\pi^2/3$.

Previous *ab initio* computations were performed ignoring magnetism, but spin Hamiltonian models have predicted that disordered local moments in Fe persist to high P and temperature (T) based on entropy effects. Here, we address this issue in *ab initio* calculations by performing both the molecular dynamics simulations – to obtain uncorrelated liquid configurations – and the linear response calculations for transport properties taking spin-polarization into account. We perform computations for liquid iron at high T and ambient P by using experimentally determined molar volumes/densities. Our results show that unordered atomic magnetic moments persist to at least T = 3700 K, *i.e.*, that liquid Fe is in a paramagnetic state, and lead to a significant decrease in both σ and λ, bringing our results in good agreement with well constrained experimental data (Fig. 3.5-13). At the same time, pressures computed from the stresses on the simulation cells are significantly less negative for the spin-polarized cases, supporting the notion that magnetism plays an important factor in describing physical properties of liquid iron well beyond the melting point.

Our simulations show a loss of magnetic moments at $P \sim 50$ GPa, in agreement with predictions of the disappearance of magnetism in solid hcp iron. Beyond this P, the spin-polarized and spin-degenerate results become indistinguishable, confirming the validity of previous results on high values for σ and λ at core conditions from previous *ab initio* simulations.

3.6 Rheology

Rheology describes how materials deform and flow in response to an applied stress. The rheology of Earth's mantle, for example, is a fundamental property that controls the nature and rate of solid-state convection and thus processes such as the dynamics of plate tectonics and heat transport in Earth's interior. Because of its importance for understanding Earth processes, the rheology of Earth materials has been studied experimentally for many years. Conventionally this is done through deformation experiments whereby a rock or mineral sample is deformed by applying a known stress; strain rates are then measured as a function of variables such as temperature, pressure and microstructure. A significant problem with this approach is that experimental strain rates are many orders of magnitude faster than strain rates in the Earth. This means that very large extrapolations of experimental data are necessary in order to apply experimental results to Earth processes. The validity of such large extrapolations can be questionable.

Experimental deformation studies of olivine rheology have shown that water that is dissolved in its atomic structure has a large weakening effect. Thus, based on such studies, the viscosity of the upper mantle is considered to decrease significantly with increasing water content. The upper mantle likely deforms predominantly by the dislocation creep mechanism which is controlled by the rate at which dislocations are annihilated. The first study below takes an alternative approach to investigating the effect of water on olivine rheology by studying its effect on the rate of dislocation annihilation. It is found that water has, at most, a very small effect on rates of dislocation annihilation which means that its effect on mantle rheology should be small. Thus, these new results question the validity of the conclusions of high-strain-rate deformation studies.

Grain size is an important parameter that determines the deformation mechanism. When the grain size is small the dominant deformation mechanism is diffusion creep and when it is large dislocation creep dominates. Grain growth occurs under static conditions at high temperature and is driven by a reduction in grain boundary area and therefore grain boundary energy. Studies of the rate of grain growth of olivine have previously been pursued only at low pressures ($\leq$1 GPa). The second contribution below describe results obtained at much higher pressures of 1-12 GPa. The results show that high pressure has a significant effect in slowing rates of grain growth and could cause diffusion creep to be the dominant deformation mechanism in the deep upper mantle at depths greater than about 200 km.

Quantitative deformation experiments on minerals of Earth's mantle transition zone and lower mantle are technically very difficult because of the high pressures that are required. However, rheological behaviour can be estimated if rates of diffusion of silicon and oxygen are known because such diffusion is expected to control rheology. In the third project described below, rates of diffusion of silicon and oxygen have been measured in single crystals of Mg_2SiO_4 wadsleyite at 1300-1600 °C as a function of water content and crystallographic orientation. Water significantly enhances diffusion rates, in contrast to its effect on olivine. At water

concentrations < 1000 ppm, silicon is the slowest diffusing species whereas at higher concentrations oxygen becomes the slowest diffusing species.

Earth's lower mantle consists mainly of bridgmanite (silicate perovskite) with a relatively small volume fraction of (Mg,Fe)O ferropericlase. The latter is much weaker than bridgmanite and it has previously been believed that its presence would only affect the bulk rheology of the lower mantle if the ferropericlase grains are interconnected. The fourth project involves a computational study of the rheology of bridgmanite-ferropericlase aggregates as a function of the volume fraction of ferropericlase, the viscosity contrast between the two phases, and the extent by which ferropericlase grains are elongated. The results show that elongation of ferropericlase grains leads to a significant reduction in mantle viscosity even when the grains are not interconnected.

The final contribution in this section presents preliminary results of an experimental study designed to determine if the olivine-spinel phase transformation is the cause of deep-focus earthquakes and how it is affected by grain size. Deformation experiments have been performed on samples of Mg_2GeO_4 olivine, which is an analogue of silicate olivine that transforms to spinel at relatively low pressures.

a. *Precise determination of the C_{H2O} dependence of the rate of the annihilation rate of a-dislocations in olivine (A.D. Chanyshev, L. Wang, S. Blaha and T. Katsura)*

Olivine is the most abundant mineral of Earth's upper mantle and thus is considered to control upper mantle rheology. Plastic deformation of olivine is controlled by the motion of defects such as point defects, dislocations, and grain boundaries. In the upper mantle, dislocation creep is considered to be the dominant deformation mechanism. Therefore, understanding dislocation mobility in olivine is essential for investigations of mantle dynamics. Many deformation experiments have demonstrated that creep rates are dramatically increased by the incorporation of water into mineral structures. However, deviatoric stresses and strain rates in deformation experiments are orders of magnitude higher than those in the upper mantle, and therefore such results need to be examined by an independent technique other than deformation experiments.

Here we report the results of high-pressure dislocation recovery experiments on hydrous olivine as a function of water content and crystallographic orientation. The experiments were performed at 2.8-5.0 GPa and 1200 °C for 1-20 hours. Our results show that the dependence of the annihilation rate of *a*-dislocations on water content is both minor and negative (Fig. 3.6-1). The fitted water exponent is determined to be $r = -0.4 \pm 0.1$ (Pearson coefficient R = -0.77). Based on deformation experiments at conditions where dislocation creep is the controlling process, the exponent has been determined to be positive with $r = 1.2$.
At low water content (20 ppm), the viscosity in the upper mantle at 4 GPa was calculated to be 3.5×10^{19} Pa s, which is about one order of magnitude higher than estimated for $r = 1.2$. At high water concentrations of 400 ppm, the viscosity was calculated to be $5x10^{20}$ Pa s, that is about 2

orders of magnitude higher than estimated for r = 1.2. For r = -0.4 the viscosity increases slightly with increasing water concentration. Based on this study we conclude that water incorporated into the olivine structure has a negligible effect on upper mantle rheology.

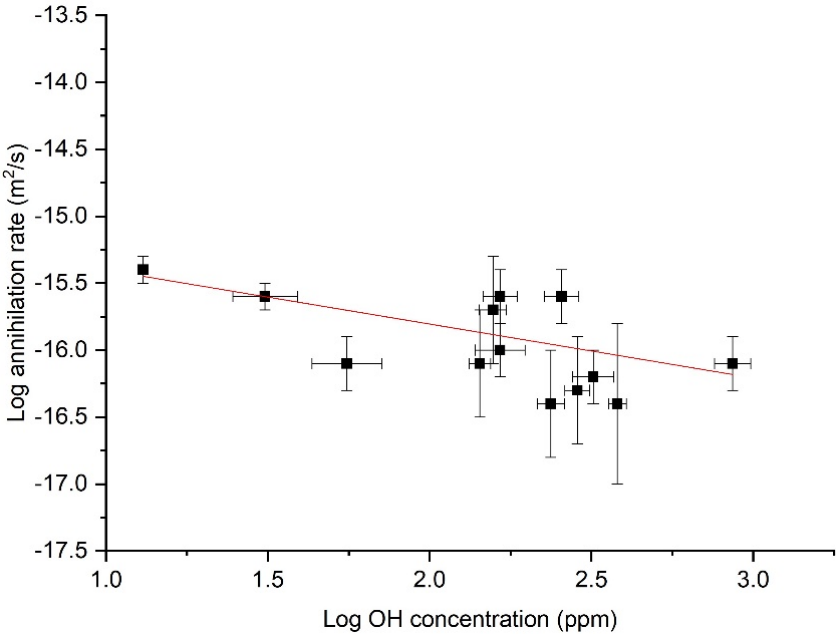

Fig. 3.6-1: Logarithmic dislocation annihilation rate of a-dislocations versus logarithmic OH concentration. The annihilation rate constant is determined to be r = -0.4 ± 0.1.

b. *Olivine grain growth kinetics at high pressure and temperature (F. Ferreira and K. Marquardt/London)*

Grain size is a fundamental property of a material that determines the dominance of different deformation mechanisms. For instance, deformation of olivine in the upper mantle is likely to occur by two distinct deformation mechanisms: dislocation creep (± grain boundary sliding) and diffusion creep. As diffusion creep is grain size dependent, a change in grain size, and by consequence a transition in deformation mechanism, could cause major changes to the viscosity of the upper mantle. The grain size in the upper mantle is a matter of debate, and is controlled by opposing factors: grain size reduction occurs mainly by stress-induced dynamic recrystallization, while on the other hand, grains grow in response to high temperature and time to minimize surface area/energy. Previous experimental data on grain growth kinetics of olivine is restricted to relative low pressures (≤1 GPa). In order to evaluate the effects of pressure on grain growth of olivine, we perform experiments at pressures ranging from 1 to 12 GPa at a fixed temperature of 1623 K. We found that the rate of grain growth decreases as pressure increases. At 7 GPa and 1623K, the rate of grain growth of olivine is similar to the growth rate at 1423K and 1 GPa, as previously reported. A further increase of pressure above 7 GPa does not substantially change the grain growth rate. These results suggest that a change of deformation mechanism from dislocation to diffusion creep in the upper mantle (depths > ~ 200 km) could be influenced by the inhibition of grain growth at high pressures.

c. *Silicon and oxygen self-diffusion coefficients in wadsleyite (D. Druzhbin, H. Fei, R. Dohmen/Bochum, Y. Lin/Beijing, C. Zhang/Beijing and T. Katsura)*

Wadsleyite, a high-pressure polymorph of olivine, is one of the most abundant minerals in the upper part of the Earth's mantle transition zone (depth range 410-520 km) and is the main constituent mineral of subducting slabs at such depths. Although silicon and oxygen diffusion in wadsleyite has been studied previously, a robust evaluation of the effect of H_2O content on rates of diffusion in wadsleyite has not been determined. In addition, previous diffusion data were obtained using polycrystalline samples. Even with a special mathematical approach developed to determine volume diffusivity from obtained diffusion profiles, grain-boundary diffusion may overlap with volume diffusion concentration profiles, which can lead to the determination of incorrect diffusion coefficients. So far, there has been no study of the anisotropy of the self-diffusion of silicon and oxygen in wadsleyite. Its orthorhombic structure suggests that diffusion might be significantly anisotropic (though that has not been observed in olivine). Considering all of the above, the primary goal of this work was to study silicon and oxygen volume diffusion in wadsleyite single crystals with a wide range of water contents and for different crystallographic orientations.

In order to avoid grain-boundary diffusion, all diffusion annealing experiments were conducted using previously-synthesized single crystals of Mg_2SiO_4 wadsleyite. Sample synthesis and the sample preparation procedures have been described in previous reports. Thin films with a thickness of 500-600 nm and an ^{18}O and ^{29}Si enriched Mg_2SiO_4 composition were deposited on the polished faces of Fe-free wadsleyite crystals by a pulsed laser deposition technique at the Institute of Geology, Mineralogy and Geophysics at Ruhr-Universität Bochum. For diffusion experiments, each sample was loaded in a gold capsule with an outer diameter of 2 mm and inner diameter of 1.8 mm. Gold powder was used as a surrounding buffer to maintain a near hydrostatic stress and prevent crystal damage at high pressure. A small amount of dry, pure $MgSiO_3$ enstatite powder was placed in contact with the end of the sample opposite to that on which diffusion was occurring. The experiments were performed using a Kawai-type multianvil apparatus at 1600, 1400 and 1300 °C and at 20, 19, and 18.5 GPa. The annealing durations varied from 10 minutes to 10 hours.

The isotopic depth profiles were analyzed by NanoSIMS (Cameca NanoSIMS 50L instrument in Institute of Geology and Geophysics, Chinese Academy of Sciences, Beijing). The depth of the craters was determined using a 3D-Nanofocus confocal microscope. Diffusion coefficients D_{Si} and D_{Si} were obtained by fitting Fick's second law to the depth profiles:

$$C(x,t) = \frac{C_0 + C_1}{2} - \frac{C_1 - C_0}{2} \cdot \mathrm{erf}\left(\frac{x-h}{\sqrt{4D^{\mathrm{V}}t + L_0^2}}\right)$$

where C_1 is the initial ratio of isotopic concentrations in the thin film, C_0 is the initial ratio of isotopic concentrations in the single crystals, x is the distance from the surface (depth), h is the diffusion interface position (boundary between isotopically enriched film and the crystal), L is

the diffusion length in zero-time diffusion experiments, related to surface roughness. The resulting diffusion coefficients for Si and O in wadsleyite as a function of temperature are shown in Fig. 3.6-2. The activation enthalpies for Si and O diffusion are similar: $\Delta H_O^V = \Delta H_{Si}^V = 170(90)$ kJ/mol. The measurements show that Si and O volume diffusivities are strongly dependent on water content and are anisotropic (Fig. 3.6-3): $D_{Si}^V(100) \propto C_{H_2O}^{0.6}$, $D_{Si}^V(010) \propto C_{H_2O}^{1.9(2)}$, $D_{Si}^V(001) \propto C_{H_2O}^{5.2(5)}$; $D_O^V(100) \propto C_{H_2O}^0$, $D_O^V(010) \propto C_{H_2O}^{0.5(2)}$, $D_O^V(001) \propto C_{H_2O}^{3.5(4)}$.

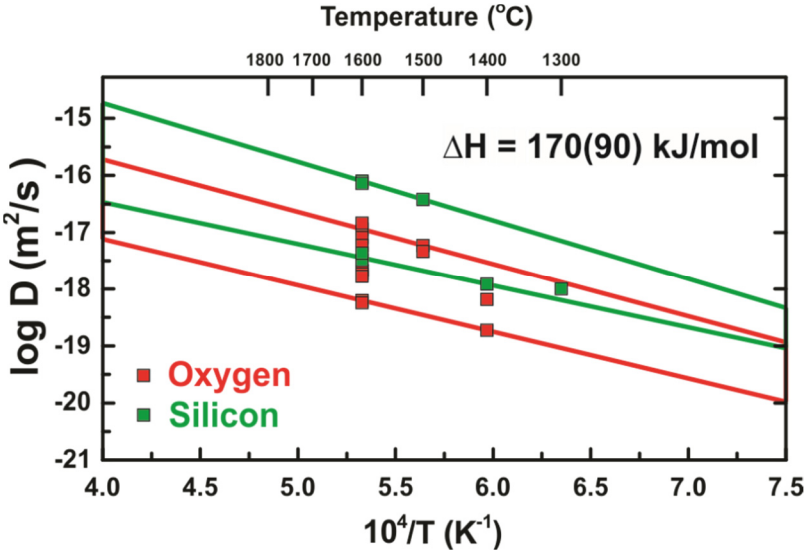

Fig. 3.6-2: Si and O volume diffusion coefficients (in log units) in Mg_2SiO_4 wadsleyite as a function of temperature. Solid lines represent Arrhenius fitting.

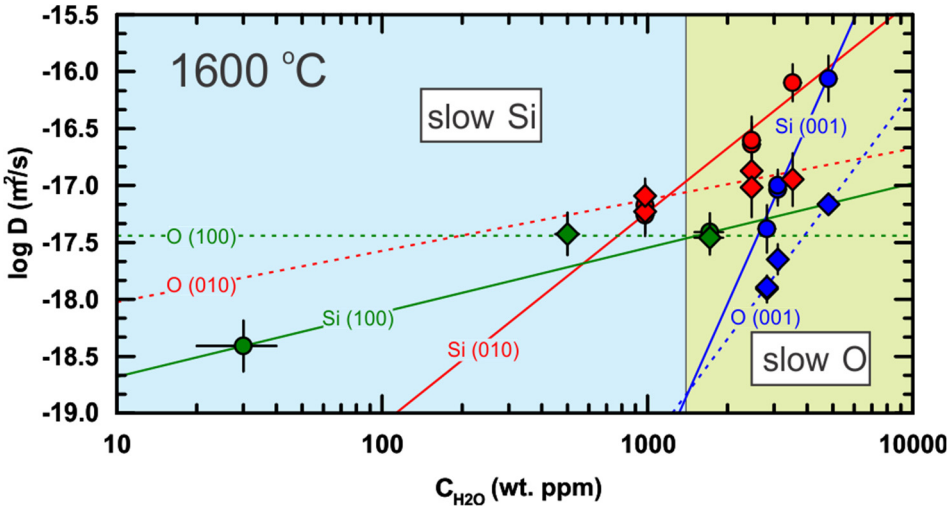

Fig. 3.6-3: Si and O volume diffusion coefficients (in log units) in Mg_2SiO_4 wadsleyite as a function of water content. The solid and broken lines denote Arrhenius fits for Si (round symbols) and O (diamonds) diffusivities. The green, red and blue symbols denote a, b and c crystallographic directions, respectively. The blue zone corresponds to water concentrations where Si diffusion is the slowest and the green zone where O diffusion is slowest.

d. *Ferropericlase control of lower mantle rheology (M. Thielmann and G.J. Golabek, in collaboration with H. Marquardt/Oxford)*

The rheological properties of Earth's lower mantle play a key role in controlling global mantle dynamics. The mineralogy of the lower mantle can be approximated as a two-phase mixture of bridgmanite and ferropericlase. Previous work has suggested that the deformation behaviour of the two-phase mixture might be dramatically affected by the large differences in viscosity between high-viscosity bridgmanite and low-viscosity ferropericlase and resulting stress-/strain-partitioning effects. Here, we employ numerical models to establish a connection between the distribution of ferropericlase and the effective rheology of the Earth's lower mantle using a numerical-statistical approach. This approach consists of three steps:

(1) Employing a statistical measure (given by the 2-point cluster function) to characterize the morphology of ferropericlase-bridgmanite mixtures. This measure essentially reduces the complicated random morphology of these mixtures to an ellipse with an aspect ratio r and an inclination θ.

(2) Combining the properties of this statistical measure with simplified analytical approximations for two-phase mixtures with aligned elliptical inclusions to predict the effective viscosity of ferropericlase-bridgmanite mixtures.

(3) Direct numerical modeling of random ferropericlase-bridgmanite mixtures with different morphologies. For statistical significance, we artificially generate a large number of samples for different values of r using random correlated fields and compute their normal and shear viscosities η_n and η_s.

Results show that the analytical approximations are capable of predicting the normal and shear viscosities η_n and η_s of the modeled ferropericlase-bridgmanite mixtures (Fig. 3.6-4), thus providing a link between their morphologies and viscosity. While our findings confirm previous endmember models that suggested a change of mantle viscosity due to interconnected weak layer formation, we show that the effective viscosity changes continuously with elongation of the weak ferropericlase phase. Even without forming an interconnected weak layer, the bulk viscosity is significantly reduced when ferropericlase grains are elongated.

Besides its effect on bulk viscosity, the alignment of weak ferropericlase grains leads to a pronounced viscous anisotropy that develops with bulk strain. The development of viscous anisotropy may have implications for understanding the viscosity structure of Earth's lower mantle as well as for modelling the behaviour of subducting slabs.

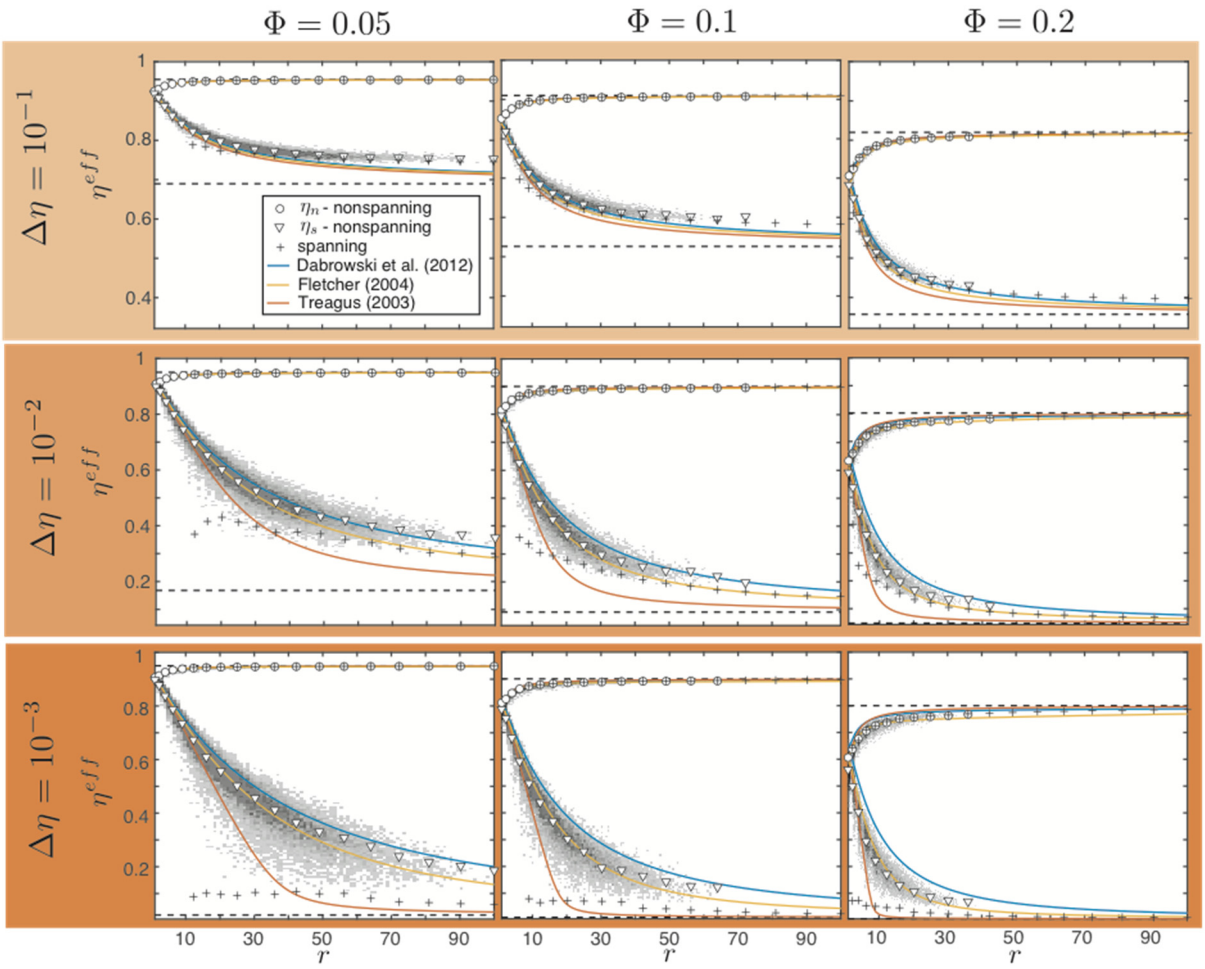

Fig. 3.6-4: Effective viscosity of ferropericlase-bridgmanite mixtures as a function of ferropericlase morphology (given by the aspect ratio r), ferropericlase volume fraction Φ, and viscosity contrast between bridgmanite and ferropericlase $\Delta\eta$. Shown are the effective normal and shear viscosities η_n and η_s as a function of the aspect ratio r. Grey colors indicate the frequency of η_n and η_s determinations for a given aspect ratio (and only for nonspanning clusters, *i.e.*, non-interconnected ferropericlase inclusions), with darker and less transparent colors indicating higher frequencies. White symbols indicate a fit to the maxima of the frequency distribution. Crosses indicate the results for spanning clusters (*i.e.*, interconnected ferropericlase networks). Dashed lines indicate the Reuss and Voigt bounds. Solid lines denote the aDEM approximation by Dabrowski *et al.* (2012) and the SCA approximations by Treagus (2003) and Fletcher (2004) .

e. *Experimental investigations of the mechanism of deep-focus earthquakes (S. Sawa, J. Muto and H. Nagahama/Sendai, N. Miyajima)*

Deep-focus earthquakes occur at depths that range from 440 km to 660 km in subducting slabs. A number of theories have been proposed concerning the mechanism of deep-focus earthquakes, but based on geophysical observations and deformation experiments, the olivine-spinel phase transformational faulting mechanism may be the precursor of deep-focus

earthquakes. According to this mechanism, metastable olivine undergoes phase transformation to fine-grained spinel and a shear instability results because of the small spinel grain size. The initial grain size of olivine may be important in controlling the pressure- and temperature-conditions of the phase transformation and thus the regions where the deep-focus earthquakes occur. However, previous studies have not investigated the effect of the initial grain size of metastable olivine on the phase transformational faulting mechanism. Therefore, we are conducting deformation experiments on germanate (Mg_2GeO_4) olivine with different grain sizes. (Germanate olivine is an analogue of silicate olivine that undergoes the phase transformation to spinel at much lower pressures than silicate olivine.)

We prepared two sets of germanate olivine aggregates with different grain sizes: sample A: < 10 μm and B: > 30 μm. So far, we have conducted deformation experiments on sample A with a Griggs-type solid-confining media deformation apparatus. Confining pressure, temperature and strain rate are 1.2 GPa, 500 ~ 800 °C, 2.0×10^{-4} s^{-1}, respectively. The recovered samples were examined with a scanning electron microscope (SEM), micro-Raman spectroscopy and transmission electron microscope (TEM).

We observed shear instability events with apparent stress drops only at temperatures of 600 and 700 °C. SEM observations show the presence of several faults in these two samples (Fig. 3.6-5). Micro-Raman spectroscopy showed that germanate olivine deformed at temperatures lower than 700 °C hardly underwent any phase transformation whereas germanate olivine deformed at temperatures higher than 700 °C underwent complete phase transformation to spinel. TEM observations show the presence of small platelets (< 50 nm in size) along a fault in the sample deformed at 600 °C (Fig. 3.6-6a). On the other hand, we have not observed such platelets in the sample deformed at 700 °C (Fig. 3.6-6b). According to FTIR measurements, the sample contained a small amount of water. Based on the water content and the diffraction pattern of the platelets, they probably consist of germanate serpentine.

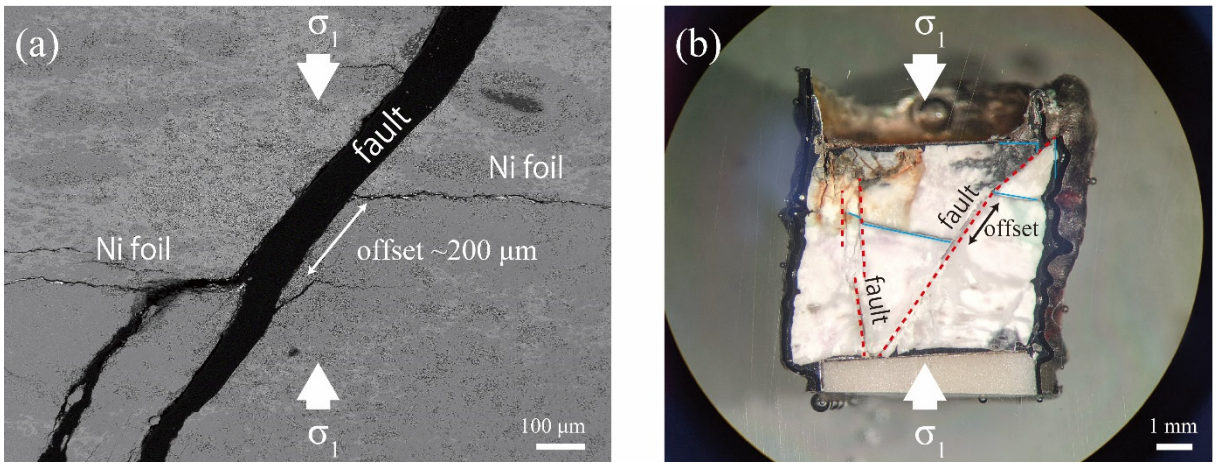

Fig. 3.6-5: (a) Back-scattered electron image of a fault in the sample deformed at 600 °C. A Ni foil is displaced by 200 m by the fault. (b) Optical image of the sample deformed at 700 °C. Several faults are observed.

Our results imply that the viscosity of the platelets is lower than that of the surrounding germanate olivine, so that faults in the sample deformed at 600 °C may form due to strain localization where fine-grained germanate serpentine crystallizes. However, we observed neither nanocrystalline spinel nor fine-grained materials such as small platelets in the sample deformed at 700 °C. The faulting mechanism of the sample deformed at 700 °C is therefore unclear.

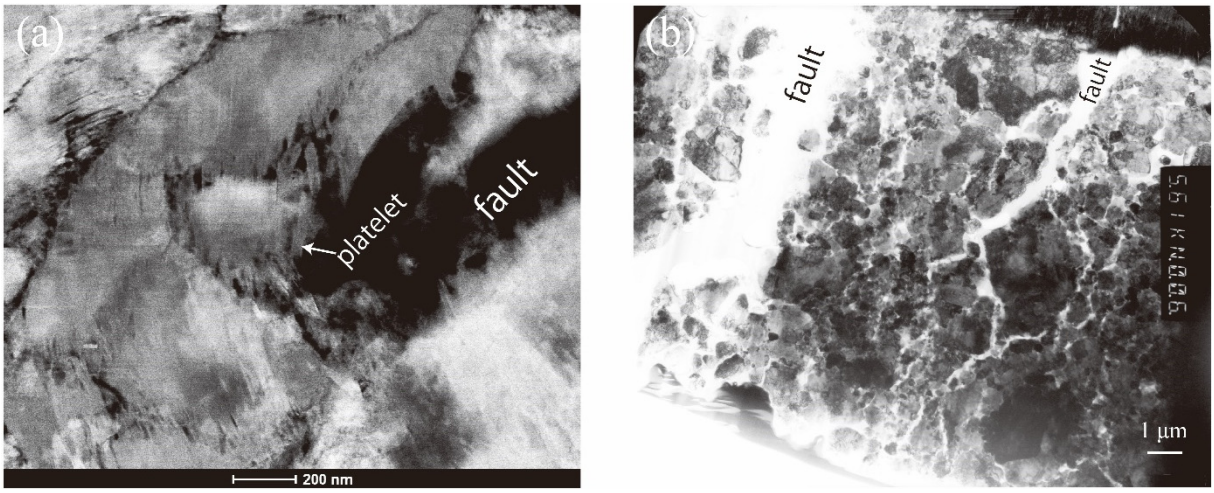

Fig. 3.6-6: (a) Dark field STEM image of the sample deformed at 600 °C. Many platelets are observed near the fault. (b) Bright field TEM image of the sample deformed at 700 °C. A mixture of rounded fine-grained and coarse-grained germanate spinel is observed.

3.7 Material Science

Compression is a powerful tool to add energy to a system that can transform the structure and properties of inorganic solid compounds in ways that are not accessible in ambient-pressure chemistry. The Bayerisches Geoinstitut is equipped with a unique combination of high-pressure experimental devices and methods for *in situ* and *post mortem* characterization of samples that give access to physical and chemical properties of materials synthesized this way. In terms of methodological development, the highlight of the year is the ability to perform *in situ* X-ray diffraction studies at pressures exceeding 100 GPa which is used in a number of studies presented in this section of the Annual Report.

To this day, diamond remains the hardest material known due to the strong sp^3-bond between the carbon atoms, and various pathways for the synthesis to the sp^3-bonded carbon systems from sp^2-bonded starting materials have been explored. The first contribution of this section continues this type of study by using C_{60} as a starting material. At 30 GPa, the experiments reveal that the sp^3-bonded run product shows medium-range order, bridging the gap between amorphous and crystalline diamond.

Nitrogen-based compounds show great potential, ranging from abrasives with exceptional hardness to ultrahigh-performing propellants and explosives with high energy density. Occurring in a variety of forms (isolated N as nitrides, N_2 pernitride molecules and polynitrogen entities), nitrogen is a particularly interesting alloying element. Despite significant advances in conventional chemistry, high pressure provides an alternative route to create nitrogen-bearing materials with exceptional properties. Three contributions look at nitrogen incorporation into rhenium and magnesium metals. The high-pressure studies presented here report the synthesis of a novel type of compound in which nitrogen occurs both as nitride and pernitride, induce and track a chemical reaction in the TPa range, and synthesize high energy density salts MgN_4 and Mg_2N_4. In the latter, nitrogen forms N_4^{4-} entities that can be quenched to ambient conditions, providing a potential new building block for the synthesis of energetic materials. The subsequent study on rhenium carbides complements the work on the rhenium-nitrogen compounds as it illustrates similarities and differences between these two systems and links to the C-bonding in the first contribution.

With the discovery of high-temperature superconductivity at high pressure in the sulfur-hydrogen system, hydrides have become an important subject in high-pressure physics. Their study has been aided by the development of proton nuclear magnetic resonance (NMR) spectroscopy in the diamond anvil cell at Bayerisches Geoinstitut over the past few years. Two studies on hydrides are presented in this section. The first one looks in detail at phases occurring in the sulfur-hydrogen system, confirming the presence of two phases with different stoichiometry existing in the pressure-range in which superconductivity has been observed. This coexistence can largely explain varying properties described in different experimental studies. With the NMR technique using copper resonators in the diamond anvil cell, the possible reaction between copper and hydrogen is a concern as it may influence measurements on other metal hydrides. This is addressed by the synthesis and direct characterization of copper hydrides

in the diamond anvil cell: two CuH_x structures are described in the experiments, covering a pressure-range of 35 to 150 GPa both a room and high temperature.

Iron oxides with exotic stoichiometries synthesized and characterized over the past decade – including significant work performed at Bayerisches Geoinstitut – have ignited interest in the behaviour of other transition metal oxides. Here, a study on the high-pressure phase and physical properties of Mn_3O_4 is presented that shows this phase to become – unexpectedly – a narrow bandgap semiconductor. In hydrous environments, transition metal anions typically adopt their highest oxidation state and form hydrites of oxyhdroxydes, for iron this is FeOOH goethite, an important ore mineral. The possible transport of this phase into the Earth's deep interior gives its properties geophysical and geochemical significance. In diamond anvil cell experiments, samples are often loaded with salts as a pressure-transmitting medium, and no reaction is assumed between these two materials. The final contribution in this section, however, demonstrates that FeOOH and NaCl react at high pressure and from a complex compound, putting prior experimental results in question.

a. *Synthesis of disordered diamond with medium-range order from C_{60} (H. Tang and H. Gou/ Beijing, T. Katsura, H. Fei, and T. Ishii)*

Carbon is one of the most variable elements, forming a wide range of allotropes with sp^1-, sp^2-, and sp^3-hybridized bonds. Over the past decades, the discoveries of numerous allotropes for sp^2-bonded carbon have attracted considerable attention due to the interesting properties and promising applications, sorted by morphological differences: zero-dimensional (0D) fullerenes, one-dimensional (1D) carbon nanotube, two-dimensional (2D) graphene, and there-dimensional (3D) graphites (including graphite, glassy carbon and amorphous carbon). By contrast, for sp^3-bonded carbon the 4-fold coordinated carbon atom determines a single 3D network structure. All sp^3-bonded carbon allotropes (such as hexagonal and M-diamonds) are variants of cubic diamond by distortion of C-C bonds. Even so, the sp^3 carbon allotropes attract widespread attention due to the unique properties, such as cubic diamond with the highest hardness and highest thermal conductivity. The theoretical search for sp^3-bonded allotropes has seen considerable progress, but the proposed structures have rarely been experimentally confirmed. The key to understanding this problem is that sp^3-carbon is always thermodynamically stable at high pressure and metastable at ambient conditions. Therefore, most of discoveries of sp^3-bonded allotropes are achieved by compressing sp^2 carbons, using diamond anvil cell technology combined with *in situ* characterization techniques, such as Raman spectroscopy, X-ray diffraction (XRD) or X-ray scattering.

Unlike long-range order (LRO) crystals, amorphous materials are highly disordered in structure – with short-rang ordered (SRO) clusters (2-5 Å) – and show a variety of interesting properties including high strength, elasticity and hardness. The sp^3-bond in carbon is the strongest 3D covalent bond, and amorphous diamonds are therefore expected to have superior properties, especially in hardness. Due to limitations in bulk size, the high hardness has remained elusive. In order to provide appropriate samples to address this issue, we have synthesized large-size

disordered diamond from C_{60} at 30 GPa and 1400-1800 K in the large-volume press. The nanostructure and bonding of the sample was analyzed in-house by XRD, Raman spectroscopy and transmission electron microscopy using electron energy loss spectra (Fig. 3.7-1). The analysis reveals medium-range order at a length scale of 5-20 Å, between SRO in amorphous materials and LRO in crystal, a feature that can be observed similarly in some amorphous metals. The synthesis of a new form of sp^3-bonded carbon at high temperature and pressure illustrates a possible pathway to new diamond-like allotropes and to understanding the underlying phase transition mechanisms.

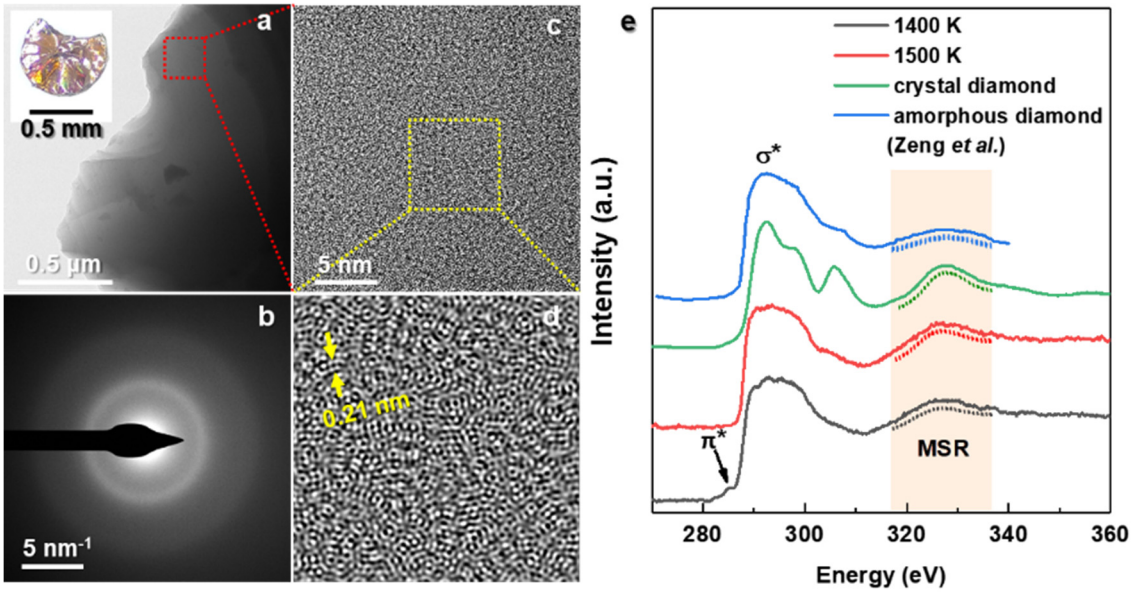

Fig. 3.7-1: Transmission electron microscopy (TEM) and electron energy loss spectra (EELS) of the carbon samples synthesized under 30 GPa and 1400-1500 K. (a) TEM image of the sample with the inset showing an optical photograph, indicating that the sample has a diameter of 0.7 mm and is transparent in the visible light range. (b) Selected area electron diffraction pattern for the red box in panel (a). (c) High-resolution TEM image of the area marked with the red box in panel (a). (d) Inverse fast Fourier transform image corresponding to the yellow box marked in panel (c). (e) EELS of crystalline diamond, amorphous diamond, and the samples synthesized here. The feature centered at ~ 330 eV is identified to be a multiple scattering resonance (MSR) peak due to the excited wave backscattered from the parent atom's second nearest neighbors.

b. *High-pressure synthesis of ultraincompressible hard rhenium nitride pernitride ReN_2 stable at ambient conditions (M. Bykov, S. Chariton and H. Fei, T. Fedotenko and G. Aprilis/Bayreuth, A.V. Ponomareva/Moscow, F. Tasnádi and I.A. Abrikosov/Linköping, B. Merle and P. Feldner/Erlangen, S. Vogel and W. Schnick/Munich, V.B. Prakapenka and E. Greenberg/Chicago, M. Hanfland/Grenoble, A. Pakhomova and H.-P. Liermann/Hamburg, T. Katsura, N.A. Dubrovinskaia/Bayreuth and L.S. Dubrovinsky)*

As diamond is the naturally occurring prototype of a superhard material, the standard approach to new superhard materials is to mimic its crystal structure and bonding. Due to localized

electron density, these materials are wide band-gap insulators. However, some technological applications require superhard conductive materials, which are much less common. An alternative strategy to synthesize superhard materials is based on the modification of ultra-incompressible, but not hard compounds, a strategy that we pursue here: At high pressure, we combine the heavy transition metal rhenium – itself quite incompressible but not hard – with nitrogen that forms directional covalent bonds. The resulting compound with the nominal composition ReN_2 is a very hard, incompressible but also conductive material.

To synthesize ReN_2, rhenium metal was loaded into a diamond anvil cell (DAC) with nitrogen that served both as a pressure-transmitting medium and as a reagent. The sample was then laser-heated at 42 GPa and the course of the reaction was monitored *in situ* by single-crystal X-ray diffraction using synchrotron radiation. Drastic changes of the diffraction pattern clearly indicate that rhenium reacted with nitrogen and we were able to identify the crystal structure of the reaction product. Unlike nitrides and pernitrides, this compound exhibits a very peculiar crystal structure as it contains isolated nitrogen atoms – similar to "standard" interstitial nitrides – and covalently bound dinitrogen units (Fig. 3.7-2). Therefore, this compound is a nitride pernitride – the first of a kind. Compressibility measurements show that ReN_2 is an ultra-incompressible compound with a bulk modulus of 428 GPa (Fig. 3.7-2) – almost reaching values of diamond.

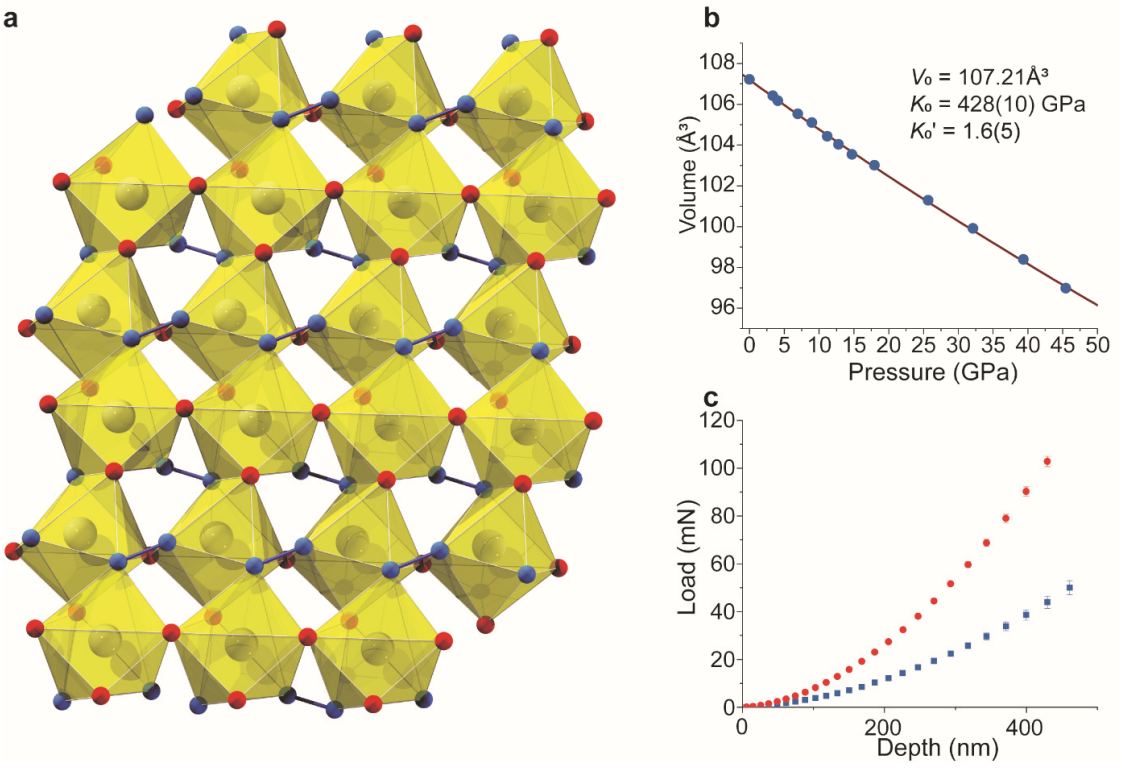

Fig. 3.7-2: (a) Crystal structure of ReN_2 at ambient conditions. Blue spheres show nitrogen atoms that form covalently bound N-N units, red spheres isolated N atoms. ReN_7 polyhedra are shown in yellow. (b) Pressure-dependence of the unit-cell volume of ReN_2. The solid line shows the fit of the third order Birch–Murnaghan equation of state to the experimental data. (c) Average indentation load-displacement data for Re (blue squares) and for ReN_2 (red circles).

A key challenge for high-pressure synthesis of materials is scalability. The size of a pressure chamber in a DAC is limited to a few tens of microns not allowing the synthesis of bulk samples. We solve the problem of scaling up the synthesis by using a solid nitrogen precursor, ammonium azide NH_4N_3, that was sealed with Re metal in a capsule of a multianvil (MA) apparatus. The synthesis at 33 GPa results in polycrystalline ReN_2 of the size sufficient for hardness and electrical resistance measurements. The developed method for scaling up the synthesis of ReN_2 in the MA press using NH_4N_3 may be applied for producing nitrides of other transition metals, with samples large enough for physical property measurements.

Nanoindentation measurements allow to determine the hardness and Young's modulus of the material from the dependence of the indenter displacement (200 and 400 nm) on the applied load. The average hardness and Young's modulus are 36.7(8) GPa and 493(14) GPa, respectively (Fig. 3.7-2). Hardness approaching 40 GPa – a threshold for superhard materials – and an extreme stiffness – comparable to that of diamond – makes the mechanical properties of ReN_2 exceptional among metal nitrides. ReN_2 can be thought of as a composite material on an atomic level, where nitrogen atoms and molecules are inserted into the metallic Re matrix. It is this combination of interstitial nitride anions and covalently bound pernitride units that makes this compound ultra-incompressible and extremely hard at the same time. Electrical conductivity measurements demonstrate that ReN_2 is conductive, an extremely rare property for superhard compounds.

c. *Chemical synthesis at sub-TPa range: Novel rhenium nitride obtained in laser-heated ds-DAC (L.S. Dubrovinsky, S. Khandarkhaeva, T. Fedotenko/Bayreuth, A. Kurnosov, N.A. Dubrovinskaia/Bayreuth, S. Petitgirard/Zurich, P. Sedmak/Grenoble, V.B. Prakapenka and S. Chariton/Chicago)*

Hundreds of years of systematic research, reinforced by contemporary diffraction and spectroscopic methods and detailed quantum mechanical investigations allow a characterization of atomic structures and electronic states of inorganic compounds and provide a fundamental understanding of solid chemistry at ambient (or close to ambient) pressure. However, a major portion of condensed matter in the Universe exists under much higher pressures, deep inside planets and stars. Theoretical modelling predicts very unusual chemical and physical properties of materials subjected to pressures over several hundred gigapascal. Still, experimental studies on chemical reactions of matter at such conditions has been considered unrealistic for obvious reasons: there are no examples of successful (laser) heating at static pressures over 500 GPa (without high temperatures chemical reactions at such compression are unlikely), and characterizing the composition of reaction products at really extreme conditions has not been feasible. Here we report the synthesis of a novel rhenium nitride, Re_7N_3, from elements in the laser-heated double stage diamond anvil cell (ds-DAC) in the terapascal pressure range.

Originally, the experiment presented here was designed to use toroidal anvils. Conventional Boehler-Almax type single beveled diamond anvils with 80 μm culets were milled by FIB in

order to produce a toroidal surface on the central culet (~ 10 µm in diameter). We used 0.20 mm thick Re foil as gaskets material, indented to a thickness of ~ 4 µm by a procedure based on multiple indentations. The sample chamber was formed by drilling a ~ 6 µm hole with FIB in the center of the indented section. Few grains of rhenium powder were loaded into the pressure chamber, and N_2 at about 1.4 kbar was loaded using high-pressure gas-loading set-up at BGI. Four attempts were made to compress the cell, but each time at pressures between 50 to 70 GPa the toroidal culets started to misalign, resulting in a loss of nitrogen and hole collapse. Eventually, the toroidal culets on each anvil were destroyed, leaving flat surfaces of ~ 15 µm in diameter. In order to continue the experiment, two half-spheres prepared by FIB-cutting of a transparent nanocrystalline diamond sphere with diameter of ~ 14 µm were placed in the center of the toroidal parts of the anvils, and used with a rhenium gasket prepared for toroidal culets. As such, the resulting DAC combined design elements of the toroidal anvils and the ds-DAC assemblies. The cell was loaded with N_2 and Re powder, and starting pressure in the chamber measured after closing the cell in the gas-loading device was about 78 GPa. After compression to ~ 130 GPa on first-stage anvils, the cell was transferred to 13-IDD at GSECARS (APS, USA). Powder X-ray diffraction data showed hexagonal Re with lattice parameters a=2.2527(3) Å, c=3.5934(8) Å, V=15.793(5) Å^3. Depending on the choice of the equation-of-state for Re, this corresponds to a pressure between 930 GPa to 1298(10) GPa. At this pressure the sample was twice laser-heated and further investigated at ID11 at ESRF (Grenoble, France).

Single crystal diffraction patterns collected at ID11 from a number of locations in the sample area show numerous spots, and the analysis reveals the presence of two phases. The first phase is hexagonal Re (space group *P6₃/mmc*) (Fig. 3.7-3), and using 64 reflections its lattice parameters are determined as a= 2.2546(7) Å, c= 3.6142(13) Å, V=15.91(1) Å^3 (pressure of 905(5)-1240(15) GPa): Re recrystallizes from the liquid after heating, and not contaminated by carbon or nitrogen (at least in quantities detectable in our data). The second phase found in the

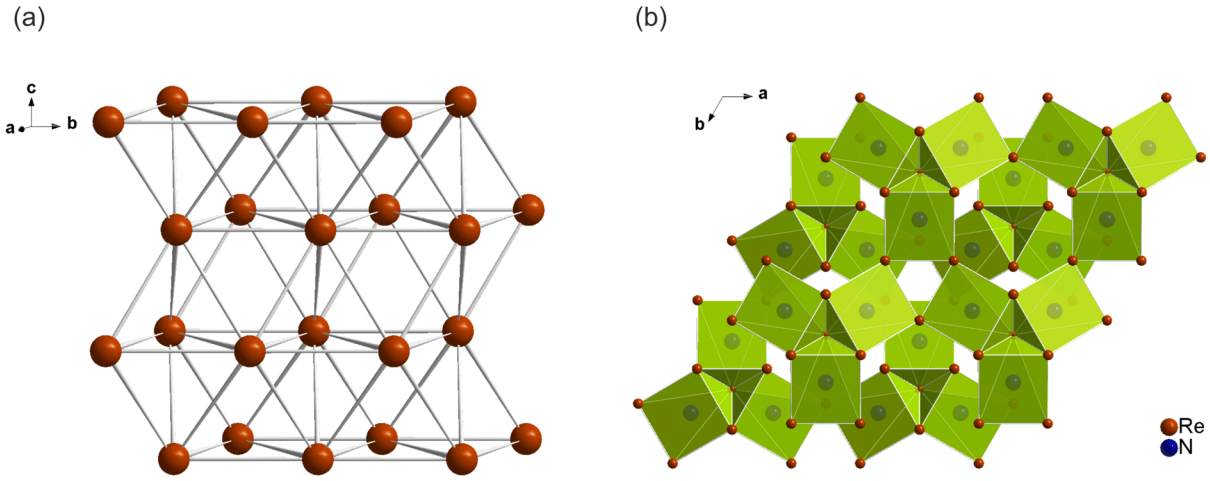

Fig. 3.7-3: Crystal structures of Re (a) and Re_7N_3 (b) observed in dsDAC after pulsed laser heating of rhenium and nitrogen at sub-TPa pressures. Nitrogen atoms occupy prismatic sites in crystal structure of Re_7N_3.

ds-DAC after heating is also hexagonal (space group *P6₃mc*) and has lattice parameters *a*=6.278(2) Å, *c*=4.000(2) Å, *V*=136.57(9) Å^3. Based on 394 independent reflections, the structure of this phase is solved and refined in the anisotropic approximation for heavy atoms to R1=7.7 %, with a composition of Re_7N_3 (Fig. 3.7-3). Considering a possible reaction between rhenium and carbon from the anvils as an alternative, we checked whether Re_7C_3 carbide was synthesized instead of a nitride; however, the isotropic thermal parameter of carbon become negative, supporting the assignment of the atomic position to nitrogen. The structure units of Re_7N_3 are distorted NRe_6 trigonal prisms (Fig. 3.7-3), with three prims connected through shared vertices in a triad. Triads are arranged in layers perpendicular to the 6_3-axis, and triads in neighboring layers are rotated by 60° with respect to each other (Fig. 3.7-3). If each triad is represented by a sphere, the spheres would form a hexagonal closed packed structure.

d. *Pressure-formed novel polynitrogen specie in the Mg-N_2 system (D. Laniel/Bayreuth, B. Winkler/Frankfurt, E. Koemets, T. Fedotenko/Bayreuth, M. Bykov, L.S. Dubrovinsky and N.A. Dubrovinskaia/Bayreuth)*

Due to their potential as ultrahigh-performing propellants and explosives, the study of polynitrogen compounds has been a very active field for chemical studies. Despite remarkable breakthroughs over the past two decades, conventional chemical methods have fallen short of fully exploiting their potential. Pressure, however, has recently been demonstrated to permit the synthesis of exotic and highly energetic novel polynitrogen (poly-N) entities with relevance as high energy density materials (HEDM). Indeed, the $[N_5]^-$ species, synthesized as LiN_5, was obtained at moderate pressure (< 50 GPa) and could be recovered at ambient conditions. Based on this success, alkaline earth metals mixed with N_2 were thought to be the next logical step to produce even better performing nitrogen-based HEDM on account of their low ionization energy and their preferred oxidation state of 2+.

In this investigation, magnesium and molecular nitrogen were compressed to about 50 GPa and laser-heated to above 2000 K. Under these conditions, Raman spectroscopy and single-crystal X-ray diffraction from multigrain samples reveal the formation of two new Mg-N salts of polynitrogen anions: MgN_4 and Mg_2N_4 (Fig. 3.7-4). Infinite anionic polythiazyl-like 1D N-N chains were determined to form the MgN_4 solid, at half the pressure previously shown necessary for this type of chains in ReN_8•xN_2 (106 GPa). The Mg_2N_4 compound was found to be comprised of an exotic *cis*-tetranitrogen N_4^{4-} entity, never experimentally synthesized before or predicted by theoretical calculations. For both Mg-salts, the N-N distances and Raman modes indicate a N-N bond order close to one, suggesting the highly energetic nature of these species.

Following their synthesis, the Mg-N samples were decompressed in order to determine the stability domain of Mg_2N_4 and MgN_4 solids. The Raman modes of MgN_4 could be identified to ~ 1 GPa, below which they disappeared. For Mg_2N_4, an isostructural phase transition was observed below 2 GPa, retaining the energetic N_4^{4-} unit in the recovered sample.

This investigation adds the $(N_4)^{4-}$ anion to a yet very short list of bulk poly-N entities stabilized at ambient conditions. As such, the tetranitrogen anion can spark further research in producing improved energetic polynitrogen compounds. Moreover, these results underline the potential and possibilities that are enabled by high-pressure chemistry, along with its applicability to produce compounds compatible with ambient conditions.

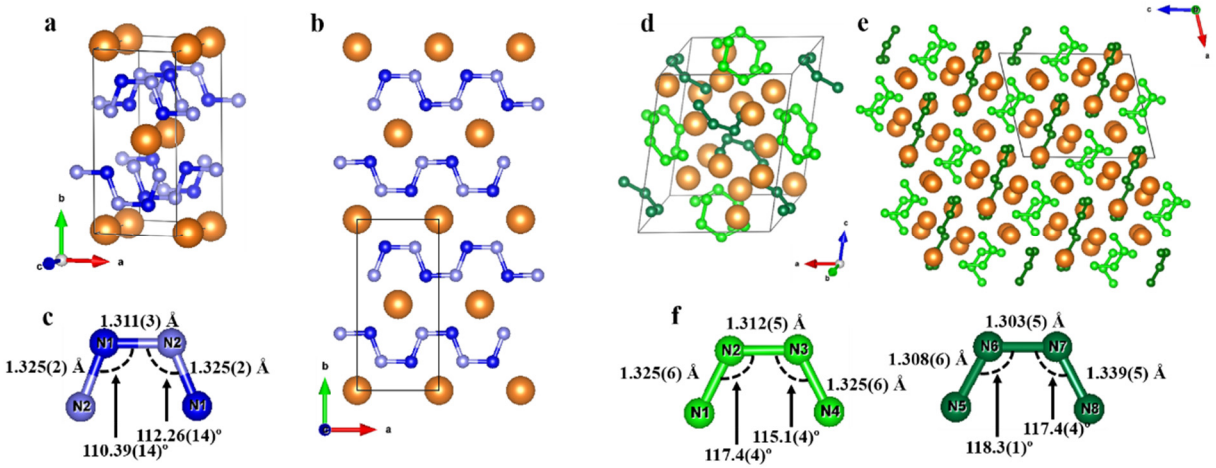

Fig. 3.7-4: Crystal structure of the MgN_4 and Mg_2N_4 salts at 58.5 GPa. (a) The unit cell of MgN_4 (light blue, dark blue and orange spheres represent the N1, N2 and Mg atoms, respectively); (b) a projection of the MgN_4 structure along the *c*-axis, emphasizing 1D chains of nitrogen atoms aligned along the *a*-axis; (c) a repeating N_4^{2-} subunit of a chain with the N-N distances and angles indicated; (d) the unit cell of Mg_2N_4 (light green and dark green spheres represent the four distinct nitrogen atoms forming the *a*-N_4^{4-} and *b*-N_4^{4-} units, respectively, the orange spheres show Mg atoms); (e) a projection of the Mg_2N_4 structure along the *b*-axis allowing to see the alternating layers of isolated *a*-N_4^{4-} and *b*-N_4^{4-} units, intercalated with Mg^{2+} ions. (f) The *a*-N_4^{4-} (left) and *b*-N_4^{4-} (right) entities with bond lengths and angles indicated.

e. *Novel rhenium carbides at 200 GPa (S. Khandarkhaeva, T. Fedotenko/Bayreuth, N.A. Dubrovinskaia/Bayreuth, L.S. Dubrovinsky, M. Bykov, E. Bykova/Washington D.C., P. Sedmak/Grenoble; S. Chariton and V. Prakapenka/Chicago; K. Glazyrin/Hamburg)*

The rhenium-carbon system is a striking example of the influence of pressure on a binary phase diagram and elemental reactivity. At ambient pressure, there is only limited solubility of carbon in rhenium – with a maximum of 11.7 at. % C at the eutectic temperature (2773 K) – and no ordered stoichiometric carbides are formed. However, even very moderate pressure just above 6 GPa (and high temperatures) can induce the formation of hexagonal rhenium carbide (space group $P6_3/mmc$) Re_2C with anti-MoS_2 type structure. No other carbides apart of hP-Re_2C have been observed at pressures up to ~ 70 GPa and temperatures ~ 4000 K in the Re-C system. However, very complex and unexpected behaviour of Re-N system with formation numerous nitrogen-rich compounds around and above 100 GPa and high temperatures was observed recently (see contribution **c**), starting from the isostructural Re_2N. The potential analogy in the

behaviour of the Re-C and Re-N systems is one of reasons to explore potential reactions between Re and C in the megabar pressure range.

Another reason to pay special attention to interaction of rhenium and carbon is the development of methodology in ultra-high-pressure high-temperature experiments. The accesible static pressure range has recently been extended to over 500 GPa due to implementation of double-stage diamond anvil cells (ds-DAC) and toroidal type anvils (t-DAC). At pressures above ~ 150 GPa, the diameter of the pressure chamber is usually smaller than 50 μm, and in ds-DACs above 300 GPa it is less than 10 μm. At the same time, the size of the laser beam in a typical heating setup used in DAC experiments varies from 15 to 50 μm at FWHM. As a result, laser heating of (at least) the edge of Re-gasket becomes unavoidable, and may consequently lead to chemical reaction between Re and carbon of the anvils. Therefore, the interpretation of results from laser-heating experiments at these conditions requires knowledge about possible reaction products of rhenium and carbon.

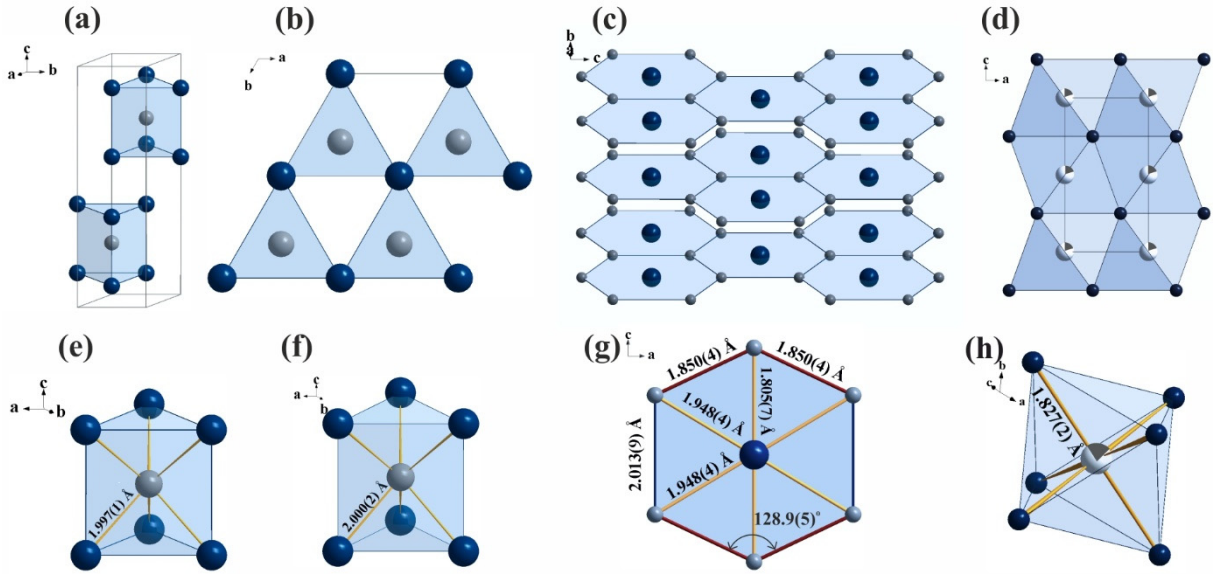

Fig. 3.7-5: Crystal structures of Re-C compounds observed at ~ 200 GPa: (a,e) hP-Re_2C, (b,f) WC-type structured ReC, (c,g) oF-ReC_2 and (d,h) B8-type structured interstitial $ReC_{0.2}$. Carbon atoms occupy prismatic sites in the crystal structure of Re_2C (e) and ReC (f) with Re-C bond length of ~ 2 Å (shown in yellow). Atomic arrangement of ReC_2 (c) composed by C hexagons built around Re atom (g) with shortest C-C distance 1.850(4) Å (shown in red). (d,h) $ReC_{0.2}$ consists of closely packed octahedra, with relatively short Re-C distances (1.828 Å), and the positions of C atoms are occupied with a probability of 0.20 (h).

Here, we report results from an *in situ*-study of Re-C compounds formed due to the chemical interaction between secondary stage diamond anvils and rhenium gasket after pulsed laser heating of a ds-DAC at ~ 200 GPa. We observe the formation of several high-pressure rhenium carbides with varying amounts of carbon (Fig. 3.7-5). Comparing our data for Re-C compounds

and recent reports on Re-N system shows that obvious crystal-chemical similarities in two systems exist for compositions with Re:C≥1:1. By contrast, ReC_2 and ReN_2 structures have nothing in common. A possible explanation of such differences is the tendency of nitrogen to form di-nitrogen and poly-nitrogen anions (based on N_4^{4-} units as discussed in contribution **d**), while rhenium carbides do not show the formation of polycarbon anions.

However, a number of experiments and theoretical predictions suggest the progressive polymerization of carbon atoms in carbides at high temperature, especially for alkali metal polycarbides. In all cases, the polymerization results in the formation of short C-C bonds (≲1.6 Å) for single bonded carbon atoms. For predominantly ionic carbides (like hP-Re_2C or hP-ReC) at ~ 200 GPa, C-C distances are larger than 2.5 Å. In case of oF-ReC_2 (Fig. 3.7-5), we observe the formation of graphene-like layers, but C-C distances (~ 1.7-1.85 Å) are still larger than expected for sp^2- or sp^3-bonded carbon atoms, and thus our observations suggest that at very high pressures mechanism of interaction between carbon atoms may be different from that considered so far.

f. *Sulfur-hydrides: The missing phases (D. Laniel/Bayreuth, E. Bykova/Hamburg, T. Fedotenko/Bayreuth, L.S. Dubrovinsky and N.A. Dubrovinskaia/Bayreuth)*

Achieving room temperature superconductivity has been a long-standing scientific objective, ever since the very discovery of the physical phenomenon. If achieved, it would completely transform electric power systems and drastically reduce the cost of energy transport. In 2015, high-pressure experiments have shown superconducting temperatures (T_c) of 203 K in the S-H system at 150 GPa – surpassing previous T_c records considerably – ushering in a golden age for high-pressure studies on hydrides. Despite the large number of investigations that followed these measurements, critical questions remain open. Notably, depending on the sample and study, a large range of T_c values (80-203 K) were measured, suggesting the presence of numerous phases in the sample cavity. While theoretical calculations have predicted an *Im*-3*m* H_3S solid as the phase with the highest T_c, conclusive experimental demonstration has been missing and all other phases hypothesized to also be present were left uncharacterized.

In this investigation, we compressed pure sulfur embedded in paraffin oil (C_nH_{2n+2}), acting both as a pressure-transmitting media as well as a hydrogen source. Samples were isothermally compressed up to 150 GPa at ambient temperature and laser-heated to above 2000 K every ~ 15 GPa beyond that pressure. Following heating, samples were characterized by single-crystal X-ray diffraction in order to identify the reaction products. In this fashion, two new phases of S-H were discovered.

Between 45 and 130 GPa, a tetragonal ($I4_1$ space group, Fig. 3.7-6) was identified and, based on volume per sulfur atom, a stoichiometry close to 1:1 S/H was inferred. The $I4_1$ compound is composed of a complex arrangement of sets of wavelike S-S chains running along the *a*- and

b-axes. In that same pressure range, a previously identified H_3S ($I4/mcm$ space group) solid was observed. At 150 GPa – in the pressure regime where ultrahigh T_c was detected – a $P3$ space group compound was observed. With an assumed stoichiometry of 1:1 S/H, the structure can be viewed as a 2D sulfur networks in the *ab*-planes stacked along the *c*-axis and puckered with rows of S atoms running parallel to the *c*-axis (Fig. 3.7-6). Coexisting with the $P3$ phase at 150 GPa, the H_3S Im-$3m$ was also fully characterized, confirming its previously presumed existence.

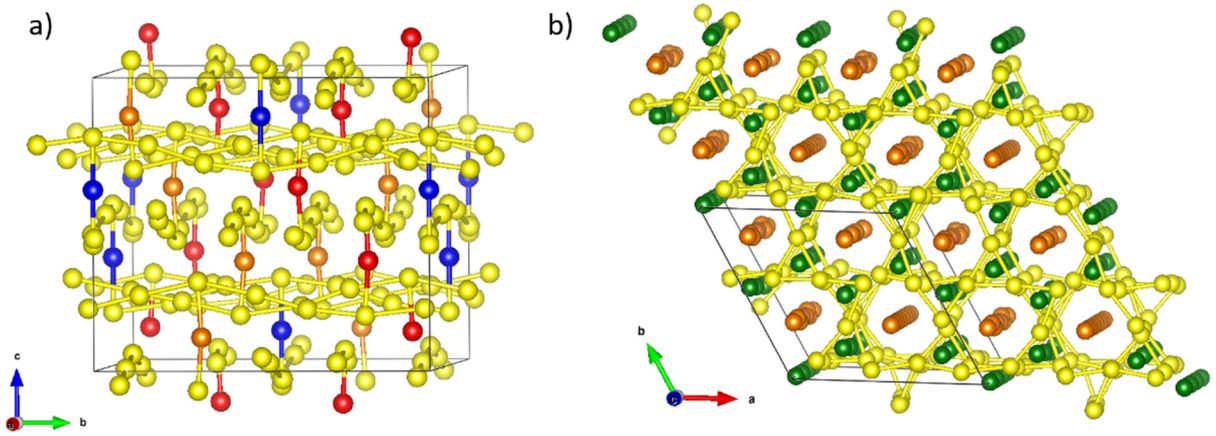

Fig. 3.7-6: (a) Sulfur lattice of the tetragonal HS solid (space group $I4_1$). (b) Sulfur lattice of the hexagonal HS solid (space group $P3$). All spheres represent sulfur atoms, different colors help to identify different substructures.

Theoretical calculations are currently underway to determine the position of H atoms—almost completely invisible to X-rays – in the two newly discovered compounds. These results bring to light the full range of compounds and stoichiometries that may be produced under pressure in the S-H system. Moreover, the newly identified solids can explain the sample-dependent discrepancies between the measured T_c and provide all the necessary tools to achieve a complete understanding of the S-H system, and of its exceptional superconductivity.

g. *Synthesis and structure of copper hydrides at high pressure (G. Criniti, T. Meier, T. Fedotenko/Bayreuth, S. Khandarkhaeva, E. Koemets, D. Laniel/Bayreuth, S. Chariton/Chicago and L.S. Dubrovinsky)*

The application of nuclear magnetic resonance (NMR) spectroscopy in the diamond anvil cell (DAC) has recently been established as a valuable tool in probing electronic properties of H-bearing materials at high pressure. This has been possible by the implementation of Lenz lens resonator structures in the DAC, which is cut with a focus ion beam from a thin layer of Cu. If a material is synthesized *in situ* in such a setting, it is possible that Cu from Lenz lenses can react with the H-reservoir during heating and copper hydrides can form accidentally. In such a scenario, a better understanding of the structure and NMR signals of copper hydrides over a

wide range of pressure and temperature becomes of crucial importance to identify undesired signals in NMR-DAC experiments.

Here we report the successful synthesis of trigonal and cubic copper hydrides at high pressure and high temperature from Cu and paraffin oil in the DAC reaching pressures of ~ 155 GPa and temperatures of 2000 K. Synchrotron radiation X-ray diffraction measurements were conducted *in situ* to investigate the structure of copper hydrides. In the trigonal phase, Cu atoms form a distorted *hcp* lattice with H preferentially occupying every second interstitial layer. The stability field of the trigonal phase (Cu_2H), already reported in previous studies, was extended to 35 GPa at high temperature and to 58 GPa at room temperature. A cubic phase with stoichiometry CuH_x ($x > 1/2$) and *fcc* structure was synthesized at 58 GPa and 2000 K and was found to exist to ~ 155 GPa (Fig. 3.7-7). It is observed that, when heated and quenched, the volume of the cubic hydride increases at pressures up to ~ 140 GPa, but remains unchanged at higher pressure (Fig. 3.7-7). This suggests that either the cubic hydride has reached a stoichiometric composition of CuH, or that the H-reservoir was exhausted. We conclude that the hydrogen content in cubic copper hydride is pressure dependent and approaches or exceeds one at pressures above 1 Mbar.

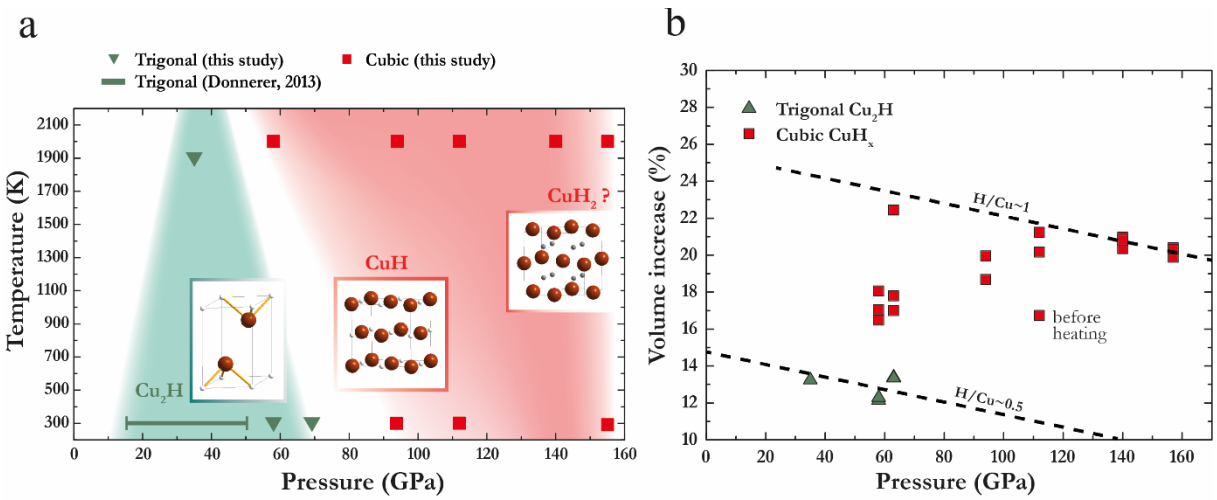

Fig. 3.7-7: (a) Appearance diagram of trigonal (green) and cubic (red) copper hydrides. The green bar represents the pressure range investigated by Donnerer *et al.* (2013, *J.Chem.Phys.*, 138, 13). With increasing hydrogen content, it is possible that octahedral interstitial sites in cubic CuH_x become saturated ($x = 1$) and H atoms start to fill tetrahedral sites, as the stoichiometry evolves towards CuH_2. (b) Relative volume increase of copper hydrides with respect to pure Cu. The dashed lines represent our estimate of pressure dependent volume increase for stoichiometric Cu_2H and CuH.

h. *High-pressure synthesis of an orthorhombic polymorph of Mn_3O_4 and its properties (S.V. Ovsyannikov, E. Bykova/Hamburg and L.S. Dubrovinsky)*

A wide range of novel exciting materials can be synthesized at high pressure and high temperature. Ideal candidates are imple transition metal oxides as they are inexpensive and

highly functional materials that have been shown to combine interesting electronic, optical and magnetic properties. Here, we synthesize single crystals of the high-pressure polymorph of Mn_3O_4 and examine their optical, vibrational, structural and physical properties.

High-pressure high-temperature syntheses were performed in large-volume presses at BGI in a pressure range of 13-16 GPa and temperatures of ~ 1300 °C. We use a sample capsule made of gold to avoid undesirable chemical reactions (for example, rhenium can react with manganese oxides at high-pressure and -temperature conditions to form a perovskite), α-Mn_3O_4 (hausmannite with a spinel structure) is used as a starting material. To obtain large high-quality single crystals, we keep the α-Mn_3O_4 powder at these conditions for 24 h. We solve the crystal structure of the recovered high-pressure polymorph of Mn_3O_4 using single crystal X-ray diffraction, and find an orthorhombic space group (*Pbcm* ,#57) with the following cell parameters: a = 3.0276(1) Å, b = 9.8176(3) Å, c = 9.5799(3) Å, V = 284.751(16) Å^3, and Z = 4. The Mn ions in this structure occupy two different crystallographic sites: octahedral and trigonal prisms formed by oxygens (Fig. 3.7-8). A bond valence sums analysis suggests that the octahedra are filled by trivalent Mn and the trigonal prisms by divalent Mn. Generally, this crystal structure resembles the high-pressure polymorph of Fe_3O_4. Since the octahedral chains comprise only Mn^{3+} cations, this polymorph is expected to be a poor electrical conductor.

Near infrared and optical absorption spectra on a double-polished thin section of the high-pressure polymorph of Mn_3O_4 show a distinct absorption edge near 10000 cm^{-1} (Fig. 3.7-8), and the edge profile suggests a parabolic nature of the energy bands, and hence, a band gap values may be estimated using the standard "parabolic" model. Based on this analysis we compute an indirect fundamental band gap of E_g ~ 0.95 eV, much smaller than in the conventional spinel-structured hausmannite (α-Mn_3O_4) with E_g ~ 2.5 eV; the minimal direct band gap can be estimated from the data as 1.3 eV. This finding suggests that the high-pressure polymorph of Mn_3O_4 is a narrow gap semiconductor with interesting potential in the semiconductor industry.

Using Raman spectroscopy using the red 632 nm laser line we identify a number of phonon peaks (152, 175, 213, 268, 290, 329, 367, 398, 4833, 502, 531, 618, and 663 cm^{-1}) and follow their pressure evolution (220-590 cm^{-1} range shown in Fig. 3.7-9). The Raman spectra show the expected hardening of the phonon modes with pressure that is linked to shrinking Mn-O distances. No phase transitions or crossovers are observed in the pressure range to 13.4 GPa. In order to estimate the Grüneisen parameters of the phonon modes, a bulk modulus for this polymorph is required. Currently, a high-pressure single crystal X-ray diffraction experiments is prepared for this orthorhombic polymorph.

Keeping in mind the similarity between the crystal structure of this polymorph with the high-pressure phase of magnetite and the newly discovered iron oxides with unconventional stoichiometries (*e.g.*, Fe_4O_5, Fe_5O_6, Fe_5O_7, Fe_7O_9, etc.) on the other hand, this investigation could provide insight into high-pressure behaviour of iron oxides as well.

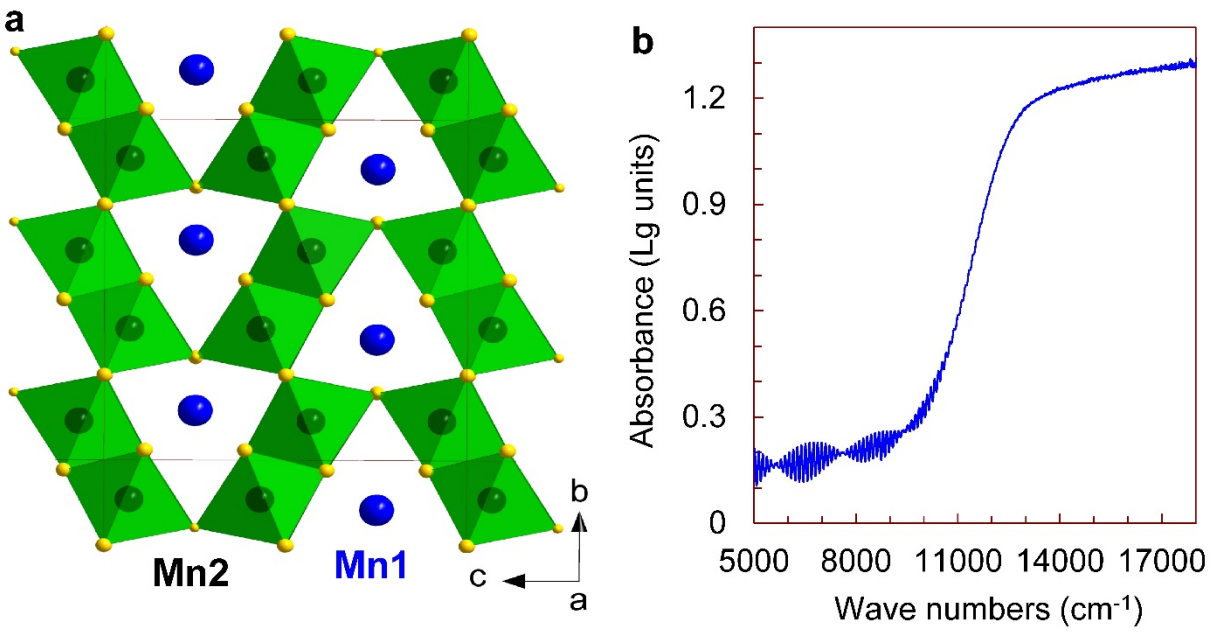

Fig. 3.7-8: (a) Orthorhombic crystal structure of the high-pressure *Pbcm* polymorph of Mn_3O_4 at ambient conditions. The labels Mn1 and Mn2 indicate two different crystallographic positions for Mn ions. The unit cell is highlighted by thin black lines. (b) Optical absorption spectrum of the high-pressure *Pbcm* polymorph of Mn_3O_4 at ambient conditions. The spectrum shows an apparent absorption edge that corresponds to indirect fundamental band gap of 0.95 eV.

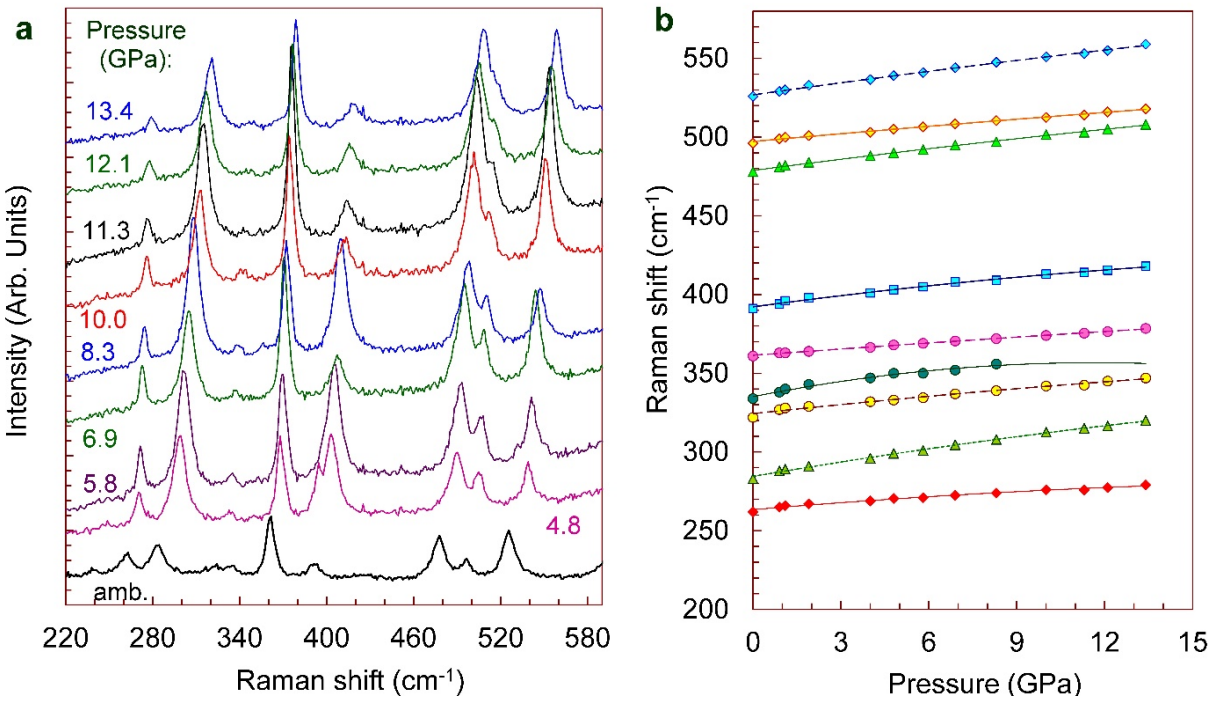

Fig. 3.7-9: (a) Pressure evolution of Raman spectra of the high-pressure *Pbcm* polymorph of Mn_3O_4 at room temperature. (b) Pressure dependence of the wave numbers of the Raman peaks.

i. *Interaction between FeOOH and NaCl at extreme conditions: Synthesis of novel $Na_2FeCl_4OH_x$ compound (E. Koemets, L.S. Dubrovinsky, E. Bykova, K. Glazyrin/Hamburg and L. Yuan, in collaboration with E. Ohtani/Sendai)*

Recently it was proposed that α-FeOOH (stable as goethite at the ambient conditions, which is a common material in the banded iron formations, BIFs) could be transported into the lower mantle with subducting slabs, bringing water to the lowermost mantle and the core-mantle boundary. A number of studies were dedicated to investigating the behaviour of FeOOH at high pressure and temperature which revealed that FeOOH undergoes a series of phase transitions, finally forming a "pyrite-type" FeO_2H_x phase which is expected to be stable at conditions of lowermost part of a mantle and core–mantle boundary. This phase has attracted the attention of the community and is being intensively investigated via density functional theory calculations and spectroscopic studies. In some experiments in the diamond anvil cell (DAC), alkali halides were used as a pressure-transmitting medium and thermal insulator for laser heating, under the assumption that alkali halides are chemically inert and do not complicate data analysis. However, at very high pressures and temperatures, the chemistry of materials may change, and iron oxyhydroxide could potentially interact with the alkali halides. Methodologically, it is of great importance to investigate the reactivity between these species.

We performed a laser-heated DAC (2400(200 K) experiment (107(2) GPa) of FeOOH loaded in NaCl. By means of *in situ* single-crystal XRD we observe the formation of an unknown compound. Results of structure solution and refinement establish that this phase is orthorhombic (Pbam, #55) with $Na_2FeCl_4OH_x$ stoichiometry (Fig. 3.7-10). Our results suggest that NaCl and other alkali metal halides are interacting with FeOOH and therefore cannot be used as a chemically inert pressure-transmitting medium in a DAC experiments.

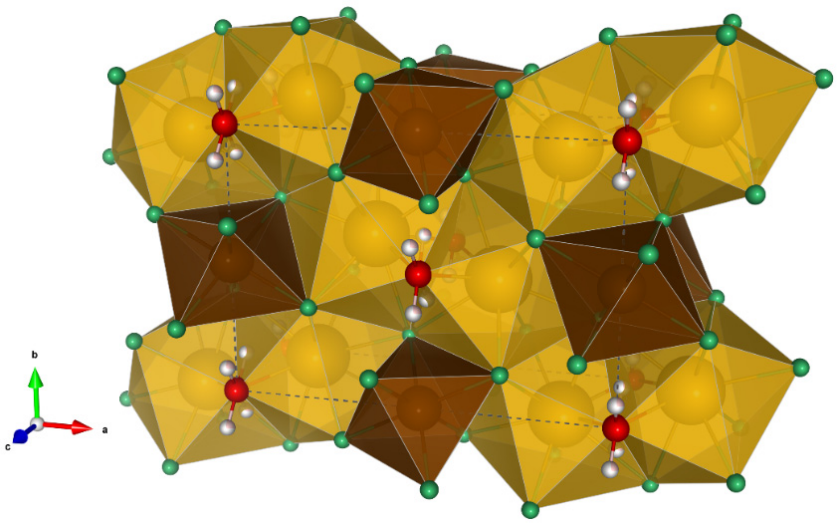

Fig. 3.7-10: Crystal structure of $Na_2FeCl_4OH_x$ at 107(2) GPa. Yellow spheres show Na atoms, brown spheres Fe atoms, Cl and O atoms are shown as green and red spheres, respectively. Yellow and brown polyhedra represent the coordination of Na and Fe irons. White spheres show the possible (partially occupied) positions of H atoms. The dashed black lines outline the unit cell boundaries.

3.8 Methodological Developments

The mission of the Bayerisches Geoinstitut (BGI) is to understand the structure, dynamics and evolution of Earth and planetary interiors based on experimental, analytical and modelling methods. Methodological development is essential for progress in any field of science, and the BGI has put much effort into the development of research technologies.

Diamond anvil cells (DAC) are currently the only static high-pressure apparatus that can generate pressures exceeding that of the Earth's centre. The BGI developed the double-anvil technique to reach a pressure of 1 TPa for the first time in the world. In the first contribution in this section, Krupp and co-workers examined various shapes of secondary anvils and demonstrated similar pressure intensification factors of 2.5 ~ 3.0 at high pressures with all investigated shapes. The transparency of diamond allows laser heating and various techniques of *in situ* observation. The second study in this chapter developed a new method of melt-detection in laser-heated samples by using *in situ* X-ray transmission microscopy. The third study installed a new high-pressure, high-temperature, single-crystal X-ray diffraction system in the DAC beam line at the German synchrotron radiation facility (DESY). This system allows step-scan data for single-crystal X-ray diffraction analysis by using a time-resolved fast-collection X-ray detector (LAMBDA) synchronized with a pulse laser heating system. The BGI has been developing a megabar-pressure NMR spectroscopy in DAC for the last three years. Efforts in the last year were made to increase the resolution of NMR spectra and to combine NMR with laser heating. The fourth and fifth contributions provided by Meier *et al.* report progresses in these efforts in the last year. Kurnosov *et al.* are developing Brillouin scattering measurement also at simultaneous high-pressure-temperature conditions by laser heating. They report the current status of this development. The last study in the development of DAC experiments concerns the evaluation of oxygen fugacity of a DAC sample using Fe-Ir alloys.

Large-volume presses are also used for high-pressure-temperature investigations in the BGI. One of the uses of such devices is to recover high-pressure, high-temperature samples to ambient condition for post-analyses. Melts and fluids are nevertheless difficult to recover to ambient conditions. Bondar *et al.* developed a fast-cooling system to quench a melt to a glass, and succeeded in quenching mafic silicate melt from pressures up to 6 GPa. Rustioni *et al.* attempted to freeze a sample capsule by liquid nitrogen, and successfully analysed solids precipitated from fluid upon quenching using a laser-ablation inductively-coupled-plasma mass spectrometry. Another study was conducted to develop a multianvil technique to produce reduced fluid and fluid inclusions at pressures above 6 GPa for post-analyses by means Raman spectroscopy and gas chromatography to understand roles of volatile components in mantle processes. The last contribution of experimental development reports ultrahigh-temperature generation by a multianvil press. Although simultaneous ultrahigh-pressure and ultrahigh-temperature generation is extremely challenging, Xie and his coworker succeeded in generating temperatures to 3000 K in a sintered-diamond assembly of a multianvil press, which should be able to generate pressures to 80 GPa.

The last three contributions are dedicated to development of numerical modelling. The two studies by Eichheimer *et al.* investigated fluid flow through porous media. Since such flow is controlled by the permeability of rocks, they attempted to predict the permeability of a non-Newtonian fluid. Although calculations for non-Newtonian fluid dynamics are numerically expensive, they succeeded in increasing the accuracy of simulations with low computational costs. In the other study, they conducted permeability experiments and analyzed their products by image processing to propose relations between permeability and effective porosity. The last contribution in this section conducted resolution tests for simulating plate tectonics, in which strongly temperature-dependent rheology is essential. The results demonstrate that high-resolution is vital to resolve thin lids of the lithosphere.

a. *Comparative study on performance of secondary anvils for dsDACs (A. Krupp, S. Khandarkhaeva, T. Fedotenko/Bayreuth, L.S. Dubrovinsky, N.A. Dubrovinskaia/Bayreuth and K. Glazyrin/Hamburg)*

Investigating Earth's lower mantle and core as well as planetary bodies and materials under extreme conditions has challenged state-of-the-art high-pressure technologies to overcome the 400 GPa limit of conventional diamond anvil cells. Recent developments reported in the literature extended the reachable pressure range up to 1 TPa. In awareness of the ongoing discussion on the suitability of various ultra-high-pressure DAC techniques, in this study several shapes of secondary anvils were tested to compare their force multiplication efficiency and stress distribution. Studied shapes include two conical designs with different top diameter sizes, a bevelled and a toroidal anvil, as well as a toroidal anvil with a semi-spherical tip (Fig. 3.8-1), all loaded individually in DACs equipped with primary diamond anvils with a culet size of 250 µm or 120 µm and Ir-foil as pressure marker. Pressure determination was performed by Raman spectroscopy using the shift in the diamond F_{2g} mode for pressures below 30 GPa. At higher pressures, samples were investigated by X-ray powder diffraction and pressures under secondary anvils were determined from the equation of state of Ir (V_0 = 14.14(4) $Å^3atom^{-1}$, K = 341(10) GPa and K′ = 4.7(3)). XRD studies were conducted on the synchrotron beam line P02.2 at DESY Hamburg, Germany (λ=0.4853 Å).

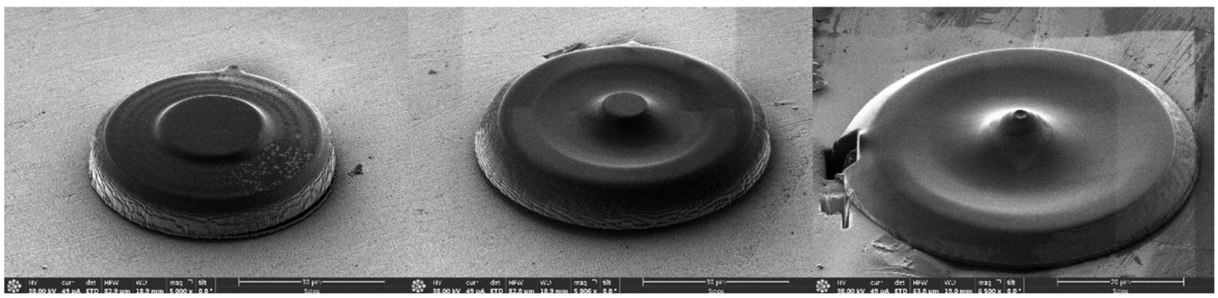

Fig. 3.8-1: FIB image of a bevelled shaped secondary stage anvil with an angle of 8° slope cut (left); FIB image of a toroidal shaped secondary stage anvil with flat tip (centre); FIB image of toroidal shaped secondary anvil with semi-spherical tip (right).

Results show that a toroidal-shaped anvil with semi-spherical tip is the most suitable to create an area of relatively uniform pressure (stress) distribution under the secondary anvil. It revealed the best performance by means of XRD experiments, based on the high intensity of the diffraction peaks of Ir at the maximum degree of compression. The highest reached pressure was 173 GPa at a confining pressure of 58 GPa, which results in a multiplication factor of ~ 3 and a shear stress of 172 GPa. The highest maximum pressure observed during this work was 212 GPa at a confining pressure of 86 GPa, achieved with a conical anvil in a DAC equipped with primary anvils which had a culet size of 120 µm.

The multiplication factor at that pressure point was 2.5 with a shear stress of 188 GPa. The observed shear stresses and yield strengths at the final pressure points exceed earlier estimations for single crystalline diamond by a factor of two.

Most shapes show similar behaviour in terms of force multiplication efficiency at confining pressures above 30 GPa (Fig. 3.8-2). Slight deviations might be explained by the different tip sizes as well as incomplete bridging between the primary anvils at pressures up to 20 GPa. Even though differences can be observed for multiplication factors below 20 GPa, all studied shapes of secondary anvils approach a common multiplication factors of 2.5-3 at pressures above 40 GPa. The similar slopes and evolution of the multiplication factor can be explained by the fact that at the highest achievable pressure point for the primary anvils, the high-pressure area on all tested secondary anvils reached a similar size of 2-3 µm. Improvements regarding the tip diameter as well as the total height to spare the primary anvils will be investigated in further studies to enhance the capability of the dsDAC technique for ultra-high-pressure generation.

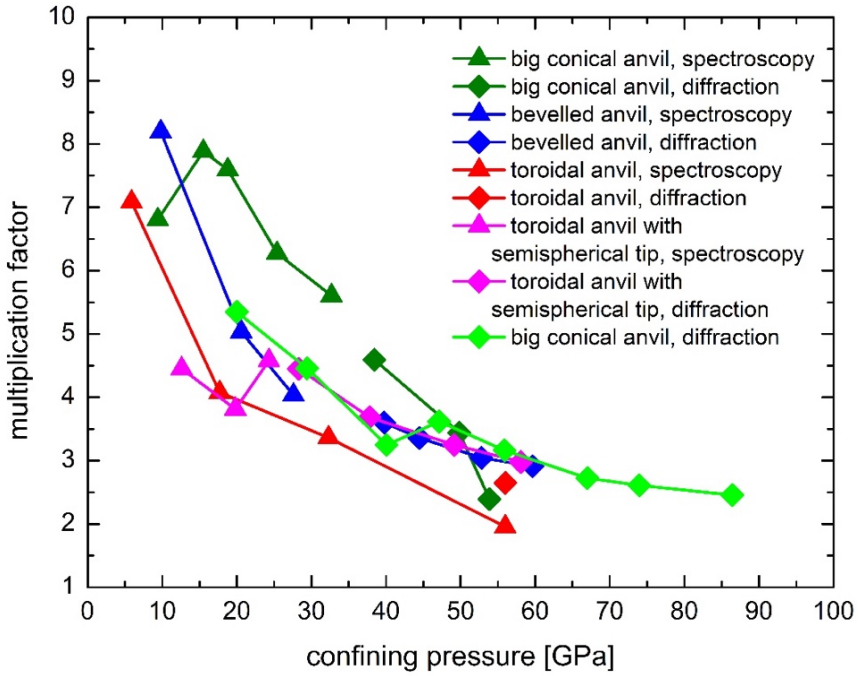

Fig. 3.8-2: Multiplication factors with respect to the confining pressure for all tested anvil shapes evaluated from both pressure determination methods, Raman spectroscopy (spectroscopy, triangles) and X-ray diffraction (diffraction, diamonds).

b. In situ *X-ray transmission microscopy in laser heating diamond anvil cells as a new method to detect melting (T. Fedotenko/Bayreuth, G. Aprilis/Hamburg, E. Koemets, L.S. Dubrovinsky, N.A. Dubrovinskaia/Bayreuth; I. Snigireva, F. Cova and M. Hanfland/Grenoble; A. Snigirev and A. Barannikov/Kaliningrad)*

Considerable difficulties associated with detection of melting at high pressures result in significant inconsistencies in reported melting curves for the same materials. Several methods of detection of melting in laser-heated diamond anvil cells (LHDACs) are known. In particular, it can be done by optical observation, X-ray diffraction, X-ray absorption, or Raman measurements.

Each of the currently used methods of detecting melting in LHDACs is associated with specific challenges, which can lead to ambiguities. *In situ* melting detection at temperatures above ~ 2000 K is possible by observation of a speckled interference pattern, but relies upon the subjective judgment of the observer. Identification of melting using X-ray diffraction is in general possible at synchrotron beamlines and in this case melting is manifested either by disappearance of Bragg reflections and/or by appearance of diffuse scattering due to the short-range order in the liquid state. However, the disappearance of reflections on still X-ray images may be a result of recrystallization (without melting). In order to produce a detectable signal, the amount of melted liquid in the sample should be significant, and the melt has to be stable for some time in the complex and highly thermally and chemically inhomogeneous environment of the DAC. Moreover, experiments can be complicated due to possible chemical reactions with the pressure medium or the diamond anvils.

In this work, we demonstrate the feasibility of *in situ* X-ray transmission microscopy (XRTM) as a new method of melting detection in LHDACs. We performed an experiment aiming to detect the melting of Pt. Platinum was chosen, because it is chemically inert and possible chemical reactions, that could affect the result, can be excluded. The relatively low melting temperature of Pt simplifies the experiment and its melting curve has been already experimentally established.

Transmission X-ray Microscopy was realized using compound refractive lenses (CRL), according to the scheme shown in Fig. 3.8-3. The objective lens assembly consisted of 66 aluminium and 45 beryllium parabolic refractive lenses. The lenses of both types have the radius of parabola apex of 50 μm. X-ray images were recorded with a high-resolution PCO X-ray CCD camera with 0.74 μm pixel size, which was installed at a distance of about 5 m from the DAC. Therefore, the magnification of about 10 was achieved. The transfocator, which was located at 44 m from the undulator, was used to provide appropriate illumination on the sample. Such an experimental arrangement allows the preservation of beam coherence and gives unique opportunities for realization of X-ray phase-contrast microscopy with a spatial resolution down to 200 nm.

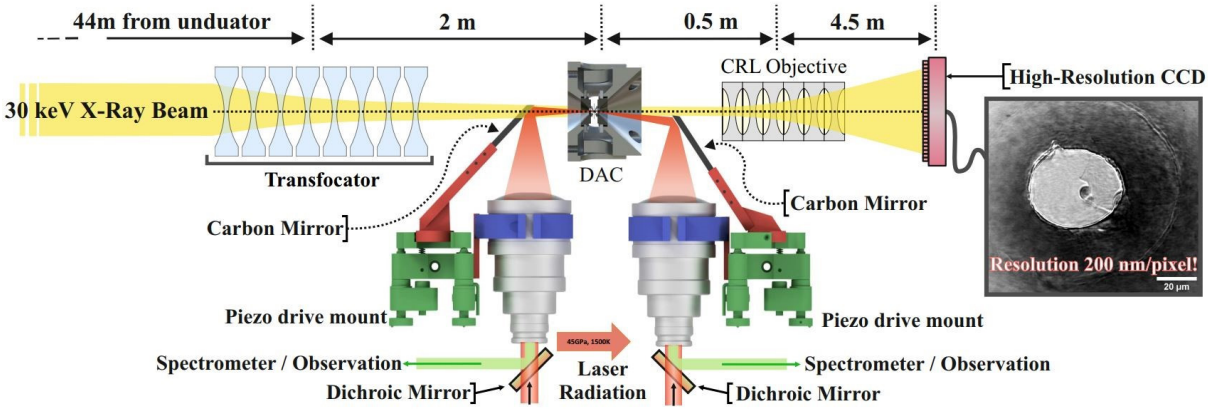

Fig. 3.8-3: Experimental layout for X-ray microscopy experiments

A piece of a Pt foil was clamped between two thin layers of NaCl from both sides and loaded inside a sample chamber of a BX90-type diamond anvil cell equipped with Boehler–Almax type diamonds (with culet diameter of 250 µm). To form the sample chamber, a rhenium gasket was pre-indented to 25 µm thickness and a hole with a 110-µm diameter was drilled in the center of the indent. NaCl was used as a pressure-transmitting medium and as a thermal insulator to minimize dissipation of heat through the diamonds. The sample was compressed up to 22(1) GPa.

We heated the sample for 200 seconds while simultaneously recording a series of XRTM images with 1-second exposure time and measuring the temperature using spectroradiometry. Figure 3.8-4 shows representative XRTM images of the sample during the heating, in which it can be seen that the sample changes its shape and texture.

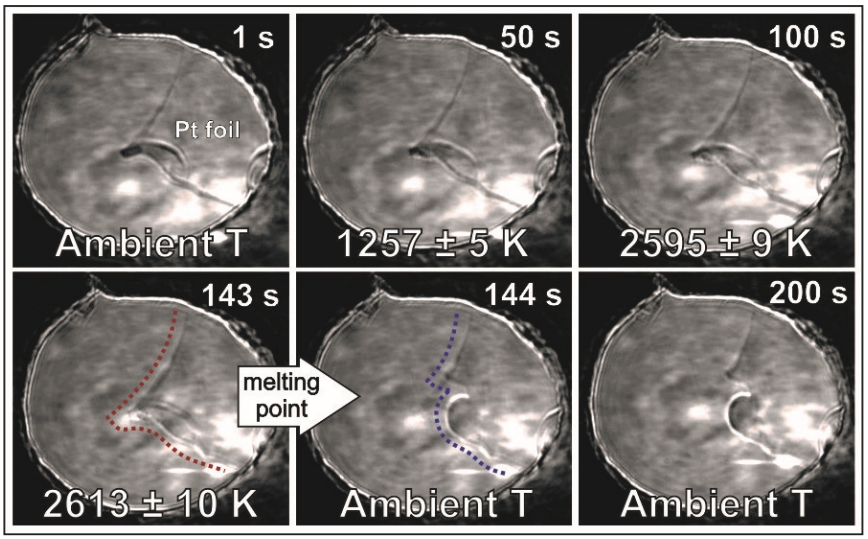

Fig. 3.8-4: XRTM images of the sample chamber taken during the heating process. Each image was collected with 1 second exposure time. Red and blue dotted lines represent the shape of the Pt foil before and after melting respectively. The melting moment was detected between 143th and 144th seconds by observation of the Pt foil shape. The melting temperature of Pt at 22 (1) GPa is 2613±10 K.

For the first 143 seconds the laser power was slowly increased. Significant change in the shape of the Pt foil caused by its melting was detected between 143th and 144th seconds. We observe the formation of a Pt droplet (the size is around 10 μm) from initial Pt foil, which excludes simple recrystallization.

Before the melting event, all visual changes in the texture and shape of the Pt foil were caused by warming up of the sample chamber and its relaxation. The temperature collected at the last moment before melting was 2613 (10) K. After melting, the sample moved out of the laser beam and no thermal emission was present. The melting temperature of Pt at 22(1) GPa (2613 ±10 K) obtained in the experiment described above due a combination of XRTM with LH-DACs is in good agreement with the literature data (2583±97 K).

c. *Development of a single-crystal diffractometer coupled with a pulsed double-sided laser heating system for time-resolved X-ray diffraction of samples at high temperatures and pressures (G. Aprilis/Bayreuth, K. Glazyrin and J.T. Roeh/Hamburg, T. Fedotenko/Bayreuth, E. Koemets, S. Khandarkhaeva; M. Wendt, S. Wenz and H.-P. Liermann/Hamburg, L.S. Dubrovinsky and N.A. Dubrovinskaia/Bayreuth)*

Single-crystal X-ray diffraction (scXRD) in DACs is an ultimate tool to determine not only the crystal structure of a material, but also to refine its chemical composition for even very complex multi-phase and/or multigrain samples. Heating is an important parameter for high-pressure experiments, especially for studies dedicated to modelling of processes in Earth's deep interior. Double-sided laser-heating (dsLH) systems are widely used at synchrotron facilities. However, until recently, all of them were stationary and did not allow DAC rotation during simultaneous heating, making *in situ* high-pressure/high-temperature scXRD impossible.

The first dedicated scXRD/dsLH setup consisting of a single-crystal X-ray diffractometer coupled with double-sided laser heating system was recently developed for beamline P02.2 the Extreme Conditions Beamline (ECB) at PETRA III, DESY. Critical temperatures of magnetically ordered geomaterials, thermal conductivity and thermal expansion coefficients of iron bearing compounds under high pressure are some of the important properties that can be investigated.

In the course of this work, the single-crystal diffractometer was modified into a pulsed laser heating system capable for time-resolved X-ray diffraction studies of crystals at high pressures and temperatures. The laser-heating setup is coupled with a fast spectrometer and camera for time-resolved spectroradiometric measurements that allow the determination of the surface temperature of the heated sample from both heating sides. The system is also synchronized with a fast-collection X-ray LAMBDA detector (developed at DESY) that allows gated X-ray diffraction data collection with an arbitrary time resolution (Fig. 3.8-5).

Using the laser heating setup, it is possible to collect wide scans with a slow ω rotation while heating by pulsed laser. In a testing experiment on silicate double-perovskite, the heating cycle

period was 50 µs with ~ 20 µs pulses, and the ω rotation was at a speed of 2 to 4 seconds per degree, that is sufficient to provide repetition rate of laser pulses for heating and X-ray exposure at every degree of rotation. It was possible to detect the change in the lattice parameters of a single crystal due to laser heating, with 3 µs resolution in the diffraction and temperature data (Fig. 3.8-6). While so far only wide-scans were collected, it is possible to acquire step-scans for single-crystal data analysis while pulse heating, with time-resolved information.

Preliminary data analysis suggests that the *d*-spacing of the tracked reflections was varying from hot (at the peak of the pulse) to cold, as expected during pulsed heating, returning back to the relaxed position after quenching.

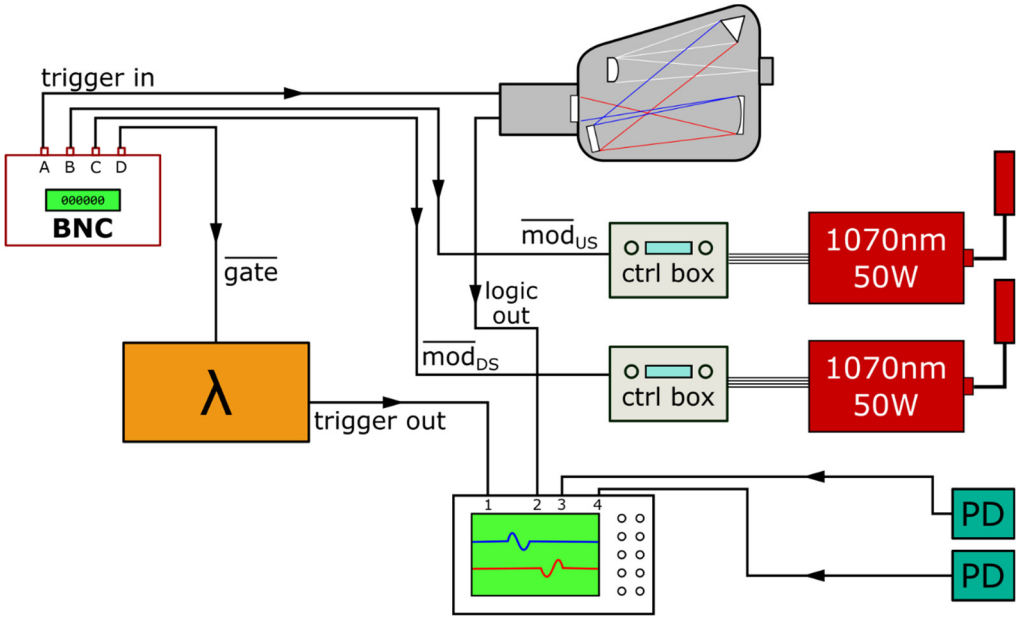

Fig.: 3.8-5: Triggering Scheme of the single-crystal diffractometer with pulsed laser heating setup coupled with a LAMBDA detector (λ) and a fast spectrometer camera at gating mode.

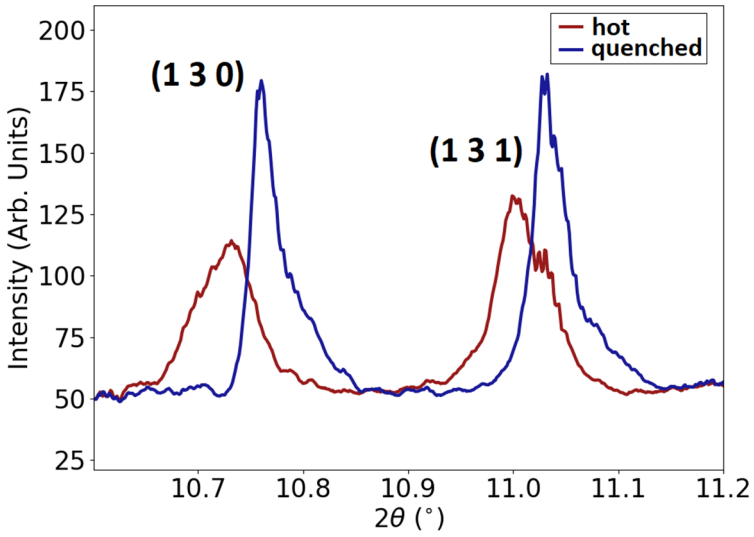

Fig.: 3.8-6: Time-resolved heating of iron-rich double perovskite crystal. The Bragg peaks are shifted to smaller angles (*i.e.*, larger d-spacings) due to heating. The diffraction patterns have a time-resolution of 3 µs, collected at the peak of the laser pulse (red line) and between the pulses, while the lasers were off (blue line).

d. *High-resolution solid-state NMR in diamond anvil cells (T. Meier, S. Khandarkhaeva, N.A. Dubrovinskaia/Bayreuth and L.S. Dubrovinsky)*

NMR spectroscopy is generally recognized as one of the most versatile spectroscopic methods available. A main pillar of the popularity of this technique originates in its ability to detect changes in the magnetic field around a nucleus or a molecular unit in the order of 1 nT. This resolution is generally unmatched by other techniques and allows for structure determination and refinement of bio-macromolecules. An application of high-resolution methods in diamond anvil cells under extreme conditions has, however, never been pursued.

In this work we demonstrate that basic spin decoupling is indeed possible. Application of so-called Lee-Goldburg irradiation prior to the standard detection pulse forces spin systems into the magic angle where the angular terms of the highly anisotropic direct dipole-dipole as well as first order quadrupole interactions become zero. This leads to an effective averaging of the non-secular part of the respective nuclear spin Hamiltonian and cancelling out of these interactions in a way that only delta-peak-like NMR signals, which are proportional to the isotropic chemical shift, are present. In this way, we have been able to narrow down the broad NMR signal of dense molecular hydrogen up to 120 GPa from initially about 5000 ppm to almost 3 ppm, a 1600-fold improvement in spectral resolution (Fig. 3.8-7).

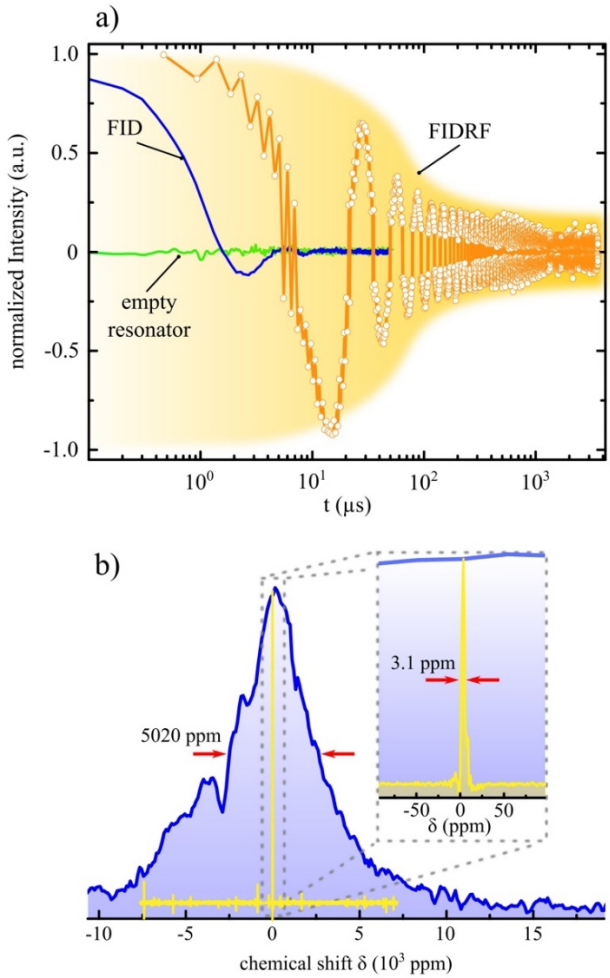

Fig. 3.8-7: (a) Time domain data of the standard FID (blue) and the FIDRF (orange) after optimization of LG conditions. The yellow envelope is a guide to the eye. (b) Corresponding 1H-NMR spectra under standard "static conditions" (blue) and under LG conditions (yellow); the inset shows a zoomed-in region of the narrowed NMR signal.

This research represents the first step towards high resolution NMR in diamond anvil cells which will eventually spark large interest in this novel method and a new way to investigate matter under extreme conditions.

e. *Table top NMR system for* in situ *laser heating (T. Meier, A.P. Dwivedi/Milwaukee, F. Trybel, S. Khandarkhaeva, T. Fedotenko/Bayreuth, N.A. Dubrovinskaia/Bayreuth and L.S. Dubrovinsky)*

Over the past three years we have been able to develop methods for nuclear magnetic resonance at high pressures into the mega-bar regime (over 100 GPa). Recently, we succeeded in *in situ* sample synthesis at high pressure under laser heating in our diamond anvil cells. This success inspired us to start developing an NMR system which enables the experimenter to perform NMR experiments under laser heating conditions at high temperatures.

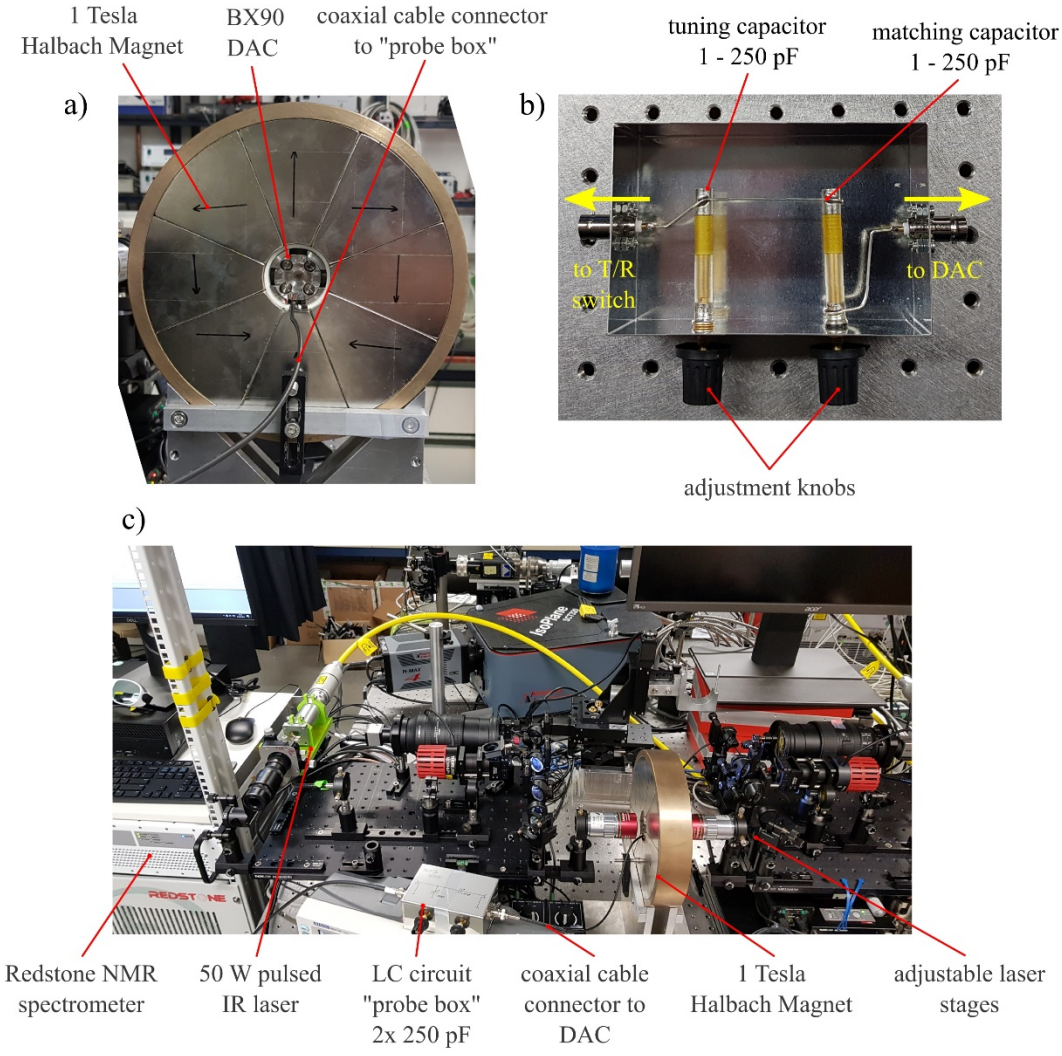

Fig. 3.8-8: Table top high-pressure NMR set-up. a) 1 Tesla Halbach array magnet with BX90 diamond anvil cell placed in its magnetic center b) photograph of the NMR probe box. c) laser heating set-up for *in situ* NMR measurements.

Owing to the rather large space requirements for regular NMR equipment (superconducting magnet and spectrometer), such an endeavor seemed unfeasible at first. However, with the use of Halbach-array magnets we succeeded in developing the first table-top NMR set-up for diamond anvil cells (Fig. 3.8-8). While the employed magnet seems unfit for NMR experiments on standard macroscopic samples due to large B_0 inhomogeneities, we found that by using diamond anvil cells, where samples are typically 6 to 7 orders of magnitude smaller, no significant difference to standard electromagnets was found.

Also, we were able to couple the NMR system to one of our laser heating systems and performed NMR experiments at about 1000 K and 25 GPa on a sample of ice VII. We found that at these temperatures, the loss of signal-to-noise can be used as a convenient way to perform radiometry within the sample chamber.

The present work represents the first step towards high-temperature, high-pressure NMR in diamond anvil cells which will eventually spark large interest in this novel method and provide a new way to investigate the most intriguing high-pressure quantum solids like superionic ices.

f. *Simultaneous HP/HT Brillouin scattering measurements of transparent samples using a CO_2 laser heating system (A. Kurnosov, G. Criniti, H. Marquardt/Oxford, T. Boffa Ballaran, A.C. Withers and D.J. Frost)*

The successful research missions on Mars (first of all the InSight mission) are giving the possibility for the first time of obtaining the necessary data, including seismic data, for understanding the internal structure and evolution of our neighbouring planet. The interpretation of seismic data, however, requires mineral physics models, which can be constructed using the high-pressure, high-temperature elastic properties of candidate materials for Mars' interior. Ideally, the variation of the full elastic tensor of these materials and their density as a function of pressure and temperature are needed in order to apply strong constraints not only on wave velocities, but also on the possible anisotropic behaviour of Martian rocks. In contrast to Earth, the Martian interior does not extend to extremely high pressures, however the temperature required for differentiation of the planet interior must have reached thousands of degrees at an early stage of Mars history. Such high temperatures at relatively high pressures can only be obtained by employing laser heating in combination with the diamond anvil cell technique.

The elastic tensor of any material can be determined by means of single-crystal Brillouin spectroscopy, which, however, requires the use of transparent samples that cannot be heated by conventional laser equipment. In the last couple of years, therefore, we have focused our effort in optimizing the use of a flexible CO_2 laser heating setup (see 2018 BGI annual report). The advantage of the CO_2 laser is that it can be absorbed by samples which are transparent for visible and near infrared light, thus enabling the sample to reach very high temperatures also when using Brillouin. The challenge at the moment is to provide constant temperature for a long period of time in order to be able to collect high-resolution Brillouin spectra.

Here we present results of the first high-pressure, high-temperature Brillouin scattering measurements of a laser-heated single crystal of pyrope in a DAC loaded with Ar as pressure-transmitting medium at the pressure of 1.3 GPa (Fig. 3.8-9). The sample has been heated at different temperatures using a fan-cooled CO_2 laser coupled to a commercially available Hollow Silica Core Waveguide and a cage system that contains ZnSe optics to focus the laser radiation on the sample inside the DAC. The system was installed on the combined Brillouin/XRD system at BGI, and the temperature during heating was measured through the Brillouin collecting optics. This approach allows us to collect thermal emission spectra from the same part of the sample from which the Brillouin spectrum is collected. The signal of thermal emission is redirected to the Raman spectrometer with the help of a flip mirror installed in the final part of the collecting optical path, in front of the entrance pinhole of the Brillouin spectrometer.

Pyrope is known to have extremely low elastic anisotropy, therefore for these preliminary tests we collect the Brillouin spectra at only one selected crystallographic direction, assuming the sample to be elastically isotropic in the whole experimental P, T range. We collected the Brillouin spectra at a constant pressure of 1.3 GPa and temperatures between 298 K and 1580 K. We were able to measure thermal emission spectra at temperatures starting from 1000 K. Lower temperatures in this test were estimated using a temperature-output laser power relationship. Figure 3.8-10 shows our measured acoustic wave velocities of laser-heated single crystal pyrope in comparison with resistive heating data reported in the literature collected at ambient pressure for anhydrous pyrope up to the temperature of 1070 K and for hydrous pyrope up to the temperature of 700 K at ambient pressure. Further high-temperature measurements at higher pressures and at different sample orientation are required to determine the PVT equation of state of pyrope and to describe its elastic properties in the relevant P-T range for the interior of Mars.

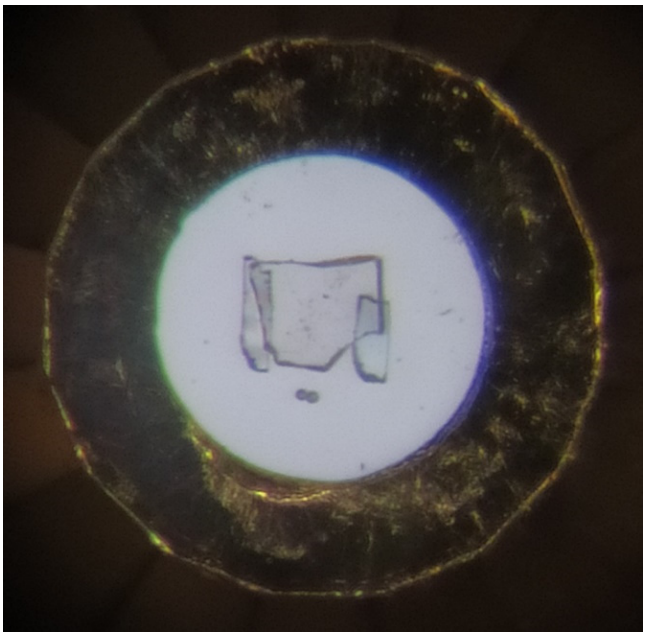

Fig. 3.8-9: 15 µm thick single crystal of pyrope separated from diamond culet using two 16 µm thick Sm:YAG platelets to avoid direct thermal contact with diamond. The sample is loaded with Ar as a pressure medium in the DAC with 500 µm culet diameter. Two ruby spheres are placed in the pressure chamber as pressure markers. Re is used as gasket material.

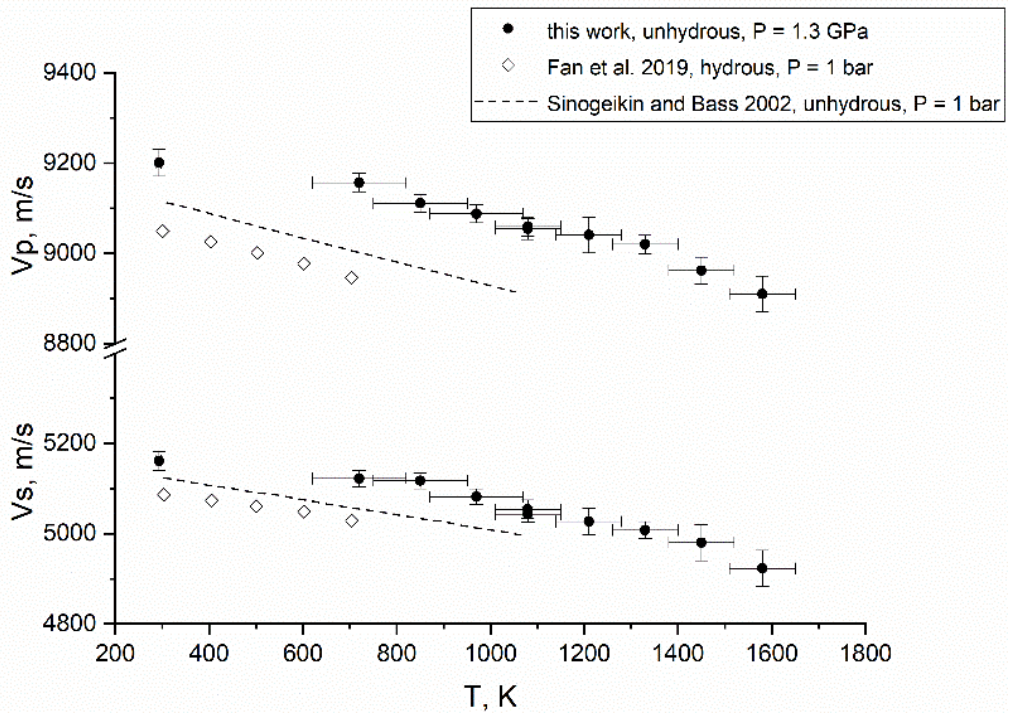

Fig. 3.8-10: Acoustic wave velocities measured for a single crystal pyrope sample in a DAC at P = 1.3 GPa and heated with CO_2 laser in temperature range from 298 K up to 1580 K.

g. *Monitoring oxygen fugacity in diamond anvil cells (S. Dominijanni, C.A. McCammon, L.S. Dubrovinsky, N. Miyajima, D.J. Frost and E. Koemets)*

Knowledge of mantle oxygen fugacity is fundamental since it influences numerous processes such as the nature and mobility of volatile species, depth of partial melting and speciation of gases that are vented to the atmosphere by volcanic degassing. Previous experimental studies have investigated mantle oxygen fugacity by performing high-pressure and high-temperature experiments in large volume presses that monitor oxygen fugacity using, for example, metal alloys as sliding redox sensors. However, so far oxygen fugacity has only rarely been controlled or even measured during diamond anvil cell (DAC) experiments, which are the gateway to the extreme pressure and temperature conditions of Earth's deep interior. Monitoring oxygen fugacity variation during these types of experiments will provide a more complete picture of high-pressure mineral phase equilibria and may reconcile contradictory results from previous studies conducted with DACs.

We are developing a new approach to measure and control oxygen fugacity in DACs using metal alloy oxygen sensors. We performed high-pressure and high-temperature experiments using ferropericlase $(Mg_{0.75}Fe_{0.25})O$ and iridium metal to synthesise an Fe-Ir alloy as a sliding redox sensor. We chose Ir over other possible candidates (*i.e.*, Pt or Pd) because the phase diagram of the Fe-Ir system is relatively simple at high temperature and room pressure.

Specifically, γ-(Fe,Ir) with the *fcc* structure is stable over a large range of temperature as a function of composition. We placed the starting mixture in a DAC with neon as pressure medium, compressed the cell to 60 GPa and heated at ~ 2000 K using a double-sided laser heating system. We measured the sample inside the DAC at the European Synchrotron Radiation Facility (Grenoble, France) using powder X-ray diffraction at beamlines ID15b and ID27, and synchrotron Mössbauer source and X-ray absorption near edge structure (XANES) spectroscopies at beamlines ID18 and ID24, respectively. After removal from the DAC the sample was prepared with a focused ion beam and analysed using transmission electron microscopy to determine chemical compositions and iron oxidation state.

Results from X-ray diffraction show that an Fe-Ir alloy is formed after laser heating. The reaction between Ir and ferropericlase is given by: (Mg,Fe)O + Ir → (Mg,Fe)O + (Fe,Ir) (Fig. 3.8-11a). Compressibility data up to 60 GPa reveal that the alloy is stable in the *fcc* structure over the entire pressure range. The oxidation state of iron ($Fe^{3+}/\Sigma Fe$) in ferropericlase appears to be below ~ 5 % based on analysis in the DAC as well as on the recovered run product. The XANES spectrum at 60 GPa after laser heating is shown in Fig. 3.8-11b, where the centroid and pre-edge features of the sample spectrum (black) match closely with those of Fe^{2+} (orange). We calculated the oxygen fugacity from the Fe in Ir thermodynamic model to be approximately one log unit above the iron-wustite buffer, which is consistent with the low concentration of Fe^{3+} in ferropericlase. Further analysis is underway to determine mass balance parameters of the reaction.

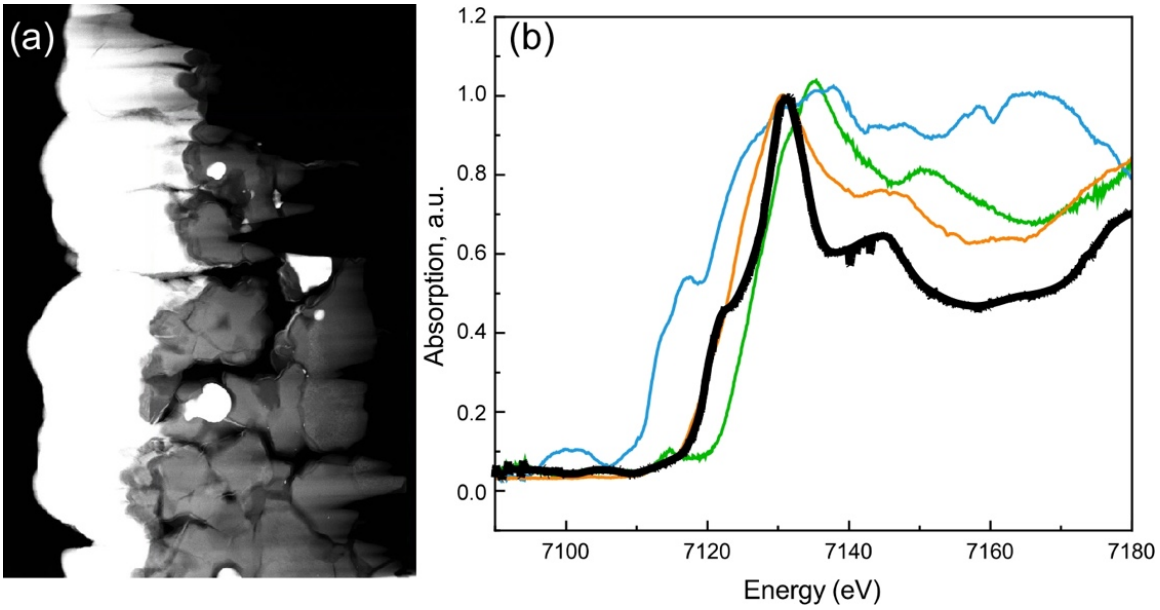

Fig. 3.8-11: a) Backscattered electron image of the recovered DAC sample containing Fe-Ir metal alloy (white) and ferropericlase (grey). The width of the image is approximately 3 µm. b) XANES spectrum of the sample in the DAC at 60 GPa after laser heating (black). For comparison, standard one bar spectra of Fe^0 metal (blue), $Fe^{2+}O$ (orange) and $Fe^{3+}{}_2O_3$ (green) are also shown.

h. *Fast-quenching multianvil technique (D. Bondar, H. Fei, A.C. Withers and T. Katsura)*

Water in the Earth's upper mantle is predominantly stored in nominally anhydrous minerals (NAMs) such as olivine, orthopyroxene, clinopyroxene, and garnet, and in silicate melts. Since incorporated water has a strong influence on mantle properties, such as melting temperature, rheology, electrical conductivity and seismic velocity, it is important to know the distribution of water among phases. Additionally, knowledge of how water partitions between upper mantle minerals and melts is essential for estimating the water content in incipient melts at different depths, the water transport by these melts, and the total amount of water in the upper mantle.

There are several studies reporting data on water partitioning between NAMs and melts. The most challenging part of these studies is to quench melt coexisting with mineral phases to form glass at elevated pressures (> 2 GPa), which is necessary to measure water partitioning with high accuracy. It also becomes more difficult to quench melt with higher Mg/Si ratio into glass, which is necessary in order to crystallize olivine from the melt. Previous studies produced mantle minerals coexisting with quenched melt up to only 5 GPa, namely olivine at ≤ 3 GPa, orthopyroxene at ≤ 4 GPa, clinopyroxene and garnet at ≤ 5 GPa. As a result, there is no systematic pressure, temperature and water content dependence of water partitioning due to the data being scattered over a narrow pressure range. Many authors also reported that glasses in some run products were not transparent, which implies micro-crystals may have crystallized in those studies.

The difficulty of quenching melt into glass lies in the insufficient cooling rate. The cooling rates of regular piston-cylinder and multianvil experiments used for these purposes are 120°/sec and 500°/sec, respectively. Quenching glass at elevated pressures and at various compositions is important not only for measuring water partitioning, but also for a number of other tasks, such as melt structure studies and partitioning of other components and elements.

The purposes of the present study are (1) to develop a multianvil technique allowing much faster cooling rate than conventional ones and (2) to measure water partitioning between upper mantle minerals and melts for a pressure range from 1 to 13 GPa, which covers the whole upper mantle overlying the transition zone.

Our fast-cooling multianvil technique is based on the idea of a rapid quench cell which includes a special assembly design and external cooling system. We use it in combination with 15-MN DIA-type multianvil press (IRIS) installed at the Bayerisches Geoinstitut, Germany.

In contrast to a regular multianvil assembly, which keeps heat inside in order to increase heating efficiency and to decrease thermal gradient, our special assembly was built in order to take heat out of the assembly as fast as possible. The outstanding feature of this assembly is the presence of tungsten ring and rods. The latter contacts with second stage anvils, providing fast heat removal from a sample.

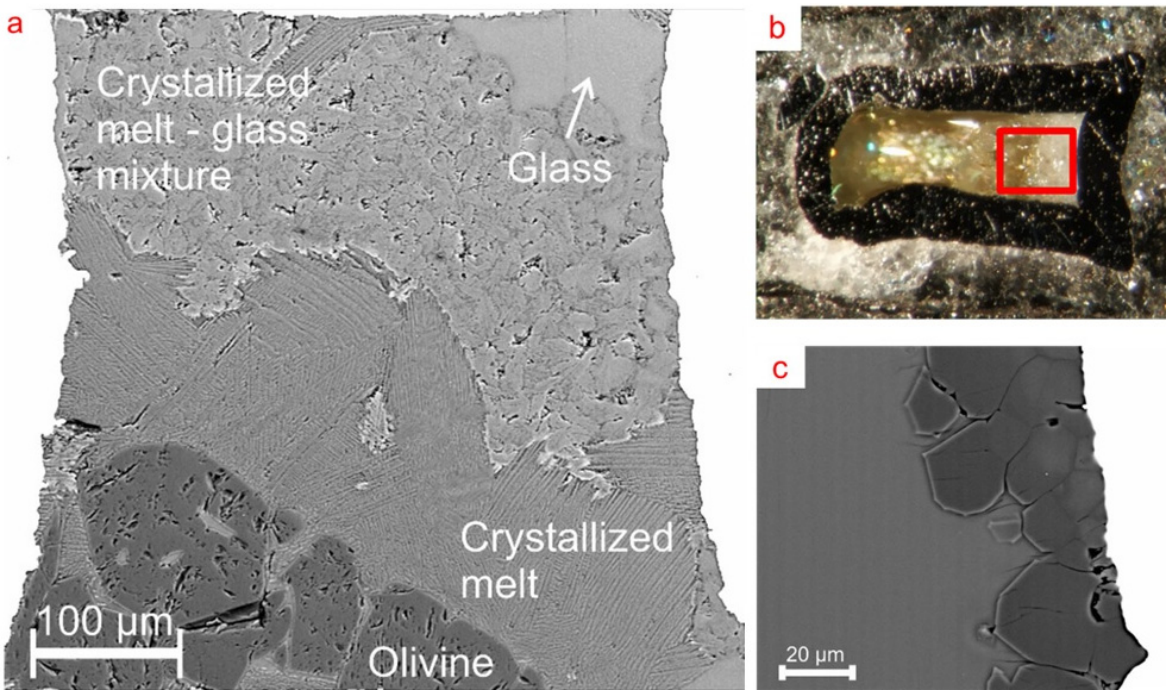

Fig. 3.8-12: (a) Glass coexisting with olivine at 6 GPa, (b) Glass coexisting with garnet at 6 GPa, (c) BSE image of the area in the red box from picture b.

Our multianvil technique has already produced a very high quenching rate (5200°/sec) compare to a regular one. More than seventy experiments were performed in order to develop a working system as we tried many different configurations, parts, materials etc.

To date, we were able to get glass coexisting with olivine (Fig. 3.8-12) in 5 melting experiments at pressures from 2 to 6 GPa respectively, with Kilbourne Hole fertile spinel peridotite (KLB-1) as starting composition. We also obtained completely transparent glass coexisting with garnet at 6 GPa (Fig. 3.8-12b, c), with a basalt-peridotite (70:30) mixture as the starting composition. We plan to improve the fast quenching technique to quench melts under even higher pressure.

i. *Assessment of the reliability of the diamond trap technique for measuring high-pressure fluid compositions (G. Rustioni, A. Audétat and H. Keppler)*

Fluids play a key role in many processes such as mass transport, melting and crystallization in a large variety of geological settings. However, the determination of fluid compositions at high pressure and temperature is challenging. Several experimental methods have been developed in the past, and one of the most used ones is the diamond trap technique. This method makes use of a diamond powder layer inserted at the centre of the capsule to provide a network of pores that are preserved at high pressure, where only the fluid is able to circulate. Therefore, it is reasonable to assume that any solid material found in the diamond trap portion of the capsule

was originally dissolved in the fluid in equilibrium with minerals at high pressure and temperature. Freezing the capsule in liquid nitrogen before cutting it open and keeping it frozen during the entire analysis performed with laser-ablation inductively-coupled-plasma mass-spectrometry allows direct measurement of the composition of the frozen fluid together with the solid precipitates that may have formed during quenching. Therefore, the method allows us to obtain the composition of the fluid as it was during experiments.

The reliability of this method was assessed by mineral solubility tests performed on simple and well-studied systems as well as on trace element partitioning experiments in the eclogite-water ± NaCl system. All experiments were conducted in a piston cylinder apparatus at conditions ranging between 1-4 GPa and 700-1000 ºC with durations of 1-7 days (Fig. 3.8-13).

Silica solubility tests in both quartz-water and forsterite-enstatite-water systems, as well as experiments conducted on albite-water supercritical fluids, provide data with an accuracy within a factor of 2 with respect to the expected values (Fig. 3.8-14). Using the diamond trap method to determine the solubility of corundum overestimates it by a factor of three. Tests were also performed in the rutile-water system, which is known to be difficult to study due to dissolution and re-precipitation effects caused by small temperature gradients. Such problems were also encountered in our experiments, and the measured solubilities were too high by about a factor of 10, if compared to recent literature data.

Fig. 3.8-13: Diamond trap capsule after piston cylinder experiment and laser ablation analysis. A diamond powder layer is sandwiched between layers of synthetic eclogite.

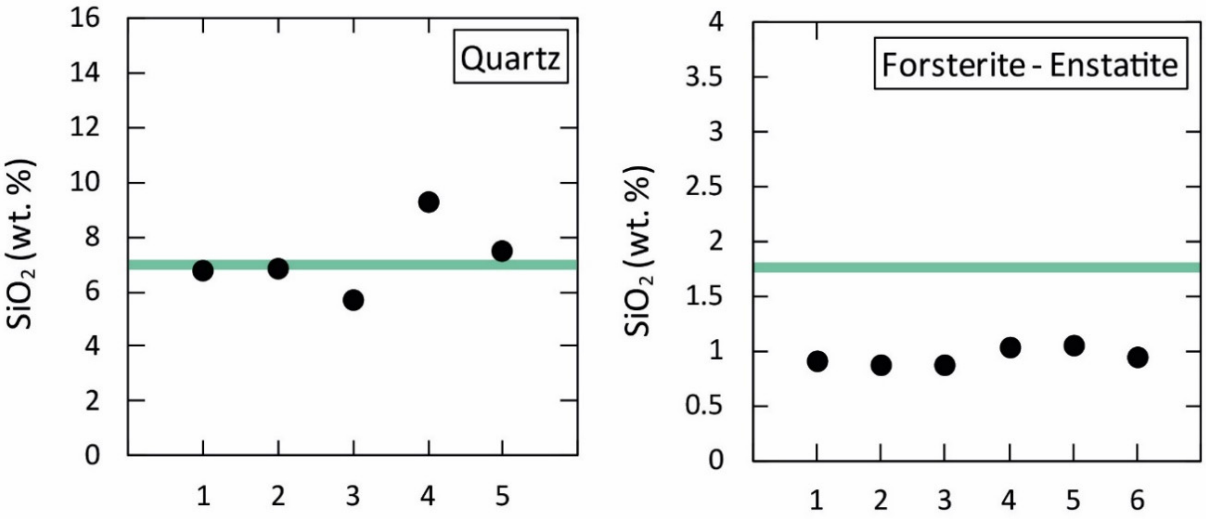

Fig. 3.8-14: SiO_2 solubilities measured in the quartz-water and forsterite-enstatite-water systems. Green lines represent expected solubilities of SiO_2 from literature.

More promising results were obtained for trace element partitioning in the eclogite-water ± NaCl system. Increasing fluid salinity was found to enhance trace element solubility. This behaviour was confirmed by experiments conducted with starting materials doped with different concentrations of trace elements. Moreover, reversed experiments where trace elements were completely doped in the fluid phase instead of the solid starting material are in very good agreement with forward experiments. This evidence demonstrates that equilibrium between fluid and eclogitic minerals was achieved.

In general, our results indicate that the diamond trap method is very useful when relatively low precision is sufficient for the purpose of the study. It is therefore a good tool to study, for example, trace-element partitioning behaviour in complex systems that are difficult to study with alternative experimental methods. It is not, however, the best method for major-element solubility measurements in simple systems, where more precise experimental methods are available.

j. *Synthesis and maintenance of CH_4-rich fluids in high-pressure multianvil experiments (V. Matjuschkin and A.B. Woodland/Frankfurt/M.; D.J. Frost)*

In magmatic processes, volatiles (*e.g.*, H_2O, CO_2, CH_4) are crucial components that control the chemical and physical behaviour of rocks, such as the conditions of partial melting and subsequent crystallisation, and as a consequence, differentiation of the Earth's interior and volcanism. Despite overall progress made in assessing the role of oxidized fluid components such as H_2O and CO_2, we still face problems in understanding the role of reduced CH_4-H_2-rich fluids in deep Earth processes. Recent experimental work suggests that CH_4-rich fluids are

relevant for the mantle environment, at $\Delta \log fO_2 \approx$IW+0.5 to IW+1.0 (IW = iron-wustite equilibrium), which is consistent with the observation of methane inclusions in some diamonds. This study further develops an experimental approach for the production of reduced fluids and fluid inclusions at high-pressure conditions > 6 GPa using the multianvil apparatus that can be subsequently investigated by Raman spectroscopy or gas chromatography.

We use a double capsule approach consisting of an outer Au capsule containing i) inner Au-capsule containing a reduced metal buffer (*i.e.*, Mo-MoO_2-H_2O), ii) powdered starting material including a fluid source, and iii) a single crystal of olivine for trapping fluids (Fig. 3.8-15A). A polycrystalline CaF_2 pressure medium is an essential part of the assembly and is used to minimise the H_2-loss from the sample. It is strongly advised not to use Pt, Pd, Fe, Mo, Si or their alloys (even < 10 at. % concentrations) as capsule materials, as they lead to uncontrolled dehydrogenation and decarbonation of the reduced fluids and cause fO_2 disequilibrium in the sample. Note that the use of "crushable" pressure materials such as extruded MgO, Al_2O_3 or other materials with high-porosity will lead to H_2-loss and physical damage to the outer Au-capsule. A mass-balance recalculation of the minerals or solid materials should be made to check for the effects of Fe-loss to the Au-capsules under reduced conditions. The Fe-loss reaction is kinetically slower compared to the fluid equilibration reaction. The amount of Fe-loss in this study was minimized by increasing the sample volume by maximising the size of the outer capsule. Contrary to that observed for Fe-FeO, the Mo-MoO_2 metal buffer exhibits no chemical reactions with Au even during long-term runs of > 4 days, and provides fO_2 conditions near the IW-buffer.

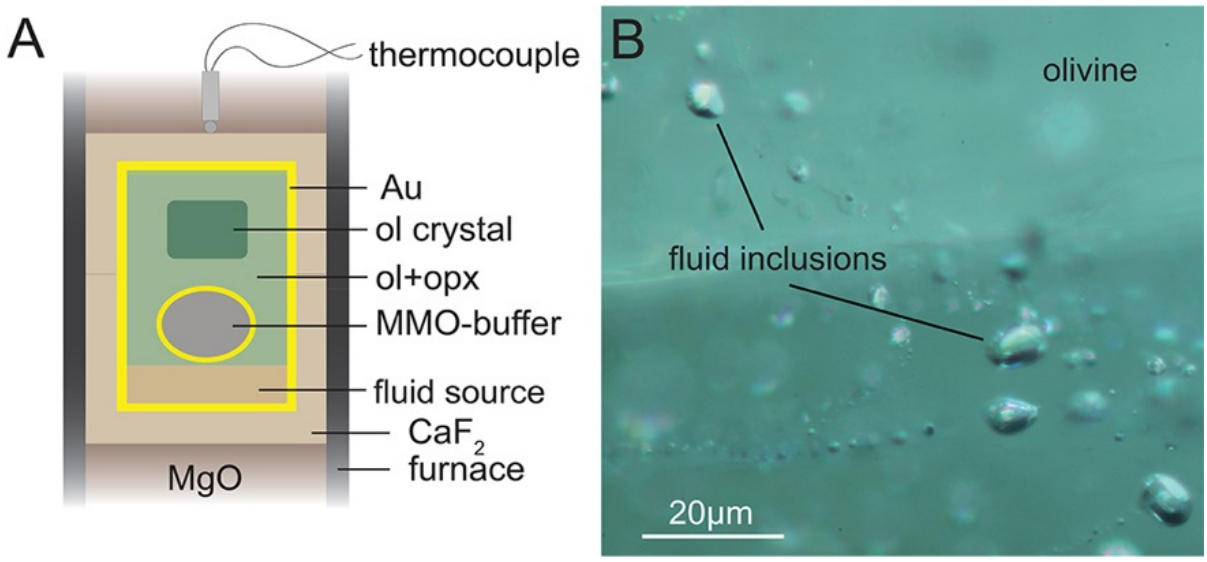

Fig. 3.8-15: (A) Experimental setup for multianvil experiments. Ol-olivine, opx-orthopyroxene, ol-crystal – single olivine crystals, MMO – Mo-MoO_2-H_2O buffer, fluid source is a solid C-bearing material (*e.g.*, stearic acid). (B) An example of fluid inclusions trapped in ol-single crystal.

Experiments were performed at 7 GPa and temperatures from 1100 to 1300 °C in the 5000-ton multianvil press (Zwick) using 25M octahedral pressure cells. The starting material was placed in an outer Au capsule (3.5 mm diameter and up to 6 mm long) that contains an inner Au buffer capsule (2.5 mm ø, 3 mm long) filled with Mo-metal and 3 µl H_2O. We used a straight vertical graphite furnace to maximise sample volume. To produce reduced magmatic fluids, solid organic material was used (lauric acid, stearic acid etc.). CaF_2 was cut to form two cups around the capsule with wall thickness > 0.3 mm. Note that reducing the wall thickness to < 0.2 mm leads to collapse of CaF_2 and contact between the graphite furnace and capsule during pressurisation. This contact promotes H_2-loss. The thermocouple is positioned ~ 0.2 mm above the capsule (Fig. 3.8-15A). Although this adds an uncertainty in temperature, the complete isolation of the capsule by CaF_2 is very important for achieving fH_2- equilibrium.

After the experiments an extensive number of fluid inclusions (Fig. 3.8-15B) is observed to have been trapped in the olivine crystals. Application of Ir-Fe redox sensors reveal that the experiments ran under the conditions of $\Delta \log fO_2$ ~ IW+0.5 to IW+1.0. All fluids exhibit similar composition and are predominantly CH_4 with minor C_2H_6 and H_2 apparent in the Raman spectra. Although some thermodynamic models predict the presence of significant proportions of H_2O in C–O–H fluids under these conditions, no water was detected. However, we do observe H_2 in Raman spectra and the incorporation of OH into the olivine from FTIR measurements. Calculated OH concentrations in olivine range from ~ 60 to 100 ppm H_2O and increase with increasing fO_2. In addition to our previous study at 3-6 GPa, the new experiments at 7 GPa give us further confirmation that fluids with significant amounts of CH_4 are likely to be stable under conditions similar to those prevailing in the deeper upper mantle. This study is a further successful demonstration of how oxygen fugacity control can be achieved in high-pressure experiments when applying the right combination of materials (capsule, pressure-medium materials).

k. *Simultaneous generation of ultra-high-pressure and -temperature in multianvil apparatus (L. Xie and T. Katsura)*

The multianvil apparatus has the advantage of generating lower mantle quasi-hydrostatic pressures in a large volume, compared with the diamond anvil cell. Therefore, the multianvil is an indispensable means to investigate the physical and chemical state of the lower mantle, especially for measurements (such as self-diffusion coefficient of elements) requiring large samples. There were remarkable breakthroughs in multianvil technology recently: the highest pressure exceeded 120 GPa at room temperature by using sintered diamond (SD) anvils, and the highest temperature reached as high as 4000 K at ~ 15 GPa by developing the boron-doped diamond (BDD) heating element. However, to cover the lower mantle conditions, simultaneous generation of ultra-high pressure (~ 120 GPa) and temperature (~ 3000 K) is required. In order to decrease the difficulty, we select a target of generation of 80 GPa and 3000 K, which already covers some important mantle regions such as viscosity peak at top lower mantle and spin transition of Fe.

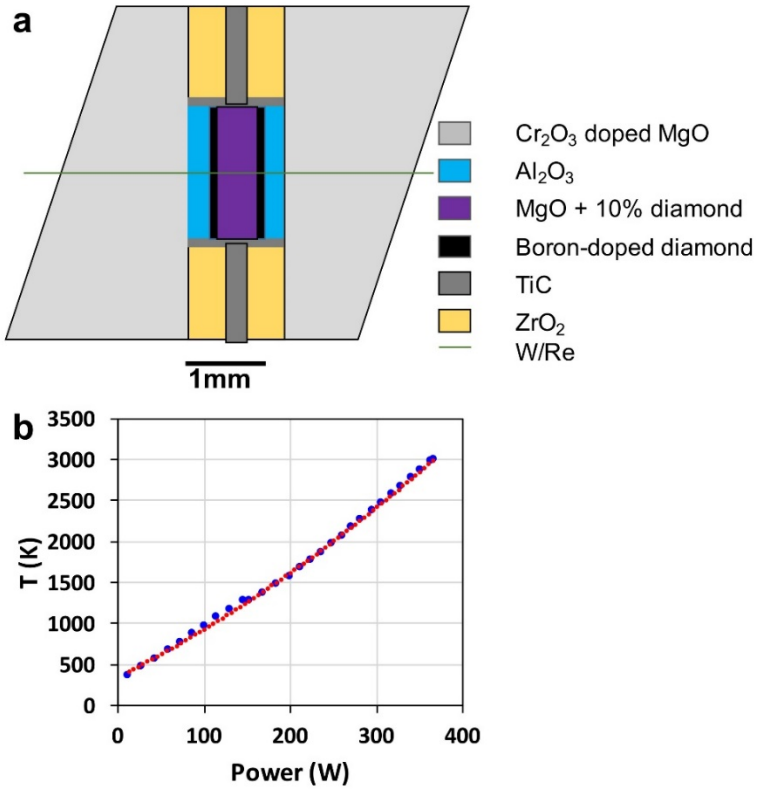

Fig. 3.8-16: Cell assembly (**a**) and power-temperature relation (**b**).

The combination of SD anvils and BDD heaters is a promising method to generate such pressures and temperatures simultaneously. Because SD anvils have much higher thermal conductivity than WC anvils, as a first step, we tried to develop the technique of ultra-high-temperature (~ 3000 K) generation with SD anvil at relative low pressures (~ 25 GPa). Figure 3.8-16a shows the cell assembly. SD cubes with 14 mm edge-length and 1.5 mm truncation-edge-length were used as second stage anvils. An MgO octahedron with 5.7 mm edge length was used as pressure medium. A mixture of MgO+10 wt. % diamond was used as pressure marker. Temperature was measured by W/Re thermocouple. Figure 3.8-16b shows the power-temperature relationship: We confirmed that generating temperature as high as 3000 K is possible using SD anvils. In the future, we will develop the technique for simultaneous generation of ultra-high-pressure and ultra-high-temperature generation.

l. *Numerical/experimental study of microstructure and permeability in porous granular media (P. Eichheimer, M. Thielmann, W. Fujita/Sendai, G.J. Golabek; M. Nakamura, S. Okumura and T. Nakatani/Sendai; M.O. Kottwitz/Mainz)*

Fluid flow on different scales is of interest for several geoscience disciplines like petrophysics, hydrogeology and volcanology. To simulate fluid flow in large-scale numerical simulations (of, *e.g.*, groundwater and volcanic systems), flow properties on the microscale need to be considered. For this purpose, experimental and numerical investigations of porous media over

a wide range of porosities are necessary. In the present study we sinter low porosity porous glass media and investigate the microstructure, namely effective porosity, effective specific surface and hydraulic tortuosity, using image processing. To estimate flow properties like permeability on the large-scale, we provide a modified Kozeny-Carman relation depending only on porosity (Fig. 3.8-17).

The estimates are then compared to permeability determinations based on both experimental and numerical investigations (Fig. 3.8-18). Additionally, we have produced a dataset of segmented input files to serve as benchmark for future numerical studies.

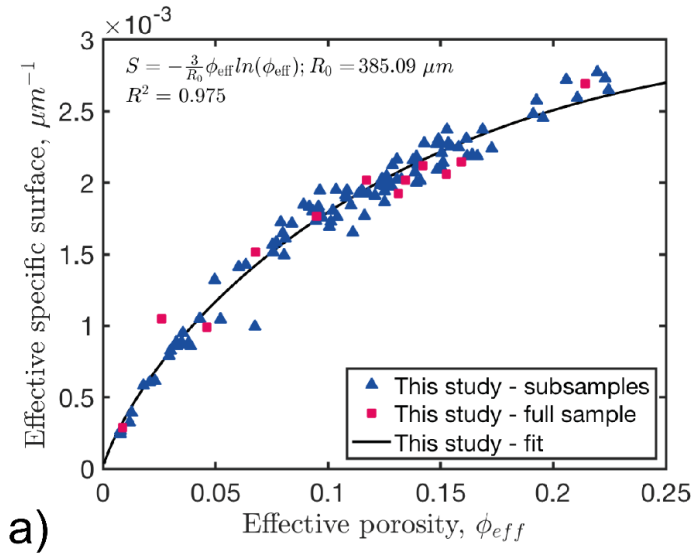

Fig. 3.8-17: Computed effective specific surface for each subsample (blue triangles) and all full samples (red squares). The fit corresponds to the given equations in the top left.

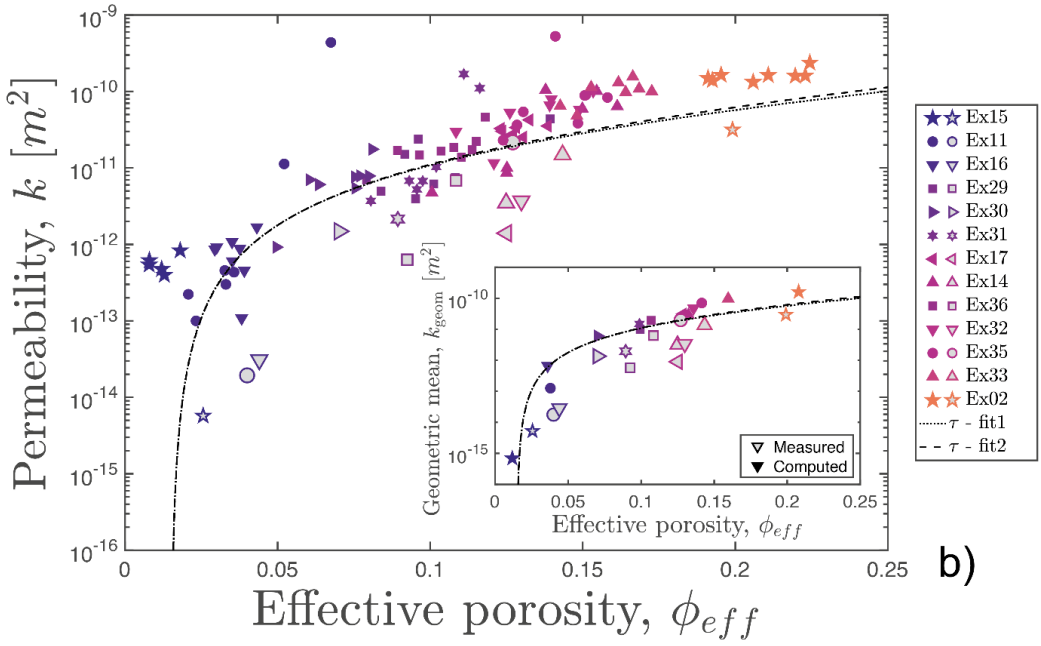

Fig. 3.8-18: Computed permeabilities in filled symbols and measured permeabilities in colored symbols with grey edges. The fitted Kozeny-Carman lines using the computed microstructural parameters are displayed as black lines.

m. *Pore-scale permeability prediction for Newtonian and non-Newtonian fluids (P. Eichheimer, M. Thielmann, A. Popov/Mainz, G.J. Golabek, W. Fujita/Sendai; M.O. Kottwitz and B.J.P. Kaus/Mainz)*

The flow of fluids through porous media, such as occurs during groundwater flow or magma migration, is a key process in geological sciences. Flow is controlled by the permeability of the rock; thus, an accurate determination and prediction of its value is of crucial importance. For this reason, permeability has been measured across different scales. As laboratory measurements exhibit a range of limitations, the numerical prediction of permeability at conditions where laboratory experiments struggle has become an important method to complement laboratory approaches. At high resolutions, this prediction becomes computationally very expensive, which makes it crucial to develop methods that maximize accuracy. In recent years, the flow of non-Newtonian fluids through porous media has gained additional importance due to, *e.g.*, the use of nanofluids for enhanced oil recovery. Numerical methods to predict fluid flow in these cases are therefore required.

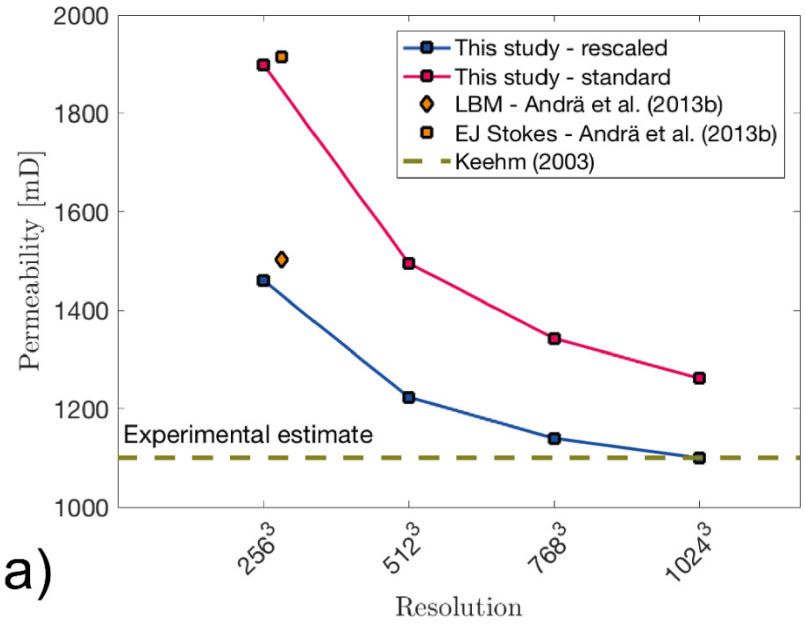

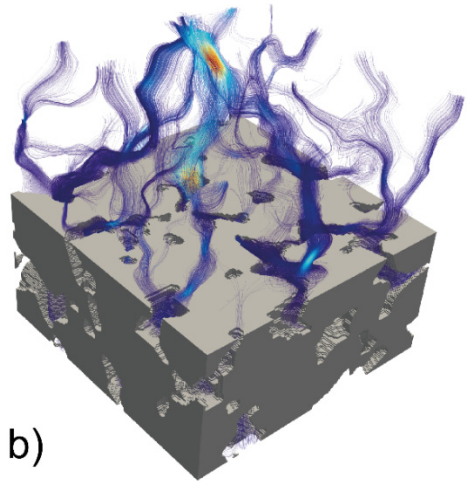

Fig. 3.8-19: **a)** Numerical convergence with increasing spatial resolution. Blue curve represents computations using stencil rescaling, red curves denote standard finite difference approach. Yellow dotted line displays the experimental measured value for this specific sample. **b)** shows flowlines colored with the computed velocities.

Here, we employ the open-source finite difference solver LaMEM (Lithosphere and Mantle Evolution Model) to predict numerically the permeability of porous media at low Reynolds numbers for both Newtonian and non-Newtonian fluids. We employ a stencil rescaling method to describe better the solid–fluid interface. The accuracy of the code is verified by comparing numerical solutions to analytical ones for a set of simplified model setups. Results show that stencil rescaling significantly increases the accuracy at no additional computational cost. Finally, we use our modeling framework to predict the permeability of a Fontainebleau sandstone and demonstrate numerical convergence. Results show very good agreement with experimental estimates as well as with previous studies (Fig. 3.8-19). We also demonstrate the ability of the code to simulate the flow of power-law fluids through porous media. As in the Newtonian case, results show good agreement with analytical solutions.

n. *Effect of grid resolution on tectonic regimes in global-scale convection models (E. Marzotto, M. Thielmann and G.J. Golabek)*

A key ingredient to reproduce plate-tectonics in numerical models is a visco-plastic rheology. Strongly temperature-dependent rheology generates a rigid lid at the surface, whereas plastic rheology allows for the formation of plate boundaries. The yield stress limiter (τ_y) is the parameter that controls the strength of the lithosphere. By changing τ_y, different tectonic regimes can be reproduced:

Dripping behaviour **(**low τ_y): the lithosphere is continuously sinking into the mantle, but lacks rigidity to sustain continuous subduction.
Plate-like behaviour **(**intermediate-low τ_y): plate boundaries are formed and, once subduction starts, the slab is rigid enough to avoid repetitive slab breakoff.
Episodic behaviour **(**intermediate-high τ_y): long-term stagnant lid stages are followed by episodic overturn events.
Stagnant lid behaviour (high τ_y): the elevated strength the lithosphere leads to the formation of one continuous plate.
Each lid behaviour can be distinguished by comparing the evolution profile of several parameters (Fig. 3.8-20).

Here we use the code StagYY in a 2D spherical annulus geometry to determine the resolution-dependent tectonic regime for different τ_y.

We tested 12 resolutions (ranging from 128×32 to 1024×128 grid nodes), keeping all physical parameters unchanged (Fig. 3.8-21).

A sufficiently high resolution is necessary in order properly to resolve the thin lid. Low radial resolution favours weak lid regimes because the lithosphere is under-resolved, meaning that nodes are too far apart from each other. Low azimuthal resolution causes a strong lithosphere because plate boundaries are not spotted by the code. Therefore, a fragmented lid is perceived as intact.

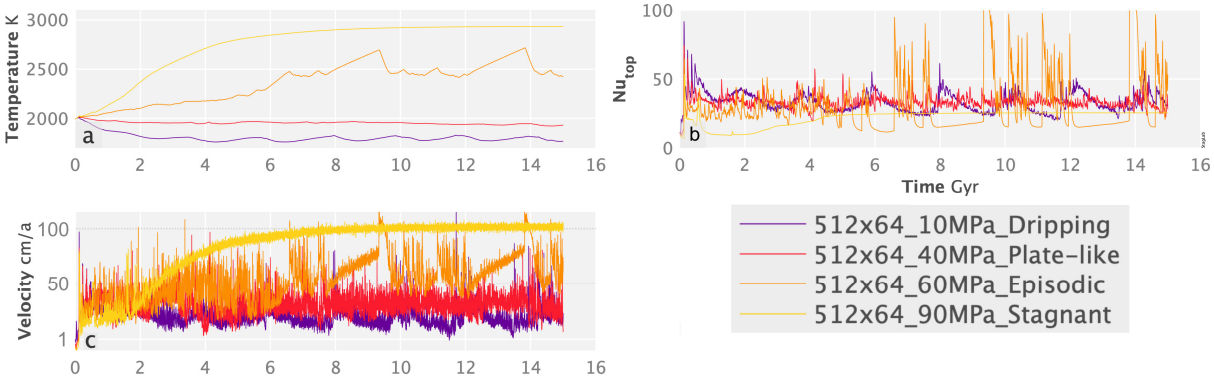

Fig. 3.8-20: Different lid regimes over time: (a) temperature, (b) surface Nusselt number, (c) whole mantle velocity. Dripping (purple), plate-like (red), episodic (orange) and stagnant (yellow).

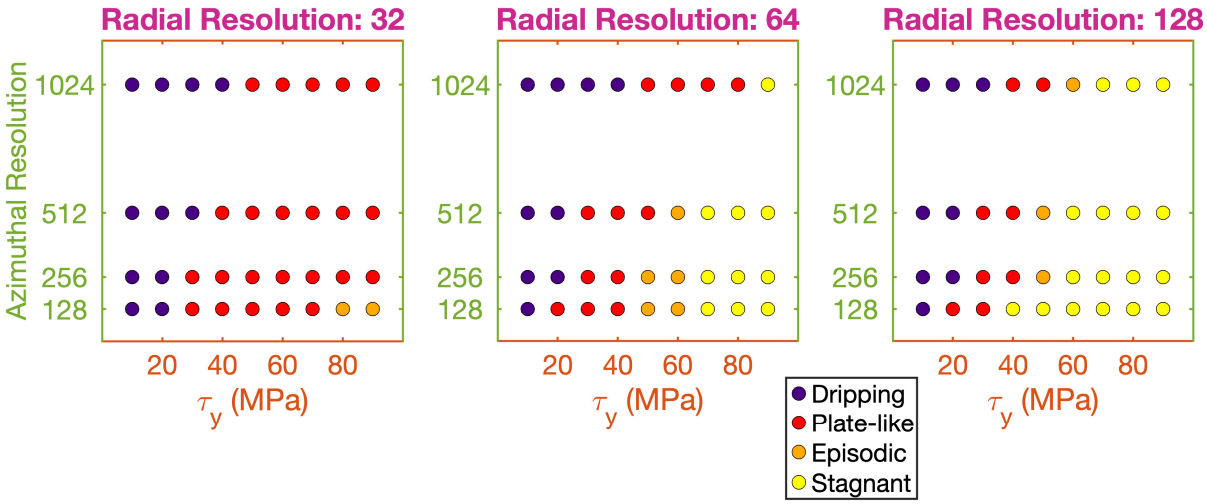

Fig. 3.8-21: Lid regimes obtained for various yield stresses. Each dot represents a simulation. In each box the radial resolution is kept constant (32, 64 and 128 nodes) whereas the azimuthal resolution is changed.

4. The International Research and Training Group – "Deep Earth Volatile Cycles" (DFG GRK 2156/1)

The International Research and Training Group (IRTG), "Deep Earth Volatile Cycles", is funded by the *Deutsche Forschungsgemeinschaft* (DFG). This graduate school for doctoral studies started in April 2016, and is funded for a period of 4.5 years. It is a cooperation between the Bayerisches Geoinstitut (BGI) and the Department of Earth Sciences at Tohoku University, Sendai/Japan. The IRTG is chaired by Dan Frost (Bayreuth) and Michihiko Nakamura (Sendai).

The objective of this collaborative research effort is to study the cycling of volatile elements through the deep interior of the Earth. Using mainly experimental and computational methods, the group's goal is to quantify how volatile elements such as carbon, hydrogen and nitrogen are transported, stored and expelled from the interior, as a result of plate tectonic processes. Doctoral researchers receive training in modern experimental and modelling techniques employed in solid Earth geosciences, in a structured learning program. At the same time, they pursue independent research into geochemical and geophysical aspects of the internal volatile cycle. Doctoral researchers from the BGI spend between 6 and 12 months at Tohoku University (TU) as part of a complementary research exchange which, in turn, sees scientists from TU spending time at the BGI.

IRTG Activities for 2019:

Short Course on Physics and Chemistry of the Earth's Interior: February 14-15, 2019

A two-day, compact short course which is given every year in Sendai, to TU and visiting BGI doctoral students. This course focuses on topics concerning the deep Earth, such as the physical and chemical properties of geomaterials that are essential for investigating the structure and dynamics of the Earth's interior. In the first year (2016), this course was given in both Japanese and English, which was well received and helped with terminology.

DMG-Short Course: February 18-22, 2019

In February, 31 doctoral and master students took part in a five-day short course, "*High-Pressure Experimental Techniques and Applications to the Earth's Interior*" at the BGI. Three doctoral students from TU joined the course, along with participants from 11 countries in total. The students received a practical introduction into high-pressure and high-temperature experiments, as well as analytical techniques commonly used in the investigation of high-pressure samples. The course was very well received, and fostered exchange and collaboration between participants and lecturers.

Participants and lecturers of the DMG-Short Course, "*High-Pressure Experimental Techniques and Applications to the Earth's Interior*", at the BGI.

Field Trip to the Hawaiian Islands: March 4-13, 2019

Michihiko Nakamura organized a field trip for TU and visiting BGI IRTG students to the Hawaiian Islands (The Big Island, Maui, and O'ahu). This was an invaluable opportunity for the IRTG students from both the BGI and TU to examine the active volcanic fields of a hot spot volcano. Most notably, the IRTG students were able to visit the Kīlauea Volcanic Fields and the Haleakalā High Altitude Observatory Site.

BGI IRTG student pictures from the Kīlauea (left) and Haleakalā (right) volcanic parks.

Field Trip to Miyake Island, in the Philippine Sea: May 11-13, 2019

A field trip was organized by Michihiko Nakamura to Miyake Island, (a stratovolcano in the Philippine Sea), which is located approximately 180 kilometers southeast of Honshu, Japan. The field trip provided an opportunity to collect samples from the "Ofunato scoria" – which contain a few tiny olivine grains, with some relatively primitive melt inclusions.

Field Trip to the Volcanic Complexes of Mount Zaō: May 25, 2019

The BGI IRTG and TU students visited the strato-volcanic complexes of Mount Zaō, which is conveniently located only a few hours from Sendai. This field trip served as an introduction to an active arc volcanic complex, and was compulsory for the visiting BGI IRTG students.

IRTG International Workshops in Tokyo and Sendai: May 31-June 4, 2019

The workshop entitled "*Deep Volatile Cycling in the Earth*" was organized to bring together students and scientists from TU and the BGI, at the Tohoku branch in Tokyo. All IRTG students from the BGI and TU gave presentations about their research projects, as well as six invited speakers from other research institutions. This meeting was followed by another workshop entitled "*Earth, Sea and Sky V: International Joint Graduate Program Workshop in Earth and Environmental Sciences*" in Sendai. The program included: a one-day field trip to the tsunami disaster area from the Great East Japan Earthquake of 2011, a day of qualifying examinations for GP-EES students from TU (with mixed TU/BGI examiners), as well as one day of scientific presentations given by guests from overseas research institutions, which was accompanied by a poster session. All together, these five days of programs were an ideal opportunity for the PhD students to present their scientific results and discuss them with experts in the field, as well as to intensify their contacts with the respective partner institution and colleagues.

Group photo from the IRTG International Workshop on "*Deep Volatile Cycling in the Earth*".

IRTG Field Trip to Mount Fuji and the Surrounding Area: June 2, 2019

Naoki Araya (a TU PhD student), organized a field trip to Mount Fuji and the neighboring Shizuoka and Yamanashi Prefectures, on the Sunday between the IRTG International Workshops in Tokyo and Sendai. This field trip included a visit to a volcanic pipe, and also provided an introduction to an active arc volcano for many of the BGI IRTG and TU students.

Participants of the IRTG field trip to Mount Fuji and the surrounding area.

Field Trip to Ries Impact Crater, Nördlingen: September 27-28, 2019

A two-day excursion to the Nördlinger Ries was organized by Prof. Audrey Bouvier (BGI). The group, which included Dr. Florian Heidelbach, Prof. Michihiko Nakamura, 11 IRTG BGI and TU students, and four BGI Masters students, visited various outcrops to examine the large-scale effects of impact cratering and shock metamorphism. The Ries is one of the best-preserved large impact crater structures on Earth (~ 25 km diameter), and very accessible. The visit commenced with an overview lecture on impact cratering provided by Dr. Stefan Hölzl and Dr. Jörg Fritz, at the Rieskrater Museum and ZERIN Research Centre. These facilities include unique rock and meteorite collections. The group then climbed the bell tower of the Church of St Georg in Nördlingen, which is constructed of the local shock metamorphic rock called suevite; they were rewarded with an amazing 360˚ view of the medieval city and the crater structure. Visits to the field sites and quarries were coordinated with Gisela Pösges and Cindy Cooper, of the Ries Geopark (www.geopark-ries.de). The variety of impact-formed and displaced rocks and the unusual structural geology are spectacular, and result from a series if sequential processes that can be traced through the very short timescale of the impact. The significance of the impact crater itself has been recognized since the 1960s, when it was used as a training ground for Apollo astronauts. In the evening, Dr. Vera Assis Fernandes (University of Manchester) gave a presentation about the bombardment history of the Moon. The group travelled from the northern to the southern rim of the crater to observe and compare the lithologies involved within the breccias, exposure of the crystalline rocks, lake reef, and distal deposits of suevite. In addition to the unique impact-related features, such as impact rocks and high-pressure shock minerals, the Ries Geopark has much more to offer; the students were also exposed to paleontology and sedimentary geology, archaeology, and links between geology and historical architecture in Nördlingen.

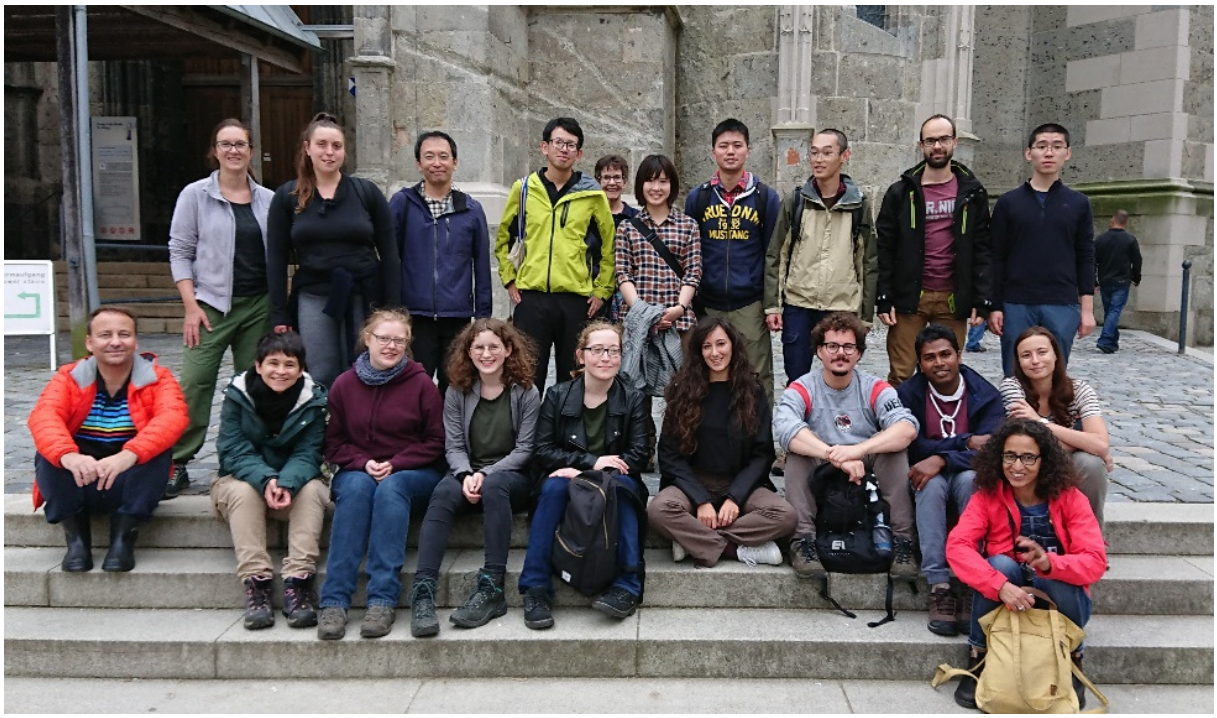

Field trip participants in Nördlingen, in front of the St Georg Church, which was built using suevite impact melt rock.

IRTG Soft Skills Course, "Presentation and Rhetorical Skills": September 30-October 1, 2019

A two-day soft skills course entitled "*Presentation and Rhetorical Skills*" was organized at the BGI, and was attended by 12 PhD students (four of them from TU). During the course, participants gave short presentations which were recorded on video and reviewed afterwards. The course provided very valuable advice for giving presentations and presenting posters, and was very well received by the students.

The instructor and some of the participants of the IRTG soft skills course, "*Presentation and Rhetorical Skills*" at the BGI.

IRTG Career Evening for Female Scientists: October 18, 2019

In the framework of equal opportunity initiatives of the IRTG program, a career evening was organized for female scientists at the BGI. Former PhD students of the BGI, Dr. Martha Pamato (Università di Padova, Italy), and Dr. Micaela Longo (Canon Inc, UK), were invited to this evening; they described their experiences during their professional career in science and industry, respectively. Their entertaining talks were very well received, and were followed by a lively discussion among the attendees.

Presenters and attendees of the IRTG Career Evening for Female Scientists.

A Humboldt Research Award for Professor Eiji Ohtani, from Tohoku University: Professor Ohtani received a prestigious Humboldt Research Award from the Alexander von Humboldt Foundation, for his achievements in experimental high-pressure Earth sciences. As part of the award, he was able to spend three months at the BGI in 2019, where he started several projects with BGI colleagues, and IRTG students. He is also supervising students from the BGI during their research stays at Tohoku University, and will return to Bayreuth in the coming years to further strengthen the ties between the BGI and Tohoku University.

In 2019, several staff members, researchers and students from the two participating institutes made visits to the collaborating institutions for the discussion of projects, to give and attend presentations, to perform experiments, and to complete internships:

Tohoku colleagues who visited the BGI in 2019:

Name	Period	Name	Period
Suzuki, Akio, Prof.	22.12.18-14.01.	Nakajima, Ayano	19.08.-30.08.
Ohashi, Tomonori	22.12.18-14.01.	Suzuki, Akio	19.08.-16.09.
Araya, Naoki	13.02.-22.02.	Ban, Rintaro	19.08.-16.09.
Furukawa, Yoshihiro	14.02.-15.02.	Ikeda, Osamu	19.08.-16.09.
Huang, Yongsheng	23.02.-22.03.	Huang, Yongsheng	24.08.-15.10.
Suzuki, Akio, Prof.	28.02.-10.03.	Muranushi, Miki	01.09.-16.09.
Muranushi, Miki	28.02.-10.03.	Sawa, Sando	18.09.-24.10.
Ban, Rintaro	28.02.-10.03.	Takahashi, Naoko	26.09.-09.10.
Yutani, Taku	08.03.-28.03.	Nakamura, Michihiko	26.09.-09.10.
Sakamaki, Tatsuaya	11.03.-15.03.	Tsushima, Naoya	26.09.-09.10.
Ozawa, Shin	11.03.-15.03.	Araya, Naoki	30.09.-08.10.
Kawanobe, Hiroyuki	11.03.-15.03.	Fujita, Wakana	30.09.-11.10.
Yuan, Liang	17.03.-16.04.	Muto, Jun, Prof.	06.10.-10.10.
Huang, Yongsheng	06.04.-22.04.	Tsujimori, Taksuki	03.11.-09.11.
Ohashi, Tomonori	11.07.-05.08.	Fukushima, Ryo	03.11.-16.11.
Ohtani, Eiji, Prof.	07.08.-31.10.		

BGI colleagues who visited Tohoku University in 2019:

Name	Period	Name	Period
Satta, Niccoló	16.01.-09.07.	Cialdella, Laura	24.05.-04.06.
Marzotto, Enrico	01.03.-31.08.	Criniti, Giacomo	24.05.-04.06.
Putak Juriček, Marija	27.05.-28.06.	Ishii, Takayuki	24.05.-03.06.
Eberhard, Lisa	21.03.-28.09.	Eichheimer, Philipp	25.05.-03.06.
Rustioni, Greta	25.03.-30.06.	Thielmann, Marcel	27.05.-07.06.
Dominijanni, Serena	07.05.-01.08.	Frost, Dan, Prof.	28.05.-05.06.
Steinle-Neumann, Gerd	22.05.-11.06.	Huang, Rong	29.05.-07.06.
Bondar, Dmitry	23.05.-05.06.	McCammon, Catherine	29.05.-06.06.
Koemets, Egor	23.05.-27.06.	Miyajima, Nobuyoshi	29.05.-03.06.
Koemets, Iuliia	23.05.-04.06.	Boffa Ballaran, Tiziana	29.05.-05.06.
Melai, Caterina	24.05.-18.08.	Siersch, Nicki	29.05.-14.06.
Abeykoon, Sumit	24.05.-04.06.		

5. Publications, Conference Presentations, Seminars

5.1 Publications (published)

Supplement to **2018** (papers published at the end of 2018):

KICHANOV, S.E.; MEHDIYEVA, R.Z.; DANG, N.T.; JABAROV, S.H.; KOZLENKO, D.P.; DUBROVINSKY, L.S.; MAMMADOV, A.I.; LUKIN, E.V.; KURNOSOV, A.V.; SAVENKO, B.N. (2018): Features of the crystal structure and vibrational spectra of $Ba_{1.65}Sr_{3.35}Nb_{10}O_{30}$-$Ba_4Na_2Nb_{10}O_{30}$ barium-strontium niobates with the structure of tetragonal tungsten bronze. Journal of Surface Investigation 12(6), 1149-1154

2019

a) Refereed international journals

AKAOGI, M.; ABE, K.; YUSA, H.; ISHII, T.; TAJIMA, T.; KOJITANI, H.; MORI, D.; LIU, Z.D.; AKAOGI, M.; KATSURA, T. (2019): Increase of the oxygen vacancy component in bridgmanite with temperature. Earth and Planetary Science Letters 505, 141-151

APRILIS, G.; KANTOR, I.; KUPENKO, I.; CERANTOLA, V.; PAKHOMOVA, A.; COLLINGS, I.E.; TORCHIO, R.; FEDOTENKO, T.; CHARITON, S.; BYKOV, M.; BYKOVA, E.; KOEMETS, E.; VASIUKOV, D.M.; MCCAMMON, C.; DUBROVINSKY, L.; DUBROVINSKAIA, N. (2019): Comparative study of the influence of pulsed and continuous wave laser heating on the mobilization of carbon and its chemical reaction with iron in a diamond anvil cell. Journal of Applied Physics 125, 095901

ARMSTRONG, K.; FROST, D.J.; MCCAMMON, C.A.; RUBIE, D.C.; BOFFA BALLARAN, T. (2019): Deep magma ocean formation set the oxidation state of Earth's mantle. Science 365 (6456), 903-906

AUDÉTAT, A. (2019): The metal content of magmatic-hydrothermal fluids and its relationship to mineralization potential. Economic Geology 114, 1033-1056

AUDÉTAT, A.; ZHANG, D. (2019): Abundances of S, Ga, Ge, Cd, In, Tl and 32 other major to trace elements in high-temperature (350-700 °C) magmatic-hydrothermal fluids. Ore Geology Reviews 109, 630-642

BHAT, S.; WIEHL, L.; HASEEN, S.; KROLL, P.; GLAZYRIN, K.; LEIDREITER, P.G.; KOLB, U.; FARLA, R.; TSENG, J.-C.; IONESCU, E.; KATSURA, T.; RIEDEL, R. (2019): A novel high-pressure tin oxynitride Sn_2N_2O. Chemistry – A European Journal, doi: 10.1002/chem.201904529

BYKOV, M.; CHARITON, S.; FEI, H.; FEDOTENKO, T.; APRILIS, G.; PONOMAREVA, A.; TASNÁDI, F.; ABRIKOSOV, I.; MERLE, B.; FELDNER, P.; VOGEL, S.; SCHNICK, W.; PRAKAPENKA, V.; GREENBERG, E.; HANFLAND, M.; PAKHOMOVA, A.; LIERMANN, H.; KATSURA, T.; DUBROVINSKAIA, N.; DUBROVINSKY, L. (2019): High-pressure synthesis of ultraincompressible hard rhenium nitride pernitride $Re_2(N_2)(N)_2$ stable at ambient conditions. Nature Communications 10, 2994

BYKOV, M.; YUSENKO, K.; BYKOVA, E.; PAKHOMOVA, A.; KRAUS, W.; DUBROVINSKAIA, N.A.; DUBROVINSKY, L.S. (2019): Synthesis of arsenopyrite-type rhodium pernitride RhN_2 from a single-source azide precursor. European Journal of Inorganic Chemistry 32, 3667-3671

BYKOVA, E.; APRILIS, G.; BYKOV, M.; GLAZYRIN, K.; WENDT, M.; WENZ, S.; LIERMANN, H.-P.; ROEH, J.T.; EHNES, A.; DUBROVINSKAIA, N.A.; DUBROVINSKY, L.S. (2019): Single-crystal diffractometer coupled with double-sided laser heating system at the Extreme Conditions Beamline P02.2 at PETRAIII. Review of Scientific Instruments 90(7), 073907

CERANTOLA, V.; WILKE, M.; KANTOR, I.; ISMAILOVA, L.; KUPENKO, I.; MCCAMMON, C.; PASCARELLI, S.; DUBROVINSKY, L.S. (2019): Experimental investigation of $FeCO_3$ (siderite) stability in the Earth's lower mantle using XANES spectroscopy. American Mineralogist 104, 1083-1091

COLLINGS, I.; VASIUKOV, D.; MCCAMMON, C.; DUBROVINSKY, L.; CERANTOLA, V.; PETITGIRARD, S.; HÜBSCHLE, C.; SCHÖNLEBER, A.; CHERNYSHOV, D.; VAN SMAALEN, S.; DUBROVINSKAIA, N. (2019): Local structure of ferroic iron formates at low temperature and high pressure studied by Mössbauer spectroscopy. Journal of Physical Chemistry C 123, 35, 21676-21684

EICHHEIMER, P.; THIELMANN, M.; POPOV, A.; GOLABEK, G.J.; FUJITA, W.; KOTTWITZ, M.O.; KAUS, B.J.P. (2019): Pore-scale permeability prediction for Newtonian and non-Newtonian fluids. Solid Earth 10, 1717-1731

ELAZAR, O.; FROST, D.; NAVON, O.; KESSEL, R. (2019): Melting of H_2O and CO_2-bearing eclogite at 4-6 GPa and 900-1200 °C: Implications for the generation of diamond-forming fluids. Geochimica et Cosmochimica Acta 255, 69-87

FEDORTCHOUK, Y.; LIEBSKE, C.; SCHMIDT, M.; MCCAMMON, C. (2019): Diamond destruction and growth during mantle metasomatism: an experimental study of diamond resorption features. Earth and Planetary Science Letters 506, 493-506

FEDOTENKO, T.; DUBROVINSKY, L.; APRILIS, G.; KOEMETS, E.; SNIGIREV, A.; SNIGIREVA, I.; BARANNIKOV, A.; ERSHOV, P.; COVA, P.; HANFLAND, M.; DUBROVINSKAIA, N. (2019): Laser heating setup for diamond anvil cells for *in situ* synchrotron and in house high and ultra-high pressure studies. Review of Scientific Instruments 90(10), 104501

FROSSARD, P.; BOYET, M.; BOUVIER, A.; HAMMOUDA, T.; MONTEUX, J. (2019): Evidence for anorthositic crust formed on an inner solar system planetesimal. Geochemical Perspective Letters 11, 28-32

GATTACCECA, J.; BOUVIER, A.; GROSSMAN, J.; METZLER, K.; UEHARA, M. (2019): The Meteoritical Bulletin, No. 106. Meteoritics and Planetary Science, 54, 469-471

GORELOVA, L.A.; PAKHOMOVA, A.S.; KRIVOVICHEV, S.V.; DUBROVINSKY, L.; KASATKIN, A.V. (2019): High pressure phase transitions of paracelsian $BaAl_2Si_2O_8$. Scientific reports 9 (1), 1-11

GRUENINGER, H.; LIU, Z.; SIEGEL, R.; BOFFA BALLARAN, T.; KATSURA, T.; SENKER, J.; FROST, D.J. (2019): Oxygen vacancy ordering in aluminous bridgmanite in the Earth's lower mantle. Geophysical Research Letters 46, 8731-8740

GU, Y.; LIU, H.; QIU, R.; LIU, Z.; WANG, C.; KATSURA, T.; ZHANG, H.; WU, M.; YAO, M.; ZHENG, H.; LI, K.; WANG, Y.; WANG, K.; YANG, B.; MA, Y.; ZOU, B. (2019): Pressure-induced emission enhancement and multicolor emission for 1,2,3,4-tetraphenyl-1,3-cyclopentadiene: Controlled structure evolution. Journal of Physical Chemistry Letters 10, 5557-5562

GUO, H.; KEPPLER, H. (2019): Electrical conductivity of NaCl bearing aqueous fluids to 900 °C and 5 GPa. Journal of Geophysical Research: Solid Earth 124 (2), 1397-1411

HECK, P.R.; HERD, C.; GROSSMAN, J.N.; BADJUKOV, D.; BOUVIER, A.; BULLOCK, E.; CHENNAOUI, H.; DEBAILLE, V.; DUNN, T.L.; EBEL, D.; FERRIÈRE, L.; GARVIE, L.; GATTACCECA, J.; GOUNELLE, M.; HERD, R.; IRELAND, T.; JACQUET, E.; MACKE, R.J.; MCCOY, T.; MCCUBBIN, F.M.; MIKOUCHI, T.; METZLER, K.; ROSKOSZ, M.; SMITH, C.; WADHWA, M.; WELZENBACH-FRIES, L.; YADA, T.; YAMAGUCHI, A.; ZEIGLER, R.A.; ZOLENSKY, M. (2019): Best practices for the use of meteorite and astromaterial names in publications. Meteoritics & Planetary Science 54, 1397-1400

HIKOSAKA, K.; SINMYO, R.; HIROSE, K.; ISHII, T.; OHISHI, Y. (2019): The stability of Fe_5O_6 and Fe_4O_5 at high pressure and temperature. American Mineralogist 104(9), 1356-1359

HUECK, M.; STIPP BASEI, M.A.; WEMMER, K.; ORIOLO, S.; HEIDELBACH, F.; SIEGESMUND, S. (2019): Evolution of the Major Gercino Shear Zone in the Dom Feliciano Belt, South Brazil, and implications for the assembly of southwestern Gondwana. International Journal of Earth Sciences 108, 403-425

IIZUKA-OKU, R.; SOUSTELLE, V.; MIYAJIMA, N.; WALTE, N.P.; FROST, D.J.; YAGI, T. (2019): Experimentally deformed lawsonite at high pressure and high temperature: Implication for low velocity layers in subduction zones. Physics of the Earth and Planetary Interiors 295, 106282

ISHII, T.; HUANG, R.; MYHILL, R.; FEI, H.; KOEMETS, I.; LIU, Z.; MAEDA, F.; YUAN, L.; WANG, L.; DRUZHBIN, D.; YAMAMOTO, T.; BHAT, S.; FARLA, R.; KAWAZOE, T.; TSUJINO, N.; KULIK, E.; HIGO, Y.; TANGE, Y.; KATSURA, T. (2019): Sharp 660-km discontinuity controlled by extremely narrow binary post-spinel transition. Nature Geoscience 12, 869-872

ISHII, T.; LIU, Z.; KATSURA, T. (2019): A breakthrough in pressure generation by Kawai-type multi-anvil apparatus with tungsten carbide anvils. Engineering 5, 434-440

ISHII, T.; KOJITANI, H.; AKAOGI, M. (2019): Phase relations of harzburgite and MORB up to the uppermost lower mantle conditions: Precise comparison with pyrolite by multi-sample cell technique with implication to dynamics of subducted slabs. Journal of Geophysical Research: Solid Earth 124, 3491-3507

JABAROV, S.H.; DANG, N.T.; KICHANOV, S.E.; KOZLENKO, D.P.; DUBROVINSKY, L.S.; THAO, L.T.P. (2019): Crystal structure and vibrational spectra of hexagonal manganites $YMnO_3$ and $LuMnO_3$ under high pressure. Materials Research Express 6 (8), 6110-6117

JÖNSSON, H.J.M.; EKHOLM, M.; BYKOV, M.; DUBROVINSKY, L.S.; VAN SMAALEN, S.; ABRIKOSOV, I.A. (2019): Inverse pressure-induced Mott transition in $TiPO_4$. Physical Reivew B 99(24), 245132

KATSURA, T.; TANGE, Y. (2019): A simple derivation of the Birch–Murnaghan equations of state (EOSs) and comparison with EOSs derived from other definitions of finite strain. Minerals 9(12), 745

KEPPLER, H.; GOLABEK, G. (2019): Graphite floatation on a magma ocean and the fate of carbon during core formation. Geochemical Perspectives Letters 11, 12-17

KERL, C.F.; BOFFA BALLARAN, T.; PLANER-FRIEDRICH, B. (2019): Iron plaque at rice roots: No barrier for methylated thioarsenates. Environmental Science & Technology 53 (23), 13666-13674

KORELL, J.-A.; FRENCH, M.; STEINLE-NEUMANN, G.; REDMER, R. (2019): Paramagnetic-to-diamagnetic transition in dense liquid iron and its influence on electronic transport properties. Physical Review Letters 122, 086601

KOROBEINIKOV, I.V.; MOROZOVA, N.V.; LUKYANOVA, L.N.; USOV, O.A.; OVSYANNIKOV, S.V. (2019): On the power factor of bismuth-telluride-based alloys near topological phase transitions at high pressures. Semiconductors 53, 732-736

KOZLENKO, D.P.; DUBROVINSKY, L.S.; KICHANOV, S.E.; LUKIN, E.V.; CERANTOLA, V.; CHUMAKOV, A.I.; SAVENKO B.N. (2019): Magnetic and electronic properties of magnetite across the high pressure anomaly. Scientific reports 9 (1), 4464-4469

KULIK, E.; NISHIYAMA, N.; HIGO, Y.; GAIDA, N.A.; KATSURA, T. (2019): Hardness of polycrystalline SiO_2 coesite, Journal of the American Ceramic Society 102, 2251-2256

KUPENKO, I.; APRILIS, G.; VASIUKOV, D.M.; MCCAMMON, C.; CHARITON, S.; CERANTOLA, V.; KANTOR, I.; CHUMAKOV, A.I.; RÜFFER, R.; DUBROVINSKY, L.; SANCHEZ-VALLE, C. (2019): Magnetism in cold subducting slabs at transition zone depths. Nature 570, 102-106

KURNOSOV, A.; MARQUARDT, H.; DUBROVINSKY, L.; POTAPKIN, V. (2019): A waveguide-based flexible CO_2-laser heating system for diamond-anvil cell applications. Comptes Rendus Geoscience 351, 280-285

LANIEL, D.; WINKLER, B.; KOEMETS, E.; FEDOTENKO, T.; BYKOV, M.; BYKOVA, E.; DUBROVINSKY, L.S.; DUBROVINSKAIA, N.A. (2019): Synthesis of magnesium-nitrogen salts of polynitrogen anions. Nature Communications 10, 4515

LANIEL, D.; BYKOV, M.; FEDOTENKO, T.; PONOMAREVA, A.V.; ABRIKOSOV, I.A.; GLAZYRIN, K.; SVITLYK, V.; DUBROVINSKY, L.S.; DUBROVINSKAIA, N.A. (2019): High pressure investigation of the S–N_2 system up to the megabar range: Synthesis and characterization of the SN_2 solid. Inorganic Chemistry 58(14), 9195-9204

LICHTENBERG, T.; GOLABEK, G.J.; BURN, R.; MEYER, M.R.; ALIBERT, Y.; GERYA, T.V.; MORDASINI, C.A. (2019): A water budget dichotomy of rocky protoplanets from ^{26}Al-heating. Nature Astronomy 3, 307-313

LICHTENBERG, T.; KELLER, T.; KATZ, R.F.; GOLABEK, G.J.; GERYA, T.V. (2019): Magma ascent in planetesimals: Control by grain size. Earth and Planetary Science Letters 507, 154-165

LIU, Z.; AKAOGI, M.; KATSURA, T. (2019): Increase of the oxygen vacancy component in bridgmanite with temperature. Earth and Planetary Science Letters 505, 141-151

LIU, Z.; BOFFA BALLARAN, T.; HUANG, R.; FROST, D.J.; KATSURA, T. (2019): Strong correlation of oxygen vacancies in bridgmanite with Mg/Si ratio. Earth and Planetary Science Letters 523, 115697

LIU, Z.; GREAUX, S.; CAI, N.; SIERSCH, N.; BOFFA BALLARAN, T.; IRIFUNE, T.; FROST, D.J. (2019): Influence of aluminum on the elasticity of majorite-pyrope garnets. American Mineralogist 104, 929-935

LIU, Z.; DUBROVINSKY, L.; MCCAMMON, C.; OVSYANNIKOV, S.V.; KOEMETS, I.; CHEN, L.; CUI, Q.; SU, N.; CHENG, J.; CUI, T.; LIU, B.; KATSURA, T. (2019): A new $(Mg_{0.5}Fe^{3+}_{0.5})(Si_{0.5}Al^{3+}_{0.5})O_3$ $LiNbO_3$-type phase synthesized at lower mantle conditions. American Mineralogist 104, 1213-1216

MATROSOVA, E.A.; ISMAILOVA, L.; BOBROV, A.V.; BYKOVA, E.; BYKOV, M.; GLAZYRIN, K.; BINDI, L.; OVSYANNIKOV, S.V.; AKSENOV, S.M.; PUSHCHAROVSKY, D.Yu.; DUBROVINSKY, L. (2019): Compressibility of two Na-rich clinopyroxenes: A synchrotron single-crystal X-ray diffraction study. American Mineralogist 104(6), 905-913

MCCAMMON, C. (2019): What is the future of Mössbauer spectroscopy? Mössbauer Effect Reference and Data Journal 42(1), 15-17

MEIER, T.; KHANDARKHAEVA, S.; JACOBS, J.; DUBROVINSKAIA, N.; DUBROVINSKY, L. (2019): Improving resolution of solid state NMR in dense molecular hydrogen. Applied Physics Letters 115(13), 131903

MEIER, T.; DWIVEDI, A.P.; KHANDARKHAEVA, S.; FEDOTENKO, T.; DUBROVINSKAIA, N.; DUBROVINSKY, L. (2019): Table-top nuclear magnetic resonance system for high-pressure studies with *in situ* laser heating. Review of Scientific Instruments 90(12), 123901

MEIER, T.; TRYBEL, F.; KHANDARKHAEVA, S.; STEINLE-NEUMANN, G.; CHARITON, S.; FEDOTENKO, T.; PETITGIRARD, S.; HANFLAND, M.; GLAZYRIN, K.; DUBROVINSKAIA, N.; DUBROVINSKY, L. (2019): Pressure induced hydrogen-hydrogen interaction in metallic FeH revealed by NMR. Physical Review X 9, 031008

MIYAJIMA, N.; MANDOLINI, T.; HEIDELBACH, F.; BOLLINGER, C. (2019): Combining ECCI and FIB milling techniques to prepare site-specific TEM samples for crystal defect analysis of deformed minerals at high pressure. Comptes Rendues Geosciences 351, 295-301

MOROZOVA, N.V.; KOROBEINIKOV, I.V.; OVSYANNIKOV, S.V. (2019): Strategies and challenges of high-pressure methods applied to thermoelectric materials (Perspective, Invited and Featured Paper). Journal of Applied Physics 125, 220901

MOUSSALLAM, Y.; LONGPRÉ, M.-A.; MCCAMMON, C.; GOMEZ-ULLA, A.; ROSE-KOGA, E.F.; SCAILLET, B.; PETERS, N.; GENNARO, E.; PARIS, R.; OPPENHEIMER, C. (2019): Mantle plumes are oxidized. Earth and Planetary Science Letters 527, 115798

PAKHOMOVA, A.; APRILIS, G.; BYKOV, M.; GORELOVA, L.; KRIVOVICHEV, S.S.; BELOV, M.P.; ABRIKOSOV, I.A.; DUBROVINSKY, L.S. (2019): Penta- and hexa-coordinated beryllium and phosphorus in high-pressure modifications of $CaBe_2P_2O_8$. Nature Communications 10, 2800

PAULMANN, C.; ZIETLOW, P.; MCCAMMON, C.; SALJE, E.K.H.; BISMAYER, U. (2019): Annealing of metamict gadolinite-(Y): X-ray diffraction, Raman, IR, and Mössbauer spectroscopy. Zeitschrift für Kristallographie 234(9), 587-593

PETITGIRARD, S.; JACOBS, J.; CERANTOLA, V.; COLLINGS, I.E.; TUCOULOU, R.; DUBROVINSKY, L.; SAHLE, C.J. (2019): A versatile diamond anvil cell for X-ray inelastic, diffraction and imaging studies at synchrotron facilities. Review of Scientific Instruments 90(9), 5107-5112

PIETTE-LAUZIÈRE, N.; GAILLARD, N.; GUILMETTE, C.; BOUVIER, A.; PERROUTY, S.; PILOTE, P. (2019): The timing of prograde metamorphism in the Pontiac Subprovince, Superior craton; implications for Archean geodynamics and gold mineralization. Precambrian Research 320, 111-136

PLOTINSKAYA, O.; CHUGAEV, A.; BONDAR, D.; ABRAMOVA, V. (2019): Mineralogy and geochemistry of ores of the Kedrovskoe-Irokinda ore field (northern Transbaikalia). Russian Geology and Geophysics 60, 1119-1140

POSNER, E.; STEINLE-NEUMANN, G. (2019): Mass transport and structural properties of binary liquid iron alloys at high pressure. Geochemistry, Geophysics, Geosystems 20, 3556-3568, doi: 10.1029/2019GC008393

RABIA, K.; MENG, F.; THOMSON, M.D.; BYKOV, M.; MERLIN, R.; VAN SMAALEN, S.; ROSKOS, H.G. (2019): Coherent photo-induced phonon emission in the charge-density-wave state of $K_{0.3}MoO_3$. New Journal of Physics 21, 013013

ROTTIER, B.; AUDÉTAT, A. (2019): *In situ* quantification of chlorine and sulfur in glasses, minerals and melt inclusions by LA-ICP-MS. Chemical Geology 504, 1-13

RUSTIONI, G.; AUDÉTAT, A.; KEPPLER, H. (2019): Experimental evidence for fluid-induced melting in subduction zones. Geochemical Perspectives Letters 11, 49-54

SATTA, N.; MARQUARDT, H.; KURNOSOV, A.; BUCHEN, J.; KAWAZOE, T.; MCCAMMON, C.; BOFFA BALLARAN, T. (2019): Single-crystal elasticity of iron-bearing phase E and seismic detection of water in Earth's upper mantle. American Mineralogist 104, 1526-1529

SEROVAISKII, A.; MUKHINA, E.; DUBROVINSKY, L.; CHERNOUTSAN, A.; KUDRYAVTSEV, D.; MCCAMMON, C.; APRILLIS, G.; KUPENKO, I.; CHUMAKOV, A.; HANFLAND, M.; KUTCHEROV, V. (2019): Fate of hydrocarbons in iron-bearing mineral environments during subduction. Minerals 9(11), 651

SINMYO, R.; NAKAJIMA, Y.; MCCAMMON, C.; MIYAJIMA, N.; PETITGIRARD, S.; MYHILL, R.; DUBROVINSKY, L.; FROST, D. (2019): Effect of Fe^{3+} on phase relations in the lower mantle: Implications for redox melting in stagnant slabs. Journal of Geophysical Research: Solid Earth 124(12), 12484-12497

SPIVAK, A.V.; LITVIN, Y.A.; ZAKHARCHENKO, E.S.; SIMONOVA, D.A.; DUBROVINSKY L.S. (2019): Evolution of diamond-forming systems of the mantle transition zone: Ringwoodite peritectic reaction $(Mg,Fe)_2SiO_4$ (experiment at 20 GPa). Geochemistry International 57 (9), 1000-1007

STAGNO, V.; CERANTOLA, V.; AULBACH, S.; LOBANOV, S.; MCCAMMON, C.; MERLINI, M. (2019): Carbon-bearing phases throughout Earth's interior: Evolution through space and time. – In: ORCUTT, B.; DANIEL, I.; DASGUPTA, R. (Eds.): Deep Carbon: Past to Present, Cambridge University Press, Cambridge, UK, 66-88

TERASAKI, H.; RIVOLDINI, A.; SHIMOYAMA, Y.; NISHIDA, K.; URAKAWA, S.; MAKI, M.; KUROKAWA, F.; TAKUBO, Y.; SHIBAZAKI, Y.; SAKAMAKI, T.; MACHIDA, A.; HIGO, Y.; UESUGI, K.; TAKEUCHI, A.; WATANUKI, T.; KONDO, T. (2019): Pressure and composition effects on sound velocity and density of core-forming liquids: Implication to core compositions of terrestrial planets. Journal of Geophysical Research: Planets 124, 2272-2293

THOMSON, A.R.; CRICHTON, W.A.; BRODHOLT, J.P.; WOOD, I.G.; SIERSCH, N.C.; MUIR, J.M.R.; DOBSON, D.P.; HUNT, S.A. (2019): Seismic velocities of $CaSiO_3$ perovskite can explain LLSVPs in Earth's lower mantle. Nature 572, 643-647

VOGEL, S.; BYKOV, M.; BYKOVA, E.; WENDL, S.; KLOß, S.D.; PAKHOMOVA, A.; DUBROVINSKAIA, N.A.; DUBROVINSKY, L.S.; SCHNICK, W. (2019): Nitride spinel: An ultraincompressible high-pressure form of BeP_2N_4. Angewandte Chemie International Edition 58, 1-6

VOGEL, S.; BYKOV, M.; BYKOVA, E.; WENDL, S.; KLOß, S.D.; PAKHOMOVA, A.; CHARITON, S.; KOEMETS, E.; DUBROVINSKAIA, N.A.; DUBROVINSKY, L.S.; SCHNICK, W. (2019): Boron phosphorus nitride at extremes: PN_6 octahedra in the high-pressure polymorph β-BP_3N_6. Angewandte Chemie International Edition 58, 9060-9063

WAGLE, F.; STEINLE-NEUMANN, G. (2019): Liquid iron equation of state to the terapascal regime from *ab initio* simulations. Journal of Geophysical Research 124, 3350-3364

WAGLE, F.; STEINLE-NEUMANN, G.; DE KOKER, N. (2019): Resistivity saturation in liquid iron-light-element alloys at conditions of planetary cores from first principles computations. Comptes Rendus Geoscience 351, 154-162

WANG, L.; MIYAJIMA, N.; KAWAZOE, T.; KATSURA, T. (2019): Activation of 100 (001) slip system by water incorporation in olivine and the cause of seismic anisotropy decrease with depth in the asthenosphere. American Mineralogist 104, 47-52

YOSHIOKA, T.; NAKAJIMA, D.; NAKAMURA, T.; SHCHEKA, S.; KEPPLER, H. (2019): Carbon solubility in silicate melts in equilibrium with a CO-CO_2 gas phase and graphite. Geochimica et Cosmochimica Acta 259, 129-143

YUSENKO, K.V.; KHANDARKHAEVA, S.; FEDOTENKO, T.; PAKHOMOVA, A.; GROMILOV, S.A.; DUBROVINSKY, L.; DUBROVINSKAIA, N. (2019): Equations of state of rhodium, iridium and their alloys up to 70 GPa. Journal of Alloys and Compounds 788, 212-218

b) Popular scientific magazines

MEIER, T. (2019): Unter Hochdruck zur Supraleitung. Physik in unserer Zeit 50(6), 267-268

5.2 Publications (submitted, in press)

ARMSTRONG, K.; SIERSCH, N.C.; BOFFA BALLARAN, T.; FROST, D.J.; YU, T.; WANG, Y.: Equations of state, phase relations, and oxygen fugacity of the Ru-RuO_2 buffer at high pressures and temperatures. American Mineralogist (accepted)

BEYER, C.; MYHILL, R.; MARQUARDT, K.; MCCAMMON, C.: Redox gradients in Earth's mantle transition zone. Nature (submitted)

BLANCHARD, I.; JENNINGS, E.S.; FRANCHI, I.A.; ZHAO, X.; PETITGIRARD, S.; MIYAJIMA, N.; JACOBSON, S.; RUBIE, D.C.: The fate of carbon during Earth's core-mantle differentiation. Nature (submitted)

BLANCHARD, I.; ABEYKOON, S.; RUBIE, D.C.; FROST, D.J.: The effects of pressure and temperature on sulfur content at sulfide saturation of peridotitic liquid. Geochemical Perspective Letters (submitted)

CHARITON, S.; MCCAMMON, C.; VASIUKOV, D.; STEKIEL, M.; KANTOR, A.; CERANTOLA, V.; KUPENKO, I.; FEDOTENKO, T.; KOEMETS, E.; HANFLAND, M.; CHUMAKOV, A.; DUBROVINSKY, L.: Seismic detectability of carbonates in the deep Earth: a Nuclear Inelastic Scattering study. American Mineralogist (in press)

CRAMERI, F.; MAGNI, V.; DOMEIER, M.; SHEPHARD, G.E.; CHOTALIA, K.; COOPER, G.; EAKIN, C.M.; GRIMA, A.G.; GÜRER, D.; KIRALY, A.; MULYUKOVA, E.; PETERS, K.; ROBERT, B.; THIELMANN, M.: Subduction zone initiation on the recent Earth strongly tied to ongoing subduction. Nature Communications (submitted)

DOBSON, D.P.; LINDSAY-SCOTT, A.; HUNT, S.A.; BAILEY, E.; WOOD, I.G.; BRODHOLT, J.P.; VOCADLO, L.; WHEELER, J.: Anisotropic diffusion creep in post-perovskite: a new model for deformation at the core-mantle boundary. Proceedings of the National Academy of Sciences (PNAS) (accepted)

DORFMAN, S.M.; POTAPKIN, V.; LV, M.; GREENBERG, E.; KUPENKO, I.; CHUMAKOV, A.; BI, W.; ALP, E.; LIU, J.; MAGREZ, A.; DUTTON, S.; CAVA, R.; MCCAMMON, C.; GILLET, P.: Effects of composition and pressure on electronic states of iron in bridgmanite. American Mineralogist (submitted)

DU, J.; AUDÉTAT, A.: Early sulfide saturation is not detrimental to porphyry Cu-Au formation. Geology (submitted)

FEI, H.; KATSURA, T.: High water solubility of ringwoodite at mantle transition zone temperature. Earth and Planetary Science Letters (in press)

GILLMANN, C.; GOLABEK, G.J.; RAYMOND, S.; TACKLEY, P.J.; SCHÖNBÄCHLER, M.; DEHANT, V.; DEBAILLE, V.: Dry late accretion inferred from Venus' coupled atmosphere and internal evolution. Nature (submitted)

GABORIEAU, M.; LAUBIER, M.; BOLFAN-CASANOVA, N.; MCCAMMON, C.; VANTELON, D.; CHUMAKOV, A.I.; SCHIAVI, F.; NEUVILLE, D.; VENUGOPAL, S.: $Fe^{3+}/\Sigma Fe$ of olivine-hosted melt inclusions inferred from Mössbauer and XANES spectroscopy. Chemical Geology (submitted)

HECK, *ET AL.* (30 authors including BOUVIER A., consortium): The fall, recovery and classification of the Hamburg, Michigan L4 chondrite. Meteoritics & Planetary Science (submitted)

HUANG, Y.; NAKATANI, T.; NAKAMURA, M.; MCCAMMON, C.: Shallow fluid circulation in mantle wedge inferred from the dihedral angle in an olivine-NaCl-H_2O system. Nature Communications (in press)

HUECK, M.; WEMMER, K.; STIPP BASEI, M.A.; PHILIPP, R.P.; ORIOLO, S.; HEIDELBACH, F.; OYHANTÇABAL, P.; SIEGESMUND, S.: Structural evolution and white mica K-Ar geochronology of Neoproterozoic structures in the Sul-rio-grandense Shield, South Brazil: Constraining recurrent shear zone activity and the transition from ductile to brittle deformation. Journal of Structural Geology (submitted)

ISHII, T.; MIYAJIMA, N.; SINMYO, R.; KOJITANI, H.; MORI, D.; INAGUMA, Y.; AKAOGI, M.: Discovery of new-structured post-spinel $MgFe_2O_4$: Crystal structure and high-pressure phase relations. Geophysical Research Letters (submitted)

ISHII, T.: Crystal structure of a novel Fe-Mg oxide and deep Earth science. Nihon Kessho Gakkaishi (accepted)

ISRAEL, C.; BOYET, M.; DOUCELANCE, R.; BONNAND, P.; FROSSARD, P.; AUCLAIR, D.; BOUVIER, A.: Formation of the Ce-Nd mantle array: Crustal extraction vs. recycling by subduction. Earth and Planetary Science Letters, doi:10.1016/j.epsl.2019.115941 (in press)

KHANDARKHAEVA, S.; FEDOTENKO, T.; BYKOV, M.; BYKOVA, E.; CHARITON, S.; SEDMAK, P.; GLAZYRIN, K.; PRAKAPENKA, V.; DUBROVINSKAIA, N.; DUBROVINSKY, L.: Novel rhenium carbides at 200 GPa. Angewandte Chemie (submitted)

KOEMETS, E.; BYKOV, M.; BYKOVA, E.; CHARITON, S.; APRILIS, G.; FEDOTENKO, T.; CLÉMENT, S.; ROUQUETTE, J.; HAINES, J.; CERANTOLA, V.; GLAZYRIN, K.; ABAKUMOV, A.; ISMAILOVA, L.; MCCAMMON, C.; PRAKAPENKA, V.B.; HANFLAND, M.; LIERMANN, H.-P.; SVITLYK, V.; ROSA, A.; IRIFUNE, T.; LEONOV, I.; PONOMAREVA, A.V.; ABRIKOSOV, I.A.; DUBROVINSKAIA, N.; DUBROVINSKY, L.: Variation of oxygen oxidation state at the base of Earth's lower mantle. Science Advances (submitted)

KOEMETS, E.; FEDOTENKO, T.; KHANDARKHAEVA, S.; BYKOV, M.; BYKOVA, E.; THIELMANN, M.; CHARITON, S.; APRILIS, G.; KOEMETS, I.; LIERMANN, H.-P.; HANFLAND, M.; OHTANI, E.; DUBROVINSKAIA, N.; MCCAMMON, C.; DUBROVINSKY, L.: Role of FeOOH in oxygen recycling in early Earth history. Nature (submitted)

KOEMETS, E.; YUAN, L.; BYKOVA, E.; GLAZYRIN, K.; OHTANI, E.; DUBROVINSKY, L.: Interaction between FeOOH and NaCl at extreme conditions: Synthesis of novel $Na_2FeCl_4OH_x$ compound. Minerals (in press)

KOEMETS, I.; SATTA, N.; KURNOSOV, A.; MARQUARDT, H.; KISEEVA, E.S.; STACHEL, T.; HARRIS, J.W.; DUBROVINSKY, L.: Elastic properties of majoritic garnet inclusions in diamonds and the seismic signature of pyroxenites in Earth's upper mantle. American Mineralogist (in press)

KRESSALL, R.D.; FEDORTCHOUK, Y.; MCCAMMON, C.; ELLIOT, B.: Stability of chromite and ilmenite in a silicate melt at various fO_2 at 0.1 MPa: new insights into use of oxides as diamond indicator minerals in kimberlites. Journal of Petrology (submitted)

LIU, Z.; MCCAMMON, C.; WANG, B.; DUBROVINSKY, L.; ISHII, T.; BONDAR, D.; NAKAJIMA, A.; TANGE, Y.; HIGO, Y.; CUI, T.; LIU, B.; KATSURA, T.: Stability and solubility of the $FeAlO_3$ component in bridgmanite at the uppermost lower mantle. Journal of Geophysical Research – Solid Earth (submitted)

MASHINO, I.; MURAKAMI, M.; MIYAJIMA, N.; PETITGIRARD, S.: Experimental evidence for silica-enriched Earth's lower mantle with 3 ferrous iron dominant bridgmanite. PNAS (submitted)

MATJUSCHKIN, V.; WOODLAND, A.B.; FROST, D.J.; YAXLEY, G.M.: Reduced methane-bearing fluids as a source for diamond. Nature Scientific Reports (submitted)

MCCAMMON, C.: Mössbauer spectroscopy with high spatial resolution: Spotlight on geoscience. – In: YOSHIDA, Y.; LANGOUCHE, G. (Eds.): Modern Mössbauer Spectroscopy: New Challenges Based on Cutting-Edge Techniques, Springer (submitted)

MCCAMMON, C.: Communicating science through stories with the Deep Carbon Observatory. Eos (submitted)

MCCAMMON, C.; BUREAU, H.; CLEAVES, H.J.; COTTRELL, E.; DORFMAN, S.M.; KELLOGG, L.H.; LI, J.; MIKHAIL, S.; MOUSSALLAM, Y.; SANLOUP, C.; THOMSON, A.; BROVARONE, A.V.: Deep Earth carbon reactions through time and space. American Mineralogist (in press)

MCGOWAN, N.; GRIFFIN, W.L.; O'REILLY, S.Y.; CLARK, S.M.; ROQUE-ROSELL, J.; MARCUS, M.A.; MCCAMMON, C.A.; PEARSON, N.J.: The oxidation state of Fe in chromite by μ-XRD and K-edge μ-XANES: A record of deep Earth processes? Geochimica et Cosmochimica Acta (submitted)

MÉNDEZ, A.S.J.; MARQUARDT, H.; HUSBAND, R.; LIERMANN, H.-P.: Elastic softening of $(Mg_{0.8}Fe_{0.2})O$ ferropericlase across the iron spin crossover measured by time-resolved X-ray diffraction. American Mineralogist (submitted)

MEZGER, K.; SCHÖNBÄCHLER, M.; BOUVIER, A.: Accretion of the Earth – missing components? Space Science Reviews (submitted)

MORBIDELLI, A.; LIBOUREL, G.; PALME, H.; JACOBSON, S.J.; RUBIE, D.C.: Sub-solar Al/Si and Mg/Si ratios of the enstatite chondrites reveal planetesimal formation during early condensation in the protoplanetary disk. Earth and Planetary Science Letters (submitted)

MOROZOVA, N.V.; KOROBEINIKOV, I.V.; OVSYANNIKOV, S.V.: Controlling the thermoelectric power of silicon-germanium alloys in conventional and metastable phases by applied high pressure. Journal of Materials Chemistry C (submitted)

NAKAJIMA, M.; GOLABEK, G.J.; WÜNNEMANN, K.; RUBIE, D.C.; BURGER, C.; MANSKE, L.; MELOSH, H.J.; JACOBSON, S.A.; NIMMO; F.; HULL, S.D.: Scaling laws for the geometry of an impact-induced magma ocean. Earth and Planetary Science Letters (submitted)

NISHIDA, K.; SHIBAZAKI, Y.; TERASAKI, H.; HIGO, Y.; SUZUKI, A.; FUNAMORI, N.; HIROSE, K.: Effect of sulfur on sound velocity of liquid iron under Martian core conditions. Nature Communications (submitted)

OVSYANNIKOV, S.V.; BYKOV, M.; MEDVEDEV, S.A.; NAUMOV, P.G.; JESCHE, A.; TSIRLIN, A.A.; BYKOVA, E.; CHUVASHOVA, I.; KARKIN, A.A.; MCCAMMON, C.; DYADKIN, V.; CHERNYSHOV, D.; DUBROVINSKY, L.S.: Room-temperature Peierls transition in simple iron oxide. Science Advances (submitted)

PAPA, S.; PENNACCHIONI, G.; MENEGON, L.; THIELMANN, M.: High-stress creep preceding coseismic rupturing in amphibolite-facies ultramylonites. Earth and Planetary Science Letters (submitted)

PARMENTER, S.; IVANIC, T.J.; KORHONEN, F.J.; BOUVIER, A.; YAKYMCHUK, C.: Metamorphism of the Mougooderra Formation: Implications for Neoarchean tectonics in the Murchison Domain. Precambrian Research (submitted)

PATRICK, M.; INDARES, A.; MCCAMMON, C.: The influence of ferric iron on phase stability in midpressure anatectic aluminous gneisses. Canadian Mineralogist (submitted)

ROTTIER, B.; AUDÉTAT, A.; KODĚRA, P.; LEXA, J.: Magmatic evolution of the mineralized Štiavnica volcano (Central Slovakia) evidence from thermobarometry, melt inclusions, and sulfide inclusions. Contributions to Mineralogy and Petrology (submitted)

ROTTIER, B.; AUDÉTAT, A.; KODĚRA, P.; LEXA, J.: Origin and evolution of magmas in the porphyry Au-mineralized Javorie volcano (Central Slovakia): Evidence from thermobarometry, melt inclusions, and sulfide inclusions. Journal of Petrology (accepted)

SAWA, S.; MUTO, J.; MIYAJIMA, N.; SHIRAISHI, R.; KIDO, M.; NAGAHAMA, H.: Strain localization bands in fine-grained aggregates of germanate olivine deformed by a Griggs type apparatus. Tectonophysics (submitted)

SCHIERJOTT, J.C.; THIELMANN, M.; ROZEL, A.B.; GOLABEK, G.J.; GERYA, T.V.: Can grain size reduction initiate transform faults? – Insights from a 3D numerical study. Tectonics (submitted)

SINMYO, R.; NAKAJIMA, Y.; MCCAMMON, C.A.; MIYAJIMA, N.; PETITGIRARD, S.; MYHILL, R.; DUBROVINSKY, L.; FROST, D.J.: Effect of Fe^{3+} on phase relations in the lower mantle: Implications for redox melting in stagnant slabs. Journal of Geophysical Research – Solid Earth (in press)

THIELMANN, M.; GOLABEK, G.J.; MARQUARDT, H.: Ferropericlase control of lower mantle rheology: Impact of phase morphology. Geochemistry, Geophysics, Geosystems (submitted)

VASIUKOV, D.M.; DUBROVINSKY, L.; KUPENKO, I.; CERANTOLA, V.; APRILIS, G.; ISMAILOVA, L.; BYKOVA, E.; MCCAMMON, C.; PRESCHER, C.; CHUMAKOV, A.I.; DUBROVINSKAIA, N.: Pressure-induced spin pairing transition of Fe^{3+} in oxygen octahedra. Physical Review B (submitted)

WALTE, N.P.; SOLFERINO, G.F.D.; GOLABEK, G.J.: Two-stage evolution of a pallasite parent body revealed by novel deformation experiments (submitted)

WITTKOP, C.; BARTLEY, J. K.; KRUEGER, R.; BOUVIER, A.; GEORG, R.B.; KNAEBLE, A.R.; ST. CLAIR, K.; PIPER, C.: Influence of provenance and depositional process on the geochemistry and radiogenic (Hf, Nd, and Sr) isotopic composition of Pleistocene glacial tills, Minnesota USA. Chemical Geology, doi:10.1016/j.chemgeo.2019.119390 (in press)

XIE, L.; YONEDA, A.; MANTHILAKE, G.; YAMAZAKI, D.; HIGO, Y.; TANGE, Y.; GUIGNOT, N.; ANDRAULT, D.: Formation of bridgmanite-enriched layer at the top lower-mantle during Magma Ocean solidification. Nature Communications (submitted)

XIE, L.; YONEDA, A.; XU, F.; WANG, C.; GUIGNOT, N.; KING, A.; HIGO, Y.; TANGE, Y.: Boron-MgO composite as a X-ray transparent pressure medium in the Kawai high pressure apparatus. Review of Scientific Instruments (submitted)

YUSENKO, K.V.; SPEKTOR, K.; KHANDARKHAEVA, S.; FEDOTENKO, T.; PAKHOMOVA, A.; KUPENKO, I.; ROHRBACH, A.; KLEMME, S.; CRICHTON, W.A.; DYACHKOVA, T.V.; TYUTYUNNIK, A.P.; ZAINULIN, Y.G.; DUBROVINSKY, L.S.; GROMILOV, S.A.: Decomposition of single-source precursors under high-temperature high-pressure to access osmium–platinum refractory alloys. Journal of Alloys and Compounds (accepted)

ZHANG, B.; LIN, Y.; MOSER, D.E.; ZHANG, J.; SHIEH, S.R.; BOUVIER, A.: Imbrium age for zircons in Apollo 17 South Massif Impact Melt Breccia 73155. Journal of Geophysical Research: Planets, doi:10.1029/2019JE005992 (in press)

5.3 Presentations at scientific institutions and at congresses

ABEYKOON, S.; LAURENZ, V.; FROST, D.J.; MIYAJIMA, N: 26.-30.05.2019, Japan Geoscience Union Meeting (JpGU2019), Chiba, Japan: "The oxygen content of sulphides in the mantle and a geothermometer for diamond formation"

ABEYKOON, S.; AUDÉTAT, A: 31.05.-01.06.2019, JSPS Japanese-German graduate externship International Workshop on 'Volatile Cycles', Tokyo, Japan: "Single-crystal diamond trap (SCDT) method; Determining the composition of fluids at high temperature and high pressure"

ABEYKOON, S.; LAURENZ, V.; FROST, D.J.; MIYAJIMA, N: 18.-23.08.2019, Goldschmidt 2019, Barcelona, Spain: "A new geothermometer based on the oxygen content of sulphide inclusions in diamonds"

ABEYKOON, S.; REBAZA, A.M.; LAURENZ, V.; FROST, D.J.; MIYAJIMA, N: 22.-25.09.2019, GeoMünster 2019, Münster, Germany[*A]: "A new geothermometer based on the oxygen content of sulphide inclusions in diamonds"

ANDRAULT, D.; GABORIEAU, M.; LAUBIER, M.; BOLFAN-CASANOVA, N.; MUNOZ, M.; MCCAMMON, C.; CERANTOLA, V.; CHUMAKOV, A.; RÜFFER, R.; KANTOR, I.; PASCARELLI, S.: 11.-12.03.2019, EBS Workshop on Nuclear Resonance Scattering, ESRF, Grenoble, France: "Redox state of the molten Earth's mantle"

BLANCHARD, I.: 22.01.2019, Institut de Minéralogy, de Physique de Matériaux et de Cosmochimie, Paris, France: "Metal silicate partitioning experiments: Insights on Earth's differentiation"

BLANCHARD, I.: 01.02.2019, Universität Potsdam, Institut für Geowissenschaften, Potsdam, Germany: "Metal silicate partitioning experiments: Insights on Earth's differentiation"

BLANCHARD, I.: 16.05.2019, Center of Earth Evolution and Dynamics, Oslo, Norway: "Metal silicate partitioning experiments: Insights on Earth's differentiation"

BLANCHARD, I.; JENNINGS, E.S.; PETITGIRARD, S.; FRANCHI, I.A.; ZHAO, X.; RUBIE, D.C.: 03.-05.06.2019, 'The Evolving Earth' workshop, IPGP, Paris, France: "Fate of carbon during the formation of Earth's core"

BLANCHARD, I.; JENNINGS, E.S.; PETITGIRARD, S.; FRANCHI, I.A.; ZHAO, X.; RUBIE, D.C.: 24.-26.10.2019, Deep Carbon 2019, Washington D.C., USA (*invited*): "Fate of carbon during the formation of Earth's core"

BLUNDY, J.; MELEKHOVA, L.; ULMER, P.; PICHAVANT, M.; HUMPHREYS, M.; ZIBERNA, L.; CERANTOLA, V.; BROOKER, R.; MCCAMMON, C.: 18.-23.08.2019, Goldschmidt 2019, Barcelona, Spain: "Fe-Mg-Mn exchange between olivine and melt and an oxybarometer for basaltic systems"

BONDAR, D.; FEI, H.; WITHERS, T.; KATSURA, T.: 26.-30.05.2019, Japan Geoscience Union Meeting (JpGU2019), Chiba, Japan: "Water partitioning between upper mantle minerals and melts"

BONDAR, D.; FEI, H.; WITHERS, T.; KATSURA, T.: 22.-25.09.2019, GeoMünster 2019, Münster, Germany*A: "Water partitioning between upper mantle minerals and melts"

BOUVIER, A.: 01.05.2019, Workshop MSR Contamination Control, Leicester, U.K. (*invited*): "Mars sample return: Contamination Control (CC) and Contamination Knowledge (CK) associated with inorganic contamination, the case of transition metals"

BOUVIER, A.; VAN KESSEL, A.; GEIGER, J.; LINNEN, R.L.; GEORG, R.B.; ZAJACZ, Z.; WITHERS, A.C.: 18.-23.08.2019, Goldschmidt 2019, Barcelona, Spain: "Sm-Nd and Sr isotope systematics of Western Abitibi scheelites and andradite garnets, implications for gold mineralization"

BOWER, D.J.; WOLF, A.S.; SANAN, P.; JUTZI, M.; RUBIE, D.C.: 07.-12.04.2019, European Geosciences Union General Assembly 2019, Vienna, Austria: "On the evolving P-T conditions in a magma ocean with implications for terrestrial core formation", Geophysical Research Abstracts 21, EGU2019-7244, 2019

BYKOVA, E.; BYKOV, M.; MCCAMMON, C.; OVSYANNIKOV, S.V.; LIERMANN, H.-P.; KUPENKO, I.; CHUMAKOV, A.I.; RÜFFER, R.; HANFLAND, M.; PRAKAPENKA, V.; DUBROVINSKY, L.: 11.-12.03.2019, EBS Workshop on Nuclear Resonance Scattering, ESRF, Grenoble, France: "Chemistry at extreme conditions: Fe-O system at ultra-high pressure"

BYKOVA, E.; CERANTOLA, V.; BYKOV, M.; MERLINI, M.; ISMAILOVA, L.; MCCAMMON, C.; KANTOR, I.; SVITLYK, V.; HANFLAND, M.; MEZOUAR, M.; PRESCHER, C.; DUBROVINSKY, L.: 24.-26.10.2019, Deep Carbon 2019, Washington D.C., USA: "Stability of iron-bearing carbonates in the deep Earth's interior"

BYRNE, J.; SCHAD, M.; MCCAMMON, C.; TOMASZEWSKI, E.; SMITH, A.; CERANTOLA, V.; KAPPLER, A.: 18.-23.08.2019, Goldschmidt 2019, Barcelona, Spain: "Did bacteria induce redox cycling of magnetite within Banded Iron Formations (BIFs)?"

CHARITON, S.; KOEMETS, I.: 09.-13.09.2019, Yes Congress 2019, Freie Universität, Berlin, Germany: "The elastic properties and crystal chemistry of carbonates in the deep Earth"

CHOTALIA, K.; COOPER, G.; CRAMERI, F.; DOMEIER, M.; EAKIN, C.; GRIMA, A.G.; GÜRER, D.; KIRÁLY, Á.; MAGNI, V.; MULYUKOVA, E.; PETERS, K.; ROBERT, B.; SHEPHARD, G.; THIELMANN, M.: 07.-12.04.2019, European Geosciences Union General Assembly 2019, Vienna, Austria: "Subduction zone initiation database 1.0", Geophysical Research Abstracts 21, EGU2019-14257, 2019

DOMINIJANNI, S.; MCCAMMON, C.A.; DUBROVINSKY, L.S.; FROST, D.J.; MIYAJIMA, N.: 11.-12.03.2019, EBS Workshop on Nuclear Resonance Scattering, ESRF, Grenoble, France: "Experimental investigation of the oxygen fugacity in laser heated DAC experiments"

DOMINIJANNI, S.; MCCAMMON, C.A.; DUBROVINSKY, L.S.; FROST, D.J.; MIYAJIMA, N.: 21.-22.03.2019, 3th Meeting of FOR 2125/2 CarboPat, Kloster Steinfeld, Germany: "Update on project 6: Understanding the oxygen fugacity variation in laser heated DAC experiments"

DOMINIJANNI, S.; MCCAMMON, C.A.; DUBROVINSKY, L.S.; FROST, D.; MIYAJIMA, N.: 26.-30.05.2019, Japan Geoscience Union Meeting (JpGU2019), Chiba, Japan: "Probing the variation of the oxygen fugacity in diamond anvil cells using the Fe-Ir alloy as redox sensor"

DOMINIJANNI, S.; MCCAMMON, C.A.; DUBROVINSKY L.S.; FROST, D.J.; MIYAJIMA, N.; BOFFA BALLARAN, T.: 31.05.-01.06.2019, JSPS Japanese-German graduate externship International Workshop on 'Volatile Cycles', Tokyo, Japan: "Probing the fO_2 variation in laser heated DAC experiments"

DOMINIJANNI, S.; MCCAMMON, C.A.; DUBROVINSKY, L.S.; FROST, D.J.; MIYAJIMA, N.; BOFFA BALLARAN, T.: 03.-04.06.2019, Earth, Sea and Sky V: International Joint Graduate Program Workshop, Tohoku University, Sendai, Japan: "Experimental study of the mantle redox state through DACs experiments"

DOMINIJANNI, S.; MCCAMMON, C.A.; DUBROVINSKY, L.S.; FROST, D.J.; MIYAJIMA, N.; BOFFA BALLARAN, T.: 09.-13.09.2019, Yes Congress 2019, Freie Universität, Berlin, Germany: "Probing the fO_2 conditions in laser heated DACs experiments using the Fe-Ir redox sensor"

DOMINIJANNI, S.; MCCAMMON, C.A.; DUBROVINSKY, L.; FROST, D.J.; MIYAJIMA, N.; BOFFA BALLARAN, T.: 22.-25.09.2019, GeoMünster 2019, Münster, Germany*A: "Understanding the redox conditions during diamond anvil cells experiments"

DOMINIJANNI, S.; MCCAMMON, C.; DUBROVINSKY, L.; FROST, D.J.; MIYAJIMA, N.: 10.-11.10.2019, 4th Meeting of FOR 2125/2 CarboPat, Wehrheim, Germany: "Update on project 6: Understanding the redox conditions in diamond anvil cells"

DU, J.; AUDÉTAT, A.: 18.-23.08.2019, Goldschmidt 2019, Barcelona, Spain: "Early sulfide saturation is not detrimental to porphyry Cu-Au formation"

DUBROVINSKY, L.; DUBROVINSKAIA, N.: 04.-08.03.2019, APS March Meeting, Boston, USA (*invited*): "Single crystal X-ray diffraction in laser heated DACs"

DUBROVINSKY, L.: 25.-28.03.2019, 27th Annual Meeting of the German Crystallographic Society (DGK), Leipzig, Germany: "Oxygen's oxidation state at very high pressures"

DUBROVINSKY, L.; DUBROVINSKAIA N.: 04.-09.08.2019, The 27th AIRAPT International Conference on High Pressure Science and Technology, Rio de Janeiro, Brazil: "Inorganic synthesis and crystal chemistry at multimegabar pressures"

EBERHARD, L.; FROST, D.J.; MCCAMMON, C.A.: 26.-30.05.2019, Japan Geoscience Union Meeting (JpGU2019), Chiba, Japan: "The oxygen fugacity of serpentinites: implications for subduction zone redox evolution"

EBERHARD, L.; FROST, D.J.; MCCAMMON, C.A.: 31.05.-01.06.2019, JSPS Japanese-German graduate externship International Workshop on 'Volatile Cycles', Tokyo, Japan: "The influence of oxygen fugacity on the stability of ophicarbonate and the compositions of subduction zone derived fluids"

EBERHARD, L.; FROST, D.J.; MCCAMMON, C.A.: 03.-04.06.2019, Earth, Sea and Sky V: International Joint Graduate Program Workshop, Tohoku University, Sendai, Japan: "The role of fO_2 on the stability of serpentinites in subduction zones"

EBERHARD, L.; FROST, D.J.; MCCAMMON, C.A.: 18.-23.08.2019, Goldschmidt 2019, Barcelona, Spain: "The effect of oxygen fugacity on the stability and ferric iron content of antigorite"

EBERHARD, L.; FROST, D.J.; MCCAMMON, C.A.: 22.-25.09.2019, GeoMünster 2019, Münster, Germany[*A]: "The role of oxygen fugacity on the stability of serpentnites in subduction zones"

EBERHARD, L.; FROST, D.J.; MCCAMMON, C.A.: 09.-13.12.2019, AGU Fall Meeting, San Francisco, USA[*B]: "Redox evolution of serpentinised oceanic crust during subduction and implications for subduction zone fluids", Abstract DI43A-0034

EICHHEIMER, P.; FUJITA, W.; THIELMANN, M.; POPOV, A.; KAUS, B.J.P.; GOLABEK, G.J.; OKUMURA, S.; NAKAMURA, M.; NAKATANI, T.: 07.-12.04.2019, European Geosciences Union General Assembly 2019, Vienna, Austria: "Permeability prediction of porous media with the finite difference Stokes solver LaMEM", Geophysical Research Abstracts 21, EGU2019-5728, 2019

EICHHEIMER, P.; FUJITA, W.; THIELMANN, M.; POPOV, A.; KAUS, B.J.P.; GOLABEK, G.J.; OKUMURA, S.; NAKAMURA, M.; NAKATANI, T.: 26.-30.05.2019, Japan Geoscience Union Meeting (JpGU2019), Chiba, Japan: "Permeability prediction of porous media with the finite difference Stokes solver LaMEM"

EICHHEIMER, P.; FUJITA, W.; THIELMANN, M.; POPOV, A.; GOLABEK, G.J.; KAUS, B.J.P.; OKUMURA, S.; NAKAMURA, M.; NAKATANI, T.: 31.05.-01.06.2019, JSPS Japanese-German graduate externship International Workshop on 'Volatile Cycles', Tokyo, Japan: "Numerical and experimental permeability prediction of porous media using finite differences"

EICHHEIMER, P.; THIELMANN, M.; POPOV, A.; GOLABEK, G.J.; FUJITA, W.; KOTTWITZ, M.O.; KAUS, B.J.P.; OKUMURA, S.; NAKAMURA, M.; NAKATANI, T.: 25.-30.08.2019, 2019 Ada Lovelace Workshop on Numerical Modelling of Mantle and Lithosphere Dynamics, Siena, Italy: "Numerical and experimental permeability prediction of porous media"

FEI, H.; KATSURA, T.: 18.-21.03.2019, Joint Symposium of Misasa 2019 & Core-Mantle Coevolution, Misasa, Japan: "High water solubility of ringwoodite at mantle transition zone temperature"

FEI, H.: 04.06.2019, China University of Geosciences, School of Earth Science, Wuhan, P.R. China: "Part I: Proton incorporation mechanism in olivine. Part II: Water content in the dehydration melting layer at 660 km depth"

FERREIRA, F.; MARQUARDT, K. (2019): 09.-13.12.2019, AGU Fall Meeting, San Francisco, USA[*B]: "Olivine grain growth kinetics at high pressure and temperature", Abstract MR51B-0054

FERREIRA, F.; MARQUARDT, K.; HANSEN, L.: 11.-14.06.2019, 22nd International Conference on Deformation Mechanisms, Rheology and Tectonics, Tübingen, Germany: "Crossing boundaries: Grain boundary effects on plastic deformation of olivine"

FROSSARD, P.; BOYET, M.; BOUVIER, A.; HAMMOUDA, T.; MONTEUX, J.: 18.-22.03.2019, 50th Lunar and Planetary Science Conference, Houston, USA: "Magma ocean-derived anorthositic crust on early (< 5 Ma) planetesimal", Abstract 1772

FROSSARD, P.; BOYET, M.; BOUVIER, A.; HAMMOUDA, T.: 18.-23.08.2019, Goldschmidt 2019, Barcelona, Spain: "Sm and Nd nucleosynthetic anomalies in EL and EH chondrites"

FROST D.J.: 15.01.2019, Ludwig-Maximilians-Universität, München, Germany: "Diamond formation in the Earth's interior and the deep carbon cycle"

FROST, D.J.; NOVELLA, D.; HUANG, R.; CONDAMINE, P.: 26.-30.05.2019, Japan Geoscience Union Meeting (JpGU2019), Chiba, Japan: "The nature of water induced small degree melts in the deep mantle"

FROST D.J.: 18.-21.06.2019, Fondation des Treilles workshop on Origin and Evolution of Planetary Atmospheres, Les Treilles, France: "The effect of oxygen fugacity on the stability and ferric iron content of antigorite"

FUJITA, W.; NAKAMURA, M.; EICHHEIMER, P.; THIELMANN, M.; GOLABEK, G.; UESUGI, K.: 09.-13.12.2019, AGU Fall Meeting, San Francisco, USA*B: "Permeability computation of CHO-fluid bearing monomineralic aggregates: effects of dihedral angle and microstructural evolution", Abstract H23M-2084

GABORIEAU, M.; LAUBIER, M.; BOLFAN-CASANOVA, N.; MCCAMMON, C.; VANTELON, D.; CHUMAKOV, A.: 18.-23.08.2019, Goldschmidt 2019, Barcelona, Spain: "Iron speciation in olivine-hosted melt inclusions inferred from Mössbauer spectroscopy"

GOLABEK, G.; NIMMO, F.; SCHENK, P.; GERYA, T.: 25.01.2019, Rhein-Main Biannual Geodynamics Workshop, Johannes Gutenberg University, Mainz, Germany: "3D numerical models of thermal convection inside Triton's icy shell"

GOLABEK, G.; SOLFERINO, G.; WALTE, N.; NIMMO, F.; SCHMIDT, M.: 20.02.2019, Universität Bern, Switzerland: "Laboratory and numerical experiments on stony-iron meteorite formation"

GOLABEK, G.; SOLFERINO, G.; WALTE, N.; NIMMO, F.; SCHMIDT, M.: 04.03.2019, University of Rochester, USA: "Laboratory and numerical experiments on stony-iron meteorite formation"

GOLABEK, G.; LICHTENBERG, T.; BURN, R.; MEYER, M.; ALIBERT, Y.; GERYA, T.; MORDASINI, C.: 08.03.2019, University of Rochester, USA: "A water budget dichotomy of rocky protoplanets from ^{26}Al-heating"

GOLABEK, G.; LICHTENBERG, T.; BURN, R.; MEYER, M.; ALIBERT, Y.; GERYA, T.; MORDASINI, C.: 13.03.2019, University of Alabama, Tuscaloosa, USA: "A water budget dichotomy of rocky protoplanets from ^{26}Al-heating"

GOLABEK, G.; LICHTENBERG, T.; BURN, R.; MEYER, M.; ALIBERT, Y.; GERYA, T.; MORDASINI, C.: 07.-12.04.2019, European Geosciences Union General Assembly 2019, Vienna, Austria: "A water budget dichotomy of rocky protoplanets from ^{26}Al-heating", Geophysical Research Abstracts 21, EGU2019-5414, 2019

GOLABEK, G.; NIMMO, F.; GERYA, T.; SCHENK, P.; PLATTNER, A.: 07.-12.04.2019, European Geosciences Union General Assembly 2019, Vienna, Austria: "3D numerical models of thermal convection inside Triton's icy shell", Geophysical Research Abstracts 21, EGU2019-4392, 2019

GOLABEK, G.; LICHTENBERG, T.; BURN, R.; MEYER, M.; ALIBERT, Y.; GERYA, T.; MORDASINI, C.: 09.10.2019, Université de Bordeaux, France: "A water budget dichotomy of rocky protoplanets from ^{26}Al-heating"

GOLABEK, G.; LICHTENBERG, T.; BURN, R.; MEYER, M.; ALIBERT, Y.; GERYA, T.; MORDASINI, C.: 30.10.2019, Royal Holloway University, London, U.K.: "A water budget dichotomy of rocky protoplanets from ^{26}Al-heating"

GOLABEK, G.; PLATTNER, A.; NIMMO, F.; GERYA, T.; SCHENK, P.: 25.-30.08.2019, 2019 Ada Lovelace Workshop on Numerical Modelling of Mantle and Lithosphere Dynamics, Siena, Italy: "3D numerical models of thermal convection inside Triton's icy shell"

GREER, J.; HECK, P.R.; BOESENBERG, J.S.; BOUVIER, A.; *ET AL.* (30 AUTHORS): 18.-22.03.2019, 50th Lunar and Planetary Science Conference, Houston, USA: "Hamburg: A pristine H4 chondrite fall", Abstract 1638

GUO, Z.; BOUVIER, A.; WEBB, L.; ALEXANDRE, A.; LONGSTAFFE, F.J.; KOROTEV, R.A.; ZAJACZ, Z.; BOYET, M.: 18.-22.03.2019, 50th Lunar and Planetary Science Conference, Houston, USA: "A new not so eucrite-like ungrouped achondrite: Northwest Africa 12338", Abstract 1583

GUO, Z.; LIU, J.; QIN, L.; GANNOUN, M.; BOYET, M.; ZAJACZ, Z.; BOUVIER, A.: 07.-12.07.2019, 82nd Annual Meeting of the Meteoritical Society, Sapporo, Japan: "Sm-Nd, Lu-Hf and Mn-Cr compositions of eucrite, diogenite and ungrouped achondrites: Implications for the formation and sources of differentiated planetesimals", Abstract 6352

HSIEH, W.-P.; CHAO, K.-H.; ISHII, T.; OHTANI, E.: 09.-13.12.2019, AGU Fall Meeting, San Francisco, USA^{*B}: "Thermal conductivity of carbonate and hydrous minerals in Earth's deep interior", Abstract MR31B-0076

HU, S.; ANAND, M.; FRANCHI, I.A.; ZHAO, X.; CHAN, Q.H.S.; ZHANG, B.; BOUVIER, A.; LIN, Y.T.; ZHANG, J.C.; HAO, J.L.; YANG, W.; LIU, Y.; TANG, G.Q.; LI, Q.L.; AGEE, C.: 07.-12.07.2019, 82nd Annual Meeting of the Meteoritical Society, Sapporo, Japan: "U-Pb dating, hydrogen and chlorine isotopic systematics of the whitlockite and apatite from the ungrouped achondrite Northwest Africa 11119", Abstract 6099

HUANG, R.; BOFFA BALLARAN, T.; MCCAMMON, C.A.; MIYAJIMA, N.; FROST, D.J.: 31.05.-01.06.2019, JSPS Japanese-German graduate externship International Workshop on 'Volatile Cycles', Tokyo, Japan: "The effect of Fe-Al substitution on $MgSiO_3$ bridgmanite: A single-crystal X-ray diffraction study"

HUANG, Y.; NAKATANI, T.; NAKAMURA, M.; MCCAMMON, C.: 07.-12.04.2019, European Geosciences Union General Assembly 2019, Vienna, Austria: "Experimental constraint on the dihedral angle in olivine-H_2O-CO_2 system in subduction zones", Geophysical Research Abstracts 21, EGU2019-12536, 2019

HUANG, Y.; NAKATANI, T.; NAKAMURA, M.; MCCAMMON, C.: 26.-30.05.2019, Japan Geoscience Union Meeting (JpGU2019), Chiba, Japan: "Fluid circulation in the forearc mantle wedge inferred from the dihedral angle in an olivine-H_2O-NaCl system"

ISHII, T.; UENVER-THIELE, L.; WOODLAND, A.B.; ALIG, E.; BOFFA BALLARAN, T.: Crystal structure of Mg-bearing Fe_9O_{11}: 26.-30.05.2019, Japan Geoscience Union Meeting (JpGU2019), Chiba, Japan: "New insight in the complexity of Fe-Mg oxides at conditions of the deep upper mantle"

ISHII, T.: 23.-25.10.2019, The 60th High Pressure Conference of Japan, Sapporo, Japan: "Development of high-pressure experimental techniques using multianvil presses and their applications to Earth science"

ISHII, T.; FROST, D.J.; CHANYSHEV, A.; NISHIDA, K.; BAN, R.; SU, X.; Higo, Y.; TANGE, Y.; KATSURA, T.: 09.-13.12.2019, AGU Fall Meeting, San Francisco, USA*B: "Non-linear temperature dependence of the post-garnet transition boundary in $Mg_3Al_2Si_3O_{12}$ revealed by accurate equilibrium experiment in a multianvil press with *in situ* X-ray diffraction", Abstract DI31B-0014

JENNINGS, E.; RUBIE, D.; JACOBSON, S.; MORBIDELLI, A.; NAKAJIMA, Y.; VOGEL, A.; ROSE-WESTON, L.; FROST, D.: 15.-20.09.2019, European Planetary Science Congress (EPSC) – Division of Planetary Science (DPS) Joint Meeting, Geneva, Switzerland: "Metal-silicate partitioning of Mo and W in Earth's mantle during core formation"

KATSURA, T.: 04.-06.03.2019, 4th International HiPeR Symposium, Hiroshima University, Higashi-Hiroshima, Japan (*invited*): "Water enhancement of ionic conductivity of olivine"

KATSURA, T.; FEI, H.-F.; DRUZHBIN, D.: 18.-21.03.2019, Joint Symposium of Misasa 2019 & Core-Mantle Coevolution, Misasa, Japan (*invited*): "H_2O-enhanced ionic conductivity of olivine"

KATSURA, T.: 23.08.2019, Seoul National University, Seoul, South Korea: "Sharp 660-km discontinuity controlled by extremely narrow binary post-spinel transition"

KATSURA, T.: 29.08.2019, Jilin University, Changchun, P.R. China: "Development of multianvil technology, and its application to geophysics"

KATSURA, T.: 26.11.2019, Shizuoka University, Shizuoka, Japan: "Sharp 660-km discontinuity controlled by extremely narrow binary post-spinel transition"

KATSURA, T.; FEI, H.; LIU, Z.; MCCAMMON, C.A.: 09.-13.12.2019, AGU Fall Meeting, San Francisco, USA*B: "Oxygen vacancy component ($MgFeO_{2.5}$) produced by Fe^{3+} in bridgmanite and its implications for viscosity variation in the mid-mantle", Abstract DI31B-0012

KEPPLER, H.: 27.-29.05.2019, Outgassing Processes Workshop, Villefranche sur Mer, France: "Volcanoes and the atmosphere"

KHANDARKHAEVA, S.; KRUPP, A.; DUBROVINSKAIA, N.; DUBROVINSKY, L.: 09.-11.10.2019, 8th Joint Workshop on High Pressure, Planetary and Plasma Physics (HP4), Dresden, Germany: "X-ray diffraction studies of materials laser-heated in double stage diamond anvil cells"

KHANDARKHAEVA, S.; DUBROVINSKY, L.; DUBROVINSKAIA, N.: 11.-12.12.2019, Workshop 'Experimental Work at DESY and EuXFEL', European XFEL, Schenefeld, Germany: "Extending of structural studies up to 200 GPa"

KISEEVA, E.S.; WOOD, B.; MCCAMMON, C.; ASHCHEPKOV, I.: 18.-23.08.2019, Goldschmidt 2019, Barcelona, Spain: "Ferric ferrous ratios in mantle xenoliths by synchrotron Mössbauer source spectroscopy"

KOEMETS, E.; BYKOV, M.; APRILIS, G.; FEDOTENKO, T.; CHARITON, S.; KHANDARKHAEVA, S.; KOEMETS, I.; THIELMANN, M.; DUBROVINSKAIA, N.; DUBROVINSKY, L.: 26.-30.05.2019, Japan Geoscience Union Meeting (JpGU2019), Chiba, Japan: " Goethite instability at the lower mantle conditions and implications for the origin of the Great Oxidation"

KOEMETS, E.; BYKOV, M.; APRILIS, G.; FEDOTENKO, T.; CHARITON, S.; BYKOVA, E.; KHANDARKHAEVA, S.; KOEMETS, I.; THIELMANN, M.; MCCAMMON, C.A.; DUBROVINSKAIA, N.A.; DUBROVINSKY, L.S.: 26.-30.05.2019, Japan Geoscience Union Meeting (JpGU2019), Chiba, Japan: "Goethite behaviour at the conditions of a subducting slab"

KOEMETS, E.; BYKOV, M.; APRILIS, G.; FEDOTENKO, T.; CHARITON, S.; BYKOVA, E.; KHANDARKHAEVA, S.; KOEMETS, I.; THIELMANN, M.; MCCAMMON, C.; DUBROVINSKAIA, N.; DUBROVINSKY, L.: 22.-25.09.2019, GeoMünster 2019, Münster*A, Germany: "Goethite decomposition at the lower mantle conditions"

KOEMETS, I.; LIU, Z.; KOEMETS, E.; MCCAMMON, C.; CHANYCHEV, A.; KATSURA, T.; HANFLAND, M.; CHUMAKOV, A.: 26.-30.05.2019, Japan Geoscience Union Meeting (JpGU2019), Chiba, Japan: "Crystal chemistry and compressibility of $F_{e0.5}Mg_{0.5}Al_{0.5}Si_{0.5}O_3$ and $FeMg_{0.5}Si_{0.5}O_3$ silicate perovskites at pressures up to 95 GPa"

KOEMETS, I.; LIU, Z.; KOEMETS, E.; MCCAMMON, C.; CHANYSHEV, A.; KATSURA, T.; DUBROVINSKY, L.S.; HANFLAND, M.; CHUMAKOV, A.: 31.05-02.06.2019, JSPS Japanese-German graduate externship International Workshop on 'Volatile Cycles', Tokyo, Japan: "Combination of single crystal X-ray diffraction and Synchrotron Mössbauer Spectroscopy at lower mantle conditions: Study of crystal chemistry and compressibility of silicate perovskites at pressures up to 95 GPa"

KOEMETS, I.; LIU, Z.; KOEMETS, E.; MCCAMMON, C.; KATSURA, T.; DUBROVINSKY, L.; HANFLAND, M.; CHUMAKOV, A.: 18.-23.08.2019, 32nd European Crystallographic Meeting, Vienna, Austria: "Structure, crystal chemistry, and compressibility of iron-rich silicate perovskite at pressures up to 95 GPa"

KORELL, J.-A.; FRENCH, M.; STEINLE-NEUMANN, G.; REDMER, R.: 09.-11.10.2019, 8th Joint Workshop on High Pressure, Planetary and Plasma Physics (HP4), Dresden, Germany: "Paramagnetic-to-diamagnetic transition in dense liquid iron and its influence on electronic transport properties"

KUBIK, E.; SIEBERT, J.; MAHAN, B.; BLANCHARD, I.; CREECH, J.; AGRANIER, A.; MOYNIER, F.: 18.-23.08.2019, Goldschmidt 2019, Barcelona, Spain: "Tracing Earth's volatile element delivery with tin"

KURNOSOV, A.; CRINITI, G.; BOFFA BALLARAN, T.; MARQUARDT, H.; FROST, D.J.: 18.-23.08.2019, Goldschmidt 2019, Barcelona, Spain: "Earth's lower mantle elasticity from mineral-physics constraints"

KURNOSOV, A.; CRINITI, G.; BOFFA BALLARAN, T.; MARQUARDT, H.; FROST, D.J.: 22.-25.09.2019, GeoMünster 2019, Münster, Germany*A: "Earth's lower mantle elasticity from mineral-physics constraints"

LEE, K.; CREASY, N.; GIRARD, J.; DOBROSAVLJEVIC, V.; GU, T.; MCCAMMON, C.A.; LI, M.: 09.-13.12.2019, AGU Fall Meeting, San Francisco, USA[*B] (*invited*): "Mapping mantle heterogeneities through redox state", Abstract U42B-05

LIU, Z.; ISHII, T.; RONG, H.; BOFFA BALLARAN, T.; FROST, D.J.; AKAOGI, M.; KATSURA, T.: 23.-25.10.2019, The 60th High Pressure Conference of Japan, Sapporo, Japan: "Pressure, temperature and bulk composition dependence of the oxygen vacancy component in aluminous bridgmanite"

MARQUARDT, H.; BUCHEN, J.; MÉNDEZ, A.S.J.; KURNOSOV, A.; WENDT, M.; ROTHKIRCH, A.; PENNICARD, D.; LIERMANN, H.-P.: 13.-15.02.2019, MML Workshop 'From Matter to Materials and Life', Dresden, Germany: "Direct measurements of the bulk modulus softening in (Mg,Fe)O across the iron spin change measured at seismic frequencies in a dynamic DAC using time-resolved XRD"

MARQUARDT, K.; FERREIRA, F.; HANSEN, L.; FAUL, U.: 18.-23.08.2019, Goldschmidt 2019, Barcelona, Spain: "Olivine interface distributions in static and dynamic equilibrium; effects of diffusion vs. effects of dislocation motion"

MARZOTTO, E.; THIELMANN, M.; GOLABEK, G.J.: 15.04.2019, Workshop on Earth's Deep Interior, Academia Sinica, Institute of Earth Sciences, Taipei, Taiwan: "Effect of grid resolution on tectonic regimes in global-scale convection models"

MARZOTTO, E.; THIELMANN, M.; GOLABEK, G. J.: 26.-30.05.2019, Japan Geoscience Union Meeting (JpGU2019), Chiba, Japan: "Effect of grid resolution on tectonic regimes in global-scale convection models"

MARZOTTO, E.; THIELMANN, M.; GOLABEK, G. J.: 31.05-02.06.2019, JSPS Japanese-German graduate externship International Workshop on 'Volatile Cycles', Tokyo, Japan: "Effect of grid resolution on tectonic regimes in global-scale convection models"

MCCAMMON, C.: 11.-12.03.2019, EBS Workshop on Nuclear Resonance Scattering, ESRF, Grenoble, France: "New frontiers in geoscience with submicron SMS"

MCCAMMON, C.; WAN, M.; SCHRÖDER, C.; PEIFFER, S.: 07.-12.04.2019, European Geosciences Union General Assembly 2019, Vienna, Austria: "Mackinawite oxidation: Reaction pathways and kinetics", Geophysical Research Abstracts 21, EGU2019-14050, 2019

MCCAMMON, C.: 22.-25.09.2019, GeoMünster 2019, Münster, Germany[*A]: "When history is written in sample heterogeneity"

MCCAMMON, C.: 07.-09.10.2019, EBS Workshop on X-ray Spectroscopy of Magnetic Materials, ESRF, Grenoble, France: "Who cares about magnetism at extreme conditions?"

MCCAMMON, C.: 10.-11.10.2019, 4th Meeting of FOR 2125/2 CarboPat, Wehrheim, Germany: "Update on sub-micron resolution for the synchrotron Mössbauer source"

MCCAMMON, C.; ARMSTRONG, K.; FROST, D.; RUBIE, D.; BOFFA BALLARAN, T.: 24.-26.10.2019, Deep Carbon 2019, Washington D.C., USA: "How Earth's early magma ocean captured mantle carbon"

MCCAMMON, C.: 09.-13.12.2019, AGU Fall Meeting, San Francisco, USA[*B]: "Tiny light things went round and round inside our world and gave us life", Abstract ED43A-10

MCCAMMON, C.; DOMINIJANNI, S.; MIYAJIMA, N.; FROST, D.; DUBROVINSKY, L.: 09.-13.12.2019, AGU Fall Meeting, San Francisco, USA[*B]: "Deciphering deep volatile cycles in early Earth", Abstract MR51D-0072

MEIER, T.: 08.01.2019, Physikalisches Kolloquium der Universität Bayreuth, Physikalisches Institut, Bayreuth, Germany: "From metallizations to hydrogen bond symmetrizations – NMR as a new tool to study condensed matter at extreme conditions"

MEIER, T.; TRYBEL, F.; KHANDARKHAEVA, S.; PETITGIRARD, S.; STEINLE-NEUMANN, G.; CHARITON, S.; FEDOTENKO, T.; DUBROVINSKAIA, N.; DUBROVINSKY, L.: 04.-08.03.2019, APS March Meeting, Boston, USA: "Probing hydrogen in metal hydrides: Proton-NMR study of FeH up to 2 Mbar"

MEIER, T.: 04.-09.08.2019, The 27th AIRAPT International Conference on High Pressure Science and Technology, Rio de Janeiro, Brazil (*invited*): "Nuclear Magnetic Resonance spectroscopy at mega-bar pressures"

MEIER, T.: 25.-30.08.2019, 21st ISMAR – 15th EUROMAR, Berlin, Germany: "Squeeze it until it breaks: *In situ* NMR at geophysical relevant conditions"

MEIER, T.; TRYBEL, F.; KHANDARKHAEVA, S.; PETITGIRARD, S.; STEINLE-NEUMANN, G.; CHARITON, S.; FEDOTENKO, T.; DUBROVINSKAIA, N.; DUBROVINSKY, L.: 01.-06.09.2019, 57th EHPRG, Prague, Czech Republic: "What can we learn from ^{1}H-NMR in metal hydrides at mega-bar pressures?"

MEIER, T.; TRYBEL, F.; KHANDARKHAEVA, S.; CRINITI, G.; KOEMETS, E.; FEDOTENKO, T.; CHARITON, S.; STEINLE-NEUMANN, G.; GLAZYRIN, K.; BYKOV, M.; HANFLAND, M.; DUBROVINSKAIA, N.; DUBROVINSKY, L.: 09.-11.10.2019, 8th Joint Workshop on High Pressure, Planetary and Plasma Physics (HP4), Dresden, Germany: "Hydrogen-hydrogen interaction in metal hydrides at multi mega-bar pressures"

MEIER, T.: 02.12.2019, Geophysical Laboratory, Washington D.C., USA: "Magnetic resonance in tight spaces: Perspectives and new directions"

MELAI, C.; FROST, D.J.; BOFFA BALLARAN, T.; MCCAMMON, C.A.: 11.-12.03.2019, EBS Workshop on Nuclear Resonance Scattering, ESRF, Grenoble, France: "Pressure, temperature and oxygen fugacity effect on Fe^{3+}content in ferropericlase"

MELAI, C.; FROST, D.; BOFFA BALLARAN, T.; MCCAMMON, C.: 26.-30.05.2019, Japan Geoscience Union Meeting (JpGU2019), Chiba, Japan: "The conditions of sublithospheric diamond formation constrained from ferric iron-rich exsolution from ferropericlase inclusions"

MELAI, C.; FROST, D.J.; BOFFA BALLARAN, T.; MCCAMMON, C.A.: 31.05.-01.06.2019, JSPS Japanese-German graduate externship International Workshop on 'Volatile Cycles', Tokyo, Japan: "Ferric iron rich exsolution in ferropericlase as a proxy for sub-lithospheric diamond formation"

MELAI, C.; FROST, D.J.; BOFFA BALLARAN, T.; MCCAMMON, C.; MARQUARDT, K.: 22.-25.09.2019, GeoMünster 2019, Münster, Germany[*A]: "The oxygen fugacity of sublithospheric diamond formation and the conditions encountered during their ascent to the surface"

MÉNDEZ, A.S.J.; MARQUARDT, H.; HUSBAND, R.; WENDT, M.; SCHWARK, I.; EHNES, A.; GLAZYRIN, K.; KURNOSOV, A.; SATTA, N.; LIERMANN, H.-P.: 24.-25.01.2019, DESY Photon Science Users' Meeting, Hamburg, Germany: "A dynamic diamond anvil cell (dDAC) setup for time-resolved high-temperature X-ray diffraction experiments under dynamic compression"

MÉNDEZ, A.S.J.; MARQUARDT, H.; HUSBAND, R.; WENDT, M.; SCHWARK, I.; EHNES, A.; GLAZYRIN, K.; KURNOSOV, A.; SATTA, N.; LIERMANN, H.-P.: 08.08.2019, EPA-PLP Workshop 'Atmospheres & Interiors', DLR Berlin, Germany: "H_2O ice at high pressure and temperature studied by X-ray diffraction in a Resistively Heated dynamic Diamond Anvil Cell (RHdDAC)"

MÉNDEZ, A.S.J.; MARQUARDT, H.; TRYBEL, F.; STEINLE-NEUMANN, G.; LIERMANN, H.-P.: 09.-11.10.2019, 8th Joint Workshop on High Pressure, Planetary and Plasma Physics (HP4), Dresden, Germany: "H_2O ice at high pressure and temperature studied by X-ray diffraction in a Resistively Heated dynamic Diamond Anvil Cell (RHdDAC)"

MIYAJIMA, N.: 26.08.2019, Kyoto University, Kyoto, Japan: "Characterization of crystal defects using electron microscopy: Antiphase domain boundaries and Dauphiné twin"

MIYAJIMA, N.; SOUZA, D.S.; HEIDELBACH, F.: 22.-25.09.2019, GeoMünster 2019, Münster, Germany^{*A}: "Dauphiné twin in a naturally deformed quartz: Characterization by electron channelling contrast imaging and large-angle convergent-beam diffraction"

MORBIDELLI, A.; LIBOUREL, G.; PALME, H.; JACOBSON, S.; RUBIE, D.: 15.-20.09.2019, European Planetary Science Congress (EPSC) – Division of Planetary Science (DPS) Joint Meeting, Geneva, Switzerland: "Sub-solar Al/Si and Mg/Si ratios of the enstatite chondrites reveal planetesimal formation during early condensation in the protoplanetary disk"

MOROZOVA, N.V.; KOROBEINIKOV, I.V.; TITOV, A.N.; OVSYANNIKOV, S.V.: 04.-09.08.2019, The 27th AIRAPT International Conference on High Pressure Science and Technology, Rio de Janeiro, Brazil: "Vanadium tetrasulfide under high pressure: thermoelectric and electrical properties"

MOROZOVA, N.V.; KOROBEINIKOV, I.V.; TITOV, A.N.; OVSYANNIKOV, S.V.: 01.-06.09.2019, 57th EHPRG, Prague, Czech Republic: "Electronic transport properties of VS_4 under high pressures"

MYHILL, R.; BEYER, C.; MCCAMMON, C.A.; MARQUARDT, K.: 09.-13.12.2019, AGU Fall Meeting, San Francisco, USA^{*B}: "Iron disproportionation in majorite-bearing rocks of the Earth's transition zone and in Mars' deep mantle", Abstract DI24A-07

OHTANI, E.; OHIRA, I.; JACKSON, J.; ISHII, T.; HSIEH, W.-P.: 22.-25.09.2019, GeoMünster 2019, Münster, Germany^{*A}: "Role of high pressure hydrous phase in lower mantle dynamics"

OVSYANNIKOV, S.V.; BYKOV, M.; BYKOVA, E.; GLAZYRIN, K.; MANNA, R.S.; TSIRLIN, A.A.; CERANTOLA, V.; KUPENKO, I.; KURNOSOV, A.V.; KANTOR, I.; PAKHOMOVA, A.S.; CHUVASHOVA, I.; CHUMAKOV, A.I.; RÜFFER, R.; MCCAMMON, C.; DUBROVINSKY, L.S.: 18.-23.08.2019, 32nd European Crystallographic Meeting, Vienna, Austria: "High-pressure synthesis and properties of iron oxides"

OVSYANNIKOV, S.V.; BYKOV, M.; BYKOVA, E.; GLAZYRIN, K.; MANNA, R.S.; TSIRLIN, A.A.; CERANTOLA, V.; KUPENKO, I.; KURNOSOV, A.V.; KANTOR, I.; PAKHOMOVA, A.S.; CHUVASHOVA, I.; CHUMAKOV, A.I.; RÜFFER, R.; MCCAMMON, C.; DUBROVINSKY, L.S.: 01.-06.09.2019, 57th EHPRG, Prague, Czech Republic: "Low-temperature phase transitions in Fe_4O_5 under high pressure"

OVSYANNIKOV, S.V.; BYKOV, M.; BYKOVA, E.; GLAZYRIN, K.; MANNA, R.S.; TSIRLIN, A.A.; CERANTOLA, V.; KUPENKO, I.; KURNOSOV, A.V.; KANTOR, I.; PAKHOMOVA, A.S.; CHUVASHOVA, I.; CHUMAKOV, A.I.; RÜFFER, R.; MCCAMMON, C.; DUBROVINSKY, L.S.: 04.-09.08.2019, The 27th AIRAPT International Conference on High Pressure Science and Technology, Rio de Janeiro, Brazil: "Phase transitions in Fe_4O_5 under high pressure"

PAKHOMOVA, A.; SIMONOVA, D.; KOEMETS, E.; KOEMETS, I.; APRILIS, G.; BYKOV, M.; GORELOVA, L.; PRAKAPENKA, V.; DUBROVINSKY, L.S.: 22.-25.09.2019, GeoMünster 2019, Münster, Germany[*A]: "High-pressure phases of feldspars with five- and six-fold coordinated aluminium"

PAPA, S.; PENNACCHIONI, G.; MENEGON, L.; THIELMANN, M.: 09.-13.12.2019, AGU Fall Meeting, San Francisco, USA[*B]: "High-stress creep in amphibolite-facies ultramylonites hosting pseudotachylytes: Ductile instability or brittle failure?", Abstract T43D-0458

PETITGIRARD, S.; KUPENKO, I.; COLLINGS, I.E.; JENNINGS, E.; BLANCHARD, I.; MALFAIT, W.J.; CERANTOLA, V.; COTTE, M.; JOHANNES, A.W.; MURAKAMI, M.: 15.-20.09.2019, European Planetary Science Congress (EPSC) – Division of Planetary Science (DPS) Joint Meeting, Geneva, Switzerland: "Fe-rich silicate melt densities to 150 GPa"

PRIMOCERIO, J.; CHAKRABORTY, S.; MARQUARDT, K.; FOCKENBERG, T.: 22.-25.09.2019, GeoMünster 2019, Münster, Germany[*A]: "The role of chemically induced stresses in the mechanisms of element exchange between minerals – an experimental study based on pyroxenes"

PRIMOCERIO, J.; CHAKRABORTY, S.; MARQUARDT, K.; FOCKENBERG, T.: 16.-19.10.2019, 9. Bonner Humboldt-Preisträger-Forum "Frontiers in Biogeography, Ecology, Anthropology, and Evolution. Humboldt and the 'Cosmos' revisited in the 21st Century", Bonn, Germany: "How hot are the interiors of planets? Development of a geothermometer"

PRIMOCERIO, J.; CHAKRABORTY, S.; MARQUARDT, K.; FOCKENBERG, T.: 09.-13.12.2019, AGU Fall Meeting, San Francisco, USA[*B]: "Mechanism of element exchange between solid phases – a case study using Fe-Mg exchange between ortho- and clinopyroxene", Abstract V51F-0111

PUTAK JURIČEK, M.; NAKAMURA, M.; MUJIN, M.; SCHMINCKE, H.-U.; SUMITA, M.; MIYAJIMA, M.: 26.-30.05.2019, Japan Geoscience Union Meeting (JpGU2019), Chiba, Japan: "First observation of nanolites and ultrananolites in alkaline volcanic glasses (Eifel, Germany)"

PUTAK JURIČEK, M.; KEPPLER, H.: 26.-30.05.2019, Japan Geoscience Union Meeting (JpGU2019), Chiba, Japan: "Pargasite stability in the upper mantle at H_2O-undersaturated conditions"

PUTAK JURIČEK, M.; NAKAMURA, M.; MUJIN, M.; SCHMINCKE, H.-U.; SUMITA, M.; MIYAJIMA, M.: 31.05.-01.06.2019, JSPS Japanese-German graduate externship International Workshop on 'Volatile Cycles', Tokyo, Japan: "First observation of nanolites and ultrananolites in alkaline volcanic glasses (Eifel, Germany)"

PUTAK JURIČEK, M.; KEPPLER, H.: 03.-04.06.2019, Earth, Sea and Sky V: International Joint Graduate Program Workshop, Tohoku University, Sendai, Japan: "Pargasite stability in the upper mantle at H_2O-undersaturated conditions"

PUTAK JURIČEK, M.; KEPPLER, H.: 18.-23.08.2019, Goldschmidt 2019, Barcelona, Spain: "Pargasite stability in the upper mantle at H_2O-undersaturated conditions"

PUTAK JURIČEK, M.; KEPPLER, H.: 22.-25.09.2019, GeoMünster 2019, Münster, Germany[*A]: "Pargasite stability in the upper mantle at H_2O-undersaturated conditions"

REGER, P.M.; SIMON, S.B.; GANNOUN, A.M.; GIBSON, J.; GREENWOOD, R.; BOUVIER, A.: 07.-12.07.2019, 82nd Annual Meeting of the Meteoritical Society, Sapporo, Japan: "Petrology, geochemistry and Pb-Pb age of a large igneous inclusion from the ordinary chondrite Paposo 004", Abstract 6365

RUBIE, D.C.: 18.03.-20.03.2019, Workshop on 'Disc evolution, Planetesimal and Planet Formation', Frejus, France: "Chemical gradients in the protoplanetary disc"

RUSTIONI, G.; AUDÉTAT, A.; KEPPLER, H.: 31.05.-01.06.2019, JSPS Japanese-German graduate externship International Workshop on 'Volatile Cycles', Tokyo, Japan: "Experimental constraints on trace element mobility in subduction zone fluids"

RUSTIONI, G.; AUDÉTAT, A.; KEPPLER, H.: 03.-04.06.2019, Earth, Sea and Sky V: International Joint Graduate Program Workshop, Tohoku University, Sendai, Japan: "Experimental constraints on the composition of subduction zone fluids"

RUSTIONI, G.; AUDÉTAT, A.; KEPPLER, H.: 18.-23.08.2019, Goldschmidt 2019, Barcelona, Spain: "Experimental constraints on the composition of subduction zone fluids"

SATTA, N.; MARQUARDT, H.; KURNOSOV, A.; BUCHEN, J.; KAWAZOE, T.; MCCAMMON, C.; BOFFA BALLARAN, T.: 15.04.2019, Workshop on Earth's Deep Interior, Academia Sinica, Institute of Earth Sciences, Taipei, Taiwan: "Single crystal elasticity of Fe-bearing phase E by Brillouin spectroscopy"

SATTA, N.; MARQUARDT, H.; KURNOSOV, A.; BOFFA BALLARAN, T.; BUCHEN, J.; MCCAMMON, C.; KAWAZOE, T.: 26.-30.05.2019, Japan Geoscience Union Meeting (JpGU2019), Chiba, Japan: "Single crystal elasticity of Fe-bearing phase E by Brillouin spectroscopy"

SATTA, N.; CRINITI, G.; ISHII, T.; KURNOSOV, A.; BOFFA BALLARAN, T.; BUCHEN, J.; MARQUARDT, H.: 09.-13.12.2019, AGU Fall Meeting, San Francisco, USA[*B]: "The effect of Al-Fe substitution on the elastic properties of δ-(Al, Fe) OOH", Abstract MR31B-0079

SAWA, S.; MUTO, J.; MIYAJIMA, N.; NAGAHAMA, H.: 22.-25.09.2019, GeoMünster 2019, Münster, Germany[*A]: "Grain size dependency of Ge-olivine/spinel on phase transformational faulting mechanism for deep-focus earthquakes"

SAWA, S.; MUTO, J.; MIYAJIMA, N.; NAGAHAMA, H.: 03.-04.06.2019, Earth, Sea and Sky V: International Joint Graduate Program Workshop, Tohoku University, Sendai, Japan: "Grain size dependency of olivine-spinel phase transformational mechanism responsible for deep-focus earthquakes"

SAWA, S.; MIYAJIMA, N.; MUTO, J.; NAGAHAMA, H.: 09.-13.12.2019, AGU Fall Meeting, San Francisco, USA[*B]: "Grain size dependency of the phase transformational faulting mechanism responsible for deep-focus earthquakes", Abstract S13C-0460

SCHIERJOTT, J.; THIELMANN, M.; GOLABEK, G.; ROZEL, A.; GERYA, T.: 07.-12.04.2019, European Geosciences Union General Assembly 2019, Vienna, Austria: "Grain size reduction as a weakening mechanism in 3D-numerical models: Is it sufficient to initiate and stabilise transform faults?", Geophysical Research Abstracts 21, EGU2019-16904, 2019

SIEBERT, J.; KUBIK, E.; MAHAN, B.M.; BLANCHARD, I.; CREECH, J.; MOYNIER, F.: 09.-13.12.2019, AGU Fall Meeting, San Francisco, USA[*B]: "Tracing Earth's volatile delivery with tin", Abstract V52A-06

SIERSCH, N.C.: 10.05.2019, Sorbonne Université, IMPMC, Paris, France: "Elasticity of akimotoite up to transition zone pressures"

SIERSCH, N.C.; LIU, Z.; BOFFA BALLARAN, T.; KURNOSOV, A.; ISHII, T.; CRINITI, G.; FROST, D.; YU, T.; WANG, Y.: 31.05.-01.06.2019, JSPS Japanese-German graduate externship International Workshop on 'Volatile Cycles', Tokyo, Japan: "The influence of Al substitution on the elastic and structural properties of $MgSiO_3$-akimotoite"

SIERSCH, N.C.; KURNOSOV, A.; BOFFA BALLARAN, T.; CRINITI, G.; ISHII, T.; FROST, D.: 18.-23.08.2019, Goldschmidt 2019, Barcelona, Spain: "The elastic properties of $MgSiO_3$-akimotoite at transition zone pressures"

STEINLE-NEUMANN, G.; WAGLE, F.: 26.-30.05.2019, Japan Geoscience Union Meeting (JpGU2019), Chiba, Japan: "*P-V-T* equation-of-state to the TPa regime for liquid Fe from *ab initio* simulations"

STEINLE-NEUMANN, G.: 27.05.2019, Ehime University, Geodynamics Research Center, Matsuyama, Japan: "*P-V-T* equation-of-state of liquid Fe to the TPa regime from *ab initio* simulations, and what we learn for super-Earth interiors"

STEINLE-NEUMANN, G.; WAGLE, F.: 03.-04.06.2019, Earth, Sea and Sky V: International Joint Graduate Program Workshop, Tohoku University, Sendai, Japan: "*P-V-T* equation-of-state to the TPa regime for liquid Fe from *ab initio* simulations"

STEINLE-NEUMANN, G.: 10.06.2019, Tokyo Institute of Technology, Earth-Life Science Institute, Tokyo, Japan: "*P-V-T* equation-of-state of liquid Fe to the TPa regime from *ab initio* simulations"

STEINLE-NEUMANN, G.: 10.06.2019, Tokyo Institute of Technology, Earth-Life Science Institute, Tokyo, Japan: "A few thoughts about electrical conductivity of Fe-alloys"

STEINLE-NEUMANN, G.: 12.07.2019, University of Rostock, Workshop on High Energy Density Physics, Rostock, Germany: "Electrical conductivity of compressed iron and iron alloys from *ab initio* simulations"

STEINLE-NEUMANN, G.; WAGLE, F.: 15.-20.09.2019, European Planetary Science Congress (EPSC) – Division of Planetary Science (DPS) Joint Meeting, Geneva, Switzerland: "P-V-T equation-of-state to the TPa regime for liquid Fe from *ab initio* simulations", Abstract EPSC-DPS2019-274

STEINLE-NEUMANN, G.: 09.-11.10.2019, 8th Joint Workshop on High Pressure, Planetary and Plasma Physics (HP4), Dresden, Germany: "Mass transport and structural properties of binary liquid iron alloys at high pressure"

THIELMANN, M.; GOLABEK, G.; MARQUARDT, H.: 01.02.2019, CREEP Final Workshop, Les Houches, France: "Deforming two-phase media – From Topology to Rheology"

THIELMANN, M.; MARQUARDT, H.; GOLABEK, G.: 07.-12.04.2019, European Geosciences Union General Assembly 2019, Vienna, Austria: "From topology to rheology: Impact of weak phase distribution effective rock rheology", Geophysical Research Abstracts 21, EGU2019-17390, 2019

THIELMANN, M.; DURETZ, T.: 10.05.2019, Specialist discussion meeting of the Royal Astronomical Society, London, U.K.: "Earthquakes below the brittle–ductile transition – The role of grain size assisted thermal runaway"

THIELMANN, M.; DURETZ, T.: 26.-30.05.2019, Japan Geoscience Union Meeting (JpGU2019), Chiba, Japan: "Deep intraslab earthquake rupture due to grain size assisted thermal runaway"

THIELMANN, M.; GOLABEK, G.; MARQUARDT, H.: 31.05.-01.06.2019, JSPS Japanese-German graduate externship International Workshop on 'Volatile Cycles', Tokyo, Japan: "Ferropericlase control of lower mantle rheology – Impact of phase morphology"

THIELMANN, M.; DURETZ, T.: 01.11.2019, Structural Geology and Tectonic Seminar, ETH Zürich, Switzerland: "Earthquakes and plate tectonics - the importance of ductile weakening mechanisms"

THIELMANN, M.; GOLABEK, G.; MARQUARDT, H.: 18.11.2019, Deep Earth Mini Symposium, Münster, Germany: "Ferropericlase control of lower mantle rheology – Impact of phase morphology"

TRYBEL, F.; STEINLE-NEUMANN, G.; MEIER, T.: 14.-18.01.2019, Workshop on Crystal Structure Prediction, ICTP Trieste, Italy: "Proton dynamics in high-pressure ice-VII from DFT"

TRYBEL, F.; STEINLE-NEUMANN, G.; MEIER, T.: 04.-08.03.2019, APS March Meeting, Boston, USA: "Proton dynamics in high-pressure ice-VII from DFT"

TRYBEL, F.; MEIER, T.; WANG, B.; STEINLE-NEUMANN, G.: 26.08.2019, Linköping University, Sweden: "Structural and electronic properties of compressed H-bonded systems from DFT"

TRYBEL, F.; ERREA, I.; ADAMS, D.; WENZ, M.; MONACELLI, L.; CHURAKOV, S.; CALANDRA, M.; MAURI, F.; BIANCO, R.; PASSERONE, D.; STEINLE-NEUMANN, G.: 15.-20.09.2019, European Planetary Science Congress (EPSC) – Division of Planetary Science (DPS) Joint Meeting, Geneva, Switzerland: "B1-B2 phase transition in MgO from anharmonic *ab initio* lattice dynamics at conditions of super-Earth interiors", Abstract EPSC-DPS2019-556

TRYBEL, F.; ERREA, I.; ADAMS, D.; WENZ, M.D.; MONACELLI, L.; CHURAKOV, S.; CALANDRA, M.; MAURI, F.; BIANCO, R.; PASSERONE, D.; STEINLE-NEUMANN, G.: 09.-11.10.2019, 8th Joint Workshop on High Pressure, Planetary and Plasma Physics (HP4), Dresden, Germany: "B1-B2 phase transition in MgO from anharmonic *ab initio* lattice dynamics at conditions of super-Earth interiors"

UENVER-THIELE, L.; WOODLAND, A.B.; BOFFA BALLARAN, T.; MIYAJIMA, N.: 22.-25.09.2019, GeoMünster 2019, Münster, Germany*A: "Phase relations of Al-bearing $MgFe_2O_4$: Implications for natural occurences in diamond"

WALTE, N.; SOLFERINO, G.; GOLABEK, G.: 23.-28.06.2019, Gordon Research Conference – Origins of Solar Systems, South Hadley, USA: "From microstructure to planetesimal evolution: An experimental approach to pallasite formation"

WINKLER, B.; MCCAMMON, C.: 24.-26.10.2019, Deep Carbon 2019, Washington D.C., USA: "Structures, properties and reactions of carbonates at high pressures and temperatures, CarboPaT"

XIE, L.; YONEDA, A.; YAMAZAKI, D.; MANTHILAKE, G.; HIGO, Y.; TANGE, Y.; GUIGNOT, N.; KING, A.; ANDRAULT, D.: 20.05.2019, Carnegie Institution of Washington, Geophysical Laboratory, Washington D.C., USA: "Viscosity of magma ocean and the primordial structure of Earth's silicate mantle"

XIE, L.; NISHIDA, K.; ISHII, T.; CHANYSHEV, A.; BONDAR, D.; KATSURA T.: 18.-21.03.2019, Joint Symposium of Misasa 2019 & Core-Mantle Coevolution, Misasa, Japan (*invited*): "Simultaneously generation of ultra-high pressure and high temperature by combining boron-doped diamond heater and sintered diamond anvils"

XIE, L.; YONEDA, A.; YAMAZAKI, D.; MANTHILAKE, G.; HIGO, Y.; TANGE, Y.; GUIGNOT, N.; KING, A.; ANDRAULT, D.: 28.02.-02.03.2019, Science and Technology of Nano-Polycrystalline Diamond 2019, Ehime University, Geodynamics Research Center, Matsuyama, Japan: "Boron-doped diamond in multianvil apparatus and its implication for *in situ* falling sphere viscometry"

XIE, L.; YONEDA, A.; YAMAZAKI, D.; MANTHILAKE, G.; HIGO, Y.; TANGE, Y.; GUIGNOT, N.; KING, A.; ANDRAULT, D.: 25.02.2019, Zhejiang University, School of Earth Sciences, Zhejiang, P.R. China: "Viscosity of magma ocean and the primordial structure of Earth's silicate mantle"

XIE, L.; YONEDA, A.; YAMAZAKI, D.; MANTHILAKE, G.; HIGO, Y.; TANGE, Y.; GUIGNOT, N.; KING, A.; ANDRAULT, D.: 23.02.2019, China Univeristy of Geosciences, State Key Laboratory of Geological Processes and Mineral Resources, Wuhan, P.R. China: "Viscosity of magma ocean and the primordial structure of Earth's silicate mantle"

ZHANG, B.; REGER, P.M.; GANNOUN, A.; BOYET, M.; SCHRADER, D.L.; WADHWA, M.; FERRIÈRE, L.; BOUVIER, A.: 07.-12.07.2019, 82nd Annual Meeting of the Meteoritical Society, Sapporo, Japan: "Pb-Pb chronometry of impact melts from lunar meteorite Oued Awlitis 001", Abstract 6479

ZHU, C.; SCHARDT, C.; WANG, S.; WAZYLENKI, L.; WITHERS, A.C.; BOUVIER, A.: 03.-06.03.2019, Prospectors & Developers Association of Canada Convention, Toronto, Canada: "Ni isotopic fractionation associated with Ni mineralization in the Zambales ophiolite complex and Palawan ophiolite complex, Philippines"

ZHU, C.; SCHARDT, C.; WANG, S.; WAZYLENKI, L.; WITHERS, A.C.; BOUVIER, A.: 13.-15.05.2019, Geological Association of Canada (AGC), Canada Mineralogical Association (CMA) and International Association of Hydrogeologists (IAH) Annual Meeting, Québec City, Canada: "Ni isotopic fractionation associated with Ni mineralization in the Zambales ophiolite complex and Palawan ophiolite complex, Philippines"

ZUCCHINI, A.; MCCAMMON, C.; COMODI, P.; FRONDINI, F.: 16.-19.09.2019, Congresso Nazionale Parma 2019 (SIMP-SGI-SOGEI), Parma, Italy: "*Ex situ* study of cation disorder in Fe-rich dolomites"

[*A] GeoMünster 2019 "Earth! Past, Present, Future" – the Annual Conference of the Deutsche Geologische Gesellschaft – Geologische Vereinigung (DGGV – The German Geological Society) and the Deutsche Mineralogische Gesellschaft (DMG – The German Mineralogical Society), 22.-25.09.2019, Münster, Germany

[*B] AGU: American Geophysical Union Fall Meeting, 09.-13.12.2019, San Francisco, USA

5.4 Lectures and seminars at Bayerisches Geoinstitut

BENNETT, Neil, University of California, Davis, Department of Earth and Planetary Science, Davis, USA: "Noble metal logistics: Distributing highly siderophile elements between the core and mantle", 10.07.2019

BOUVIER, Audrey, Bayerisches Geoinstitut, Bayreuth, Germany: "Making planets: finding a recipe for Earth", *Academy Commission Business Meeting*, 16.05.2019

CHEN, Huawei, Arizona State University, School of Earth and Space Exploration, Tempe, USA: "A new iron hydroxide phase stable in hydrous lower-mantle systems", 16.12.2019

CITRONI, Margherita, Nature Research Berlin, Germany: "Publishing in Nature Research journals", 15.05.2019

DI GENOVA, Danilo, Technische Universität Clausthal, Institut für Nichtmetallische Werkstoffe, Clausthal-Zellerfeld, Germany: "From macro to micro to nano: relationships between volcanic processes and dynamics of silicate melts", 17.07.2019

DIETRICH, Wieland, Max-Planck-Institut für Sonnensystemforschung, Göttingen, Germany: "Saturn's global atmospheric dynamics – effects of He-rain and a sandwiched stably stratified layer", 17.01.2019

DRĄŻKOWSKA, Joanna, Ludwig-Maximilians-Universität, University Observatory, München, Germany: "Numerical models of dust growth and planet formation", 13.06.2019

DUFFY, Thomas, Princeton University, High-Pressure Mineral Physics and Materials Science Laboratory, Princeton, USA: "Lattice structure of shock-compressed minerals", 08.10.2019

DULLEMOND, Cornelis P., Ruprecht-Karls-Universität Heidelberg, Institut für Theoretische Astrophysik, Heidelberg, Germany: "Formation of chondrules", 05.12.2019

FACCENDA, Manuele, Università di Padova, Dipartimento di Geoscienze, Padua, Italy: "Subduction zone dynamics and structure from coupled geodynamic and seismological modeling", 09.05.2019

FEI, Hongzhan, Bayerisches Geoinstitut, Bayreuth, Germany: "Water-enhanced ionic conductivity of olivine", *Academy Commission Business Meeting*, 16.05.2019

FURUKAWA, Yoshihiro, Tohoku University, Department of Earth and Planetary Materials Science, Sendai, Japan: "Prebiotic organic geochemistry and high pressure geoscience", 14.02.2019

HIN, Remco, University of Bristol, School of Earth Sciences, Bristol, U.K.: "Does accretional vapour loss play a dominant role in shaping planetary compositions?", 23.07.2019

HOWARD, Christopher, University College London, Department of Earth Sciences, London, U.K.: "*Ab initio* simulations and neutron diffraction experiments of planetary ices under extreme conditions", 07.08.2019

KIM, Eun Jeong, Seoul National University, School of Earth and Environmental Sciences, Seoul, Korea: "Pressure-induced speciation of carbon in alkali silicate glasses at high pressure up to 14 GPa: Insights from high-resolution solid-state NMR", 28.03.2019

LIANG, Yuan, Tohoku University, Department of Earth and Planetary Materials Science, Sendai, Japan: "Ultralow-velocity zones possibly explained by light element-enriched iron compounds", 01.04.2019

LOVEDAY, John, University of Edinburgh, Center for Science at Extreme Conditions, Edinburgh, U.K.: "Neutron diffraction studies of Planets. How microscopic information can address macroscopic problems", 30.01.2019

MAGNI, Valentina, University of Oslo, Department of Geosciences, Section for Earth Evolution and Dynamics, Oslo, Norway: "Subduction & Water: from the surface to the deep Earth", 14.11.2019

MEIER, Thomas, Bayerisches Geoinstitut, Bayreuth, Germany: "On the way to NMR at mega-bar pressures – Observation of nuclear quantum effects and hydrogen bond symmetrisation in high pressure ice", *Academy Commission Business Meeting*, 26.04.2018

MOHIUDDIN, Anwar, Yale University, Department of Geology and Geophysics, New Haven, USA: "An experimental study of grain-size evolution and its rheological consequences during the phase transitions of olivine to its high-pressure polymorphs", 13.03.2019

MONSERRAT, Bartomeu, University of Cambridge, Cavendish Laboratory, Cambridge, U.K.: "Hydrogen under extreme pressure", 18.07.2019

NÉRI, Adrien, Institut de Recherche en Astrophysique et Planétologie, Toulouse, France: "Scenarios of metal-silicate differentiation in small-bodies: an experimental and modelling approach", 01.08.2019

OZAWA, Shin, Tohoku University, Earth and Planetary Material Physics Research Group, Sendai, Japan: "High-pressure minerals in meteorites and its implication for impact events in the solar system", 14.03.2019

PENA ALVAREZ, Miriam, University of Edinburgh, Center for Science at Extreme Conditions (CSEC), Edinburgh, U.K.: "Temperature dependence of rotational modes in fluid hydrogen and deuterium & Quantitative rotational to librational transitions in hydrogen", 29.10.2019

PUREVJAV, Narangoo, Okayama University, Institute for Planetary Materials, Misasa, Japan: "Hydration mechanism in Earth's mantle transition zone investigated by neutron diffraction", 18.09.2019

ROLF, Tobias, Universität Oslo, Department of Geosciences, Oslo, Norway: "Venus: what geoid, topography and surface age may tell us about its interior state and evolution", 25.07.2019

SAKAMAKI, Tatsuya, Tohoku University, Earth and Planetary Material Physics Research Group, Sendai, Japan: "Sound velocity measurements of iron-alloys at high pressure and temperature", 13.03.2019

SOUBIRAN, François, ENS Lyon, Laboratoire de Géologie de Lyon: Terre, Planète, Environnement, Lyon, France: "From atoms to Super-Earths: what can we learn from *ab initio* simulations?", 04.07.2019

TACKLEY, Paul, ETH Zürich, Institute of Geophysics, Zurich, Switzerland: "The key influence of magmatism on the thermo-chemical-tectonic evolution of terrestrial planets", 24.10.2019

THIELMANN, Marcel, Bayerisches Geoinstitut, Bayreuth, Germany: "Impact of ferropericlase elongation on lower mantle rheology", 11.07.2019

THIELMANN, Marcel, Bayerisches Geoinstitut, Bayreuth, Germany: "The importance of the microscale for localization processes in the Earth", 07.11.2019

VAN HUNEN, Jeroen, Durham University, Department of Earth Sciences, Durham, U.K.: "The evolution of subduction from the Archean to today", 31.01.2019

XIE, Longjian, Bayerisches Geoinstitut, Bayreuth, Germany: "Viscosity of the magma ocean and the primordial structure of Earth's silicate mantle", 10.10.2019

5.5 Conference organization

01.-02.04.2019, Workshop on Giant Collisions and their Effects on the Thermochemical Evolution of Planets, Berlin, Germany (G. GOLABEK)

07.-12.04.2019, European Geosciences Union General Assembly 2018, Vienna, Austria: "Terrestrial Planet Evolution: Interior/exterior coupling, feedbacks and interaction" (G. GOLABEK, C. GILLMANN)

07.-12.04.2019, European Geosciences Union General Assembly 2019, Vienna, Austria: "Experimental Mineralogy, Petrology and Geochemistry" (J. INGRIN, C.A. MCCAMMON, B. WOOD, M. WILKE)

07.-12.04.2019, European Geosciences Union General Assembly 2018, Vienna, Austria: "Quantitative structural geology: 3D characterisation, analysis and modelling" (B. GRASEMANN, M. DABROWSKI, F. HAWEMANN, M. THIELMANN, A. BISTACCHI, L. PENASA, S. THIELE)

26.-30.05.2019, Japan Geoscience Union Meeting (JpGU2019), Chiba, Japan: "Role of volatiles on Earth and planetary dynamics" (T. ISHII, B. MYSEN, E. OHTANI, M. NAKAMURA)

26.-30.05.2019, Japan Geoscience Union Meeting (JpGU2019), Chiba, Japan: "Intraslab and intraplate earthquakes" (S. KITA, T. OHUCHI, M. THIELMANN, R. OKUWAKI)

07.-12.07.2019, Member of Scientific Program Committee for the 82nd Annual Meeting of the Meteoritical Society, Sapporo, Japan (A. BOUVIER, full list https://www.metsoc19-sapporo.com/organizing-committee/)

18.-23.08.2019, Co-Convener of 4 sub-sessions 01a "Planetary Chemistry in the Age of Solar System Exploration", Goldschmidt Conference, Barcelona, Spain (A. BOUVIER, M. TUITE)

15.-20.09.2019, European Planetary Science Congress (EPSC) – Division of Planetary Science (DPS) Joint Meeting, Geneva, Switzerland: Session TP10/OPS14 "Characterizing Matter in Planetary Interiors: From Massive Giants to Volcanic Worlds" (F. SOHL, K. APPEL, D.J. BOWER, C. DORN, M. FRENCH, H. MASSOL, N. NETTELMANN, L. NOACK, A.V. OZA, G. STEINLE-NEUMANN)

22.-25.09.2019, GeoMünster 2019, Münster, Germany: Session 5f) "The distribution and influence of volatile elements in the Earth's interior and their exchange with the surface" (D.J. FROST, V. MATJUSCHKIN)

09.-13.12.2019, AGU Fall Meeting 2019, San Francisco, USA: "Earth and Planetary Volatiles from the Inside out" (T. GU, J. LIU, C.A. MCCAMMON, W. DU, C. GILLMANN, V. STAGNO)

6. Visiting scientists

6.1 Visiting scientists funded by the Bayerisches Geoinstitut

BENNETT, Neil, University of California, Davis, Department of Earth and Planetary Science, Davis, USA: 08.-13.07.2019

CHEN, Huawei, Arizona State University, School of Earth and Space Exploration, Tempe, USA: 15.-17.12.2019

DI GENOVA, Danilo, Technische Universität Clausthal, Institut für Nichtmetallische Werkstoffe, Clausthal-Zellerfeld, Germany: 16.-19.07.2019

DOLEJŠ, David, Universität Freiberg, Institut für Geo- und Umweltnaturwissenschaften, Freiberg, Germany: 18.-22.02.2019

DOLINSCHI, Jonathan, Arizona State University, School of Earth and Space Exploration, Tempe, USA: 06.-12.01.2019

DRĄŻKOWSKA, Joanna, Ludwig-Maximilians-Universität, University Observatory, München, Germany: 13.06.2019

DULLEMOND, Cornelis P., Ruprecht-Karls-Universität Heidelberg, Institut für Theoretische Astrophysik, Heidelberg, Germany: 04.-06.12.2019

DWIVEDI, Anand, University of Wisconsin-Milwaukee, Department of Physics, Milwaukee, USA: 25.06.-20.08.2019

FACCENDA, Manuele, Università di Padova, Dipartimento di Geoscienze, Padua, Italy: 07.-10.05.2019

HIN, Remco, University of Bristol, School of Earth Sciences, Bristol, U.K.: 21.-24.07.2019

HOWARD, Christopher, University College London, Department of Earth Sciences, London, U.K.: 07.-08.08.2019, 29.09.-01.10.2019

MARQUARDT, Katharina, Imperial College London, Department of Materials, London, U.K.: 24.-29.11.2019

MASOTTA, Matteo, Università di Pisa, Dipartimento di Scienze della Terra, Pisa, Italy: 14.-21.02.2019

MOHIUDDIN, Anwar, Yale University, Department of Geology and Geophysics, New Haven, USA: 11.-14.03.2019

MONSERRAT, Bartomeu, University of Cambridge, Cavendish Laboratory, Cambridge, U.K.: 17.-18.07.2019

PENA ALVAREZ, Miriam, University of Edinburgh, Center for Science at Extreme Conditions (CSEC), Edinburgh, U.K.: 28.-30.10.2019

PUREVJAV, Narangoo, Okayama University, Institute for Planetary Materials, Misasa, Japan: 16.-20.09.2019

REGER, Philip, University of Western Ontario, London, Ontario, Canada: 22.-24.05.2019

ROLF, Tobias, Universität Oslo, Department of Geosciences, Oslo, Norway: 23.-26.07.2019

SCHMALHOLZ, Stefan, Université de Lausanne, Institut des sciences de la Terre, Lausanne, Switzerland: 06.-08.11.2019

SELIUTINA, Natalia, Moscow State University, Institute of Experimental Mineralogy, Chernogolovka, Moscow region, Russia: 01.08.-29.09.2019

SOUBIRAN, François, ENS Lyon, Laboratoire de Géologie de Lyon: Terre, Planète, Environnement, Lyon, France: 02.-05.07.2019

TACKLEY, Paul, ETH Zürich, Institute of Geophysics, Zurich, Switzerland: 23.-25.10.2019

VAN HUNEN, Jeroen, Durham University, Department of Earth Sciences, Durham, U.K.: 30.01.-01.02.2019

WALTE, Nico, TU München, Forschungs-Neutronenquelle Heinz Maier-Leibnitz (FRM II), Garching, Germany: 18.-20.02.2019, 07.-08.08.2019, 30.09.-01.10.2019

6.2 Visiting scientists supported by other externally funded BGI projects

ASLANDUKOV, Andrey, Lomonossow-Universität Moskau, Russia: 15.-18.04.2019 (DFG[*B])

ASSIS FERNANDES, Vera, University of Manchester, School of Earth and Environmental Sciences, Manchester, U.K.: 29.09.-01.10.2019 (IRTG[*C])

CITRONI, Margherita, Nature Research Berlin, Germany: 15.-16.05.2019 (DFG[*B])

LONGO, Michaela, CANON, London, U.K.: 18.-19.10.2019 (IRTG[*C])

MAN, Lianjie, Center for High Pressure Science & Technology Advanced Research (HPSTAR), Shanghai, P.R. China: 30.04.-04.05.2019 (DFG[*B])

NÉRI, Adrien, Institut de Recherche en Astrophysique et Planétologie, Toulouse, France: 31.07.-02.08.2019 (DFG[*B])

PAMATO, Martha, Università di Padova, Dipartimento di Geoscienze, Padua, Italy: 18.-19.10.2019 (IRTG[*C])

WALTE, Nico, TU München, Forschungs-Neutronenquelle Heinz Maier-Leibnitz (FRM II), Garching, Germany: 12.-13.02.2019, 14.-17.05.2019, 22.-23.05.2019 (BMBF[*A])

[*A] BMBF: Bundesministerium für Bildung und Forschung

[*B] DFG: Deutsche Forschungsgemeinschaft

[*C] IRTG: International Research Training Group "Deep Earth Volatile Cycles" (DFG)

6.3 Visiting scientists supported by the DFG Core Facility programme

ALLABAR, Anja, Eberhard Karls Universität Tübingen, Experimentelle Mineralogie, Tübingen, Germany: 04.-08.03.2019

KISEEVA, Kate, University College Cork, School of Biological, Earth and Environmental Sciences, Cork, U.K.: 06.-15.05.2019

KUBIK, Edith, Institut de Physique du Globe de Paris, France: 24.02.-01.03.2019

LIBON, Lélia, Universität Potsdam, Institut für Geowissenschaften, Potsdam, Germany: 10.-13.07.2019

MATJUSCHKIN, Vladimir, Johann Wolfgang Goethe-Universität, Physikalisch-Chemische Mineralogie, Frankfurt/M., Germany: 11.-17.02.2019, 21.-27.07.2019

NOWAK, Marcus, Eberhard Karls Universität Tübingen, Experimentelle Mineralogie, Tübingen, Germany: 04.-08.03.2019

OTTERSBERG, Niklas, Ruhr-Universität Bochum, Institut für Geologie, Mineralogie und Geophysik, Bochum, Germany: 04.-09.02.2019

PLÜCKTHUN, Christian, European XFEL, Schenefeld, Germany: 19.-25.05.2019, 01.-15.07.2019

UENVER-THIELE, Laura, Johann Wolfgang Goethe-Universität, Physikalisch-Chemische Mineralogie, Frankfurt/M., Germany: 11.-17.02.2019, 21.-27.07.2019

6.4 Visitors (externally funded)

AKULENKO, Alena, Lomonosov Moscow State University, Moscow, Russia: 17.-24.02.2019

ARAYA, Naoki, Tohoku University, Department of Earth Science, Sendai, Japan: 13.-22.02.2019, 30.09.-08.10.2019

BAN, Rintaro, Tohoku University, Earth and Planetary Material Physics Research Group, Sendai, Japan: 28.02.-10.03.2019, 19.08.-16.09.2019

BERGERMANN, Armin, Universität Rostock, Institut für Physik, Rostock, Germany: 06.-09.10.2019

DIETRICH, Wieland, Max-Planck-Institut für Sonnensystemforschung, Göttingen, Germany: 17.01.2019

DUFFY, Thomas, Princeton University, High-Pressure Mineral Physics and Materials Science Laboratory, Princeton, USA: 06.-09.10.2019

FUKUSHIMA, Ryo, Tohoku University, Center for Northeast Asian Studies, Sendai, Japan: 03.-16.11.2019

FURUKAWA, Yoshihiro, Tohoku University, Department of Earth and Planetary Materials Science, Sendai, Japan: 14.-15.02.2019

GORELOVA, Liudmila, Saint-Petersburg State University, Department of Crystallography, 14.10.-13.12.2019

HUANG, Yongsheng, Tohoku University, Department of Earth and Planetary Materials Science, Sendai, Japan: 23.02.-22.03.2019, 06.-22.04.2019, 24.08.-15.10.2019

IKEDA, Osamu, Tohoku University, Department of Earth Science, Sendai, Japan: 19.08.-16.09.2019

ISKRINA, Anastasiya, Lomonosov Moscow State University, Department of Petrology, Moscow, Russia: 08.07.-18.08.2019

KAWANOBE, Hiroyuki, Tohoku University, Earth and Planetary Material Physics Research Group, Sendai, Japan: 11.-15.03.2019

KIM, Eun Jeong, Seoul National University, School of Earth and Environmental Sciences, Seoul, Korea: 27.-30.03.2019

KUDRYAVTSEV, Daniil, Gubkin Russian State University of Oil and Gas, Moscow, Russia: 26.02.-30.04.2019

LANDI, Anna Irene, Università degli Studi di Firenze, Dipartimento di Scienze della Terra, Firenze, Italy: 01.01.-31.01.2019

LIANG, Yuan, Tohoku University, Department of Earth and Planetary Materials Science, Sendai, Japan: 17.03.-06.04.2019, 12.-16.04.2019

LOVEDAY, John, University of Edinburgh, Center for Science at Extreme Conditions, Edinburgh, U.K.: 30.01.-02.02.2019

MAGNI, Valentina, University of Oslo, Department of Geosciences, Section for Earth Evolution and Dynamics, Oslo, Norway: 13.-16.11.2019

MARQUARDT, Katharina, Imperial College London, Department of Materials, London, U.K.: 23.-26.04.2019

MATJUSCHKIN, Vladimir, Johann Wolfgang Goethe-Universität, Physikalisch-Chemische Mineralogie, Frankfurt/M., Germany: 21.-26.10.2019, 26.11.-01.12.2019

MURANUSHI, Miki, Tohoku University, Earth and Planetary Material Physics Research Group, Sendai, Japan: 28.02.-10.03.2019, 01.-16.09.2019

MUTO, Jun, Tohoku University, Division of Geosphere Evolution, Sendai, Japan: 06.-09.10.2019

NAKAJIMA, Ayano, Tohoku University, Department of Earth Science, Sendai, Japan: 19.-30.08.2019

NAKAMURA, Michihiko, Tohoku University, Department of Earth Science, Sendai, Japan: 26.09.-09.10.2019

OHASHI, Tomonori, Tohoku University, Department of Earth Science, Sendai, Japan: 01.-14.01.2019, 11.07.-05.08.2019

OZAWA, Shin, Tohoku University, Earth and Planetary Material Physics Research Group, Sendai, Japan: 11.-15.03.2019

PETITGIRARD, Sylvain, ETH Zurich, Institute of Geochemistry and Petrology, Zurich, Switzland: 23.-26.07.2019

PRIMOCERIO, Jennifer, Ruhr-Universität Bochum, Institut für Geologie, Mineralogie und Geophysik, Bochum, Germany: 05.-28.04.2019, 24.11.-01.12.2019

REGIER, Margo, University of Alberta, Faculty of Science, Edmonton, Canada: 04.-11.09.2019

RIDOLFI, Filippo, Università degli Studi di Urbino "Carlo Bo", Department of Earth, Life and Environmental Sciences DISTEVA, Urbino, Italy: 09.-20.12.2019

ROBERT, Boris, University of Oslo, Center of Earth Evolution and Dynamics, Oslo, Norway: 04.-08.02.2019, 15.-24.04.2019, 11.-14.06.2019, 05.-09.08.2019, 08.-11.10.2019

SAKAMAKI, Tatsuya, Tohoku University, Earth and Planetary Material Physics Research Group, Sendai, Japan: 11.-15.03.2019

MÉNDEZ, Alba San José, Deutsches Elektronen-Synchrotron DESY, Hamburg, Germany: 03.-06.12.2019

SAWA, Sando, Tohoku University, Department of Earth Science, Sendai, Japan: 18.-19.09.2019, 26.09.-24.10.2019

SPIVAK, Anna, Institute of Experimental Mineralogy, Chernogolovka, Moscow region, Russia: 01.07.-31.07.2019

SUZUKI, Akio, Tohoku University, Earth and Planetary Material Physics Research Group, Sendai, Japan: 01.-14.01.2019, 28.02.-10.03.2019, 19.08.-16.09.2019

TAKAHASHI, Naoko, Tohoku University, Department of Earth Science, Sendai, Japan: 26.09.-05.10.2019

TAKAYA, Masaki, Kyoto University, Division of Earth and Planetary Sciences, Kyoto, Japan: 24.-28.02.2019

TANG, Hu, Center for High Pressure Science & Technology Advanced Research (HPSTAR), Shanghai, P.R. China: 20.05.-21.06.2019

TSUJIMORI, Tatsuki, Tohoku University, Center for Northeast Asian Studies, Sendai, Japan: 03.-09.11.2019

TSUSHIMA, Naoya, Tohoku University, Department of Earth Science, Sendai, Japan: 26.09.-09.10.2019

UENVER-THIELE, Laura, Johann Wolfgang Goethe-Universität, Physikalisch-Chemische Mineralogie, Frankfurt/M., Germany: 21.-26.10.2019, 26.11.-01.12.2019

WANG, Liao, Leibnitz Universität Hannover, Institute of Dynamics and Vibration Research, Hannover, Germany: 25.-26.02.2019

WEI, Chen, University of Chinese Academy of Sciences, Beijing, P.R. China: 01.-26.01.2019

WEI, Qingguo, Ludwig-Maximilians-Universität, Department für Geo- und Umwelt-wissenschaften, München, Germany: 02.-06.05.2019

SU, Xiaowan, Center for High Pressure Science & Technology Advanced Research (HPSTAR), Beijing, P.R. China: 22.09.-15.10.2019

XU, Fang, Sorbonne Université, Institut de minéralogie, de physique des matériaux et de cosmochimie (IMPMC), Paris, France: 10.-16.11.2019, 22.-31.12.2019

XU, Jianing, Center for High Pressure Science & Technology Advanced Research (HPSTAR), Beijing, P.R. China: 25.09.-31.12.2019

YUTANI, Taku, Tohoku University, Center for Northeast Asian Studies, Sendai, Japan: 01.01.-28.02.2019

ZAKHARCHENKO, Egor, Institute of Experimental Mineralogy, Chernogolovka, Moscow region, Russia: 01.07.-31.07.2019

7. Additional scientific activities

7.1 Habilitation/Theses

Habilitation

MARQUARDT, Katharina: Crystallization preferences at surfaces and interfaces.

Ph.D. theses

CHARITON, Stella: The sulfur content at sulfide saturation of carbonate melts and the origin of sulfide inclusions in diamonds.
DRUZHBIN, Dmitry: Silicon and oxygen volume diffusion in wadsleyite and implications to mantle transition zone rheology.
SIERSCH, Nicki-Caroline: The effect of Fe and Al on the elasticity of akimotoite.

M.Sc. theses

CRINITI, Giacomo: Seismic wave velocities in the middle of the Earth's lower mantle.
REBAZA, Anna M.: The sulfur content at sulfide saturation of carbonate melts and the origin of sulfide inclusions in diamonds.
WANG, Biao: Effect of $MgAlO_{2.5}$ component on element diffusivity of bridgmanite.

7.2 Honours and awards

EICHHEIMER, Philipp	JpGU 2019 Outstanding Student Presentation Award
ISHII, Takayuki	The Encouragement Prize awarded by The Japan Society of High Pressure Science and Technology
KEPPLER, Hans	Cross of Merit, Federal Republic of Germany

7.3 Editorship of scientific journals

AUDÉTAT, Audrey	Editor "Journal of Petrology"
BOUVIER, Audrey	Associate Editor "Geochimica et Cosmochimica Acta"
DUBROVINSKY, Leonid	Member, Editorial Board of the Journal of "High Pressure Research"
KEPPLER, Hans	Editorial Board "Contributions to Mineralogy and Petrology" Editorial Board "ACS Earth and Space Chemistry"
MCCAMMON, Catherine	Chief Editor and Managing Editor "Physics and Chemistry of Minerals"

MIYAJIMA, Nobuyoshi	Associate Editor "European Journal of Mineralogy"

7.4 Membership of scientific advisory bodies

BOFFA BALLARAN, Tiziana	Member of the Review Panel for allocation of beam-time at the Advanced Light Source, Berkeley Member, Dana Medal Committee, American Mineralogical Society
BOUVIER, Audrey	Vice-President, Committee AAPG 2019 "CE31 Physique subatomique, sciences de l'univers, structure et histoire de la Terre", Agence Nationale de la Recherche Chair, Nomenclature Committee of the Meteoritical Society Member, Scientific Committee of ATTARIK (All Together Taskforce for Advancing Research Innovation and Knowledge) Foundation for Meteoritics and Planetary Science for promoting the science of meteorites, planets and astronomy in the Arab world and African continent countries
DUBROVINSKY, Leonid	Member, Review Panel of Canadian Light Source Chair, Subcomission on Spectroscopy, Diffraction, and new Instrumentations in Mineral Physics of the International Mineralogical Association Member, Deep Carbon Observatory Scientific Steering Committee Member, Review Panel of PETRA III Member, Review Panel of Research Council of Lithuania
FROST, Dan	Chair of the Executive Committee for Elements Magazine Elected member of the Bavarian Academy of Sciences Member, German National Academy of Sciences (Leopoldina) Member of the Selection committee for Alexander von Humboldt Professorships Chair of the organizing committee for Goldschmidt 2021
KEPPLER, Hans	Member, German National Academy of Sciences (Leopoldina) Member, Bavarian Academy of Sciences Member, Deep Carbon Observatory Scientific Steering Committee Member, Alexander von Humboldt Foundation Selection Panel for Humboldt Awardees Member, Advisory Board, Dachverband Geowissenschaften

MCCAMMON, Catherine	Chair, Starting Grant Panel PE10, European Research Council Member, Board of Directors, American Geophysical Union Member, Council, International Mineralogical Association Member, Project Review Panel Nuclear and Inelastic Scattering, X-ray Emission, PETRA III Member, Science Programme Committee Deep Carbon 2019 Member, Scientific Committee EMPG XVII Member, Award Committee of the International Board on the Applications of Mössbauer Spectroscopy Chair, Sub-committee "Earth's Deep Interior" of the Commission of the Physics of Minerals, International Mineralogical Association Member, IASPEI/IAVCEI/IAGA Commission on Physics and Chemistry of Earth Materials

8. Scientific and Technical Personnel

Name		Position	Duration in 2019	Funding source
ABEYKOON, Sumith	M.Sc.	Wiss. Mitarbeiter	to 13.04. 14.04.-13.11. from 14.11.	IRTG DFG IRTG
AUDÉTAT, Andreas	Dr.	Akad. Oberrat		BGI
BAUER, Gerald	Dipl.-Ing. (FH)	Techn. Angestellter		BGI
BHAT, Shrikant	Dr.	Wiss. Mitarbeiter	to 30.06.	BMBF
BLANCHARD, Ingrid	Dr.	Wiss. Mitarbeiterin		DFG
BOFFA BALLARAN, Tiziana	Dr.	Akad. Oberrätin		BGI
BONDAR, Dmitry	M.Sc.	Wiss. Mitarbeiter		IRTG
BOUVIER, Audrey	Prof. Dr.	Professorin		BGI
BUCHERT, Petra		Fremdsprachen-sekretärin		BGI
BYKOV, Maxim	Dr.	Wiss. Mitarbeiter	to 15.07.	DFG
BYKOVA, Elena	Dr.	Wiss. Mitarbeiterin	01.05.-31.08.	DFG
CHANYSHEV, Artem	M.Sc.	Wiss. Mitarbeiter		BMBF
CHARITON, Stella	M.Sc.	Wiss. Mitarbeiterin	to 31.03.	DFG
CIALDELLA, Laura	M.Sc.	Wiss. Mitarbeiterin		IRTG
CRINITI, Giacomo	M.Sc.	Wiss. Mitarbeiter	from 15.10.	DFG
CZEKAY, Laura	M.Sc.	Wiss. Mitarbeiterin	from 01.09.	DFG
DINIUS, Anna		Verwaltungsangestellte	from 01.02.	BGI
DOMINIJANNI, Serena	M.Sc.	Wiss. Mitarbeiter		IRTG
DRUZHBIN, DMITRY	M.Sc.	Wiss. Mitarbeiter	to 30.09. from 01.10.	DFG EU
DUBROVINSKY, Leonid	Apl. Prof. Dr.	Akad. Direktor		BGI
EBERHARD, Lisa	M.Sc.	Wiss. Mitarbeiterin		IRTG
EICHHEIMER, Philipp	M.Sc.	Wiss. Mitarbeiter		IRTG
FANG, Jing	Dr.	Stipendiat	from 04.11.	DAAD
FEI, Hongzhan	Dr.	Wiss. Mitarbeiter	to 14.10. from 15.10.	DFG BGI
FERREIRA, Filippe	M.Sc.	Wiss. Mitarbeiter		DFG
FISCHER, Heinz		Mechaniker		BGI
FLANIGAN, Michaela	M.Sc.	Wiss. Mitarbeiterin	from 09.09.	Leibniz
FROST, Daniel	Prof. Dr.	Stellvertr. Leiter		BGI
GOLABEK, Gregor	Prof. Dr.	Professor		BGI
HEIDELBACH, Florian	Dr.	Wiss. Mitarbeiter		BGI
HOWARD, Christopher	Dr.	Wiss. Mitarbeiter	from 01.10.	BMBF

HUANG, Rong	M.Sc.	Wiss. Mitarbeiterin		Leibniz
IMMOOR, Julia	Dipl.-Geol.	Wiss. Mitarbeiterin	15.03.-31.10.	DFG
ISHII, Takayuki	Dr.	Forschungsstipendiat	to 31.03.	AvH
			from 01.04.	DFG
JOCHUM, Johanna	Dr.	Wiss. Mitarbeiterin	to 30.06.	BMBF
KATSURA, Tomoo	Prof. Dr.	Professor		BGI
KEPPLER, Hans	Prof. Dr.	Leiter		BGI
KHANDARKHAEVA, Saiana	M.Sc.	Wiss. Mitarbeiterin		DFG
KIM, Eun Jeong	Dr.	Wiss. Mitarbeiterin	from 01.10.	EU
KOEMETS, Egor	M.Sc.	Wiss. Mitarbeiter	to 30.09.	IRTG
			from 01.10.	BGI/VP
KOEMETS, Iuliia	M.Sc.	Wiss. Mitarbeiterin		DFG
KRAUßE, Detlef	Dipl.-Inform. (FH)	Techn. Angestellter		BGI
KRIEGL, Holger		Haustechniker		BGI
KRUPP, Alena	B.Sc.	Student. Hilfskraft	01.04.-30.09.	DFG
			from 01.10.	EU
KURNOSOV, Alexander	Dr.	Wiss. Mitarbeiter		DFG
LINHARDT, Sven		Elektrotechniker		BGI
MA, Ning	B.Sc.	Student. Hilfskraft	to 30.09.	DFG
			01.10.-30.11.	UBT
			from 01.12.	DFG
MAN, Lianjie	M.Sc.	Wiss. Mitarbeiter	from 09.12.	Leibniz
MARZOTTO, Enrico	M.Sc.	Wiss. Mitarbeiter		IRTG
MCCAMMON, Catherine	Privatdozentin Dr.	Akad. Direktorin		BGI
MEIER, Thomas	Dr.	Wiss. Mitarbeiter	to 31.05.	BGI/VP
			from 01.06.	DFG
MELAI, Caterina	M.Sc.	Wiss. Mitarbeiterin		IRTG
MIYAJIMA, Nobuyoshi	Dr.	Akad. Oberrat		BGI
NISHIDA, Keisuke	Dr.	Wiss. Mitarbeiter		DFG
NJUL, Raphael		Präparator		BGI
OHTANI, Eiji	Prof.	Forschungspreisträger	07.08.-31.10.	AvH
OVSYANNIKOV, Sergey	Dr.	Wiss. Mitarbeiter		DFG
POTZEL, Anke		Chem.-Techn. Assistentin		BGI
POTZEL, Janina		Sekretärin		BGI
PUTAK JURIČEK, Marija	M.Sc.	Wiss. Mitarbeiterin		IRTG
PUTRA, Rizaldi	B.Sc.	Student. Hilfskraft	from 11.11.	EU
RAMMING, Gerd		Elektroniker		BGI
RAUSCH, Oliver		Mechaniker		BGI

REBAZA MORILLO, Anna Mireia	B.Sc.	Student. Hilfskraft	to 31.03.	DFG
ROTHER, David Alexander		Präparator		BGI
ROTTIER, Bertrand	Dr.	Stipendiat	to 18.03.	SNSF
RUBIE, David C.	Prof. Dr.	Professor	to 30.04.	GIF
			from 01.05.	EU
RUSTIONI, Greta	M.Sc.	Wiss. Mitarbeiterin	to 30.09.	IRTG
			from 01.10.	DFG
SATTA, Niccolò	M.Sc.	Wiss. Mitarbeiter		IRTG
SCHARFENBERG, Romina	B.Sc.	Sekretärin		BGI
SCHULZE, Hubert		Präparator	to 30.11.	GIF
			from 01.12.	EU
SHCHEKA, Svyatoslav	Dr.	Wiss. Mitarbeiter	to 15.07.	DFG
SIERSCH, Nicki	M.Sc.	Wiss. Mitarbeiterin	to 10.10.	Leibniz
SILVA SOUZA, Danielle	B.Sc.	Student. Hilfskraft		DFG
SIMONOVA, Dariia	M.Sc.	Wiss. Mitarbeiterin	to 14.07.	DFG
STEINLE-NEUMANN, Gerd	Privatdozent Dr.	Akad. Oberrat		BGI
SZLACHTA, Victoria	B.Sc.	Student. Hilfskraft	to 30.09.	DFG
			01.10.-15.12.	UBT
			from 16.12.	DFG
THIELMANN, Marcel	Dr.	Wiss. Mitarbeiter		BGI/VP
TRENZ, Ulrike		Biol.-Techn. Assistentin		BGI
TRYBEL, Florian	M.Sc.	Wiss. Mitarbeiter		DFG
ÜBELHACK, Stefan		Mechaniker		BGI
VLASOV, Kirill	M.Sc.	Wiss. Mitarbeiter		DFG
WANG, Biao	B.Sc.	Student. Hilfskraft	to 30.09.	DFG
	M.Sc.	Wiss. Mitarbeiter	from 01.10.	DFG
WIESNER, Dorothea		Techn. Assistentin		BGI
WITHERS, Antony	Dr.	Wiss. Mitarbeiter		BGI
XIE, Longjian	Dr.	Wiss. Mitarbeiter	to 14.11.	EU
			from 15.11.	BGI/VP
YAO, Jie	M.Sc.	Wiss. Mitarbeiter		DFG
YUAN, Liang	Dr.	Wiss. Mitarbeiter	from 18.11.	BGI/VP

Abbreviations/explanations:

AvH	Alexander von Humboldt Foundation
BGI	Staff Position of Bayerisches Geoinstitut
BGI/VP	Visiting Scientists' Program of Bayerisches Geoinstitut
BMBF	Federal Ministry of Education and Research
DAAD	German Academic Exchange Service
DFG	German Science Foundation
EU	European Union
GIF	German-Israeli Foundation for Scientific Research and Development
IRTG	International Research Training Group "Deep Earth Volatile Cycles"
Leibniz	Leibniz-Preis der Deutschen Forschungsgemeinschaft Prof. Frost
SNSF	Swiss National Science Foundation
UBT	Universität Bayreuth

[1] freie Stellenmittel

Index

Obituary Ahmed El Goresy (* 28.10.1933, † 03.10.2019)

After his retirement at the MPI for Nuclear Physics in Heidelberg, Ahmed El Goresy worked from 2005 to 2017 as a guest scientist at Bayerisches Geoinstitut. He was famous as a meteorite researcher. Many international visitors came to Bayreuth to benefit from his unusual abilities in reflected light microscopy that allowed him to identify new and unusual phases in meteorites. While in Bayreuth, on most days he was probably the first person to start working at the institute very early in the morning. Aside from his activities in meteoritics, Ahmed also was a highly educated person with many interests. In addition to Arabic, his native language, he spoke German and English with perfection – but he also had a very good command of Latin and he could read some hieroglyphs. During his time in Bayreuth, he once gave a talk in which he pointed out that archeologists probably have misinterpreted the symbolic meaning of colors in ancient Egyptian paintings, because they did not take the long-term alteration of minerals into account, which were used as pigments in these paintings.

Ahmed El Goresy passed away peacefully at his home in Heidelberg on October 3, 2019, at the age of 85. We will miss him a lot.

Nachruf Ahmed El Goresy (* 28.10.1933, † 03.10.2019)

Nach seiner Emeritierung am MPI für Kernphysik in Heidelberg arbeitete Ahmed El Goresy von 2005 bis 2017 als Gastwissenschaftler am Bayerischen Geoinstitut. Er war ein weltberühmter Meteoritenforscher. Zahlreiche Wissenschaftler aus der ganzen Welt besuchten ihn in Bayreuth, um von seinen außergewöhnlichen Fähigkeiten in der Auflichtmikroskopie zu profitieren, die es ihm erlaubte, neue und ungewöhnliche Minerale in Meteoriten zu erkennen. In seiner Zeit in Bayreuth war er an den meisten Tagen wahrscheinlich die erste Person, die früh am Morgen angefangen hat am Institut zu arbeiten. Ahmed hatte zahlreiche Interessen neben der Meteoritenforschung. Außer Arabisch, seiner Muttersprache, sprach er perfekt Deutsch und Englisch. Er hatte jedoch auch sehr gute Kenntnisse in Latein und konnte manche Hieroglyphen lesen. Während seiner Zeit in Bayreuth gab er einen Seminarvortrag, in dem er erklärte, dass die symbolische Bedeutung verschiedener Farben in der altägyptischen Malerei von Archäologen wahrscheinlich falsch interpretiert worden ist, da sie die langfristige Umwandlung der als Pigmente verwendeten Minerale nicht berücksichtigt haben.

Ahmed El Goresy ist am 3. Oktober 2019 im Alter von 85 Jahren in seiner Wohnung in Heidelberg friedlich verstorben. Wir werden ihn sehr vermissen.